

**COMPOSITIONAL TRENDS THROUGH THE HOLOCENE MUD SUCCESSION OF THE
SOUTHWESTERN BLACK SEA SHELF, AND IMPLICATIONS FOR SEDIMENTARY
PROVENANCE AND WATER-LEVEL HISTORY**

by

© **Christopher J. Lister**

A Thesis submitted to the

School of Graduate Studies

in partial fulfillment of the requirements for the degree of

Master of Science

Department of Earth Sciences, Faculty of Science

Memorial University of Newfoundland

October 2014

St. John's, Newfoundland

Abstract

Piston core MAR02–45P and its trigger weight core (MAR02–45TWC) record sedimentation over the last 10.3 cal ka on the SW Black Sea shelf with only one hiatus (from 5.4–2.1 cal ka BP). Geochemical and mineralogical studies were undertaken on the fine fraction of these sediments in an attempt to better define lithologic units, and to search for evidence of changing provenance. Isopach maps were used to estimate the volume of sediments deposited on the shelf. This estimate of sediment volume was compared to expected deliverable volumes from local rivers, as calculated using a robust empirical equation for sediment flux, available from the literature.

Four geochemical units (Units A, B, C1, C2) were identified, in agreement with previous studies. Correlation tables expose four groups of similarly behaving elements that govern the geochemical trends throughout MAR02–45. There is carbonate group composed of Ca, Mg, and Sr, and a mainly detrital group believed to reside in aluminosilicate minerals composed of Sc, Fe, Co, Ce, La, Th and Y. In contrast, As, Rb, Br, Mn and Sr are interpreted to have entered the sediment from the water column, or were mobile during early diagenesis and Cu, Pb, Ni, Zn, U and V are interpreted to indicate adsorption onto fine-grained phyllosilicates and/or organic matter during early diagenesis. A ~45 cm upward adjustment in the placement of the previously recognized $\alpha 1$ key seismic marker in the core is suggested by the new geochemical data.

Unit C1 (10.3–8.4 cal ka BP) contains some detritus from local sources, especially marked by spikes in Cr abundance associated with sandy horizons. Unit C2 (8.4–7.5 cal ka BP) contains the familiar signatures of Unit C1 as well as a high TS concentration. This unit preserves the geochemical signature of a previously identified ‘first-pulse’ of Mediterranean water entering the Early Holocene Black Sea. Unit B (7.5–5.4 cal ka BP) records a well-oxygenated environment with abundant mollusk communities and infaunal burrows. Unit A (2.1–0 cal ka BP) chronicles the dysoxic conditions that continue to the present, and has higher than average abundances of the redox-sensitive elements Cu, Ni, Zn, Pb, U, and Th.

Grain size analysis on nearby core MAR05–50 shows a bimodal texture similar to that of loess found within the Danube drainage basin. Geochemical comparisons between two loess profiles and core MAR02–45 show similar abundances for only one element.

Mineralogically, Units A, B, and C are similar to one another except for a downcore increase in the abundance of calcite, some of which is likely detrital. Although specific sediment sources (provenance) could not be determined, it is concluded that the volume of sediment deposited in Unit C is too large to have been delivered from only local sources, indicating that the SW Black Sea shelf must have been in open communication with the larger Black Sea basin since ~10.3 cal ka BP. The geochemical and mineralogical data are consistent with this conclusion, although they cannot be used to quantify the contribution from the various potential sources in the western Black Sea.

Acknowledgements

Firstly I must express my gratitude and appreciation towards my co-supervisors, Dr. Richard Hiscott and Dr. Ali Aksu for the opportunity to undertake this thesis.

Without their support, constructive criticism, guidance, and patience this project would have never been possible.

Thank you to everyone who assisted in the collection of data. Especially Helen Gillespie for her instruction, experience, and patience, we spent many hours in the lab making (or attempting to make) clay mounts by different methods. Dr. Wanda Aylward is thanked for her time and expertise using the XRD at MUN; innumerable hours were spent in that lab, and it was always enjoyable. Lorna Williams instructed the author on the sampling, and processing procedures used to separate the various size fractions of sediment. My gratitude is also extended to Dr. Peta Mudie, for her invaluable comments, and insight into the world of micropaleontology. Thank you to G. Oiae and D. Jipa for provision of the Danube Delta samples, as well as C. Yaltrak for collecting the Thrace riverbed samples.

I would like to thank my co-workers and friends, Anna Linegar, Katey Roberts, Matt Crocker, Marina Joury, and more, for the conversations, both relevant and irrelevant to my thesis which kept me on-track, or relieved stress, both of which were essential to keep moving forward. Last but not least I would like to thank my family and friends in Kingston, Ontario.

Table of Contents

Abstract	ii
Acknowledgements	iv
Table of Contents	v
List of Tables	x
List of Figures	xiii
List of Equations	xvi
List of Symbols, Nomenclature and Abbreviations	xvii
List of Appendices	xviii
Chapter 1 Introduction.....	1
1.1 Introduction	1
1.1.1 Thesis Goals	1
1.1.2 Approach	3
1.2 Regional Overview	7
1.2.1 Oceanographic Setting.....	8
1.2.2 Geologic Setting	11
1.2.3 The Flood Hypothesis.....	12
1.2.4 The Outflow Hypothesis.....	14

1.2.5	The Oscillating Sea-level Hypothesis.....	16
1.2.6	Rivers.....	18
1.3	Geology of Surrounding Lands	20
1.3.1	Geology of Northern Thrace Drainage Basins Entering the Black Sea.....	20
1.3.2	Geology of Northwestern Anatolia.....	24
1.3.3	Geology of Mountain Belts in the Danube Drainage Basin	25
1.3.4	Loess.....	27
1.4	Relevant Previous Work in the Black Sea.....	35
1.4.1	Previous Work on Core MAR02–45 and around the core site	35
1.4.2	Previous Mineralogical and Geochemical Work in the Black Sea.....	40
1.4.3	Mineralogy and Geochemistry of the Danube System.....	48
1.5	Specific Thesis Objectives.....	50
Chapter 2	Methods	51
2.1	Sample Preparation.....	51
2.1.1	Availability of Samples and Restrictions on Sample Size	51
2.1.2	Preparation for XRD Analysis.....	53
2.2	Methods of Analyses	56
2.2.1	Selection of Geochemical Method.....	58
2.2.1	Factor Analysis	62
2.3	X–Ray Diffraction	62
2.3.1	Randomly Oriented Silt Mounts.....	63

2.3.2	Oriented Clay Mounts.....	64
2.3.3	<2 μm Mineral Abundances	66
2.4	Sediment Volumes and the BQART Equation	74
Chapter 3	Results	77
3.1	Sediment Volume Estimates.....	77
3.1.1	Isopach Measurement and Volume Estimate.....	77
3.1.2	BQART Equation and Volume Estimate.....	79
3.2	Texture.....	80
3.3	Silt Mineralogy	80
3.4	< 2 μm Fraction Mineralogy	82
3.5	Actlabs Geochemistry.....	98
3.5.1	Precision and Accuracy of Geochemical Analysis	98
3.5.2	Geochemical Data.....	112
3.5.3	X-ray Fluorescence.....	119
3.5.4	Conversion to Calcite-free Abundances	120
3.6	Factor Analysis	130
3.6.1	R-mode Factor Analysis	130
3.6.2	Q-mode Factor Analysis.....	132
3.7	Geochemical Spikes at Unit Boundaries	134
Chapter 4	Interpretation.....	138
4.1	Sediment Volume Estimate	138

4.2	Texture and Mineralogy	142
4.2.1	Silt Mineralogy	145
4.2.2	Clay Mineralogy	146
4.3	Geochemistry	149
4.3.1	Refinement in the Placement of the $\alpha 1$ Correlative Conformity	155
Chapter 5	Discussion.....	158
5.1	Unit C (10.3–7.5 cal ka BP)	159
5.2	Unit B (7.5–5.4 cal ka BP).....	164
5.3	Unit A (2.1–0 cal ka BP)	166
5.4	Changing Provenance	167
5.5	Evolution of sediment composition on the southwestern Black Sea shelf	168
5.6	Future Work.....	172
Chapter 6	Conclusions	175
References	180
Appendix 1	XRD Sample Preparation	I
Appendix 2	Underwood et al. (2003) clay mineral proportions	V
Appendix 3	Raw Geochemical Data	VI
Appendix 4	XRD Standards Analysis.....	XXVI
Appendix 5	XRF Data for Elements Analysed by XRF and ActLabs.....	XXIX

Appendix 6 Calcite-free downcore plotsXXX

List of Tables

Table 1.1 Locations and water depths of Black Sea cores used or referenced in this thesis	3
Table 1.2 Locations and elevations of Danube Delta samples taken in delta-top ponds ...	4
Table 1.3 Locations and elevations of Thrace river samples taken downstream from dammed reservoirs.	4
Table 1.4 Rivers in Thrace, extracted from Aksu et al. (2002).....	19
Table 1.5 Selected data from southwestern Hungarian loess deposits	32
Table 2.1 Detection limits of 49 elements using INAA and ICP-OES compared to elemental abundances of the average North American Shale.....	60
Table 2.2 Parameters used by Underwood et al. (2003) and in this thesis (MUN) and their effects on intensity measurements.	68
Table 2.3 Example of peak area manipulations on the clay-sized minerals found in MAR02-45 broken down into a 10-step method.....	69
Table 2.4 Values and meanings of variables found in the BQART equation.....	76
Table 3.1 Variations in abundance of minerals in the silt fraction through core MAR02- 45.....	84
Table 3.2 Variations in abundance of silt-sized minerals from potential source areas.....	87
Table 3.3 Peak areas of minerals in the clay-sized fractions of core MAR02-45, measured using MacDiff software	88

Table 3.4 Peak intensities of minerals in the clay-sized fractions of core MAR02–45, measured using MacDiff software	90
Table 3.5 Averages and standard deviations of the clay-sized minerals by unit	92
Table 3.6 INAA results for six samples from MAR02–45 with sufficient material for duplicate or triplicate analysis	100
Table 3.7 ICP-OES results for six samples from MAR02–45 with sufficient material for four to six independent analyses	102
Table 3.8 Sample codes and descriptions of eleven certified and prepared laboratory standards used by ActLabs for quality control purposes.	106
Table 3.9 Certified values for eleven standards used by ActLabs	107
Table 3.10 Measured and certified values for six elements determined by INAA, and a comparison to the mean and standard deviation of MAR02–45 samples.....	108
Table 3.11 Matrix of correlation coefficients for core MAR02–45.....	113
Table 3.12 Matrix of correlation coefficients for Unit A in core MAR02–45.....	114
Table 3.13 Matrix of correlation coefficients for Unit B in core MAR02–45.....	115
Table 3.14 Matrix of correlation coefficients for Unit C in core MAR02–45.....	116
Table 3.15 Ratios of oxide and elemental abundances in four samples run using INAA and ICP–OES at Actlabs (a) and the abundances for the same samples analyzed using XRF at Memorial University (b).....	121
Table 3.16 Average calcite-free concentration of Units A, B, and C of MAR02–45.....	128

Table 3.17 Average calcite-free concentration (ppm, unless otherwise noted) of potential source areas	129
Table 4.1 P-values for the Student t-test using calcite-free normalized data from Unit C1 of core MAR02–45, compared with calcite-free Hungarian and Moravian loess chemistry	156
Table A2.1 Clay proportions calculated using the methods of Underwood et al. (2003), after applying the kaolinite/chlorite split	V
Table A3.1 Raw geochemical data for Au, Ag, Cu, Cd, Mo, Pb, and Ni	VII
Table A3.2 Raw geochemical data for Zn, S, Al, As, Ba, Be, Bi, Br, Ca, and Co	X
Table A3.3 Raw geochemical data for Cr, Cs, Eu, Fe, Hf, Hg, Ir, K., Mg, and Mn.....	XIII
Table A3.4 Raw geochemical data for Na, P, Rb, Sb, Sc, Se, Sr, Ta, Ti, and Th	XVI
Table A3.5 Raw geochemical data for U, V, W, Y, La, Ce, Nd, Sm, Sn, and Tb	XX
Table A3.6 Raw data for Yb, Lu, mass, TS, TOC, Terr. TOC, and silicate total	XXIII
Table A4.1 Measured and certified values for elements analyzed using INAA. Only elements analyzed during both (2011 and 2014) runs are included.....	XXVII
Table A4.2 Measured and certified values for elements run using ICP analysis GXR-1, GXR-4, SDC-1, and OREAS 13b standards.....	XXVIII
Table A4.3 Measured and certified values for elements run using ICP analysis for the SCO-1, GXR-6, DNC-1a, SAR-M, and SBC-1 standards.....	XXIX

List of Figures

Figure 1.1 Isopach map from Aksu et al. (2002) showing locations and thickness of Holocene Muds	6
Figure 1.2 Major currents, gyres and eddies of the Black Sea	9
Figure 1.3 A simplified view of the coastal geology of the southwestern Black Sea.....	21
Figure 1.4 Map of loess and loess derivative deposits in the lower Danube Basin	29
Figure 1.5 The interconnections of Danube Basin loess deposits and their sources	31
Figure 1.6 Seismic section showing core site MAR02–45 and units 1B, 1C, and 1D	37
Figure 1.7 Selected proxy data from core MAR02–45	39
Figure 1.8 Clay mineral % in short cores from the southwestern Black Sea shelf.....	42
Figure 1.9 Core analysis from Major (2002) showing mineral abundances for carbonate and main clay minerals	45
Figure 2.1 Bulb-bottomed test tube and specially fabricated tapered stopper rod.....	55
Figure 2.2 Front-loaded-mount peak intensity vs. a spectrum from the same sample using the side-loaded method	57
Figure 3.1 Isopachs for seismic unit 1B showing the thickness and extent of lower Holocene mud deposits on the shelf	78
Figure 3.2 Grain size distribution plotted against composite depth in core MAR02–45 .	81
Figure 3.3 Abundance of minerals found in the silt fraction of core MAR02–45	83

Figure 3.4 Silicate mineral proportions in the silt-sized fraction through core MAR02–45	86
Figure 3.5 Cross-plots showing the inverse relationship between carbonates and clay minerals in the <2 μm size fraction (a), and the relationship between quartz and carbonate abundances in the <2 μm size fraction (b).....	93
Figure 3.6 Wt.% abundance of minerals found in the <2 μm fraction of core MAR02–45 after scaling using procedures in §2.4.3.....	94
Figure 3.7 Recalculated abundances of the four major phyllosilicate minerals scaled using Biscaye (1965) methods and normalized to 100%	96
Figure 3.8 <2 μm mineral abundances of potential source areas.....	97
Figure 3.9 Plots of measured versus certified values for all 10 elements determined by ICP-OES	109
Figure 3.10 Venn-style diagrams expressing the relationships between elements from correlation coefficient tables.....	117
Figure 3.11 % Ca in ActLabs data vs % calcite abundance determined by XRD analysis of the silt fraction of MAR02–45.....	122
Figure 3.12 Downcore plots of selected elements in MAR02–45.....	124
Figure 3.13 Downcore trends of recalculated calcite-free concentrations for the elements shown in Fig. 3.12, excluding Ca	126

Figure 3.14 Plot of loadings of variables on R-factors 1–4 and the variance accounted for by each factor	131
Figure 3.15 Q-factor plots (1–4) corresponding to R-factors (1–4) against depth	133
Figure 3.16 Calcite-free cross plots of some Unit A elements	136
Figure 3.17 Calcite-free cross plots of some Unit B elements.....	137
Figure 4.1 Comparison of grain size distribution of Hungarian loess to particle size distribution found in Unit C of core MAR05–50.....	143
Figure 4.2 Elevated chromium values seen in geochemical data compared to lithologic description of MAR02–45 between 700 and 800 cm depth	153
Figure 5.1 Dominant Q-factors and dominant elements through MAR02–45	169
Figure A6.1 Calcite-free downcore plots of As, Cu, Pb, V, Yb, Na, Hf, and U.....	XXX

List of Equations

Equation 2.1 Underwood et al. (2003) equation showing a linear relationship between the ratio of peak areas for quartz and calcite, and the ratio of their weight percentages	73
Equation 2.2 The relative proportion of dolomite to calcite using the peak intensity relationship for carbonate weight percentages (Royse et al., 1971)	74
Equation 2.3 The BQART equation (Syvitski and Milliman, 2007)	75
Equation 2.4 Calculating basin characteristics (Syvitski and Milliman, 2007)	75
Equation 2.5 The glacial erosion factor I (Syvitski and Milliman, 2007)	75

List of Symbols, Nomenclature and Abbreviations

α	A lowstand subaerial erosion surface, as well as a shelf-crossing unconformity on the southwestern Black Sea shelf.
$\alpha 1$	A local unconformity found at most core sites above the α unconformity.
$\alpha 2$	A local unconformity found above the α and $\alpha 1$ unconformities on the southwestern Black Sea shelf.
ka BP	Thousands of years before present.
^{14}C ka BP	Uncalibrated radiocarbon years before present.
cal yr BP	Calibrated calendar years before present.
Ma	Millions of years before present.
ActLabs	Activation Laboratories, Ancaster, Ontario
CTD	Conductivity, temperature, depth
HFSE	High field strength element
HREE	Heavy rare earth element
LREE	Light rare earth element
PSU	Practical salinity units
ICP-OES	Inductively coupled plasma-optical emission spectrometry
PDB	Pee Dee Belemnite
REE	Rare earth element
TOC	Total organic carbon
TS	Total Sulphur
WPF	Whole pattern fitting
XRD	X-ray diffraction
XRF	X-ray fluorescence

List of Appendices

Appendix 1 XRD Sample Preparation	I
Appendix 2 Underwood et al. (2003) Clay Proportions	IV
Appendix 3 Raw Geochemical Data.....	V
Appendix 4 Standards Analysis	XXVI
Appendix 5 XRF Data for Elements Analysed by XRF and ActLabs	XXIX
Appendix 6 Calcite-free Downcore Plots	XXX

Chapter 1 Introduction

1.1 Introduction

Since the end of the Younger Dryas (~12.9 cal ka BP) the Black Sea shelves have been transgressed from a lowstand of ~ -100 m (Aksu et al., 2002; Ryan et al., 2003; Lericolais et al., 2007). During and subsequent to the transgression, Holocene muds were deposited across the southwestern Black Sea shelf in variable thicknesses (rarely >15 m; mostly <10 m). The fine grain size of most of the Holocene succession below modern water depths of ~60 m (Hiscott and Aksu, 2002; Hiscott et al., 2007b; Flood et al., 2009) is attributed to the fact that the transgression was relatively rapid, with the Black Sea reaching a level of ~ -40 m by ~10 cal ka BP (Hiscott et al., 2007b; Giosan et al., 2009). Hence, water depths over much of the shelf have been below fair-weather wave base during most of the Holocene.

1.1.1 Thesis Goals

The primary aim of this research is to assess whether the provenance of the fine fractions (silt and clay) of the Holocene sediments on the southwestern Black Sea shelf might have changed since the earliest Holocene. This is an important question because Hiscott et al. (2007b) have claimed that the middle part of the southwestern shelf was fully open and connected to the deep Black Sea basin, and hence regional sediment sources, since ~10.3 cal ka BP (calibration from Mertens et al., 2012); whereas, Ryan et

al. (2003) and Lericolais et al. (2007) maintain that the central Black Sea had a level below the modern shelf edge until ~9.15 cal ka BP (calibration from Mertens et al., 2012) so that Holocene mud deposits on the southwestern shelf older than ~9.15 cal ka BP would have had to accumulate in a perched pond or lagoon ('liman' in local terminology). In an isolated liman, sediment can only be derived from local drainage basins. However local sediment supply is not incompatible with the scenario of an open and fully transgressed shelf. Aksu et al. (2002) suggested that some of the detritus in the lowest Holocene unit (their seismic unit 1B) might have been supplied from local rivers near the Turkish-Bulgarian border that had formed a number of small shelf-edge deltas during the Late Pleistocene lowstand. The aim of the thesis is to determine the composition of the entire Holocene transgressive succession from samples at core site MAR02–45 (Table 1.1). Possible sources of sediment are major rivers far from the southwestern shelf (e.g., the Danube River), local rivers draining northern Thrace, and the reworking of Pleistocene sediments during the Holocene transgression. By studying the fine fractions, a more complete understanding of the locations of significant sediment input through the Holocene will be attained. The fluxes from the different sources likely depended on changing climates, which affected runoff, weathering and vegetation.

The provenance of the Holocene mud units on the southwestern Black Sea shelf might also provide insight into the initiation and changing temporal importance of advection of detritus, by currents, from along-shelf sources (e.g., Danube River). Today,

the major counter-clockwise-flowing Rim Current accounts for transport of sediments from the mouth of the Danube River to the southwestern shelf of the Black Sea. This and other marine currents must have followed different pathways in the past when sea level was lower, so that their ability to advect sediment likely changed through the Holocene.

Table 1.1 Locations and water depths of Black Sea cores used or referenced in this thesis

Core Number	Location (Lat. & Long.)	Depth (m)	Length of composite core (m)
MAR02–45	41°41'170N 28°19'080E	-69	9.5
MAR08–17	41°13'614N 29°07'819E	-76	1.2
MAR05–50	41°29'63 N 29°04'45 E	-91	7.2

1.1.2 Approach

Characterization of the mineralogy and geochemistry of potential sediment sources will be based on a survey of the literature, five samples from the modern Danube Delta (Table 1.2), and two samples from modern rivers entering the Black Sea from Thrace (Table 1.3). For a more general comparison with the composition of sediment from a wider part of the northern Turkish landmass, three samples have been included from coresite MAR08–17 which is located under Mediterranean inflow at the northern exit of the Bosphorus Strait (Table 1.1). Because of the northerly directed flow in the deep part of the strait, this site is believed to receive its sediment from the margins of the strait, and several small rivers which enter the Bosphorus channel along its length. Some

specific minerals are expected to have significance and might be valuable traces.

Sediments delivered by the Danube River are expected to contain more clay-sized quartz and dolomite than sediments derived from Thrace because of contributions from glaciated mountain belts as far away as the Alps. Volcanic rocks in Thrace might be expected to yield more smectite than other potential sources (Major, 2002; Bayhan et al., 2005).

Table 1.2 Locations and elevations of Danube Delta samples taken in delta-top ponds

Sample Area	Sample Code	Location (Lat. & Long.)		Water depth (m)
Sulina Distributary (Canal)	Mile 1-2	45°09'535N	29°38'341E	-10
St. George Distributary	St. George 1	44°56'949N	29°30'200E	-5
	St. George 2	44°53'779N	29°34'902E	-6
Chilia Distributary	Chilia 1	44°24'509N	29°32'658E	-12
	Chilia 2	44°23'166N	29°35'411E	-9

Table 1.3 Locations and elevations of Thrace river samples taken downstream from dammed reservoirs.

Sample Name	Location (Lat. & Long.)	Elevation (m)
Çilingöz	41°31'31.59N 28°11'32.72E	9
Kıyıköy	41°37'35.31N 28°02'15.42E	30

Three independent methods are used to assess provenance:

(1) clay mineralogy of the $<2 \mu\text{m}$ fraction using oriented smear mounts; (2) silt mineralogy of unoriented powder mounts of the $2\text{--}63 \mu\text{m}$ fraction; and (3) trace-element geochemistry of the bulk $<63 \mu\text{m}$ sediment.

The considerable volume of Holocene sediments on the southwestern Black Sea shelf ($\sim 100 \text{ km}^3$ from isopachs in Fig. 1.1 and an assumed acoustic velocity of 1500 m s^{-1}) must be considered when evaluating inputs from the various potential sources. Over the Holocene time span of $\sim 12,000$ years, could each potential source, alone, have provided the observed volume? If not, then either sediment yields have changed significantly through the Holocene (perhaps due to changing climate), more than one source might have been tapped, or if the sum of the fluxes from all reasonable sources is not enough, then a substantial amount of the shelf succession might consist of reworked muds that were originally delivered to what is now the shelf from surrounding lands earlier in the Pleistocene.

If the reworking of unconsolidated Pleistocene sediments was a major contributor to the lower Holocene muds on the southwestern Black Sea shelf, then it might be possible to put some constraints on the pace of the most recent transgression. For example, if there had been a rapid inundation (e.g., catastrophic flood scenario of Ryan et al., 2003, and Lericolais et al., 2007) then there likely would have been little or no

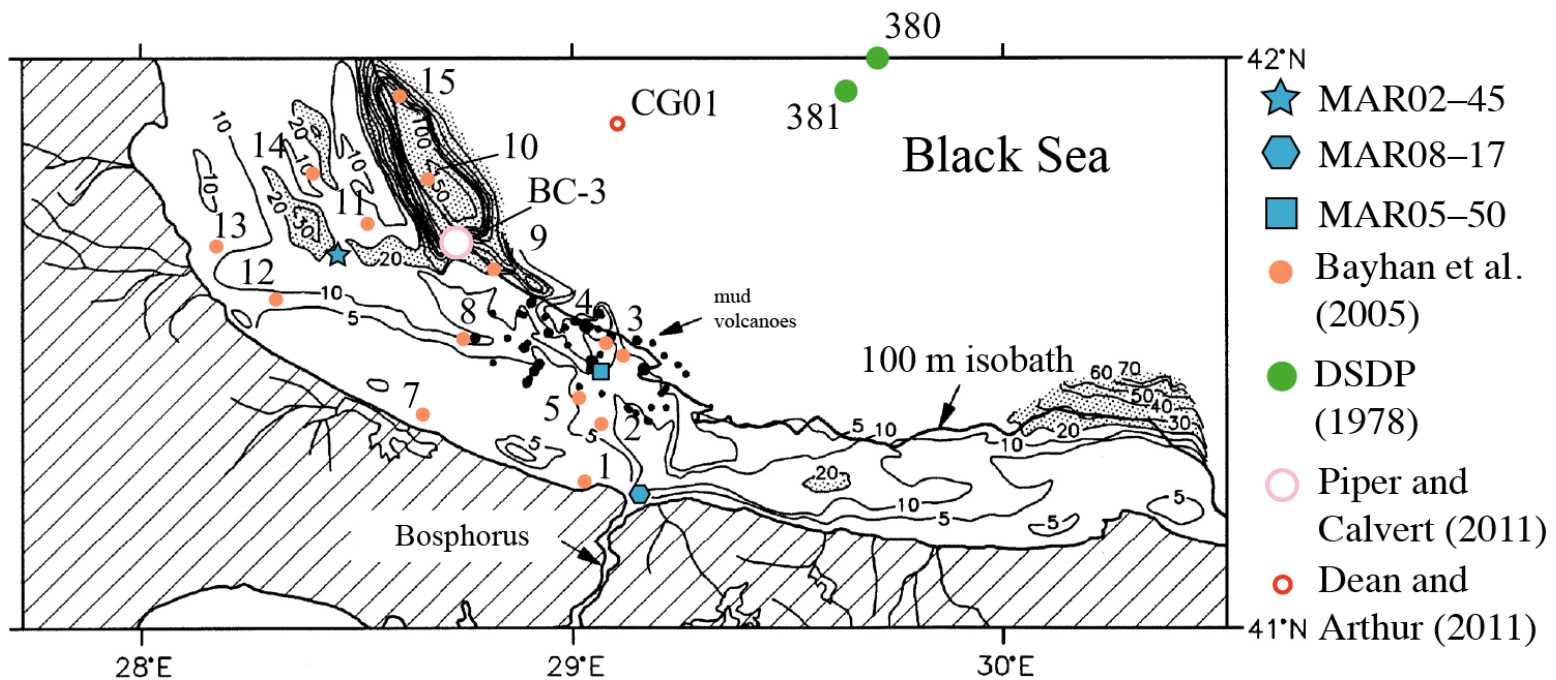


Figure 1.1 Isopach map from Aksu et al. (2002) showing locations and thickness (in milliseconds) of Holocene Muds; 20 ms \approx 15 m in thickness, approximate locations of core sites MAR02–45, MAR05–50 and MAR08–17 are marked as well as 15 cores (small, orange circle) from Bayhan et al. (2005); cores 380 and 390 from the Deep Sea Drill Program, DSDP (large, green circle), Stoffers and Müller (1978); core BC-3 (large, open circle) from Piper and Calvert (2011), and core CG01 (small, open circle), Dean and Arthur (2011).

transgressive erosion. If a gradual and slow transgression had instead occurred, the older sediments would more likely have been beveled by a ravinement surface and erosion products would be widely redistributed across the shelf. Hence, volume estimates of the amount of mud available from potential sources might lead to some general conclusions about the style of the transgression. If very little reworked material is required to satisfy the volume requirements, this would support a rapid (but not necessarily catastrophic) transgression, but if it is concluded that the volume of reworked material must have been high then a gradual rise in sea level perhaps would be more likely.

To summarize, the primary aims are to define the geochemical composition of the Holocene muds and to determine whether sedimentary provenance changed significantly through the Holocene. If data allow, constraints will be put on the relative importance during the Holocene of sediment sources like the Danube River, local drainage from Thrace, and reworking of older shelf deposits. The results might also provide fresh insight into the importance of climate change, rate of sea-level rise, and the establishment and history of marine currents (e.g., Rim Current) on the Black Sea shelf.

1.2 Regional Overview

1.2.1 Oceanographic Setting

The Black Sea is a large inland sea located between Europe, Anatolia and the Caucasus Mountains. It is connected to the Mediterranean Sea through the Bosphorus Strait, Marmara Sea, and the Dardanelles Strait. This connection consists of a two-way flow with south-flowing brackish surface waters overlying north-flowing saline waters (Oğuz et al., 1993). The surface layer is 25–100 m thick, has a salinity of 17–20 psu, a temperature of 5–15°C and in the straits flows with a velocity of 10–30 cm s⁻¹ to the south (Oğuz et al., 1993). The north-flowing Mediterranean water is warmer (15–20°C), more saline (38–39 psu) and travels in the straits at velocities of 5–25 cm s⁻¹.

The surface circulation of the Black Sea (upper 25–100 m) is dominated along basin margins by the counter-clockwise-flowing Rim Current (~20 cm s⁻¹; Fig. 1.2). Farther basinward, there are two central gyres (western and eastern). There are many coastal anti-cyclonic eddies (Fig. 1.2), the Bosphorus eddy being to the west of the Bosphorus Strait (Oğuz et al., 1993) and of greatest relevance to this study.

Flood et al. (2009) described east-directed current tails behind mounds on the southwestern Black Sea shelf, and a seabed disconformity, and attributed these to erosion and sediment transport beneath the Rim Current. They showed the predominant grain size of the Holocene succession to be silt.

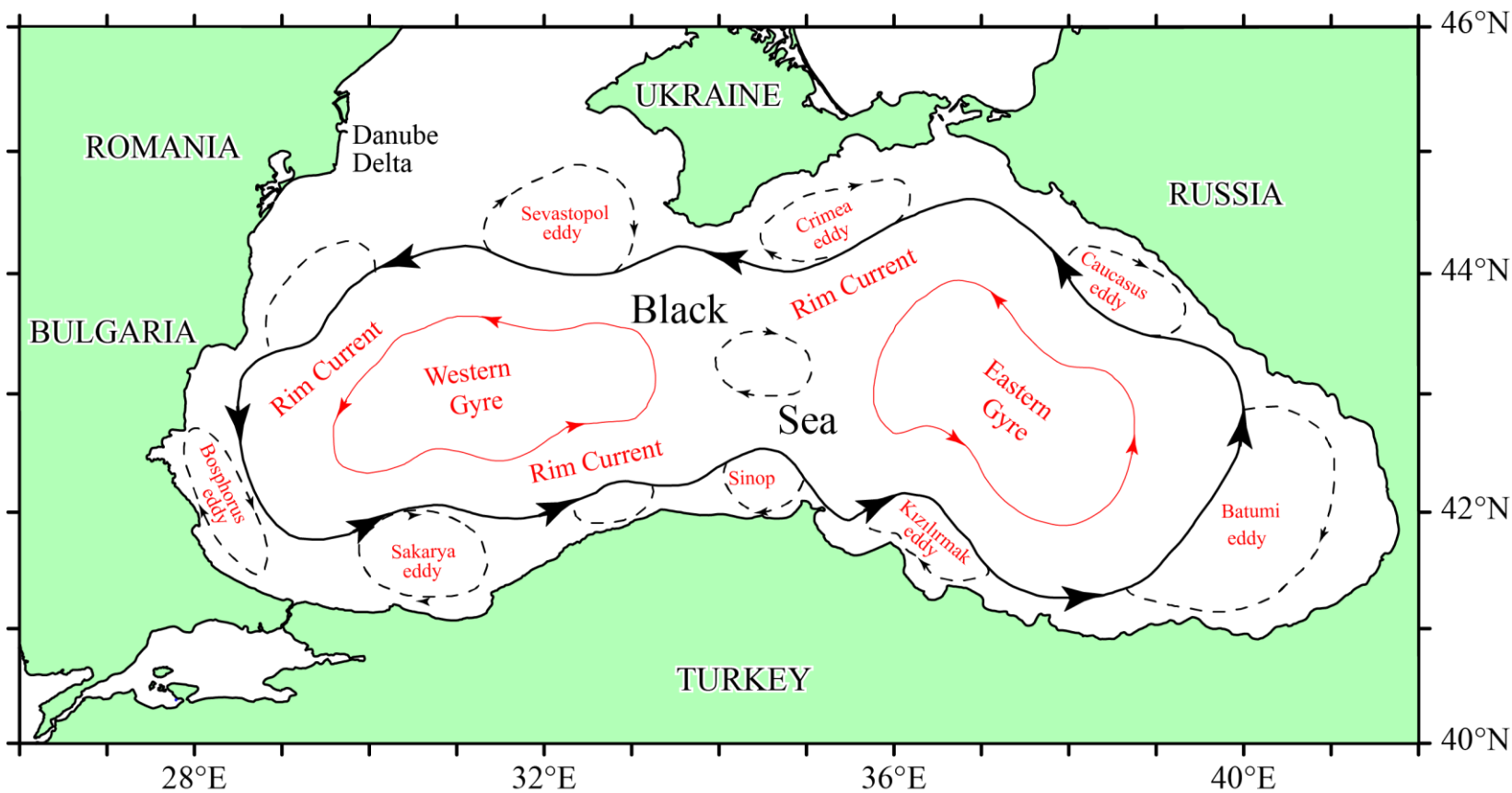


Figure 1.2 Major currents, gyres and eddies of the Black Sea. Redrawn from Oğuz et al. (1993).

Crant (2010) mapped the extent and volume of clinoform-like accretion deposits on the western bank of the saline underflow channel that leads to coresite MAR05–50 (Figure 1.1); the Rim Current apparently transported the accreted sediment from farther west, potentially from the Danube Delta.

The Black Sea is a wave-dominated environment, which prevents deposition of significant amounts of sediment in water depths less than ~70 m, the exception being regions off of river mouths. Storm wave base can rework sediments to a depth of 75 m (Aksu et al., 2002). In shallow marine systems storm-induced shelf currents begin through frictional coupling of the wind and water surface (Walker and Plint, 1992). These surface currents move water in deeper layers to the right (in the Northern Hemisphere). Sediment moving currents flow at 90° to the wind direction (Walker and Plint, 1992). Water blown onshore by storms also creates a hydrostatic pressure difference offshore, this pressure difference drives bottom flow (affected by Coriolis forces) in obliquely off-shore to shore parallel directions (Walker and Plint, 1992). In the modern Black Sea the Coriolis effect turns currents from the North → West → South → East, which would move sediments to the South and East on the southwestern Black Sea shelf (Fig 1.2).

1.2.2 Geologic Setting

Rifting during the Late Jurassic evolved into a back-arc basin during the Mid-Cretaceous (~100 Ma) forming the Black Sea basin (Gealey, 1988). In the western basin, sea floor spreading had ceased by the Late Cretaceous and basin subsidence occurred due to thermal contraction and post-rift sediment loading (Gealey, 1988). Spreading in the eastern Black Sea basin continued into the Miocene. During the late Miocene, black siltstones and dolostone suggest a shallow water environment (Muratov et al., 1978). Miocene sedimentary materials have also been linked with volcanic source rocks because the sediments contain highly-crystalline montmorillonite.

Pleistocene sediments are mainly terrigenous muds, silts and fine sands in the Black Sea. Palynological studies indicate three cold and three warm intervals, this sedimentation was closely linked with climate during this time (Muratov et al., 1978). The Black Sea basin became salinated due to Mediterranean inflow during interglacial periods. Density stratification, sapropel, and sapropelic muds were formed during this time (Muratov et al., 1978).

The Black Sea was alternately connected and isolated from the global ocean during Quaternary interglacial and glacial periods. During the glacial periods sea level dropped and large quantities of terrigenous sediments were supplied into the deep basin as turbidites. Meltwater pulses during deglacial times are believed to have reduced the salinity by flushing out more saline waters (e.g., Ryan et al., 2003). During the last

glacial maximum the Black Sea was drawn down (10–50 m) to depths below the modern shelf edge and is called the Neoeuxinian Lake or Black Sea Lake.

Sedimentation in the western Black Sea basin was mostly controlled by input from the Danube River (Muratov et al., 1978) as the sediment supply from the Danube dwarfs all over supplies to the south (Jaoshvili, 2002 his §6). Many small rivers in Thrace delivered sediment to western the Black Sea as well (Aksu et al., 2002). There is some controversy as to the timing and pace of the last, early Holocene reconnection; the three main hypotheses are examined below.

1.2.3 The Flood Hypothesis

Ryan et al. (1997) proposed that a catastrophic flood inundated the Black Sea at 7.6 cal ka BP. A major unconformity is found along the shelf edge of the northwestern Black Sea and was dated to 7.2 ka BP. A gravel bed at that level overlies terrestrial flood-plain deposits, wave-cut beaches, and coastal deltas that had been developed during the preceding lowstand to approximately –110 m. Lying atop this unconformity is a dark sapropel unit; this structureless layer is found over the majority of the northwestern shelf and is of uniform thickness. There is no evidence of transgressive systems tract geometry (Ryan et al., 1997). Using ^{14}C dates from five cores, the base of the sapropel layer was dated to 7.2 ± 0.1 ^{14}C yr BP.

Ryan et al. (1997) concluded that $\sim 100,000$ km² of land surface was inundated as Mediterranean waters cascaded through the Bosphorus Strait, filling the Black Sea basin

as water levels rose at a rate of tens of centimetres per day. According to Ryan (2007), this catastrophic flood displaced earlier settlers and gave rise to the flood myth of Noah found in the Bible and other ancient texts.

Ryan et al. (2003) revised the initial hypothesis in response to criticism. The first major revision proposed by Ryan et al. (2003) was the inclusion of a second, earlier sea-level draw down and transgression. This earlier transgression occurred during the Younger Dryas and raised the sea level from -105 to -30 m. Subsequently, the level was again drawn down to -95 m. The timing of catastrophic flooding was adjusted downward to 8.4 ^{14}C ka BP (9.1 cal ka BP as calibrated by Mertens et al., 2012), raising the sea level to -30 m (Ryan et al., 2003). Ryan et al. (2003) argued that the evidence for the first fresh-water 'flood' comes from shell fragments in sediments no younger than 10.0 ^{14}C ka BP. Sediment with high bulk density and low moisture content suggested that the Ukrainian shelf was exposed subaerially from 14.7 ^{14}C ka BP to 10.7 ^{14}C ka BP. The date for the 'catastrophic flood' was pushed back based on strontium isotope analysis of dated mollusk shells (Major et al., 2006) that suggested the first arrival of marine waters from the global ocean at 8.4 ^{14}C ka BP (9.1 cal ka BP). The species turnover of mollusks, which had suggested that the 'flood' occurred at 7.2 ^{14}C ka BP (7.6 cal ka BP), merely reflected a salinity threshold being reached, well after the time of the transgression (Ryan et al. 2003).

Lericolais et al. (2007) interpreted wave-cut terraces and aeolian sand dunes on the Romanian shelf and inferred that there had been a paleoshoreline at –90 m, between 9.58 and 8.58 ¹⁴C ka yr BP. This interpretation and the Ryan et al. (2003) conclusions are incompatible with the presence of soft muds with Caspian-type brackish dinoflagellates, molluscan, and ostracod faunas on the southwestern Black Sea shelf over this same time interval, at core site MAR02–45 in modern water depths <75 m (Hiscott and Aksu, 2002; Hiscott et al., 2007b; Bradley et al., 2012).

1.2.4 The Outflow Hypothesis

In contrast to the ‘Flood’ hypothesis, the outflow hypothesis argues that water levels in the Black Sea rose ‘gradually’ during the Holocene. Aksu et al. (1999, 2002), Hiscott et al. (2002, 2007a,b), Yanko-Hombach et al. (2004) and others have argued that a catastrophic flood could not have occurred in the Black Sea during the Holocene. Görür et al. (2001) also provided evidence against a catastrophic flood at 7.2 ¹⁴C ka (as originally proposed by Ryan et al., 1997), but the Ryan et al. (2003) revision of the age of the proposed flood to 8.4 ¹⁴C ka removed the objection raised by Görür et al. (2001).

Aksu et al. (1999) argued that about 10.0 ¹⁴C ka BP, increased fresh-water input raised the level of the Black Sea and its brackish waters entered the Marmara Sea through the Bosphorus valley. At about 9.50 ¹⁴C ka BP, the Marmara Sea reached the level of the Bosphorus Strait but could not penetrate into the Black Sea because of the strength of the outflow (Hiscott et al., 2007a). Black Sea outflow weakened by ~8.40 ¹⁴C ka BP (9.1 cal

ka BP) allowing Mediterranean water to enter the Black Sea as an initial short-duration pulse (Hiscott et al., 2007a) followed by a stronger sustained influx by ~7.50 ¹⁴C ka BP that established the two-way flow seen today.

Aksu et al. (2002) mapped five seismic units on the southwestern Black Sea shelf and dated Unit 1 (glacial to post-glacial transgression) with radiocarbon dates from six short gravity cores. The architecture of subunit 1A points to its development as low-stand, shelf-edge delta lobes deposited ~115 m below modern sea level. This suggests that the Black Sea was drawn down ~105 m during the Younger Dryas.

Hiscott et al. (2002) showed the existence of two progradational delta lobes at the southern exit of the Bosphorus Strait in the northeast Marmara Sea, and argued that they record two periods of outflow of water from the Black Sea into the Sea of Marmara. For the uppermost delta, Hiscott et al. (2002; 2008) advocated that the outflow began at ~10 ¹⁴C ka BP, necessitating that the contemporary Black Sea level was then at or above the depth of the Bosphorus sill (~ -40 m). Eriş et al. (2007) argued that the two deltas could have been formed by the Kurbağalıdere River. Hiscott et al. (2008) calculated sediment flux for the Kurbağalıdere Rivulet and determined that there was an inadequate supply of material to build the delta lobes.

Hiscott et al. (2007b) analyzed core MAR02–45 (the primary core studied in this thesis – a detailed review is found in §1.4.1) and combined paleontological and sedimentological evidence supporting a gradual Holocene reconnection with the

Mediterranean Sea. Core MAR02–45 recovered almost all of the Holocene succession above the α unconformity (see also Reynolds, 2012), which suggests that the shelf was inundated from at least 10.3 cal ka BP (Hiscott et al., 2007b; calibration from Mertens et al., 2012). The evidence for short-lived saline inflow into the Black Sea comes from sulphur geochemistry and dinocyst and freshwater alga abundances. Between ~9.4 cal ka BP and 8.6 cal ka BP these fresh/brackish water species were replaced by marine flora (calibrations from Marine 09 calibration curve with 0.4 ka reservoir age). Between 8.4 cal ka BP and ~7.9 cal ka BP the fresh/brackish water species returned until they were permanently replaced at 7.5 cal ka BP (Hiscott et al., 2007b).

1.2.5 The Oscillating Sea-level Hypothesis

It has been proposed that during the Neoeuxinian the level of the Black Sea (a lake at the time) varied through time but was never more than ~100 m below its present level (Yanko–Hombach, 2007). Based on benthic foraminiferal assemblages, Yanko–Hombach (2007) reconstructed water level in the Black Sea over the last 30 thousand years.

From ~27 ¹⁴C ka BP to 17 ¹⁴C ka BP this lake was connected to the Marmara Sea and isolated from the Caspian Sea. At 17 ¹⁴C ka BP, the climate began to warm and water level rose to -20 m; this rise has been attributed to a deluge from the Caspian Sea (Yanko–Hombach, 2007) which would have caused a spillover into the Marmara and Mediterranean seas.

Yanko-Hombach (2007) suggested that at the start of the Younger Dryas the water levels dropped from -20 m to -50 m and then rose again to -20 m. After 10 ¹⁴C ka BP the level of the Black Sea never dropped below -40 m and no fluctuations over 20 m are evident (Yanko–Hombach, 2007). It is proposed that sea level rose and fell at a rate of ~3 cm per 100 years in an oscillating manner. Yanko–Hombach (2007) also argued that the lack of Mediterranean fauna older than 5.3 ¹⁴C ka BP in the Bosphorus Strait implies that the Bosphorus valley cradled an isolated lake from 26 ¹⁴C ka BP to 5.3 ¹⁴C ka BP. The reader will notice the obvious incompatibility of this conclusion with arrival of Mediterranean water in the Black Sea by ~8.4 ¹⁴C ka BP (9.1 cal ka BP), unless it did not pass through the Bosphorus valley, but via an alternate route like the present-day Sakarya River valley to the east (Yanko–Hombach et al., 2004).

The Izmit Plain (a possible pathway of reconnection) was studied by Gürbüz and Leroy (2009); they found no evidence of marine or fluvial sediments. Gürbüz and Leroy (2009) also noted the presence of small sills higher than the modern level of Lake Sapanca, if a Marmara Sea–Black Sea connection flowed through this valley then water levels must have been higher than they are currently.

Yaltırak et al. (2012) also examined the possible reconnection pathways of Lake Sapanca and Lake İznik. 5 m long cores from Lake İznik indicate that the lake contains no marine ostracods or foraminifera for at least the last 4.3 k yr. Applying tectonic uplift rates to the area around Lake İznik Yaltırak et al. (2012) concluded the vertical

movement needed for a Holocene reconnection was well above calculated values. They also concluded that tectonic uplift in the Sapanca region would inhibit the formation of a waterway connecting the Black Sea to the Marmara Sea during the Holocene (Yaltırk et al., 2012).

1.2.6 Rivers

The modern Black Sea receives fresh water from five major rivers (Danube, Dniester, Dnieper, Southern Bug and Don) and many smaller local rivers. The major rivers deliver great volumes of sediment and fresh water to the Black Sea each year. For example the Danube River delivers $25\text{--}35 \times 10^6 \text{ t yr}^{-1}$ of sediment to the Black Sea, $4\text{--}6 \times 10^6 \text{ t}$ of which are sand. Before the building of the Iron Gates Dam (Romania), up to $67.5 \times 10^6 \text{ t}$ of sediment were delivered annually (Panin and Jipa, 2002). Many small rivers empty into the southwestern Black Sea: the Bulanık, Pabuç, Kazan, Çilingöz and Kuzulu rivers all drain to the west of core site MAR02–45 (Aksu et al., 2002). These rivers deliver $\sim 29,930 \text{ t}$ of sediment annually (Table 1.4). Small deltas, shore-parallel sand ridges, and dunes characterize the river mouths because most fine-grained sediment is now trapped in dammed reservoirs just landward of the coast. Between these small rivers and the Danube Delta, the Kamchiya River reaches the Bulgarian coast. Its pre-dammed water and sediment discharges are $0.873 \text{ km}^3 \text{ yr}^{-1}$ and $1.1 \times 10^6 \text{ t yr}^{-1}$ (Jaoshvili, 2002), making it a sediment source intermediate in scale between the Danube River and the much smaller Turkish rivers.

The Danube River is a major potential sediment source for the southwestern Black Sea shelf. This is because the sediment discharge from the Danube River dwarfs the detrital supply from all other sources along the southern margin of the Black Sea (Jaoshvili, 2002, his §6). Large river systems like the Danube are well studied worldwide, and are known to provide muds to their receiving basins that are advected hundreds of kilometres along adjacent shelves to form shore-parallel, mid-shelf sedimentary deposits 20–40 m thick (Liu et al., 2009). For this reason, a brief overview of the bedrock geology of the Danube drainage basin is provided in the next section (§1.3). The Danube headwaters extend far to the west into the Alpine chain, and tributaries extend into the Carpathian Mountains, Dinaric Alps, and Balkan Chain, so section 1.3 is necessarily very generalized. These are all Cenozoic fold-thrust belts created by the collision of the African and Eurasian plates as the Tethys Ocean was consumed. They consist mainly of low-grade metasedimentary rocks, plutonic belts, ophiolite complexes and sedimentary cover.

Table 1.4 Rivers in Thrace, extracted from Aksu et al. (2002)

River	Drainage area (km ²)	Average discharge (m ³ s ⁻¹)	Annual discharge (x10 ⁶ m yr ⁻¹)	Sediment yield (t yr ⁻¹)
Bulanık	155	1.597	59.5	9 987
Pabuç	95	0.907	27.5	5 395
Kazan	125	1.262	45.2	7 619
Çilingöz	91	0.887	39.9	5 111
Kuzulu	40	0.368	12.3	1 817

1.3 Geology of Surrounding Lands

1.3.1 Geology of Northern Thrace Drainage Basins Entering the Black Sea

The geographic area encompassing Thrace is composed of southeastern Bulgaria, northeastern Greece, and the European section of Turkey. The Thrace Basin is the largest Tertiary sedimentary basin in Turkey (Demir et al., 2012). It is underlain by pre-Tertiary metamorphic (low grade schists and gneisses) and granitic suites (Turgut and Eseller, 2000). The Tertiary infill is primarily marine interbedded siliciclastic and carbonate rocks, with sporadic lava flows (Turgut and Eseller, 2000). The primary direction of Quaternary drainage in this basin is toward the Aegean and Marmara seas (Fig. 1.3; Okay and Okay, 2002), as the coastal Strandja Mountains (Istranca in Turkish) form a drainage divide that limits runoff into the southwestern Black Sea to a narrow coastal zone. Hence, rocks of the Tertiary Thrace Basin provide limited detrital influx to the Black Sea. The geology of the eastern portion of the Thrace Basin (near Kıyıköy), where small rivers do drain into the southwestern Black Sea, is characterized by upper Eocene – lower Oligocene tidal deposits of bioturbated sandstone (5–10 m thick) and mudstones (Varol et al., 2009). Overlying these rocks are cross-bedded clastic limestones (5–10 m thick) with some meter-thick reef deposits. Bioturbated sandy limestones (10–15 m thick) transition upwards into massive bioclastic sand and sandstones with coral fragments (~50 m thick; Varol et al., 2009). These outcrops are proximal to the coast and dissected by the Kozan River.

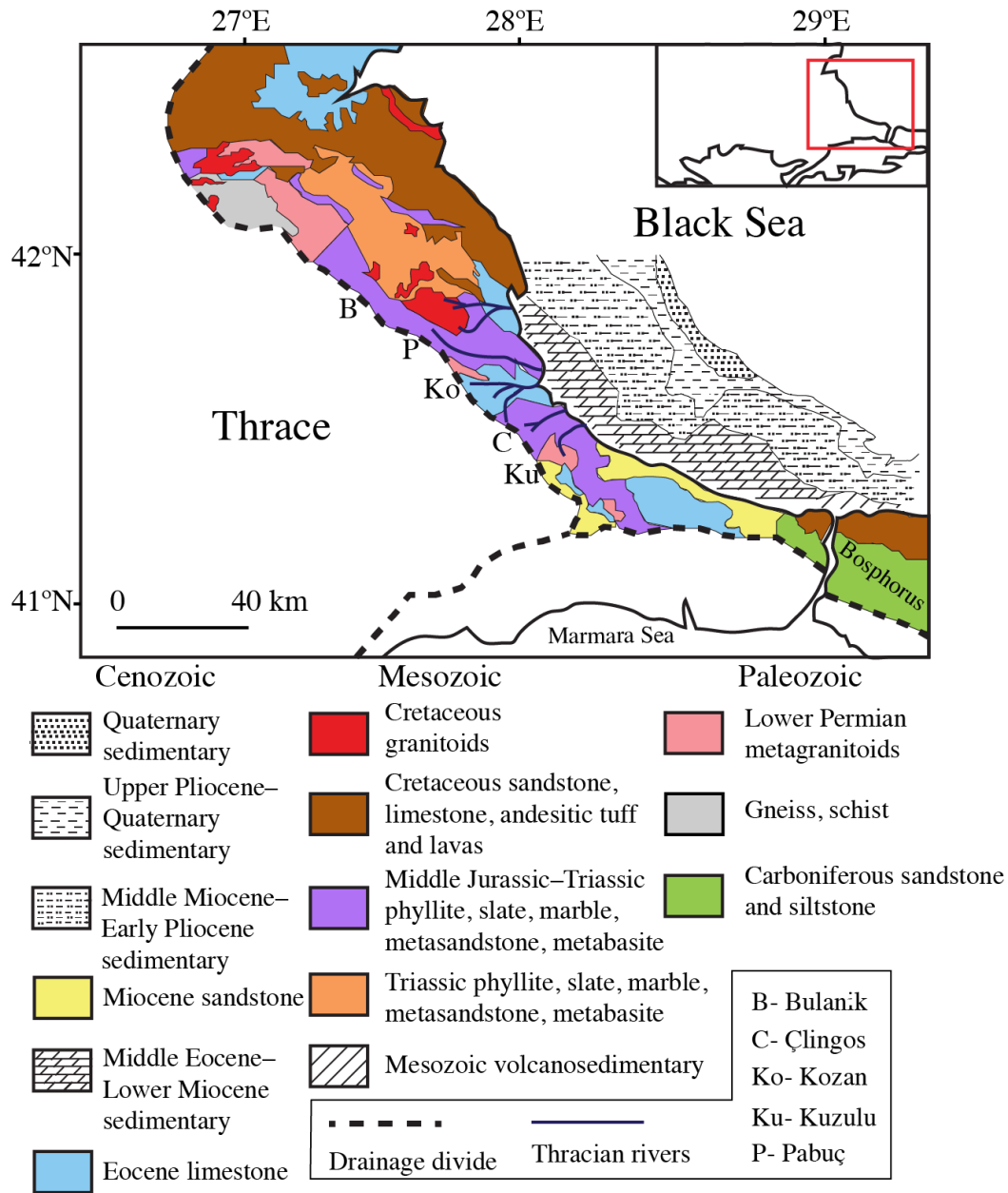


Figure 1.3 A simplified view of the coastal geology (from Okay & Okay, 2002; Okay, 2008; Natal'in et al., 2012; Bedi et al., 2013, and nearshore geology (below the α unconformity; Aksu et al., 2002) of the southwestern Black Sea.

Elsewhere, the coastal geology of the southwestern Black Sea is dominated by the Strandja-Rhodope Massif (Fig. 1.3), a metamorphic complex (Yılmaz et al., 1997). The northern termination of this Strandja Massif is the Sredna Gora zone (a package of deep-sea sediments including flysch, and mafic to intermediate volcanics). The Strandja Massif consists of a core of high grade metamorphic rocks disconformably overlain by slate, phyllite and recrystallised limestones (Yılmaz et al., 1997). In northwestern Turkey the metamorphic rocks are composed of greenschist to epidote-amphibolite facies (Natal'in et al., 2012). Paleozoic metasedimentary rocks include biotite schist, biotite-muscovite schist and gneiss with preserved relict sedimentary structures (Natal'in et al., 2012). In places, hornblende, actinolite, minor plagioclase, and garnet comprise layers of amphibolite (Natal'in et al., 2012). Samples of the biotite schist contain quartz (20–25%), K-feldspar (20–25%), plagioclase (10–15%), biotite (10–15%), muscovite (5–10%), epidote (2–5%), calcite (3–5%), minor zircon, and opaque minerals (Natal'in et al., 2012). Upper Carboniferous biotite-muscovite granitic gneiss contains plagioclase (35–40%), epidote (20–25%), biotite (15–20%), K-feldspar (10–15%), quartz (5–10%), garnet (2–5%), titanite (1–3%), and minor zircon and opaque minerals (Natal'in et al., 2012). Next in succession are Triassic conglomerates and sandstones that pass upward into interbedded fine grained siliciclastic rocks and limestones. These metasedimentary rocks contain a small tectonic lens of pillow lava and are capped by black shale (Natal'in et al., 2012). The Strandja Massif is thoroughly intruded by multifarious dykes, sills, stocks

and plutons (Yılmaz et al., 1997) with the majority having the composition of granodiorite, quartz diorite or adamellite.

The nearshore geology of the southwestern Black Sea shelf below the α unconformity is considered a possible sediment source in late Quaternary time as this subcrop would have been exposed during the late Pleistocene (and potentially early Holocene) when the Black Sea was drawn down (Fig 1.3). The erosion and reworking of these sedimentary successions could have contributed to the early transgressive and highstand Holocene–Recent sediments deposited on the shelf.

Erginal et al. (2012) record Holocene coquina and coquinite beds ~40 km northwest of Istanbul in back-beach areas of the Thracian coast. The beaches are composed mainly of shell debris and coquina, and are 20–60 m wide with ~2 m maximum thickness. The composition of the cement in the coquinite beachrock is low-magnesium calcite (Erginal et al., 2012). Near Şile (Istanbul), beaches are 10–30 m wide and are backed by a coastal dune field with a thickness no greater than 3 m (Ekinci et al., 2013). Upper Pleistocene aeolianites form the back-beach and encase foredune sands. The beach material is 9–10 m thick and overlies coquinite beds no greater than 5 m in thickness (Ekinci et al., 2013). There have been no quantitative studies on the source(s) of the siliciclastic sand fraction in these beaches, but several processes are likely responsible: (1) redistribution of locally derived river sand by wave action and associated longshore currents; (2) erosion of coastal bluffs, pre-existing Pleistocene aeolianites (such

as those reported by Ekinçi et al., 2013) and any headlands that might have existed as sea level reached its current level; (3) landward transport and winnowing of sand from the shelf during the Holocene and various late Pleistocene transgressions.

1.3.2 Geology of Northwestern Anatolia

The geology of northeastern Anatolia is characterized by the Istanbul-Zonguldak zone, which represents the northern extent of the western Pontides (Yılmaz et al., 1997). The metamorphic basement consists of gneisses, gabbros, and amphibolites intruded by arc-type granitoids (Okay, 2008). This is overlain by a Devonian package of red arkosic conglomerate, sandstone and mudstone. Silurian quartzites are found beneath dark siltstones, greywackes and shales (Okay, 2008; Yılmaz et al., 1997) that pass upward into quartzitic layers overlain by graptolitic limestones and mudstones. The limestones change from sandy to alternating coralline and bituminous limestones and marls. Devonian carbonates near Istanbul are thinly bedded cherty limestones with phosphate nodules and are overlain by Carboniferous sandy turbidites and shales (Yılmaz et al., 1997). Mesozoic outcrops are patchy near Istanbul and consist of alkaline lava flows interleaved with a thick, red, fluvial clastic unit (Okay, 2008).

1.3.3 Geology of Mountain Belts in the Danube Drainage Basin

Major mountain belts drained by the Danube River include the Calcareous Alps, the Balkans Range, the Dinaric Alps, and the Carpathian Mountains. These ranges are composed of predominantly Upper Paleozoic siliciclastic sedimentary rocks overlain by Mesozoic carbonate platforms (Channell et al., 1990; Doglioni et al., 1995; Vlahović et al., 2005; Stefanescu et al., 2006). For example, Upper Paleozoic to Lower Mesozoic sedimentary rocks of the Calcareous Alps accumulated in three environments: siliciclastic shallow-water and continental settings in the Late Permian, shallow water carbonate environments in the Triassic, and deepwater carbonate environments in the Jurassic (Channell et al., 1990).

The Balkans Range separates southeastern Europe (e.g., Greece, Bulgaria, Albania, Montenegro) from northeastern Europe (e.g., Romania, Hungary). Basement rocks consist of Precambrian high grade metamorphic rocks (amphibolite and gneiss, Burchfiel et al., 2003), marbles (Kozhoukharov and Konzalova, 1990) and a well preserved Precambrian ophiolite complex (Savov et al., 2001). These basement rocks are overlain by Mesozoic and Paleogene sedimentary rocks (Doglioni et al., 1995) and intruded by Cretaceous and Paleogene plutons.

The Balkan-Carpathian ophiolite is comprised of a mafic/ultramafic suite of Upper Precambrian rocks (Savov et al., 2001). It crops out in Bulgaria, Serbia and Romania and has been linked to a mid-ocean ridge source (Savov et al., 2001).

The Dinaric Alps (Dinarides) border the Adriatic Sea and their eastern slopes empty into the Danube drainage basin. The composition of the Dinarides is dominated by the Adriatic Carbonate Platform (Vlahović et al., 2005). Underlying this Mesozoic (Jurassic–Cretaceous) platform are Triassic sedimentary and volcanic rocks. Triassic magmatism was mafic to felsic with pyroclastic deposits and pillow basalts (Trubelja et al., 2004) generated in a subduction setting. The basaltic and gabbroic rocks show a characteristic enriched mid-ocean ridge basalt signature with an enrichment of light rare earth elements compared to heavy rare earth elements (Trubelja et al., 2004).

The Carpathian Mountains dominate the geology of Romania and extend into surrounding countries. Outcrops in Romania range in age from Precambrian to Quaternary. The Moesian Platform is bounded by the Danube River to the south, by the Sub-Carpathian domain to the north, and the Black Sea to the east (Stefanescu et al., 2006). The basement of this platform is composed of metamorphosed rocks. Lower Paleozoic rocks include black Cambrian shales and sandstones, overlain by carbonates, including limestones and dolostones with interlayered evaporite deposits (Stefanescu et al., 2006). Upper Paleozoic deposits include mafic and felsic volcanics interbedded with continental evaporite deposits (Stefanescu et al., 2006).

Jurassic ophiolite complexes can be found to the east of the Moesian Platform. Layered gabbroic units, sheeted dykes, pillow basalts and breccias define the ophiolite sequences (Bortolotti et al., 2002). The gabbroic units are sourced from high-Ti magma

while basaltic rocks show N-MORB characteristics with flat to slightly enriched rare earth element (REE) patterns. This suggests a mid-ocean ridge origin for these ophiolite complexes (Bortolotti et al., 2002). Calc-alkaline volcanics range from basalt to rhyolite with some granitoid intrusions into the ophiolite complex. These rocks are depleted in Nb, P, and Ti and enriched in Rb-Ba-Th and La-Ce. There is also a well-defined enrichment in light rare earth elements in the calc-alkaline volcanics (Bortolotti et al., 2002).

1.3.4 Loess

Surface sediment in eastern Europe is primarily wind-transported loess or reworked loess. The interfluvies of the Danube basin are blanketed by many large and thick loess deposits. Quaternary loess and paleosol deposits in eastern Europe span a number of glacial/interglacial cycles (Fitzsimmons et al., 2012). The most prevalent loess deposits are found near large rivers (e.g., Danube, Dniestr). Loess deposits modified by pedogenesis and diagenetic processes occur in the areas of transition from lowlands to mountains (Fitzsimmons et al., 2012). Figure 1.4 shows the extent of loess deposits in the Danube drainage basin.

Varga (2011) studied loess and red-clay deposits in the Carpathian Basin and determined there is a bimodal distribution of grain sizes: coarse (16–63 μm) and fine material (2–8 μm). The coarse material indicates local sourcing whilst the fine material is derived either from a more distal environment or secondary weathering. A 1:250,000

map of loess occurrences in Europe and central Asia can be accessed at <http://www.ufz.de/index.php?en=15536> (Haase et al., 2007).

Smalley and Leach (1978) studied loess deposits throughout the entire Danube basin. They define loess as 20–60 μm unstratified, calcareous, porous material: sandy loess as a mixture of 20–60 μm and 200–500 μm grain sizes, and non-calcareous, and clay-loess as unstratified, low porosity material with peak particle size between 20–60 μm with 25–30% of the particles $< 2 \mu\text{m}$.

Primary loess deposits were formed through weathering of alpine units near the Danube headwaters and wind transport to the east. Austrian loess is derived from northern European glacial debris. These two sources combine in the Danube Valley and form floodplain deposits further downstream. The floodplain deposits have been reworked through aeolian transport into a third type of loess deposits, found around Budapest (Smalley and Leach, 1978). These three loess deposits are then mixed with Carpathian derived loess when the River Tisza connects with the Danube River. The final source of loess generation in the Danube basin is the lower Danube floodplain. Loess deposits in Bulgaria and Romania are created through aeolian transport of these lower floodplain deposits.

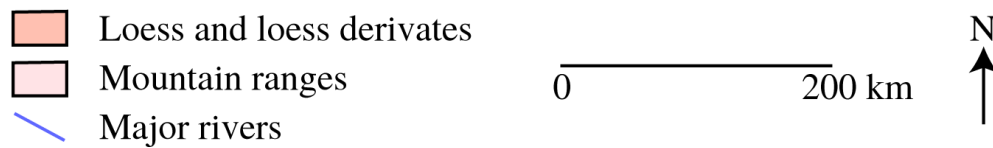
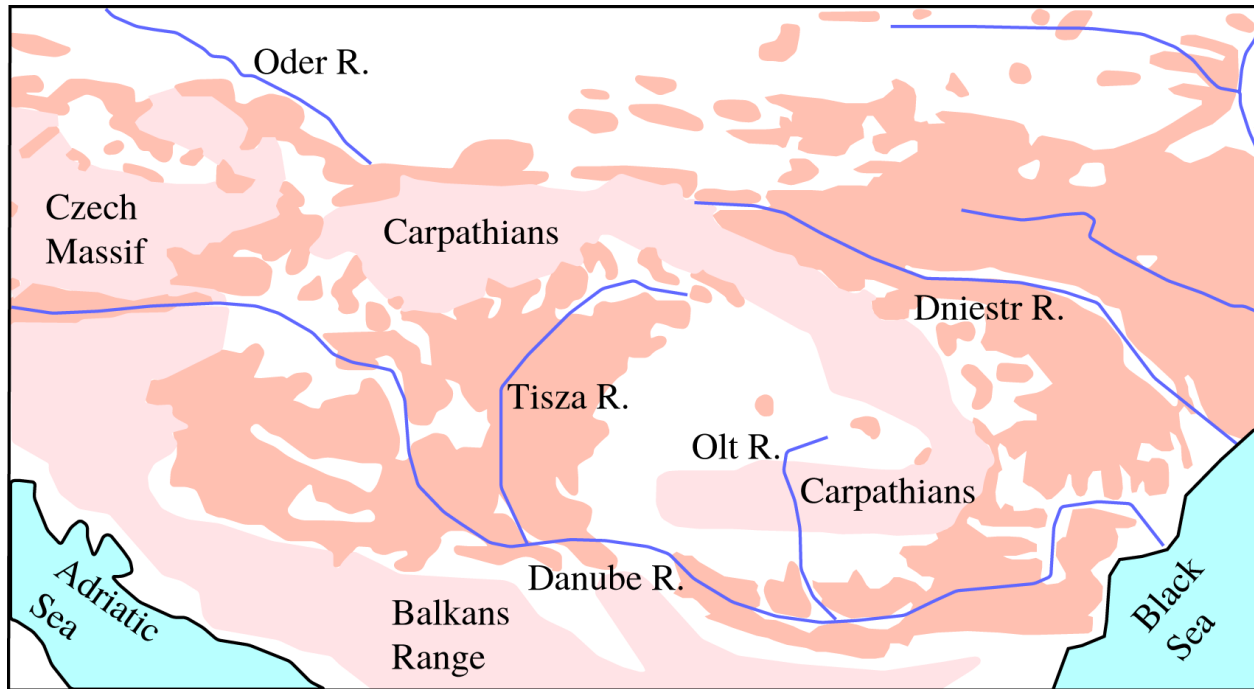


Figure 1.4 Map of loess and loess derivative deposits in the middle and lower Danube Basin, modified from Fitzsimmons et al.

(2012), their figure 2. These deposits can achieve thicknesses >5 m.

It has also been noted that Bulgarian and Romanian loess deposits are more clay-rich than loess deposits to the east. This is thought to be due to the fact that they are a combination of loess and loess derived material from Alpine, Austrian, and Carpathian sources (Smalley and Leach, 1978). Figure 1.5 from Smalley and Leach (1978, their figure 6), is a generalized diagram showing the interconnections of Danube basin loess deposits and their sources.

Újvári et al. (2008) analyzed loess deposits in southwestern Hungary (Table 1.5) to determine provenance and determined that SiO_2 varies from 61.8–67.2 wt.%; Al_2O_3 from 12.8–14.2 wt.%. They found that TiO_2 values are high (0.9–1.0 wt.%) while Na_2O and K_2O values are low (1.3–1.6 wt.%; 2.2–2.6 wt.%). They further determined that SiO_2 values coupled with the high Al_2O_3 values indicate an abundance of aluminosilicates (feldspars and/or micas). They found a correlation of SiO_2 and TiO_2 and argued for the presence of a titanium-bearing silicate phase (e.g., rutile, biotite, chlorite; Újvári et al., 2008).

Trace element data show a strong relationship between light rare earth elements (LREE) and high field strength elements (HFSE). Their behaviour is similar to TiO_2 and P_2O_5 , implying that LREE and HFSE concentrations are governed by the presence of heavy minerals (Újvári et al. 2008). Table 1.5 from Újvári et al. (2008) shows concentrations of major and trace elements from a section of loess located in southwestern Hungary.

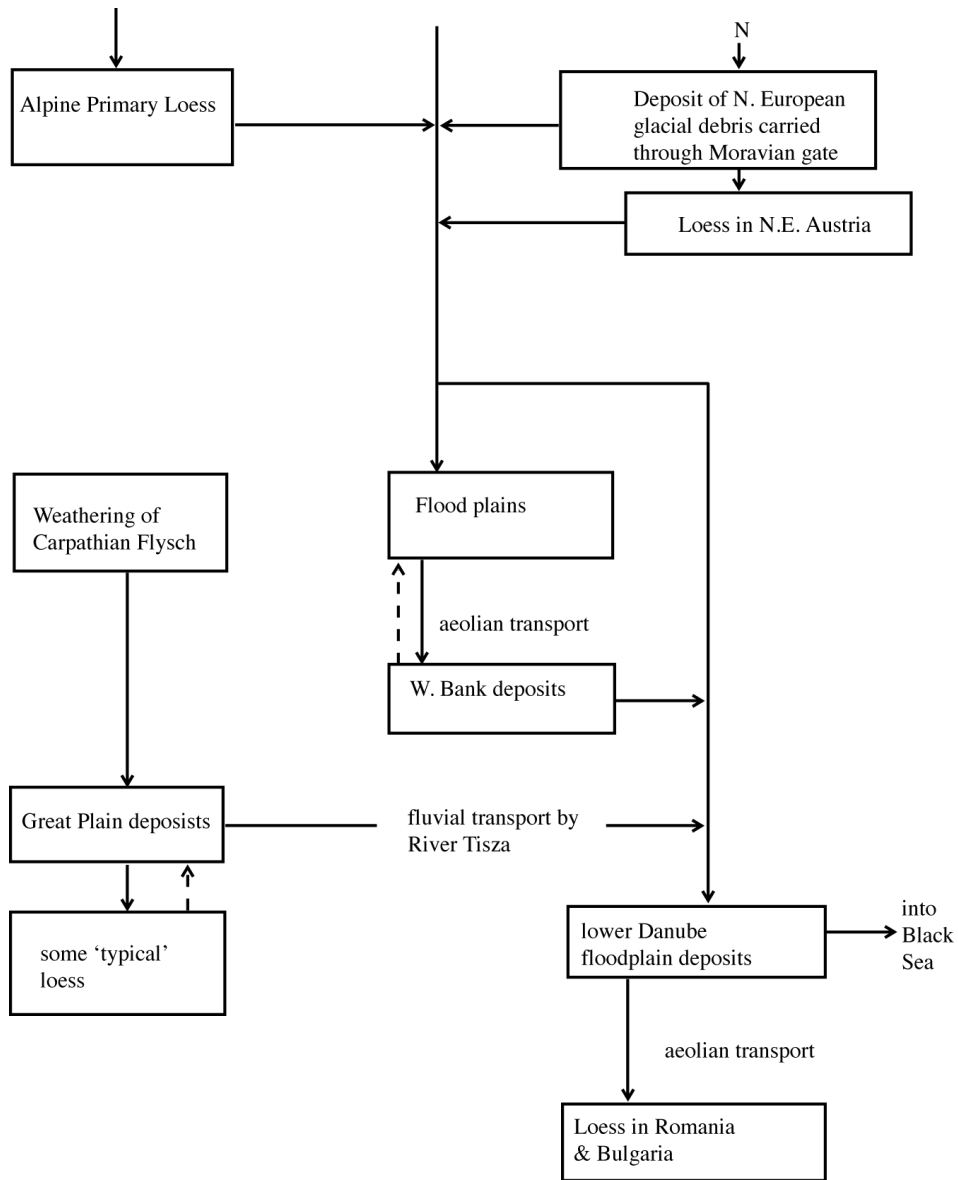


Figure 1.5 Generalized diagram showing the interconnections of Danube Basin loess deposits and their sources, modified from Smalley and Leach (1978, their figure 6, redrawn).

Table 1.5 Selected data from Újvári et al. (2008), Concentration of major (wt.%) and trace elements (ppm) from southwestern Hungarian loess deposits. CIA = Chemical index of alteration ; LOI = Loss on ignition

Sample	21	22	23	24	25	26	27	28	29	30	31	32	33	34	Mean	St. Dev.
Depth (m)	0.8	1.2	1.6	2	2.4	2.8	3.2	3.6	4	4.4	4.8	5.2	5.6	6		
SiO ₂	53.6	58.2	59.9	62.1	65.5	64.9	64.0	63.7	61.7	62.0	60.7	63.5	62.0	62.7	61.8	2.8
TiO ₂	0.8	0.8	0.9	0.9	1.0	0.9	0.9	0.9	0.9	0.9	0.9	0.9	0.9	0.9	0.9	0.0
Al ₂ O ₃	10.6	11.3	12.1	13.8	14.8	14.1	13.6	13.3	12.7	12.4	12.6	13.1	12.8	12.7	12.8	1.0
FeO _{tot}	3.8	4.0	4.3	4.9	5.1	4.7	4.5	4.3	4.2	4.1	4.4	4.3	4.2	4.3	4.3	0.3
MnO	0.1	0.1	0.1	0.1	0.1	0.1	0.1	0.1	0.1	0.1	0.1	0.1	0.1	0.1	0.1	0.0
MgO	4.4	5.0	5.0	4.3	3.0	2.6	2.9	3.1	4.0	4.5	4.6	4.4	4.7	4.7	4.1	0.8
CaO	23.5	17.0	14.0	9.7	6.1	8.5	10.1	10.6	12.5	12.0	12.8	9.5	11.4	10.5	12.0	3.9
Na ₂ O	1.1	1.4	1.4	1.6	1.7	1.5	1.5	1.5	1.4	1.5	1.5	1.5	1.5	1.6	1.5	0.1
K ₂ O	1.9	2.0	2.2	2.4	2.6	2.4	2.4	2.4	2.3	2.3	2.3	2.4	2.4	2.4	2.3	0.2
P ₂ O ₅	0.3	0.2	0.2	0.2	0.2	0.2	0.2	0.2	0.2	0.2	0.2	0.2	0.2	0.2	0.2	0.1
Total	100	100	100	100	100	100	100	100	100	100	100	100	100	100	100	0.0
LOI (%)	19.9	16.6	15.4	12.2	8.8	10.3	11.2	11.6	13.2	13.5	13.7	11.5	13.3	12.9	13.2	2.6
CIA	65	63	63	64	64	65	65	64	64	63	63	63	63	61	64	1.3
Rb	79	83	91	102	112	111	105	99	93	90	93	98	95	93	96	9.0
Sr	200	204	202	168	156	146	161	168	201	210	221	195	231	241	194	31.2
Ba	340	346	365	436	456	437	417	416	387	401	402	411	423	388	402	31.7

Table 1.5. Continued

Sample	21	22	23	24	25	26	27	28	29	30	31	32	33	34	Mean	St. Dev.
Depth (m)	0.8	1.2	1.6	2	2.4	2.8	3.2	3.6	4	4.4	4.8	5.2	5.6	6		
Pb	15	16	15	19	19	19	17	16	14	18	17	18	19	16	17	1.6
Th	11	11	14	14	14	14	14	13	14	13	12	14	15	14	13	1.2
Zr	315	351	359	356	365	368	366	368	363	368	348	366	352	371	359	13.5
Nb	17	16	17	19	20	18	18	18	17	18	17	18	17	17	18	1.0
La	35	46	52	46	54	50	60	55	40	39	43	43	42	46	46	6.6
Ce	73	82	85	81	104	103	95	94	91	89	80	82	91	88	89	8.2
Y	33	37	38	41	43	38	38	40	38	38	37	38	36	38	38	2.2
V	68	81	76	96	102	82	90	84	92	77	88	89	78	85	85	8.3
Cr	61	72	72	77	82	88	77	75	74	73	74	75	76	74	75	6.1
Ni	19	27	30	38	42	38	37	35	33	33	33	34	33	32	33	5.2
Cu	16	18	19	25	24	19	21	20	18	17	16	18	20	15	19	3.4
Zn	60	61	66	71	79	73	72	71	65	61	64	70	66	68	68	5.2
Ga	13	14	14	18	17	17	17	16	17	16	14	18	15	17	16	1.8
Rb/Sr	0.4	0.4	0.5	0.6	0.7	0.8	0.7	0.6	0.5	0.4	0.4	0.5	0.4	0.4	0.5	0.1
Ba/Sr	1.7	1.7	1.8	2.6	2.9	3.0	2.6	2.5	1.9	1.9	1.8	2.1	1.8	1.6	2.1	0.5
La/Th	3.2	4.2	3.7	3.3	3.9	3.6	4.3	4.2	2.9	3.0	3.6	3.1	2.8	3.3	3.4	0.5

Mineralogically, the loess is composed of mainly silt-sized quartz (31.1–48.8%), feldspars (5.2–13.6%), carbonates (10.7–37.2%) of which 69.4% is dolomite and the calcite/dolomite ratio is 1:2, minor micas and heavy minerals. The clay fraction consists mainly of illite and chlorite with minor smectite, kaolinite and mixed-layer clays (Újvári et al., 2008).

The Hungarian loess deposits have undergone some fluvial transport and show important chemical differences from typical upper continental crust, suggesting mixed sources for the deposits (Újvári et al., 2008). Because of the complex bedrock geology across the European continent and the possible long-distance aeolian transport of the loess, Újvári et al. (2008) concluded that ‘an accurate determination of provenance areas based on whole-rock geochemistry cannot be made’.

Adamova et al. (2002) examined loess deposits located in the southern Czech Republic and found carbonate contents to range between 16–40% near the cities of Znojmo and Pavlov with the presence of dolomite characterizing the loess around Znojmo while dolomite is ‘practically absent’ near Pavlov. The majority of their study locations provided, at a minimum, trace amounts of dolomite. Calcite content is moderate, with some samples near Pavlov reaching high abundance (Adamova et al., 2002). “Higher proportions” of dolomite at some localities may be due to the presence of dolomite in nearby pre-Quaternary sediments (Adamova et al., 2002). Average carbonate

content for their entire study area is 13.2%. Quartz content varies from 24–60% and plagioclase content ranges from 7–17%.

1.4 Relevant Previous Work in the Black Sea

1.4.1 Previous Work on Core MAR02–45 and around the core site

In 2002, Aksu and Hiscott, working aboard the R/V *Koca Piri Reis* of the Institute of Marine Sciences and Technology, Dokuz Eylül University, collected piston core MAR02–45P with a Benthos piston corer (1000 kg head weight) and a companion trigger-weight core (MAR02–45TWC). The location 41°41.170'N, 28°19.080'E on the southwestern Black Sea shelf is in a water depth of -69 m. These cores were shipped upright to Memorial University of Newfoundland (MUN), where they were split, described, and photographed by R.N. Hiscott and A.E. Aksu. Radiocarbon dates and geochemical trends suggest that the top of the piston core MAR02–45P corresponds to a depth of 110 cm in the trigger-weight core MAR02–45TWC (Hiscott et al., 2007b).

Based on seismic profiles (Huntec deep-tow system) from a grid comprising ~2800 line-kilometers of survey tracks, Aksu et al. (2002) mapped five seismic-stratigraphic units ranging in age from Miocene to Recent. Unit 1 represents the sediments deposited during the last glacial lowstand and the Holocene. This unit is underlain by the shelf crossing unconformity α . α extends to the shelf-slope break at 100–120 m depth, and across the entire width of the shelf (Aksu et al., 2002). Ryan et al.

(1997) identified an equivalent reflector on the northern Black Sea shelf. Unit 1 was subdivided into four subunits based on internal reflectors. Subunit 1A is found only along the shelf edge, and its top is defined by the α unconformity. Subunit 1B sits atop the α unconformity and the division of subunits 1B and 1C are defined by a moderately strong, regionally continuous reflector surface known as α_1 . The division between subunits 1C and 1D is defined by the presence of a weaker, locally continuous reflector (Aksu et al. 2002a) and is known as the α_2 unconformity. The relationship of these three unconformities to core MAR02–45 can be seen in Figure 1.6.

A calibrated radiocarbon age model has been published by Mertens et al. (2012). At 920 cm composite depth, a shell of *Dreissena rostriformis* was dated at 10.3 cal ka BP. Sedimentation is conformable upward to the α_2 unconformity at 270 cm composite depth where there is an extrapolated age of 5.4 cal ka BP immediately below the unconformity and an extrapolated age of 2.1 cal ka BP just above the α_2 unconformity, bracketing an hiatus of ~3.3 ka. The transgressive unconformity α is ~80 cm below the base of MAR02–45 (Reynolds, 2012). The composite core MAR02–45 samples various seismic subunits of Aksu et al. (2002): 1B (~10.5–8.1 cal ka BP), 1C (8.16–5.4 cal ka BP), and 1D (2.1–0 cal ka BP; Hiscott et al., 2007b; calibrations from Mertens et al., 2012).

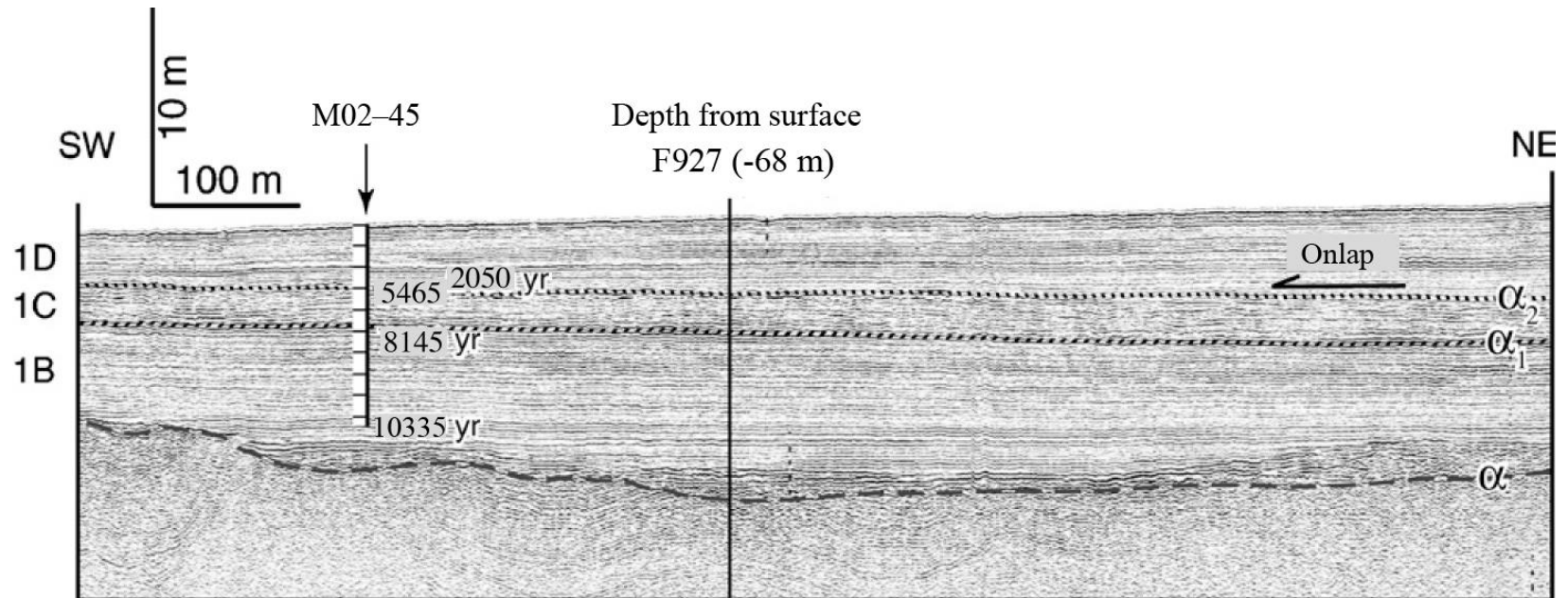


Figure 1.6 Hunttec DTS boomer seismic section showing core site M02-45 and seismic units 1B, 1C and 1D. Ages have been updated to calendar yr BP (Mertens et al., 2012). F927 refers to the seismic station along the seismic line. Original figure from Hiscott et al. (2007b).

MAR02–45 was examined visually for texture, colour and sedimentary structures. At 10 cm intervals ~20 cm³ samples were taken for geochemical, textural and micropaleontological analysis (Hiscott et al., 2007b). The samples were wet sieved at 63 µm to separate the sand fraction and to isolate foraminifera, ostracods and mollusk shells. Total sedimentary sulphur, total organic carbon, and stable isotopes of sulphur and carbon were measured using isotope-ratio mass spectrometry (Hiscott et al., 2007b). Palynological studies were undertaken on core MAR02–45 to determine vegetation patterns in the surrounding study area and any salinity changes during deposition.

Hiscott et al. (2007b) interpreted three lithologic units in core MAR02–45 (Fig. 1.7). The well-defined silt to very fine sand beds of unit C (= seismic subunit 1B) are either storm or shelf-turbidite deposits that lack features characteristic of wave reworking. They accumulated below fairweather wave base, and probably close to storm wavebase, conservatively estimated by Hiscott et al. (2007b) to be greater than ~30 m water depth. Unit C was divided into two subunits based on geochemical differences. Subunit C2 (beginning at 615 cm) shows a remarkable increase in total sulfur to a peak value of ~1.7%; sulphur declines to ~1% at the top of C2 (Fig. 1.7; Hiscott et al., 2007b).

Lithologic Unit B (= seismic subunit 1C) contains alternating beds of mud and shelly mud; bioclasts and bioclastic sand exceed 20%. The appearance of the mollusk *Modiolula phaseolina* suggests a salinity of ~18 psu, similar to today (Hiscott et al., 2007b).

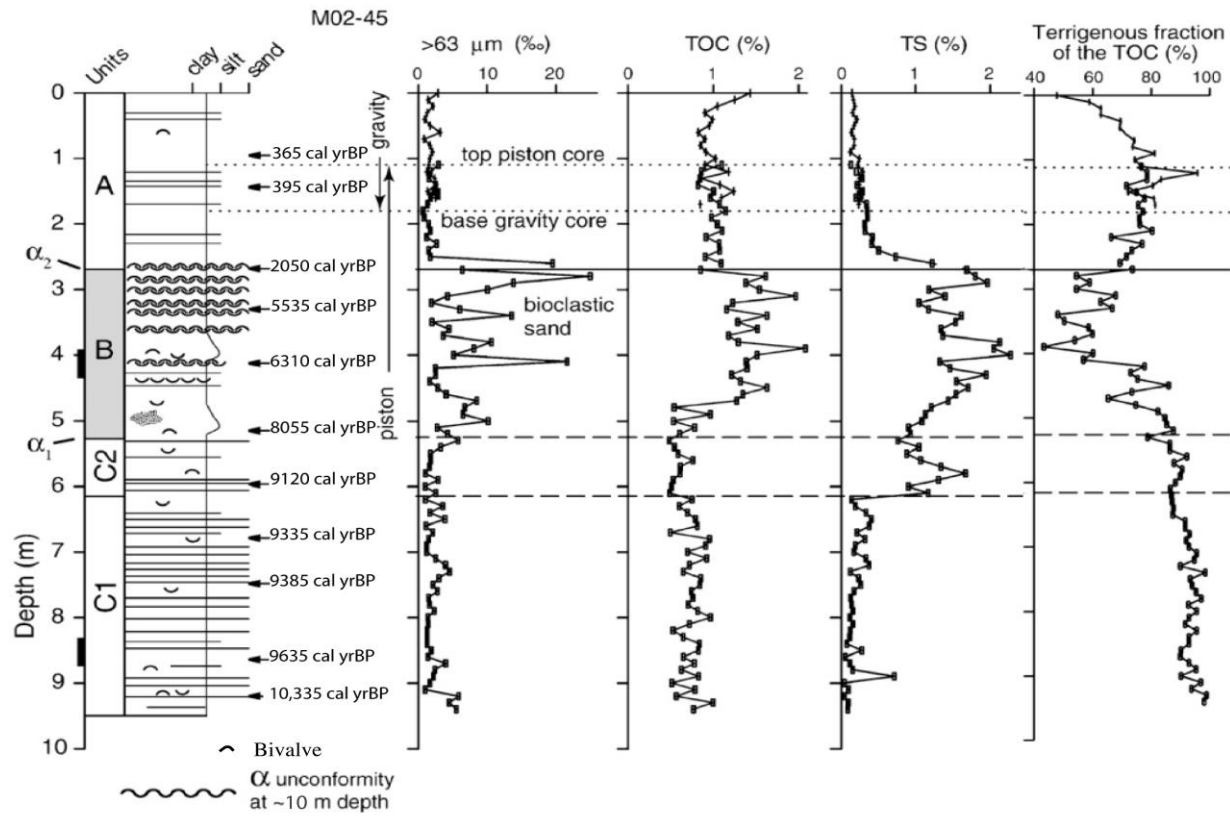


Figure 1.7 Selected proxy data from core MAR02–45 courtesy of Hiscott et al. (2007b). Age calibrations from Mertens et al. (2012).

Although the measurement of the process lengths of the dinoflagellate cyst *Lingulodinium machaerophorum* suggests a lower salinity of ~14–15 psu (Mertens et al., 2012). The mollusks in unit B lived at the coresite, suggesting a well-oxygenated shelf environment.

Lithologic Unit A (= seismic subunit 1D) is comprised of subtly colour-banded bioturbated mud with silt laminae and several mollusks of Mediterranean affinity. The deficiency of macrofossils in this unit suggests a poorly oxygenated environment (Hiscott et al., 2007b).

The age model and facies indicate that transgression occurred on the southwestern Black Sea shelf ~10.5 cal ka BP and that the outer and middle shelves have been inundated ever since. The oldest facies of MAR02–45 was deposited at or below storm wave base. By approximately 8.1 cal ka BP, continuous two-way flow was established with the Aegean Sea and by ~2.1 cal ka BP the middle shelf had become dysaerobic (Hiscott et al., 2007b; calibrations from Mertens et al., 2012).

1.4.2 Previous Mineralogical and Geochemical Work in the Black Sea

Many authors have undertaken mineralogical identification of the components of Black Sea sediments. This section will focus on the southwestern Black Sea and adjacent areas of possible influence such as the Danube River, Bosphorus Strait, and the rivers draining Thrace.

Bayhan et al. (2005) studied an area extending west-northwest from the Bosphorus entrance on the southwestern Black Sea shelf and uppermost slope bounded by the Turkish coast to the south and by longitudes 28.1–29.2°E (Fig. 1.1). Gravity cores, all <2.5 m, were taken at 15 locations: age control is poor. The <2 µm fraction was studied for its clay mineralogy; whereas, bulk samples were used for determination of non-clay minerals. The areas of diagnostic peaks in XRD spectra are not good estimators of mineral proportions, so it is general practice to apply weighing factors to certain peak areas. Weighting factors of Biscaye (1965), Mann and Müller (1980) and Gündoğdu (1982) were employed.

The major non-clay minerals reported by Bayhan et al. (2005) from bulk samples are aragonite (5–70%), 1 nm-micas (5–64%), quartz (5–58%), feldspars (4–46%), calcite (4–37%) and dolomite (2–11%). The 1 nm-mica shows an enriched zone from the inner shelf in the west to the outer shelf in the east. Bayhan et al. (2005) suggest this mica is derived from metamorphic rocks in Thrace and delivered by local rivers. The greatest abundance of aragonite was found in the northwestern part of the study area on the upper slope in sediment dated at 13.3 cal ka BP. No discernable trends were seen in the other non-clay minerals. The clay minerals measured were smectite (24–48%), illite (22–51%), kaolinite (2–32%) and chlorite (2–40%; Fig. 1.8). The short lengths of the gravity cores sampled by Bayhan et al. (2005) and their radiocarbon dates indicate that their shelf analyses do not extend into seismic subunit 1B (Unit C) of Aksu et al. (2002).

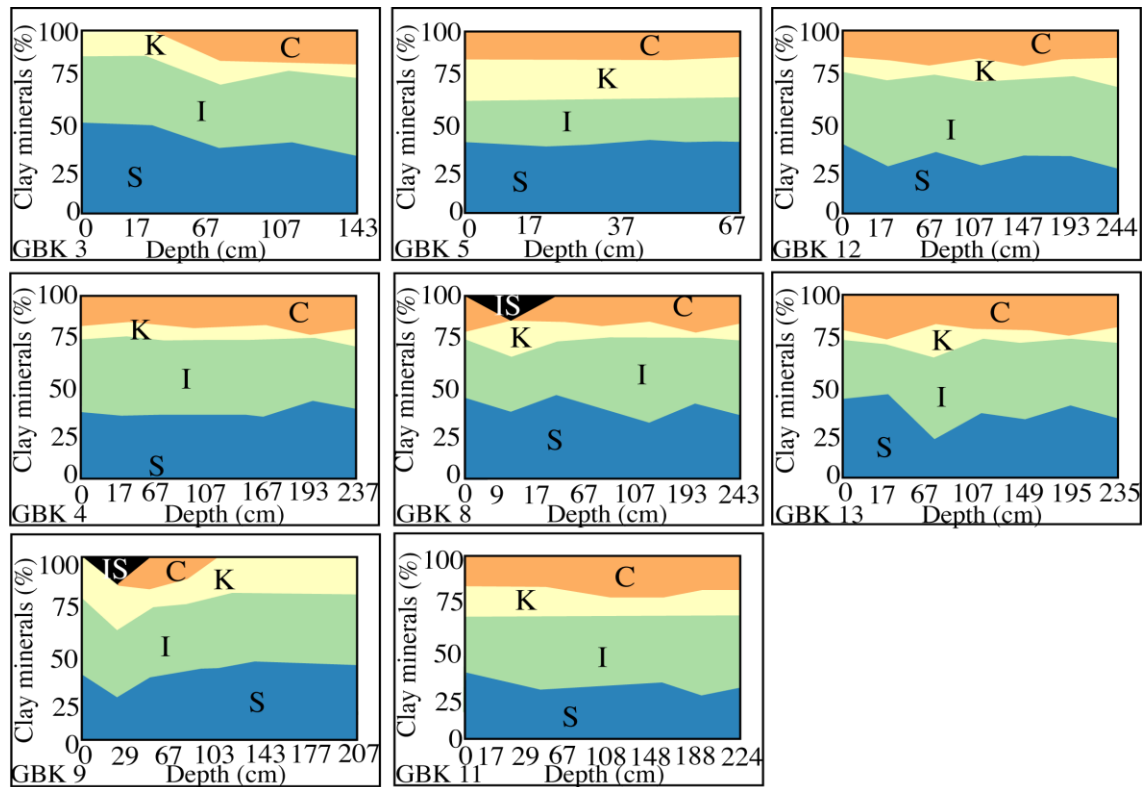


Figure 1.8 Clay mineral % in short cores from the southwestern Black Sea shelf (Bayhan et al. 2005, their figure 8).

Smectite=S, Illite=I, Kaolinite=K, Chlorite=C, Mixed Layered Clay=IS. Core numbers precede by CBK, correspond to numbered , orange filled circles in Fig. 1.1.

Bayhan et al. (2005) suggest that the dolomite has a terrigenous source and that most of the aragonite and calcite was bio-precipitated by benthic organisms. The feldspars and quartz are weathering products from magmatic sources (Bayhan et al., 2005).

The clay minerals were interpreted to have been primarily derived from coastal areas near the southwestern Black Sea shelf, but elevated illite concentrations are attributed to the Danube River. Bayhan et al. (2005) state that it is reasonable to expect some sediment input from northwesterly sources (Danube River) but the size of this contribution could not be quantified. These authors concluded that the clay minerals are homogeneously distributed by the prevailing current systems on the shelf.

Stoffers and Müller (1978) studied three deep-sea drill cores (Fig. 1.1) from the Black Sea basin. DSDP Hole 379 is located far to the east of the study area so it is not considered here. Hole 380 was drilled in 2115 m of water near the Bosphorus Strait and 1073.5 m of sediment were recovered. These sediments were divided into 5 units, numbered from the top downward. Unit 1 is comprised of 332.5 m of terrigenous Pleistocene sediments including muds, silty sands and sandy silts (Stoffers and Müller, 1978), and is the only unit relevant to this thesis.

DSDP Hole 381 was drilled landward of Hole 380 at a water depth of 1750 m (Stoffers and Müller, 1978) and was divided into four units. The uppermost unit consists

of 171 m of terrigenous silts, sandy clays, and clays with a basal sand interval (Stoffers and Müller, 1978). The older units are not relevant to this thesis.

X-ray diffraction analysis was performed on DSDP samples from Holes 380 and 381 by Stoffers and Müller (1978) and Trimonis and Ross (1978). The $<2 \mu\text{m}$ separates were analyzed. The Pleistocene sediments at Site 380 contain abundant clay minerals, particularly illite. The montmorillonite/illite ratio of these sediments ranges from 0.004 to 0.02 (Trimonis and Ross, 1978). Calcite is the predominant carbonate in these Pleistocene sediments and is often associated with minor dolomite (Trimonis and Ross, 1978). Chlorite content is approximately the same at Site 380 (14 wt.%) and kaolinite occurs in low abundances (<10 wt.%; Stoffers and Müller, 1978).

Quartz and feldspar content vary throughout Hole 381, averaging ~ 25 wt.% each (Stoffers and Müller, 1978). The highest quartz content is found in Pleistocene sediments where quartz is 1.5 to 2 times more abundant than feldspar (Trimonis and Ross, 1978).

Major (2002) sampled two cores from the western Black Sea (off the Romanian shelf) and analyzed the carbonate and clay fractions. The cores were divided into three lithologic units (Fig 1.9). Upper Holocene Unit 1 is a light-grey, organic rich, finely laminated mud (Major, 2002). Middle Holocene Unit 2 consists of a dark grey sapropel, and lower Holocene to Pleistocene Unit 3 begins at a downward change in colour from dark green, to grey, to brown (Major, 2002). Elevated abundances of illite characterize the lower unit of both cores, then decrease at the top of the brown unit.

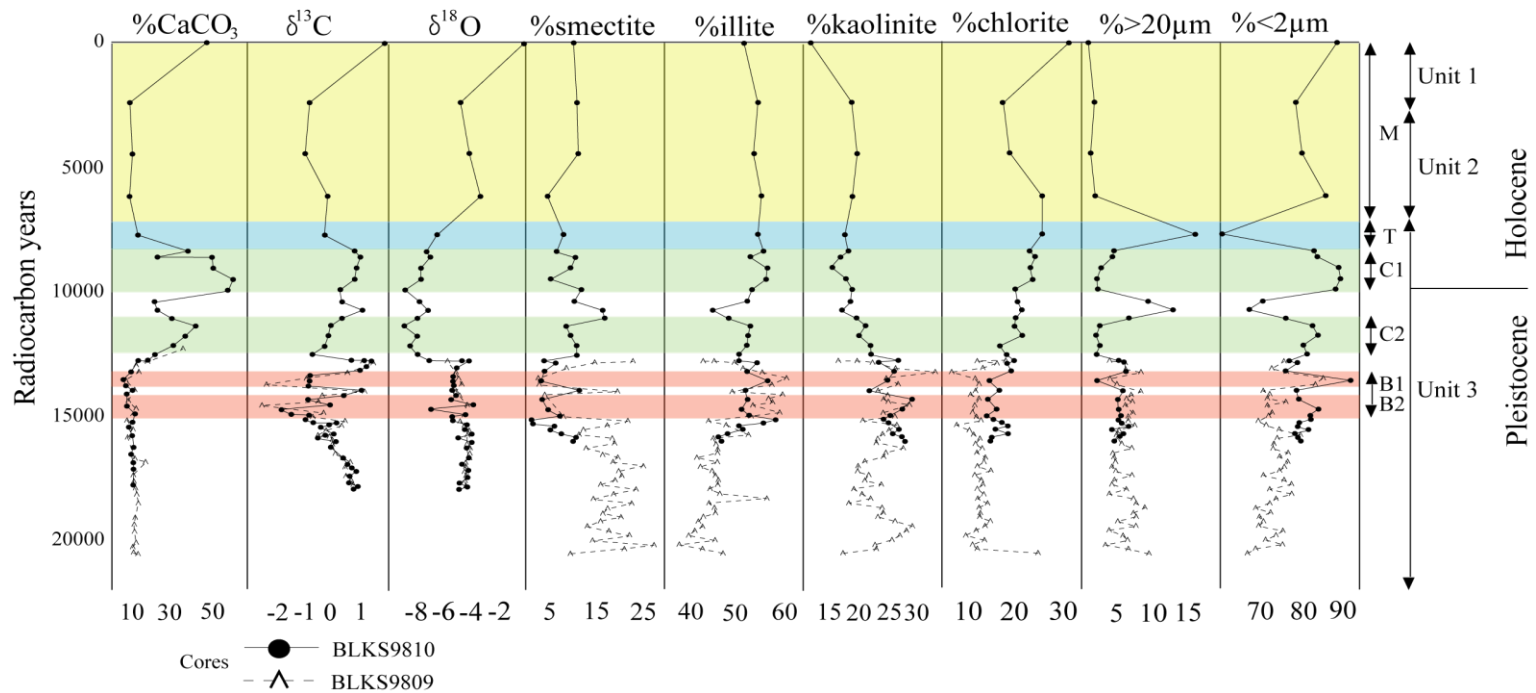


Figure 1.9 Core analyses from Major (2002; her figure 2-4, redrawn) showing mineral abundances for carbonate and the main clay minerals. Only her units 1, 2 and the uppermost 3–4 sampling positions in unit 3 overlap in age with the sediments at core site MAR02–45. All scales are in % except for $\delta^{13}\text{C}$ and $\delta^{18}\text{O}$ which are in per mil (relative to PDB). M indicates marine sediments, T a dark green mud at the base of a sapropel. C1 and C2 are areas with carbonate peaks while B1 and B2 are brown, clay-rich horizons.

Smectite is abundant in the Upper Pleistocene and during intervals when authigenic carbonate formation decreased (Major, 2002).

Major (2002) measured carbonate values from 9–13% in the lower section of Unit 3. In the upper portion of Unit 3 there are two spikes in carbonate content: the first reaches 42% and then values return to ~20% followed by a second spike with carbonate values peaking over 60% (Fig. 1.9; Major, 2002).

Major (2002) interpreted the high smectite values in the lower parts of the cores to indicate a southern source (i.e., Thrace) for clay minerals in older sediments. The modern sediments contain higher values of illite and kaolinite, which she attributed to increased erosion in northern drainage areas during the collapse of Scandinavian and Alpine glaciers (Major, 2002). Kaolinite and illite concentrations decreased once vegetation became established in deglaciated areas with resulting slower erosion (Major, 2002).

There has been considerable work on the geochemistry of Black Sea sediments below the chemocline, in the anoxic part of the basin (e.g., Kıratlı and Ergin, 1996; Dean and Arthur, 2011; Piper and Calvert, 2011; and references therein), but little work of a similar nature on the shelves where the bottom waters are oxygenated. Generally, in the deeper anoxic parts of the Black Sea, the formation of sulphide minerals and adsorption of metals on to organic particles are important (Kıratlı and Ergin, 1996; Dean and Arthur, 2011; Piper and Calvert, 2011), but other processes are expected to be important in shelf regions, like transport of a greater proportion of minor and trace elements in detrital

particles, and perhaps greater element mobility during early diagenesis as components pass from the oxygenated sediment-water interface into the subsurface with its poorly oxygenated pore waters.

Dean and Arthur (2011), in their studies of Black Sea sediments beyond the shelf edge (in anoxic bottom waters; one core located in Fig. 1.1), report that Co, Ce, La, Th and Y are generally in detrital aluminosilicates. In contrast, Dean and Arthur (2011) and Kıratlı and Ergin (1996) have determined that V, Ni, Zn and Cu tend to be concentrated in organic-rich Black Sea sediments, either because of biogenic fixation or adsorption under reducing conditions that persist from the water column into the sedimentary column. However, Dean and Arthur (2011) find that in some circumstances V and Ni are bound in detrital phases rather than residing in complex ions in the water column.

Piper and Calvert (2011; one core located in Fig. 1.1 but most in deeper water) found that Cd, Cu, Ni, and Zn are predominantly associated with the biogenic fraction of sediments, while Mo, Re, U, and V are primarily found in the hydrogenous fraction that accumulates through adsorption/precipitation reactions.

Hirst (1974) performed factor analysis on 25 elements from eleven slope and basin cores to determine the main controls on element distribution in the Black Sea. He extracted seven factors that control 88.4% of the total variance in his data. His first two factors account for 62.8% of the total variance. Factor 1 has its highest loadings on MgO, Fe₂O₃, Al₂O₃, and K₂O, with a minor contribution from Na₂O. This factor represents multiple clay minerals (chlorite and montmorillonite) contributed by a

southwesterly source (Hirst, 1974). Factor 2 is controlled primarily by Al_2O_3 , Na_2O , and K_2O with a small Zn contribution, suggesting a relationship to illite and feldspar. Scores for this factor are high in the southern and southwestern Black Sea, with some high values in the central Black Sea (Hirst, 1974).

Factor 3 controls almost all the variance of MnO, and is attributed to the precipitation of manganese micronodules that have been reported in the Black Sea with its particular Eh and pH conditions (Hirst, 1974). Factor 4 is dominated by Ba; Hirst (1974) concluded that there must be a distinct Ba mineral present (barite).

The remaining four factors extracted from the geochemical data by (Hirst, 1974) are not discussed here because they contribute little to the overall variance and are not particularly relevant to the oxygenated environments of the western and southwestern shelves.

1.4.3 Mineralogy and Geochemistry of the Danube System

The Danube River is over 2800 km long and is a major water and sediment source for the Black Sea and possibly for the nearby southwestern Black Sea shelf. The Danube River has been studied extensively. The focus of this review is on the mineralogical and chemical composition of sediments, and on the evolution of the Danube Delta.

Dinescu and Dului (2001) studied heavy metal concentrations in lake sediments of the Danube Delta. It was found that Zn, As, Sb and Br (148.8, 15.5, 2.7, and 9.7 ppm in modern sediments) concentrations were 1.2–2 times higher near the sediment surface

than in the lower portions of the cores. This distribution shows an increase in pollutants until the end of the 1980's, due to the industrialization of central and eastern Europe. After 1990 a slow decline in pollutant levels can be attributed to changing political ideals (the fall of the Soviet Union) in Europe (Dinescu and Dului, 2001). Oreščanin et al. (2005) found slightly elevated levels of Cu and Ni, but the total Pb, Cu, Zn, Cr, Mn, Fe and Ni concentrations were similar to those found in the shale and soils of Batina (Croatia) and Mohacs (Hungary).

Haslinger et al. (2006) studied the mineralogy of three Danube River floodplain horizons (DA1, DA9, and DA11) deposited at 0.1, 0.6 and <10.0 ka BP in Austria, thus closer to the headwaters of the river than to the Black Sea. Minerals in the bulk sediment are dominated by calcite and dolomite (dolomite being the dominant carbonate phase). Quartz, K-feldspar, plagioclase, chlorite, kaolinite and mica are found in low to moderate amounts. Micas and amphiboles are most abundant in younger deposits, as both are sensitive to weathering processes. High levels of feldspar are also found in the youngest samples and that may be due to the flooding bringing fresh, unweathered material (Haslinger et al., 2006).

Illite is the dominant clay mineral found in these deposits (52–64%), and increases slightly in older samples. Chlorite values range from 18–30% making it the second most abundant mineral in the clay fraction. Its highest values are in the youngest material as the chlorite is fresh and unweathered. Smectite values are low (7–17%) and vary due to the change in smectite abundance of materials eroded during flooding events. Kaolinite

values range from 4–7% while vermiculite and mixed layer clays are only present in trace amounts (Haslinger et al., 2006).

1.5 Specific Thesis Objectives

The six main goals of this thesis are:

- 1) to provide an estimate of the volume of sediment deposited in the area of core site MAR02–45 during the early Holocene (Unit C) using isopach diagrams from Hiscott et al. (2007b), and to compare these results with the amount of sediment potentially delivered (using the BQART equation) by local sources to the shelf;
- 2) to compare the texture (and any internal variations) of core MAR02–45 the texture of potential sources;
- 3) to determine the mineralogy of the silt fraction of sediments from core MAR02–45 and to compare that mineralogy to potential source materials (e.g., the Danube Delta, rivers in Thrace);
- 4) to determine the mineralogy of the clay size fraction of sediment from core MAR02–45 and to compare that mineralogy to potential source materials;
- 5) to interpret geochemical abundances and downcore trends in samples from MAR02–45, and to compare these results to data from potential sources; and
- 6) to run statistical models on raw geochemical data to create Q- and R-mode factor analyses so that downcore variations can be simplified and interpreted.

Chapter 2 Methods

The primary core studied for this project is MAR02–45; it was collected on the southwestern Black Sea shelf (Table 1.1) and has been previously studied by Hiscott et al. (2007b), Marrett et al. (2009), Mertens et al. (2012) and Bradley et al. (2012) using palynology and geochemistry as indicators of paleoenvironment through the Holocene.

X-ray diffraction (XRD), instrumental neutron activation analysis (INAA), and inductively coupled plasma-optical emitted spectrometry (ICP-OES) are used to explore the mineralogy and chemical composition of core MAR02–45, and samples from potential sources (local rivers and the Danube Delta). Sediment volume estimates are calculated using ImageJ freeware to obtain areas and volumes from the isopach diagrams of Aksu et al. (2002), supplemented by additional seismically imaged thicknesses from more recent cruises MAR–02 and MAR–05. Sediment discharges from local rivers are estimated using the BQART equation of Syvitski and Milliman (2007). The texture of MAR02–45 samples is based on sand/silt/clay ratios determined during sample preparation for mineralogical analysis.

2.1 Sample Preparation

2.1.1 *Availability of Samples and Restrictions on Sample Size*

Core MAR02–45 was collected in 2002 and the working half of the core was sampled in 2003 at 10 cm intervals for the analysis of texture, micropaleontology (foraminifera, ostracoda), and carbon and sulphur geochemistry. Additional samples

were taken for further micropaleontological studies prior to the start of this geochemical analysis. As a result, the amount of new material available for new work was limited and the collection of fresh samples was not an alternative. Doing so would have depleted the working half of the core and would have yielded samples at different depths from the initial samples so that various data sets could not be integrated with one another.

Destruction of the archive half of the core is a step of last resort, and is never undertaken except for the strongest scientific purposes, not for the type of reconnaissance study that is addressed in this thesis. The available samples consisted of (a) previously untreated, dried and bagged material left over from palynological preparations in the range of 3–10 g, and (b) <63 μm splits of samples from wet sieving that was done to isolate microfossils (e.g., foraminifera) in the sand fractions of the sediments. These fine fractions had been stored under distilled water and had dry weights in the range of 2–7 g. Because of the greater sample size needed for mineralogical studies (in order to be able to prepare XRD mounts and to recover clays from silt-rich sediments), it was decided to use the untreated material for XRD work and the <63 μm splits for geochemical analysis. This decision had repercussions for the type of geochemical analysis that could be completed, but was shown to be the best choice because of the small percentages of clay in almost all samples.

2.1.2 Preparation for XRD Analysis

The dry, bagged samples were prepared for XRD analysis using the following method (a more detailed 13-step list of processing steps can be found in Appendix 1):

In the laboratory with an ambient temperature of $\sim 25^{\circ}\text{C}$ start with 3–10 g dry sediment, or 10–15 g wet mud, in a labeled plastic beaker. Each sample was mixed with ~ 100 ml of 5% hydrogen peroxide, and subjected to ultrasonic treatment until full disaggregation was evident. Then each sample was wet sieved at $63\ \mu\text{m}$ to separate the sand fraction, which was dried, weighed and stored.

The $<63\ \mu\text{m}$ separate was flocculated with MgCl_2 and allowed to settle until the water was clear. Excess water was aspirated off and the remaining sediment was transferred to a small porcelain bowl, placed in an oven at $\sim 55^{\circ}\text{C}$ to dry, and then weighed.

The dried mud was transferred to a small beaker, combined with 40 ml 0.05% Na-hexametaphosphate (calgon) and then disaggregated with an ultrasonic probe. The dispersed sample was transferred to a 400 ml beaker filled to a mark 7 cm from the bottom with 0.05% Na-hexametaphosphate. Each beaker was also marked 2 cm from the bottom. After vigorous stirring, the suspension was allowed to settle under still conditions for 3 hours, 50 minutes (± 5 minutes). By that time, Stoke's Law indicates that only $<2\ \mu\text{m}$ particles would be in the upper 5 cm of the initial suspension. Next, the suspension between the two marks (~ 200 ml) was siphoned into a 600 ml beaker, using a siphon tube with a 90° curve at the suction end, to avoid drawing material from below the bottom line marked on the beaker. Fresh 0.05% Na-hexametaphosphate was added to the

original beaker, stirred vigorously, then the separation procedure was repeated to ensure near-complete recovery of the $<2\ \mu\text{m}$ fraction. The remaining suspension in the lower 2 cm of the 400 ml beaker was retrieved, dried, weighed and stored as the 2–63 μm fraction.

The two aliquots of $<2\ \mu\text{m}$ suspension were combined and allowed to settle overnight, and then the clear fluid was aspirated off. Using a wash bottle with 0.05% Na-hexametaphosphate, the $<2\ \mu\text{m}$ fraction was transferred to a bulb-bottomed, 20 mm-diameter glass test-tube and filled to 5 cm above the $\sim 5\ \text{mm}$ -diameter neck (the neck is located just above the lower bulb, Fig. 2.1) with more 0.05% Na-hexametaphosphate. The tubes were placed in a rack and settling was allowed to proceed for 3 hours, 50 minutes (± 5 minutes), after which time the neck of each tube was blocked with a tapered plastic rod and the upper suspension poured into a labeled plastic beaker. This final step was designed to remove any remaining $>2\ \mu\text{m}$ particles. The $<2\ \mu\text{m}$ separate was centrifuged three times, each time with fresh, distilled water, then transferred to an aluminum dish to air dry. The dried material was weighed and stored in a vial until smear mounts were made. Its weight was multiplied by a factor of 1.5 to account for the $<2\ \mu\text{m}$ material that was discarded from the lower bulb of the test tube, after determining that the volume of the lower bulb was 50% of the volume above the neck up to the 5 cm mark. One sample was analyzed using an Horiba size analyzer to verify, as was the case, that samples prepared as explained above contain only $<2\ \mu\text{m}$ material.

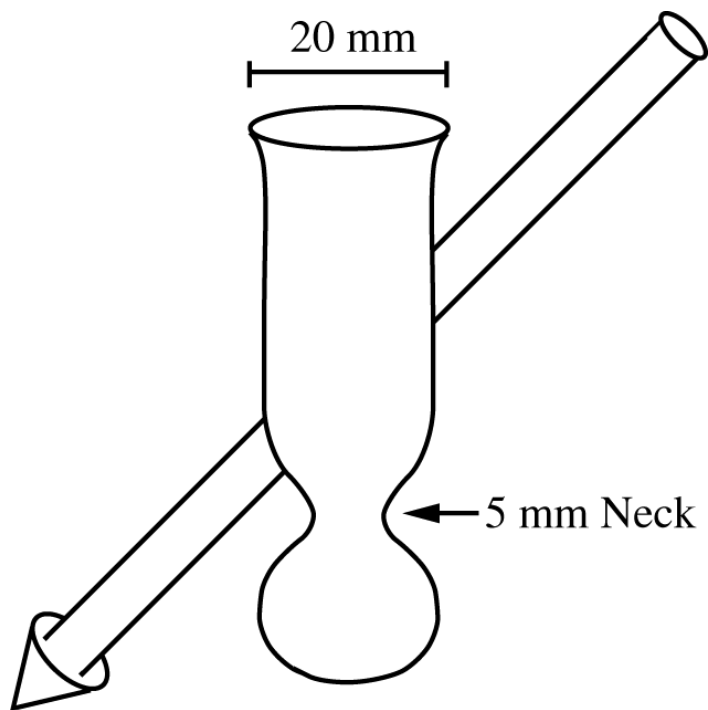


Figure 2.1 Bulb-bottomed test tube and specially fabricated tapered stopper rod. This equipment was used in the final separation procedure of the $<2 \mu\text{m}$ fraction

To prepare the 2–63 μm (silt) fraction for XRD analysis, 1.5 g of sample was combined with 75 mg \pm 2 mg (~5 wt.%) of MoS_2 (methodology of Quakernaat, 1970) and ground into a fine powder using an agate mortar and pestle. The powder was packed in a random orientation using a side-packed method (Hanchar et al., 2000), or a front-loaded method in a recessed aluminum holder available in the Memorial University XRD laboratory, with careful attention to avoid forcing an orientation. Careful packing using the front-loaded method allowed for faster analysis (more samples per day) and showed little to no loss of intensity of characteristic peaks (Fig. 2.2).

For those samples with sufficient material (70 of 80 samples), 40 mg of the $< 2 \mu\text{m}$ (clay) fraction was combined with $\sim 2 \text{ mg} \pm 1 \text{ mg}$ (~5 wt.%) MoS_2 (Quakernaat, 1970) and mixed into a homogeneous paste with sparse amounts of a 0.2 M solution of MgCl_2 . This paste was then applied to an acrylic slide using the thin edge a piece of photographic film as a "spatula" and the smear technique described by Gibbs (1965), and verified by him to give a dependable preferred mineral orientation.

109 samples shipped to Activation Laboratories (ActLabs), Ancaster, Ontario, were taken from the stored $< 63 \mu\text{m}$ wet fractions from earlier work on core MAR02–45. These samples had no prior treatment, and had been stored in sealed containers under distilled water. Samples from potential sources were prepared in a similar fashion after sand removal. These samples were ground into a fine powder in an agate mortar and pestle and $\sim 3 \text{ g}$ of material (per sample) was sent for analysis.

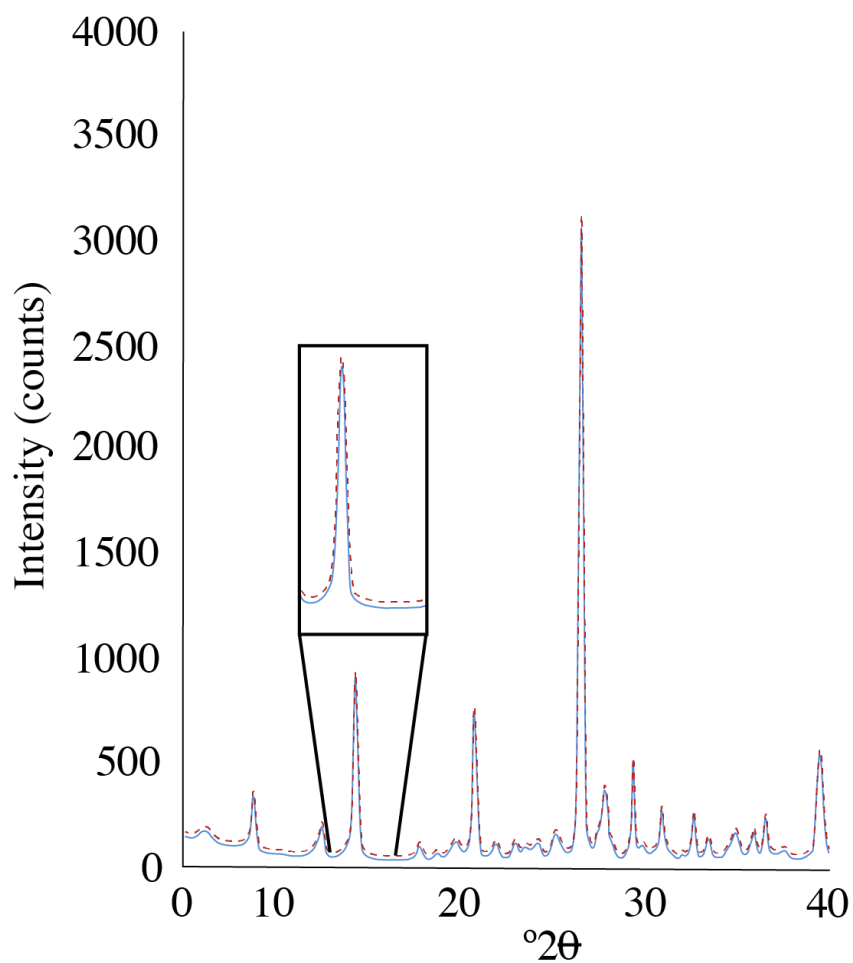


Figure 2.2 Front-loaded-mount peak intensity (solid) vs. a spectrum from the same sample using the side-loaded method (dashed) of Hanchar et al. (2000). The front-loaded method is more prone to create an orientation, so care must be taken when preparing the mounts. Front-loaded mounts allowed more samples to be run per day, while returning peaks of comparable intensity. The enlarged area shows just how little intensity was lost using the front-loaded mounts compared to the side-loaded method, and the degree of overall precision using the XRD powder mounts.

2.2 Methods of Analyses

2.2.1 Selection of Geochemical Method

Before samples underwent geochemical analysis many methods were proposed and investigated. The method(s) chosen for analysis had to take into account the limited sample size (<3–5 g for the majority of samples) while trying to maximize the number of elements analysed all at a reasonable cost. The XRD facilities at Memorial University require a minimum of 5 g per sample for analysis, and more if replicate analyses are to be undertaken. As an alternative, a range of analytical packages from a commercial laboratory, Activation Laboratories (hereafter ActLabs) of Ancaster, Ontario was investigated. Maximizing the number of trace element determinations was of utmost importance, as major elements are not considered strong indicators of provenance in fine-grained sediments. Again methods requiring 5 g or more of material could not be included. This includes the 4B WRA-ICP package, which although it provides both major and several trace elements at high accuracy, omits certain elements (except as options with increased cost) that were anticipated to have discriminating power in pointing to particular source areas or environmental conditions (e.g., Co, Cr, Mo, U, and several rare-earth elements). Other packages under the ActLabs heading “Litho geochemistry for Exploration and Research” prove to be at least twice as expensive as the package that was selected, this being the ActLabs combined 4-acid digestion ICP-OES and instrumental neutron activation (INNA) package (Code 1H). This package provides data on 6 major elements, 4 minor elements, 29 trace elements and 10 rare-earth

elements. Code 1H requires a maximum of 3 g per sample so that the <63 μm splits from previous studies could be used, permitting later integration of the results with existing TS, TOC, and isotopic data from the same depths.

Two batches of samples were sent to ActLabs for geochemical analysis. All 102 samples from MAR02–45 were sent on April 7th, 2011, while the seven samples from potential source areas were sent on February 14th, 2012. ActLabs analytical package Code 1H “Au+48” combines laboratory Code 1D (enhanced INAA) which provides data on 31 elements and Code 1F (4-acid digestion ICP technique) which determines the remaining 18 elements (ActLabs, 2010). SiO_2 is not analyzed due to volatilization by acids. The acid extractions for Al, S and Y are partial, according to laboratory documentation. Detection limits are shown in Table 2.1. Ten samples that had already been replicated from the April 7th set were sent in duplicate on January 11th, 2014 requesting full replication of each sample. These samples were <1 g each but within an acceptable range determined through discussions with ActLabs staff. This latter set was submitted to create a sufficient number of replicate analyses for statistical analysis.

During data analysis presented in Chapter 3, it became clear that downcore trends could be clarified by recalculating elemental abundances to remove the effects of dilution by calcite. Eventually this was done using the calcite abundances from XRD analysis of silt fractions after establishing a linear regression between ActLabs Ca abundances and XRD calcite percentages (needed because of no XRD results at approximately half of the 10-cm depths). A more accurate way to quantify the amount of calcite in each sample would have been to determine CO_2 loss with acidification, as done in the Terra Facility at

Table 2.1 Detection limits of 49 elements using INAA and ICP–OES compared to elemental abundances of the average North American Shale (Gromet et al. 1984). Values are in ppm unless indicated to be ppb or %.

*Cold Vapour analysis by ActLabs is used to determine Hg-CV

Symbol	Detection Limit	Avg. North American Shale
Ag	0.3	
Al	0.01%	
As	0.5	28.4
Au	2 ppb	
Ba	50	636
Be	1	
Bi	2	
Br	0.5	0.69
Ca	0.01%	3.3% CaO
Cd	0.3	
Ce	3	66.7
Co	1	25.7
Cr	2	124.5
Cs	1	5.16
Cu	1	
Eu	0.2	1.18
Fe	0.01%	5.09% FeO
Hf	1	6.3
Hg	1	
*Hg-CV	(5 ppb)	
Ir	5 ppb	
K	0.01%	3.8% K ₂ O
La	0.5	31.1
Lu	0.05	0.456
Mg	0.01%	
Mn	1	
Mo	1	
Na	0.01%	1.008% NaO
Nd	5	27.4
Ni	1	58

Table 2.1. Continued.

Symbol	Detection Limit	Avg. North American Shale
P	0.00%	
Pb	3	
Rb	15	125
S	0.01%	
Sb	0.1	2.09
Sc	0.1	14.9
Se	3	
Sm	0.1	5.59
Sn	0.01%	
Sr	1	142
Ta	0.5	1.12
Tb	0.5	0.85
Th	0.2	12.3
Tl	0.1	
Ti	0.01%	
U	0.5	2.66
V	2	
W	1	2.1
Y	1	
Yb	0.2	3.06
Zn	1	

MUN (P. King, pers. comm. to R. Hiscott, 2014), followed by back-calculation of the amount of Ca needed to form calcite with this amount of CO₂, permitting determination of the original percentage of calcite in each sample. However, this procedure at MUN requires an additional 5 g of sample, so could not be considered.

2.2.1 Factor Analysis

Q- and R-mode factor analysis was run on geochemical data returned by ActLabs, augmented by TOC, TS and stable-isotopic data previously published by Hiscott et al. (2007b). In order for these data to be analyzed, each variable was normalized. Data normalization is important to avoid bias towards dominant elements (Davis, 1973). Normalization was achieved by first subtracting the minimum value recorded for a particular variable from all other determinations of that variable – this creates a value of 0 for the sample with the lowest abundance of that component. Then all adjusted measurements of that variable were divided by the largest value in the set of data, creating a maximum value of 1. Once completed for all variables, this normalization creates a matrix with values ranging from 0 to 1 allowing the factor-analysis program QRmode, written by Klovan (1971), to extract relationships between variables and samples.

2.3 X-Ray Diffraction

X-Ray diffraction is a non-destructive technique for the analysis of small quantities of crystalline materials. The X-Ray diffractometer at Memorial University is a Rigaku Ultima IV and uses a Cu-K α radiation source. Measurements were taken using a

current of 40 kV, 44 mA, with a divergent slit size of 10 mm, a receiving slit size of 0.3 mm and a scan speed of 1° min^{-1} for most runs (see below). Scanning ranges and step size varied with the material analyzed, as described in later sections. A major drawback of X-Ray analysis is the difficulty in detecting minor phases (<5 wt.%) in a sample. As a result, it is possible that some exotic minerals with potentially helpful provenance information may have been overlooked.

2.3.1 Randomly Oriented Silt Mounts

Randomly oriented mounts of powdered silt fractions were prepared and analyzed in Memorial University of Newfoundland's Alexander Murray Building. Front-loaded mounts were run in batches of ten. Material was added to the holder by gently tapping on weighing paper containing powder, and the sample holder itself, until enough material filled the recess in the holder to its lip. Most samples required no extra steps. If the surface of a sample was uneven, a glass slide was used to gently level the surface, with care so as to not apply excessive force and induce an orientation. Samples were scanned from $5\text{--}40^\circ 2\theta$ with a step size of $0.02^\circ 2\theta$. These analyses were sporadically checked against analyses of the same samples obtained using the side-loaded method. Analysis and whole pattern fitting (WPF) refinement was done using the Jade[®] software package which computes wt.% abundance for detected minerals after using a cubic spline to resolve peaks from the background.

2.3.2 *Oriented Clay Mounts*

Oriented clay mounts were run three times: once ‘glycolated’ and twice ‘air dried’. The glycolated analyses were performed after the samples had been exposed to ethylene glycol for at least 8 hours at ~60°C; in this case, the diffractometer scanned between 5–17° 2 θ . The first ‘air-dried’ scan provided data from 5–40° 2 θ using a speed of 1° 2 θ min⁻¹ and a step size of 0.02° 2 θ . The second run focussed on the 25–28° 2 θ range and scanned using a step size of 0.005° 2 θ . This was done to differentiate partly overlapping chlorite and kaolinite peaks in this 2 θ range (Biscaye, 1964). This permitted determination of a kaolinite/(kaolinite+chlorite) ratio that could be used to partition the 0.7 nm peak. Oriented clay mounts were analyzed using MacDiff freeware (Petschick, 2002) to determine the areas of diagnostic mineral peaks in the <2 μ m fraction after fitting a background trace; Jade was not used to determine mineral peaks as Memorial University of Newfoundland does not have the proper databases to analyze diffractograms from oriented mounts. Spectra from the three separate runs were aligned and scaled to one another using the position and area of the 0.615 nm peak of MoS₂. The intensities and areas of peaks measured are listed in Tables 3.4 and 3.5.

Mid-way through the thesis research, after the first air-dried runs had been completed, the X-ray tube on the Memorial University of Newfoundland diffractometer failed and was replaced, and it became apparent that X-ray emissions from the original tube that later failed were weak. For this reason, intensities and peak areas for the same minerals are different between that first air-dried run and subsequent runs. The presence

of the 0.615 nm peak of MoS₂ in both air-dried and glycolated runs allowed all data sets to be scaled and merged regardless of different overall peak intensities.

When the same smear mount was re-run after glycolation, there were often systematic shifts in the positions of peaks, including MoS₂ peaks. Either imperfections in the alignment of the sample holder(s) or expansion of the lattice of some clays must have raised the level of the top of the clay film enough to change the geometric configuration of the X-ray beam relative to the sample surface, leading to so-called displacement errors (Pérez and Tabares, 2002). Adjustment of the position of the 0.615 nm peak of MoS₂ eliminated the effect of these shifts.

During MacDiff analysis of the chlorite/kaolinite slow scan runs, some samples did not have large enough peaks to measure and deconvolve their areas accurately. The presence of one or both of these minerals was confirmed using the 0.7 nm peak. In order to estimate the amount of chlorite and kaolinite present in a sample with no slow scan run, the 0.7 nm peak in these samples was apportioned into chlorite and kaolinite areas based on the kaolinite/(kaolinite+chlorite) ratios of samples immediately above and below (eg. hypothetical sample 2 has an unknown kaolinite/(kaolinite+chlorite) ratio while hypothetical samples 1 and 3 have known kaolinite/chlorite ratios of 0.60 and 0.70; therefore, sample 2 is assigned a kaolinite/(kaolinite+chlorite) ratio of 0.65).

2.3.3 $<2 \mu\text{m}$ Mineral Abundances

The relative abundances of the minerals in clay-sized fractions of marine sediments have been quantified in the past using empirical scaling factors applied to the peak areas of the primary minerals, in particular smectite, illite, chlorite and kaolinite. Hence these are generally viewed as semi-quantitative estimates. A widely used set of scaling factors is that of Biscaye (1965); these factors are multipliers of the following peak areas in X-ray diffractograms: smectite 1.7 nm (001) after glycolation \rightarrow multiplier = 1; illite 1.0 nm (001) \rightarrow multiplier = 4; chlorite 0.7 nm (002) \rightarrow multiplier = 2; kaolinite 0.7 nm \rightarrow multiplier = 2. This method does not provide scaling factors for the peaks of other minerals (e.g., quartz, calcite, dolomite) which can be present in marine sediments, and which are known from the fine fractions of the Black Sea region (e.g., dolomite - Bayhan et al., 2005, Haslinger et al., 2006, quartz - Major, 2002, Trimonis and Ross., 1978, calcite - Major, 2002, Trimonis and Ross., 1978, Bayhan et al., 2005).

Underwood et al. (2003) pointed out that in mixtures of clay minerals and other silicates, the peak areas for one mineral are dependent on the identity and abundances of the other minerals in the sample. Hence, it is not a simple process to obtain quantitative mineral proportions based on fixed multipliers as proposed by Biscaye (1965).

Underwood et al. (2003) used the method of "matrix singular value decomposition" to derive normalization factors for 12 artificial mixtures of pure smectite, illite, chlorite and quartz standards. When applied to the peak areas from X-ray diffractograms of the artificial mixtures, these factors reproduced the correct weight percentages in the mixtures with errors of $<5\%$ of the amount present. Both Biscaye (1965) and Underwood

et al. (2003) used the same characteristic peaks for clay minerals, along with the 0.4257 nm peak for quartz in the case of the latter study.

The peak areas for the samples analysed in this thesis were evaluated using both the Biscaye (1965) and Underwood et al. (2003) procedures. Kaolinite was not included in the artificial mixtures of Underwood et al. (2003) so the peak used for evaluation of the thesis samples is the chlorite+kaolinite peak. Because the Biscaye factor for these two minerals is the same, it is assumed that the Underwood et al. (2003) normalization factors for chlorite abundance might be reasonably applied to the composite chlorite+kaolinite peak. As a cautionary note, the diffractometer setup used by Underwood et al. (2003) differs from the Memorial University setup in ways that affect the total number of counts contributing to each peak area (Table 2.3). This accounts for the fact that mineral percentages calculated for this thesis research using the Underwood et al. (2003) normalization factors do not total 100%, so need to be adjusted by a constant multiplier in order to be compared with the Biscaye (1965) results, which themselves are normalized to 100% after applying the Biscaye (1965) multiplication factors. The results for a single representative sample are shown in Table 2.3 to explain the work flow.

The Memorial University X-ray diffraction laboratory has a variety of software to quantify mineral abundances in mixtures (e.g., JADE), but all these packages are written for unoriented powdered samples so could not be used for the diffractograms using oriented mounts.

Table 2.2 Parameters used by Underwood et al. (2003) and in this thesis (MUN) and their effects on intensity measurements.

	Underwood et al. (2003)	This Thesis (MUN)	Effects on Intensity
Radiation	CuK α	CuK α	
mA	35	44	An increase in mA increases intensity
Speed	1 deg/min	1 deg/min	
Step Size	0.01	Continuous	
Divergent Slit	0.5 mm	10 mm	Increase in div. slit size increases intensity
Receiving Slit	0.2 mm	0.3 mm	Increase in rec. slit size increases intensity
Range	2–23° 2 θ	5–40° 2 θ	

Table 2.3 Example of peak area manipulations on the clay-sized minerals found in MAR02–45 (510 cm depth) broken down into a 10-step method. A detailed explanation of each numbered step is found in the text below the table. Mineral abbreviations with the subscript ‘ss’ underwent the slow scan procedure described in the preceding text; the subscript ‘gly’ indicates that the mineral underwent glycolation before analysis, and the subscript ‘int’ means the intensities of the air-dried peaks were measured to create abundance ratios. TC, total clays, represents the calculated abundance of clay minerals; TM, total minerals, represents the calculated abundance of non-clay minerals in the clay-sized fraction. The units for entries associated with steps 1, 3 and 5 are total counts; for entries associated with steps 4, 6, 7, 8, 9, 10 the units are %.

Step	a Sm	b Ill	c Chl	d Kao	e TC	f Qtz	g Mo	h Ca	i Do	j TM	k Q/C	l Ca _{int}	m Do _{int}	n Chl _{ss}	o Kao _{ss}	p Mo _{gly}	q Sm _{gly}
1		3784	559			667	26652	4031	886			225	36	1150	835	517805	75499
2		0.14	0.02			0.03	1	0.15	0.02							1	0.08
3	13860	24154	3568			4257	170125	7729	1154							170125	13860
4	28	44	3	4	79	21				21				0.58			
5	4142	28872	895	1237	35146												
6	12	82	3	4	100												
7	9	65	2	3	79	21				21							
8						21		102		123	0.16						
9						21		102	16	140		0.14					
10	4	30	1	1	36	10		47	8	64							

Table 2.4 Step-by-step walk-through.

1) The raw peak area data from X-ray diffraction analysis is collected and organized.

Illite (Ill) and chlorite (Chl) have been measured on air-dried runs. Quartz (Qtz), molybdenite (Mo - column g), calcite (Ca) and dolomite (Do) peak areas are taken from air-dried analysis. Chlorite and kaolinite (Kao) are analysed using the slow scan method in order to differentiate their overlapping peaks (columns n and o, with the total of these peak areas not yet equated to the peak area in column c). Molybdenite and Smectite (Sm) are measured in glycolated runs as well (columns p and q).

2) The peak areas are normalized to the MoS₂ peak within the same run; when this is done the MoS₂ peak is equal to 1.

3) The normalized peak areas from step 2 are multiplied by a number, in the range 17,000–210,000, needed to scale the total area for the characteristic peaks of illite, chlorite+kaolinite, montmorillonite and quartz to 45840, this being the average sum of these same peak areas in the runs of Underwood et al. (2003) on artificial mixtures. The rationale for this step was to ensure that the application, in step 4, of the scaling factors of Underwood et al. (2003) used similar peak areas to those obtained by those authors with their different machine settings. This step also compensates for the different peak intensities obtained before and after replacement of the X-ray tube following its failure part-way through the thesis work.

4) Apply the chlorite+kaolinite slow-scan ratio to the measured chlorite air-dried peak area (column c of step 3) and then apply scaling factors from table T4 of Underwood et al. (2003) to obtain mineral abundances for the clay minerals and quartz, followed by recalculation to 100% (i.e., columns a, b, c, d and f of step 4 total 100%)

- 5) Apply the chlorite+kaolinite slow-scan ratio to peak areas from step 3 and then apply Biscaye (1965) multipliers. Smectite = area*1, Illite = area*4, Chlorite = area*2 and Kaolinite = area*2
- 6) Normalize the Biscaye (1965) adjusted peak areas to 100 by dividing individual peak areas by the cumulative peak area of all the clay minerals (TC) times 100.
- 7) Using the ratio of quartz to total clays from step 4, adjust the Biscaye (1965) abundances to incorporate quartz.
- 8) Using Underwood et al. (2003, their table T3), peak areas from step 1, columns f and h, and Eqn 2.1 to transform the quartz/calcite peak-area ratio (0.16) to a quartz/calcite wt.% ratio of 0.203. Before re-normalization, a quartz proportion of 21% (step 7) implies a calcite proportion of $21\%/0.20 = 103\%$ cal). Of course the total for the sample now exceeds 100% and the sum for all minerals must eventually be re-normalized to 100%.
- 9) Dolomite abundance is determined using the measured intensities of calcite and dolomite and then applying the ratio to calcite abundance (Eqn 2.2). At 510 cm depth, dolomite is 16% of the abundance of calcite, so a calcite un-normalized abundance of 103 wt.% calcite corresponds to 16.5 wt.% dolomite.
- 10) The final step in determining mineral abundances in the clay-sized fraction is the normalization of all minerals to 100%. After step 9, the non-clay minerals account for 140 "units" of the sample (by weight), and the clays 79 "units", for a total of 219 "units". After normalization, the final values are a combination of Biscaye (1965) scaling for the clay minerals and non-clay mineral abundances calculated from both Underwood et al. (2003) and Royse et al. (1971).

Because the Underwood et al. (2003) methodology is based on more refined procedures, it was hoped that these methods could be used to quantify the thesis mineral abundances. However, the full table of calculated values for all samples (Appendix 2) includes several negative estimates of weight percentages, particularly for the minor minerals chlorite and kaolinite. This could be caused by different behaviour of kaolinite relative to chlorite in the mineral mixtures, by differences between the Underwood et al. (2003) standard minerals and the minerals in the Black Sea sediments (e.g., the poorly crystalline smectite in thesis samples), interferences from carbonates in the thesis samples, and/or different instrument parameters (Table 2.3). Nevertheless, the quartz percentages from the Underwood et al. (2003) calculations are used as best-estimates for the true abundances in the thesis samples, since no other technique was discovered to quantify quartz in mixtures with clay minerals.

In samples with positive reported values for chlorite+kaolinite using Underwood et al. (2003) scaling, the most noticeable difference between the results using the Biscaye (1965) factors and the results using the Underwood et al. (2003) normalization technique is that the smectite abundances are nearly twice as large, and the illite abundances proportionally reduced using the latter technique (e.g., Table 2.4). This may point to truly higher smectite abundances in the thesis samples than determined using the Biscaye (1965) factors, but other workers in the Black Sea region have also relied on the Biscaye (1965) scaling factors, so comparisons with published data are simplified by reporting the lower smectite values.

To summarize the clay-mineral proportions for all thesis samples are based on application of the Biscaye (1965) multiplication factors to the appropriate peak areas for

smectite, illite, chlorite, and kaolinite, with the smectite area taken from the glycolated run (scaled to the areas in the air-dried run using the molybdenite peak area common to both runs) and the split of the chlorite+kaolinite 0.7 nm peak based on deconvolution of the doublet where secondary peaks for these minerals overlap (0.356 nm and 0.359 nm, respectively). The quartz proportion is based on the calculations using the Underwood et al. (2003) normalization factors. In order for the total mineral tally to equal 100%, the clay-mineral proportions are scaled downward to accommodate the quartz content. The Black Sea samples also contain significant calcite and minor dolomite. Their quantification requires some additional assumptions as to how their peak areas transpose into wt.% values. Underwood et al. (2003) also performed a "matrix singular value decomposition" experiment with bulk unoriented mineral mixtures of powdered smectite, illite, chlorite, quartz, plagioclase and calcite. Because quartz and calcite particles do not have a strong preferred orientation, it is assumed for the purposes of this thesis that the relationship of their peak areas would be similar in unoriented and oriented mounts, for mixtures with the same relative proportions. The results of Underwood et al. (2003; their table T3) show a linear relationship between the ratio of peak areas for quartz and calcite, and the ratio of their weight percentages (Eqn 2.1), specifically

$$\frac{(\text{qtz wt. \%})}{(\text{cal wt. \%})} = 1.2723 * \frac{\text{qtz } 0.4257 \text{ nm area}}{\text{cal } 0.3034 \text{ nm area}} \quad (\text{Eqn 2.1})$$

The additional percentage for calcite was accommodated by normalizing the total abundances for clay minerals, quartz and calcite to 100%.

Finally, the relative proportion of dolomite (dol) to calcite (calc) was quantified using the peak intensity relationship for carbonate weight percentages in Royse et al. (1971), specifically (Eqn 2.2)

$$\frac{\text{dol } 0.288 \text{ nm intensity}}{[(\text{dol } 0.288 \text{ nm intensity})+(\text{cal } 0.03034 \text{ nm intensity})]} = 0.010 * (\text{dol wt. \%}) - 0.023 \quad (\text{Eqn 2.2})$$

The final totals are normalized to 100%, which ignores any minerals present in very minor amounts, and the 5% molybdenite spike.

2.4 Sediment Volumes and the BQART Equation

An estimate of Holocene sediment volumes on the southwestern Black Sea shelf was completed to gauge the importance of local river supply to the shelf. Isopach maps from Hiscott et al. (2007b), consistent with Aksu et al. (2002), were analysed using ImageJ freeware (available at <http://rsbweb.nih.gov/ij/>) to measure the areas enclosed by different thickness contours (presented in the original articles in milliseconds [ms] of two-way travel time, and converted to thickness using an acoustic velocity of 1500 m s⁻¹).

The area enclosed by a particular isopach contour (e.g., the surface area of a 2 ms-thick slice between isopachs for 2 ms and 4 ms) was calculated by drawing a line equidistant from the 2 ms and 4 ms isopach lines (i.e. at 3 ms), then determining the enclosed area. A mid-point position (e.g. at 3 ms rather than 4 ms) was used to account for an inferred linear thinning of deposits between any two contour lines. Each area was then converted to a volume by multiplying area × contour interval (in ms) × 0.75 (to convert thickness in milliseconds to thickness in meters of unconsolidated sediment). The sum of the volumes for all contour intervals yields the total volume. This can be thought of as summing the volumes of each horizontal slice (of thickness 2 ms in this

case) constituting a particular seismic unit. The volume of mineral-density solids was obtained by multiplying the deposit volume by 1.0-(fractional porosity). Appropriate fractional porosities for surficial marine muds are in the range 0.60–0.70.

Sediment flux from local sources was calculated using the BQART Equation (Syvitski and Milliman, 2007). The BQART equation is an empirical relationship to calculate sediment yields from river drainage basins using parameters controlled by geography and regional geology. The basic equation (Eqn 2.3) is

$$Q_s = \omega B Q^{0.31} A^{0.5} R T, \text{ for } T \geq 2^\circ\text{C} \quad (\text{Eqn 2.3})$$

Q_s is the sediment discharge with dimensions of [mass/time]. $\omega = 0.0006$ to give units of megatonnes/yr. Q , water discharge, is measured in km^3/yr . Basin area, A , is in km^2 ; R , maximum relief, is measured in km, and T , temperature in $^\circ\text{C}$. B represents basin characteristics and is calculated using the following formula (Eqn 2.4):

$$B = I L 1 - T_E E_h \quad (\text{Eqn 2.4})$$

I ($I \geq 1$) is the glacial erosion factor (Eqn 2.5) which takes into account ice cover (A_g) in the basin

$$I = (1 + 0.09 A_g) \quad (\text{Eqn 2.5})$$

L is the lithology factor, which varies according to the erosional resistance of the bedrock in the drainage basin; $L = 0.5$ for basins in shield rocks and can increase to a value of 3 for basins containing abundant loess or other weak materials. T_E compensates for sediment trapping due to dam construction and ranges from 0–0.9; a value of 0 implies no damming in the basin. The final parameter, E_h , is the anthropogenic factor;

this factor recognizes population density and land use practices as influences on sediment yield.

For rivers in the Black Sea area, this thesis sets a number of parameters in the BQART equation to fixed values (Table 2.5). Parameters not in Table 2.5 vary from one river basin to the next.

Table 2.4 Values and meanings of variables found in the BQART equation and used for calculating sediment discharge of local rivers to the southwestern Black Sea shelf. * = particular values for each river under consideration.

Variable	Value	Meaning
Q_s		Sediment discharge
ω	0.0006	Conversion factor to generate final data in $MTyr^{-1}$
B	$IL(1-T_E)E_h$	
Q	*0.1844 km^3yr^{-1}	Water discharge from local rivers, taken from Aksu et al. (2002)
A	*506 km^2	Drainage-basin area of local rivers, from Aksu et al. (2002)
R	*0.4 km	Maximum relief in the drainage basin, from Google Earth
T	15 °C	Average annual temperature in the drainage basin
I	$(1+0.09A_g)$	
L	2	Lithology factor = 2 for basins with significant proportions of sedimentary rocks and alluvial deposits
T_E	1	Sediment trapping; a value of 1 assumes no dam construction in the basin
E_h	1	Appropriate for low anthropogenic impact on the drainage basin
A_g	1	Appropriate for no ice cover in the drainage basin

Chapter 3 Results

3.1 Sediment Volume Estimates

Estimates were made of: (i) the volume of Holocene sediments deposited on the southwestern Black Sea shelf, and (ii) the volumes of sediment delivered to the shelf during the Holocene by rivers. The first estimate involved measuring isopach thicknesses from maps in Hiscott et al. (2007b) and converting the data into a volume. The second set of estimates involved using the BQART equation of Syvitski and Milliman (2007), multiplying by a time interval and density to create a volume estimate. Procedures are given in §2.4. Comparison of these estimates allows an assessment of the likelihood that particular rivers provided enough sediment to account for the lower Holocene shelf succession.

3.1.1 *Isopach Measurement and Volume Estimate*

Hiscott et al. (2007b) used a seismic grid to generate isopach maps (in milliseconds [ms] of two-way travel) for seismic units corresponding to the three lithologic units penetrated by core MAR02–45. These maps were analysed using ImageJ freeware to systematically calculate areas enclosed by each isopach contour (§2.4). The total calculated volume of Holocene sediment in the region around core site MAR02–45 (bounded by the landward zero thickness, the shelf edge, and 42°20'N latitude) is 97.62 km³. Seismic unit 1B (lithologic Unit C) accounts for 17.51 km³ (Fig. 3.1), seismic unit 1C (Unit B) for 24.92 km³ and seismic unit 1D (Unit A) for 55.19 km³.

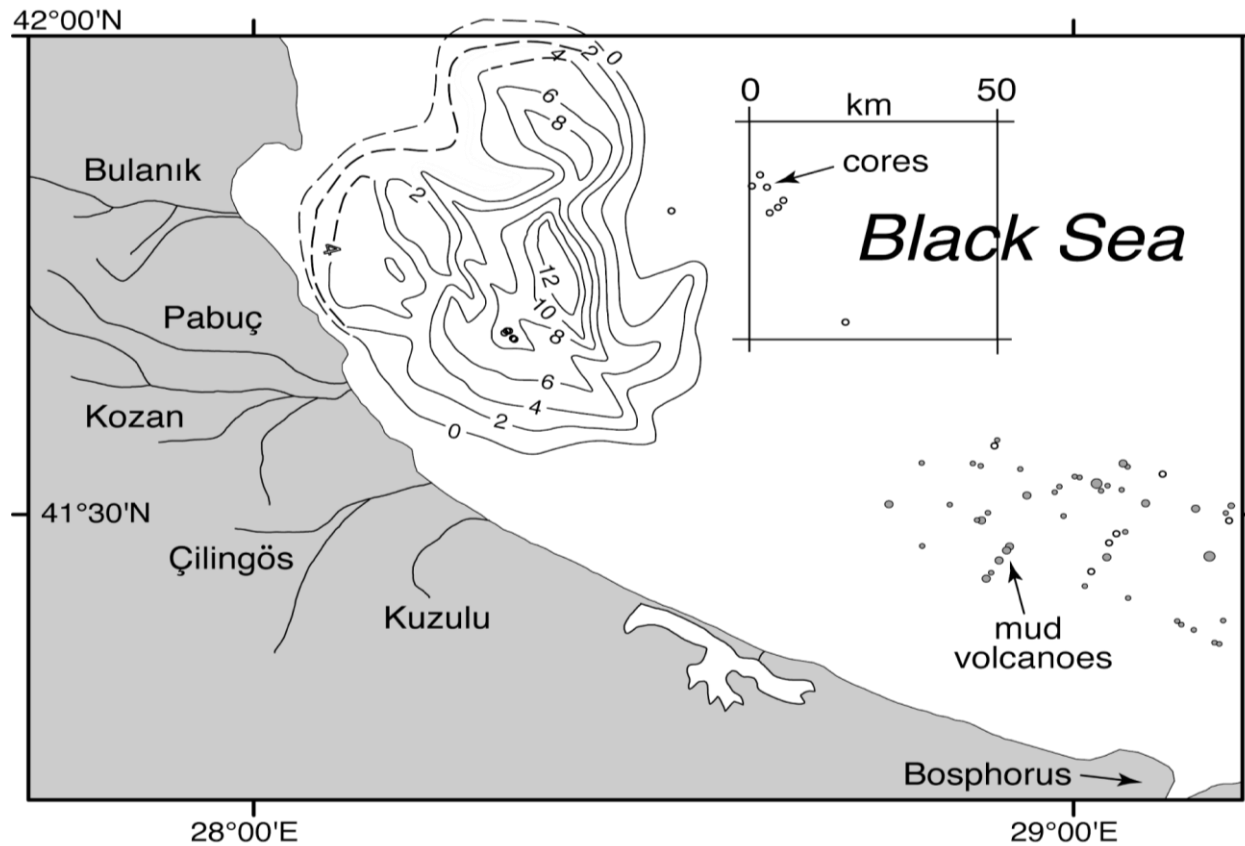


Figure 3.1 Isopachs (in milliseconds) for seismic unit 1B (Unit C) showing the thickness and extent of lower Holocene mud deposits on the shelf. The dotted lines are inferred extensions to isopach contours which were not closed within the seismic grid available to Hiscott et al. (2007b). The total volume of this unit is $\sim 17 \text{ km}^3$. Seismic units 1C and 1D were analysed in the same way. For comparison, the box has an area of 2500 km^2 Figure modified from Hiscott et al. (2007b).

3.1.2 BQART Equation and Volume Estimate

The BQART equation (Eqn. 2.3) contains many variables; Table 2.4 is a summary of the fixed values used for all rivers entering the western and southwestern Black Sea. The output is in units of megatonnes per year (MT yr⁻¹). To convert this to mass (tonnes) and eventually to a volume for intervals in the Holocene, a timespan must be selected for each time slice.

5000 years was chosen as the timespan for the river yield potentially captured in seismic unit 1B (lithologic Unit C), allowing ~2000 years for deposition after marine flooding, and ~3000 years for the prior deposition of subaerial floodplain deposits and deltaic deposits that might have been reworked into seismic unit 1B during the early Holocene transgression. If the BQART sediment yield from local rivers (Bulanık, Pabuç, Kazan, Çilingöz and Kuzulu) remained constant at its present level for 5000 years, then a mass of 522.6 MT of material could be expected from local river input.

Marine muds vary between 60–70% porosity. Porosity studies were not part of this investigation, so mass was converted to volume using 60% and 70% porosity as reasonable upper and lower limits. At 60% porosity, the 522.6 MT of mineral-density solids would occupy 40% of the sedimentary deposit. Using a mineral density of 2.65 T/m³, the equivalent volume of solids is 0.197 km³, so the volume of the sedimentary mass containing this amount of mineral matter and having 60% porosity is $(100/40)(0.197) = 0.493 \text{ km}^3$. Using a similar calculation for the case of 70% porosity, it is concluded that local sources could have contributed sediments having a volume between 0.493 km³ ($\phi=60\%$) and 0.657 km³ ($\phi=70\%$) over a 5000 year period.

3.2 Texture

During sample preparation, the total weight of each sample and the weights of the various size fractions were recorded. The average grain size distribution in the core (as weight percents) is 2.3% sand, 88.2% silt and 9.4% clay. The average size distribution for each lithologic unit is as follows: Unit A, 2.4% sand, 90.0% silt and 7.6% clay; Unit B, 5.7% sand, 82.6% silt and 11.7% clay, and the lowest Unit C, 1.6% sand, 88.6% silt and 9.8% clay. Sediment size distribution for core MAR02–45 is shown in Figure 3.2. The core is silt dominated with Unit B showing the greatest variation in grain size although silt still comprises >82% of its samples.

Sediment samples from potential sources were not dried before initial wet-sieving, so accurate determination of their size distributions is not available. Based on visual inspection of the samples, the Danube delta-top samples are silt-dominated, except for samples taken from the Chilia 1 delta and Sulina Canal, which are very sand rich. Samples from local rivers in Thrace are also sand rich, while MAR08–17 samples (characterizing detritus from the bedrock adjacent to the Bosphorus Strait) were taken just seaward of the Bosphorus exit and are silt dominated.

3.3 Silt Mineralogy

Studying the XRD mineralogy of silt-sized sediment permits a better understanding of the bedrock composition of potential sources and could potentially reveal the presence of important minor minerals. In contrast, clay minerals can be mostly weathering products that differ in mineralogy from the bedrock. In order of abundance in the silt fraction, the minerals present (as core averages, excluding the molybdenite spike) are:

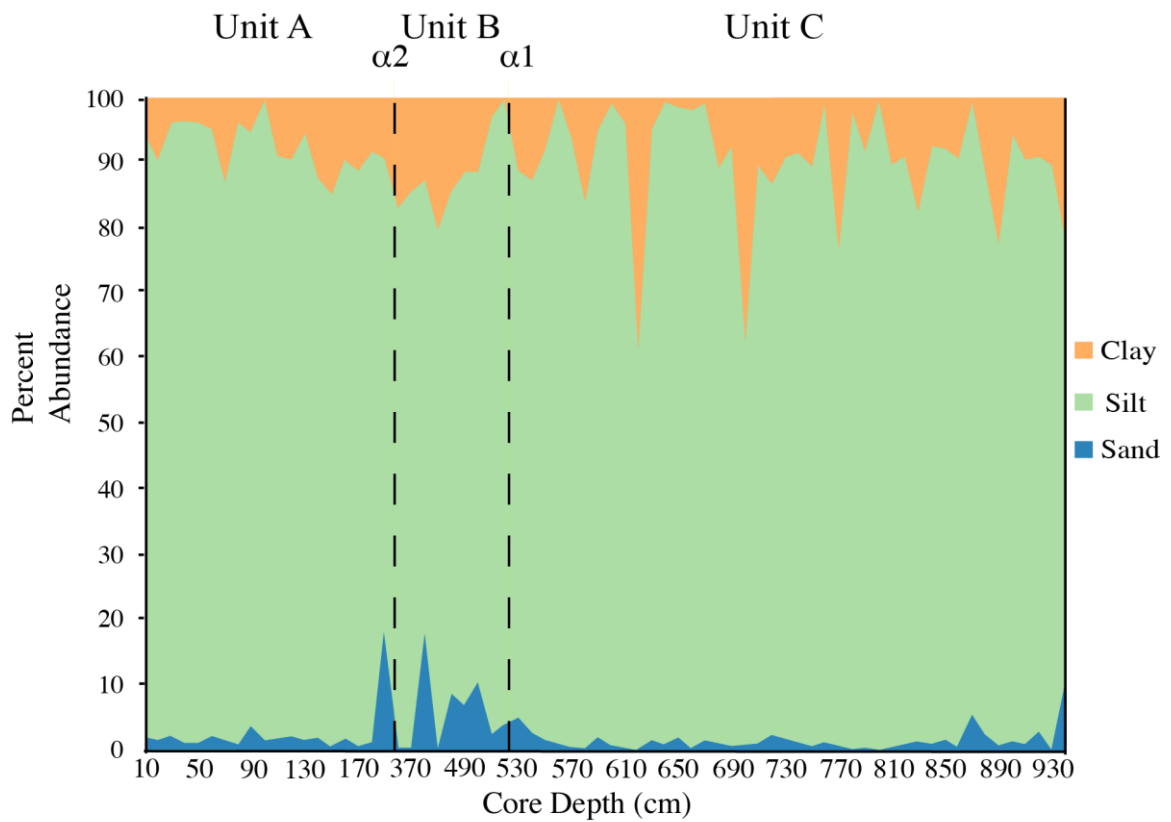


Figure 3.2 Grain size distribution plotted against composite depth in core MAR02–45.

There is limited resolution between $\alpha 1$ and $\alpha 2$, and just above the $\alpha 2$ unconformity due to a lack of sufficient material for grain size determination between 260 and 370 cm depth.

quartz (53.2 wt.%), K-rich micas (23.9 wt.%), calcite (18.6 wt.%), and sodic plagioclase (4.3 wt.%). The plagioclase abundance is close to the lower limit of detection in bulk XRD samples; minerals of lower abundance, if present, cannot be confidently discovered using this technique. Figure 3.3 and Table 3.1 show the variations in abundance of the silt-sized constituents identified through core MAR02–45. A clear trend visible through the core is an upward decrease in calcite. There is also an increase in K-mica from the top of Unit C into Units B and A. Quartz abundance increases from bottom to top while sodic plagioclase increases in Unit A. Data recalculated without calcite show that the relative proportions of silicate minerals vary little through the cored succession (Fig. 3.4).

The silt fraction mineralogy of potential source areas is shown in Table 3.2. The Danube Delta samples are the only ones for which Jade software reports dolomite, but the abundance is low as dolomite was only found in 3 of the 5 samples, (Sulina Canal at Mile 10, Chilia 1 and Chilia 2).

3.4 < 2 μm Fraction Mineralogy

Analysis of XRD spectra acquired on oriented mounts of clay-sized fractions was performed using MacDiff software. When using the MacDiff software, the background was fitted as a gentle curve constrained at every 100th point; some manual manipulations of the background curve were required in the vicinity of low intensity, broad peaks. All base-line fitting and peak-area determinations were performed by a single operator (the author), so are expected to be consistent.

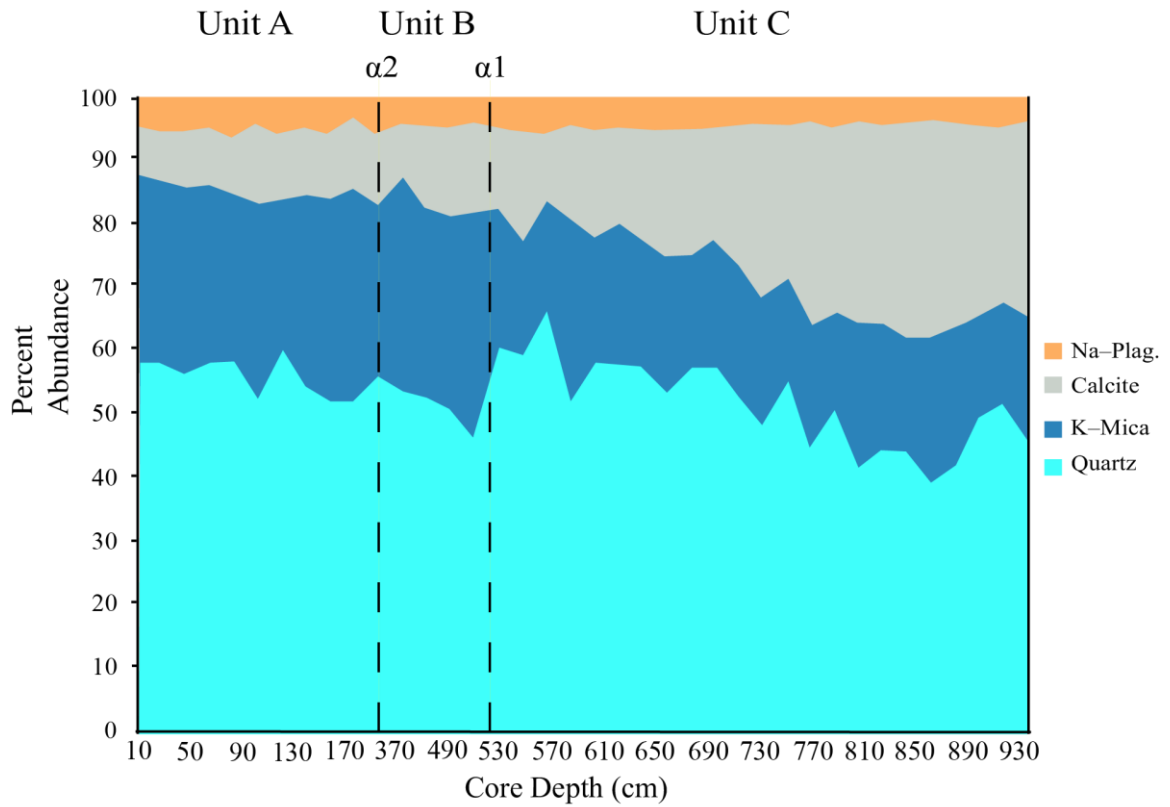


Figure 3.3 Abundance of minerals found in the silt fraction of core MAR02-45.

Materials under ~5 wt.% do not show peaks sufficiently large to be quantified by Jade software. Unit B has only a few reported analyses near the α_2 unconformity due to a lack of available material at those depths.

Table 3.1 Variations in abundance of minerals in the silt fraction through core MAR02–45; values in *italics* are calculated on a calcite-free basis.

Depth (cm)	Mineral Abundance (wt.%)						
Unit	Quartz		K-mica		Calcite	Na-Plag	
A							
10	58.5	<i>63.1</i>	29.6	<i>31.9</i>	7.3	4.7	<i>5.0</i>
30	58.2	<i>62.9</i>	29.4	<i>31.8</i>	7.4	5.0	<i>5.4</i>
50	56.7	<i>62.1</i>	29.6	<i>32.5</i>	8.8	4.9	<i>5.4</i>
70	58.6	<i>64.2</i>	28.0	<i>30.7</i>	8.8	4.6	<i>5.0</i>
90	58.2	<i>64.2</i>	26.9	<i>29.6</i>	9.2	5.7	<i>6.3</i>
110	52.6	<i>59.9</i>	31.1	<i>35.4</i>	12.2	4.2	<i>4.7</i>
130	60.5	<i>67.7</i>	23.7	<i>26.5</i>	10.6	5.2	<i>5.9</i>
150	54.5	<i>61.1</i>	30.3	<i>33.9</i>	10.7	4.5	<i>5.0</i>
170	52.3	<i>58.1</i>	32.3	<i>35.8</i>	9.9	5.5	<i>6.1</i>
Average	56.7	62.6	29.0	32.0	9.4	4.9	5.4
Std .Dev.	2.9	2.8	2.5	2.9	1.6	0.5	0.5
B							
330	52.6	<i>59.1</i>	33.3	<i>37.4</i>	11.0	3.1	<i>3.5</i>
350	56.2	<i>63.4</i>	27.5	<i>31.0</i>	11.3	5.0	<i>5.7</i>
370	53.7	<i>58.7</i>	34.0	<i>37.2</i>	8.5	3.7	<i>4.1</i>
420	53.2	<i>61.2</i>	29.5	<i>33.9</i>	13.0	4.2	<i>4.9</i>
430	51.4	<i>59.8</i>	30.1	<i>35.0</i>	14.0	4.5	<i>5.2</i>
470	46.6	<i>54.5</i>	35.3	<i>41.3</i>	14.4	3.6	<i>4.3</i>
490	60.8	<i>69.8</i>	21.9	<i>25.2</i>	12.9	4.3	<i>5.0</i>
510	59.4	<i>72.0</i>	18.1	<i>22.0</i>	17.4	5.0	<i>6.1</i>
Average	54.3	62.3	28.7	32.9	12.8	4.2	4.8
Std. Dev.	4.5	5.9	6.0	6.5	2.6	0.7	0.9

Table 3.1. Continued

Depth (cm) Unit	Mineral Abundance (wt.%)							
	Quartz		K-mica		Calcite	Na-Plag		
C								
530	66.8	74.9	17.1	19.2	10.8	5.3	5.9	
550	52.2	61.3	29.0	34.1	15.0	3.9	4.6	
570	58.5	70.1	20.1	24.1	16.5	4.8	5.8	
590	58.4	68.8	22.0	26.0	15.2	4.4	5.2	
610	57.5	69.3	20.7	25.0	17.1	4.7	5.7	
630	53.6	67.3	21.5	26.9	20.3	4.6	5.8	
650	57.7	72.1	17.8	22.2	19.9	4.6	5.7	
670	57.4	70.0	20.3	24.8	18.0	4.3	5.2	
690	53.4	68.6	20.5	26.3	22.2	3.9	5.1	
710	48.5	66.6	20.6	28.3	27.2	3.7	5.1	
730	55.6	73.1	16.3	21.5	23.9	4.1	5.4	
750	45.1	66.7	19.2	28.3	32.4	3.4	5.0	
770	51.2	72.2	15.5	21.9	29.2	4.2	5.9	
790	41.6	61.2	23.1	34.0	31.9	3.3	4.9	
810	44.5	65.0	20.2	29.5	31.5	3.7	5.5	
830	44.6	67.5	18.1	27.3	34.0	3.4	5.2	
850	39.5	60.4	22.6	34.5	34.6	3.3	5.0	
870	42.1	62.7	21.5	32.1	32.9	3.5	5.2	
890	49.9	71.2	16.1	23.0	29.9	4.1	5.8	
910	51.9	71.9	16.0	22.2	27.9	4.2	5.9	
930	46.4	66.5	19.7	28.2	30.2	3.7	5.3	
Average	51.3	68.0	19.9	26.6	24.8	4.1	5.4	
Std. Dev.	7.0	4.1	3.1	4.4	7.4	0.6	0.4	

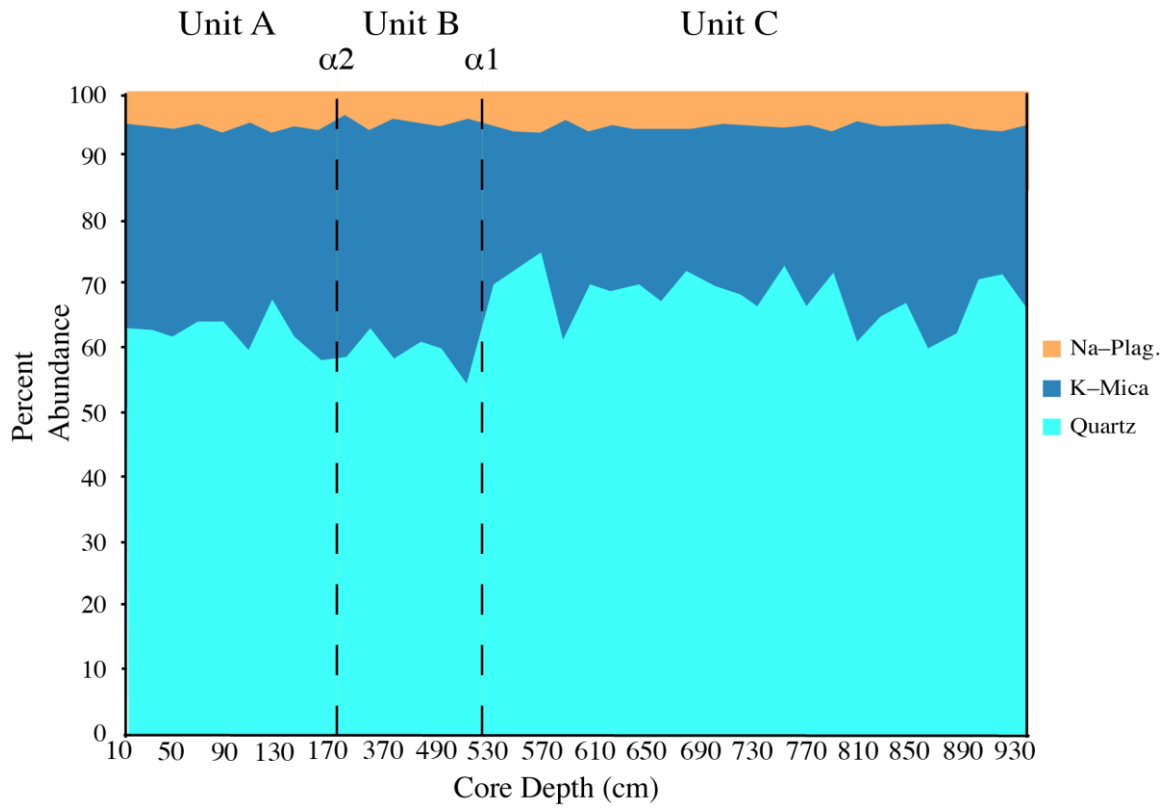


Figure 3.4 Silicate mineral proportions in the silt-sized fraction through core MAR02-

45.

Table 3.2 Variations in abundance of silt-sized minerals from potential source areas.

*Thrace river samples were taken from sandy channel banks, so the silt fraction is likely coarser than in samples from other areas.

Potential Source	Minerals (average wt.%)				
	Quartz	Mica	Calcite	Na-Plag	Dolomite
Danube Delta	54.3	27.0	9.0	6.6	3.0
Thrace Rivers*	68.3	20.8	6.7	4.2	
Bosphorus	61.7	31.8	3.9	2.7	

Due to minor variations in the elevation of samples in the automatic sample changer (i.e., displacement errors; Pérez and Tabares, 2002), it was necessary to use the major MoS₂ peak (0.616 nm, 14.38° 2 θ) to correct the peak positions of other minerals. This is easily achieved using pull-down menus in the MacDiff software. A second use for the 0.616 nm MoS₂ peak was to normalize peak areas between glycolated and unglycolated runs. The peak intensities and peak areas of minerals identified in the clay-sized fractions of core MAR02–45 can be found in Tables 3.3 and 3.4. The areas and intensities of particular peaks were used to quantify mineral abundances using the procedures outlined in §2.4.3.

There are seven key minerals (three non-clay and four phyllosilicate) in the < 2 μ m fraction of MAR02–45: quartz, calcite, dolomite, smectite, illite, chlorite, and kaolinite. The average abundances and standard deviations of these minerals in core MAR02–45, calculated using procedures in §2.4.3, are as follows: quartz 12.2 \pm 5.6 wt.%, calcite 26.4 \pm 16.7 wt.%, dolomite 6.3 \pm 3.0 wt.%, smectite 12.7 \pm 10.4 wt.%, illite 36.0 \pm 12.0 wt.%, chlorite 3.2 \pm 2.8 wt.%, kaolinite 3.2 \pm 3.7 wt.%.

Table 3.3 Peak areas of minerals in the clay-sized fractions of core MAR02–45, measured using MacDiff software. Smectite values come from glycolated runs that were normalized to the air-dried runs using the area of the 0.616 nm MoS₂ peak.

Chlorite and kaolinite areas were apportioned based on deconvolution of overlapping peaks at 0.3576 and 0.3537 nm. Values in italics are estimates based on a split of the chlorite 0.7 nm peak area using deconvolution of the overlapping kaolinite/chlorite peaks in adjacent samples, because the samples with italics entries had peaks in this region that were too small to be measured/deconvolved (see §2.4.2)

Depth (cm)	Illite 0.10 Area	Quartz 0.342 Area	Molybdenite 0.616 Area	Calcite 0.303 Area	Dolomite 0.2888 Area	Smectite 1.69 Area	Kaolinite 0.359 Area	Chlorite 0.356 Area
10	14238	1609	164576	1899	775	32301	<i>1860</i>	<i>475</i>
30	9902	2133	84005	866	861	4440	<i>7204</i>	<i>2608</i>
50	14834	1645	109343	1274	1326	24147	1221	884
70	13775	1928	42570	849	1071	9863	2241	1906
90	12938	1670	159727	1170	1744	25293	1681	884
110	11072	2288	92051	5308	1630	13422	896	851
150	14062	1775	133210	2864	1541	19198	1046	815
170	11107	2421	64562	2227	1620	8044	919	259
260	10737	2306	97273	10695	2270	18349	725	769
330	9326	2677	343231	1769	2069	4455	<i>2439</i>	<i>1040</i>
370	9606	2155	205881	961	2727	5344	<i>6840</i>	<i>2609</i>
410	12613	2306	101831	3740	3338	6233	918	626
430	10224	1068	162224	1216	1249	32321	<i>11828</i>	<i>4162</i>

Table 3.3. Continued

Depth	Illite	Quartz	Molybdenite	Calcite	Dolomite	Smectite	Kaolinite	Chlorite
470	6578	1963	392710	3461	3749	6340	12858	4524
490	14695	1809	150189	7755	1348	16127	1360	748
510	12663	2232	89190	13560	2025	7266	1150	835
530	5793	1487	346947	3744	1586	9093	16816	6942
570	9525	2337	216800	9714	1166	12004	607	569
590	24959	578	100067	18221	3971	12005	756	744
600	10255	2213	53076	929	1090	13670	2748	2208
610	10323	1745	175557	4740	1381	27468	1107	3143
630	10613	2136	83818	9637	1671	11933	424	1188
650	1210	3534	18040	1117	480	25408	294	235
670	7396	2609	50362	7107	2424	11412	2901	2319
690	10498	2331	83103	9490	3212	18915	1054	1027
720	7241	3115	68775	16799	4013	2487	957	721
730	7684	2843	92471	16781	3728	11886	849	2070
750	14817	1589	266495	11223	2937	24928	632	435
770	15915	1594	257171	11681	4163	11817	2770	3796
810	7680	2923	51768	14539	3472	6636	772	2070
830	15200	1203	379471	12200	2503	5162	5082	5560
850	9387	2538	101558	11928	2634	15954	885	968
870	11502	2246	223100	13505	3822	10950	503	911
890	14644	941	509206	11694	3214	42356	3169	3015
910	10252	2116	120784	11533	2665	9240	250	500
930	7172	2897	198320	10450	3128	5046	399	676

Table 3.4 Peak intensities of minerals in the clay-sized fractions of core MAR02–45, measured using MacDiff software.

Smectite values come from glycolated runs that were normalized to the air-dried runs using the area of the 0.616 nm MoS₂

peak. Blank cells are located at depths where intensities were too small to be measured with confidence.

Depth (cm)	Illite 0.10 Intensity	Quartz 0.342 Intensity	Molybdenite 0.616 Intensity	Calcite 0.303 Intensity	Dolomite 0.2888 Intensity	Smectite 1.69 Intensity	Kaolinite 0.359 Intensity	Chlorite 0.356 Intensity
10	254	68	6960	44	35	68	35	24
30	271	94	2953	0	32	12		
50	209	65	5248	49	26	47	19	15
70	384	71	1894	38	43	26	40	36
90	240	75	7568	60	50	85	29	15
110	203	106	3112	160	48	30	17	0
150	251	67	5241	87	40	35	16	19
170	160	55	2630	60	59	13	17	10
260	135	63	3328	228	56		12	15
330	99	33	7238	40	32	20		
370	113	34	3739	14	33			
410	153	48	2518	69	44	22	18	13
430	203	49	5196	46	36	30		
470	83	36	8852	60	35	17		
490	280	59	5283	230	32	44		
510	132	70	3045	273	37	15	19	13
530	57	35	7881	69	27	15	1	1
570	132	60	6945	192	23	37	10	16
590	538	338	3580	163	43	33	15	14

Table 3.4. Continued

Depth	Illite	Quartz	Molybdenite	Calcite	Dolomite	Smectite	Kaolinite	Chlorite
600	229	80	1969	122	60	24	21	1
610	90	57	3258	48	23	38	30	9
630	116	58	1739	200	37	22	9	15
650	46	79	3366	167	34	31		
670	88	52	1708	201	55	10		
690	222	415	3474	270	69	92	20	20
720	92	89	2538	429	73	32		
730	155	86	3225	439	69	15		
750	132	38	5755	154	18	46	12	9
770	121	47	6279	141	55	12	53	73
810	90	46	1120	375	46		15	31
830	101	35	5811	79	35	5		
850	171	54	4152	351	51	42		
870	144	32	6219	279	34		8	28
890	86	20	6048	90	21	12		
910	212	48	2893	199	65	43		
930	125	71	7545	232	73	29	9	13

Average clay-sized quartz abundance increases from the base of Unit C (10.9 wt.%) through Unit B (13.7 wt.%) and into Unit A (14.1 wt.%). Standard deviations are in Table 3.5. As was the case for the silt-sized fraction, calcite abundance in the clay-sized fraction decreases from the base to the top of the core (Unit C, 34.9 wt.%; Unit B, 21.7 wt.%; Unit A, 10.0 wt.%) and the same is true for dolomite (Unit C, 7.5 wt.%; Unit B, 6.0 wt.%; Unit A, 3.7 wt.%). Because the percentage data form a closed array, increases in the carbonate minerals automatically cause decreases in the total of phyllosilicate minerals (Fig. 3.5a). Quartz shows a more scattered relationship with carbonate abundance (Fig. 3.5b) perhaps because it has low abundance so is not so strongly affected by closed-array considerations. The distribution of all the minerals found in the clay-sized fraction can be found in Figure 3.6.

Table 3.5 Averages and standard deviations of the clay-sized minerals by unit.

Unit	Minerals (wt.%)						
	Smectite	Illite	Chlorite	Kaolinite	Quartz	Calcite	Dolomite
A							
Average	16.1	50.5	2.3	3.4	14.1	10.0	3.6
St. Dev.	8.1	6.0	2.1	2.8	4.6	7.8	2.0
B							
Average	10.4	39.1	3.9	5.2	13.7	21.7	6.0
St. Dev.	8.4	10.1	3.6	5.0	5.9	16.3	3.4
C							
Average	12.2	29.0	3.2	2.3	10.9	34.9	7.5
St. Dev.	11.9	8.4	2.8	3.2	5.6	14.0	2.6

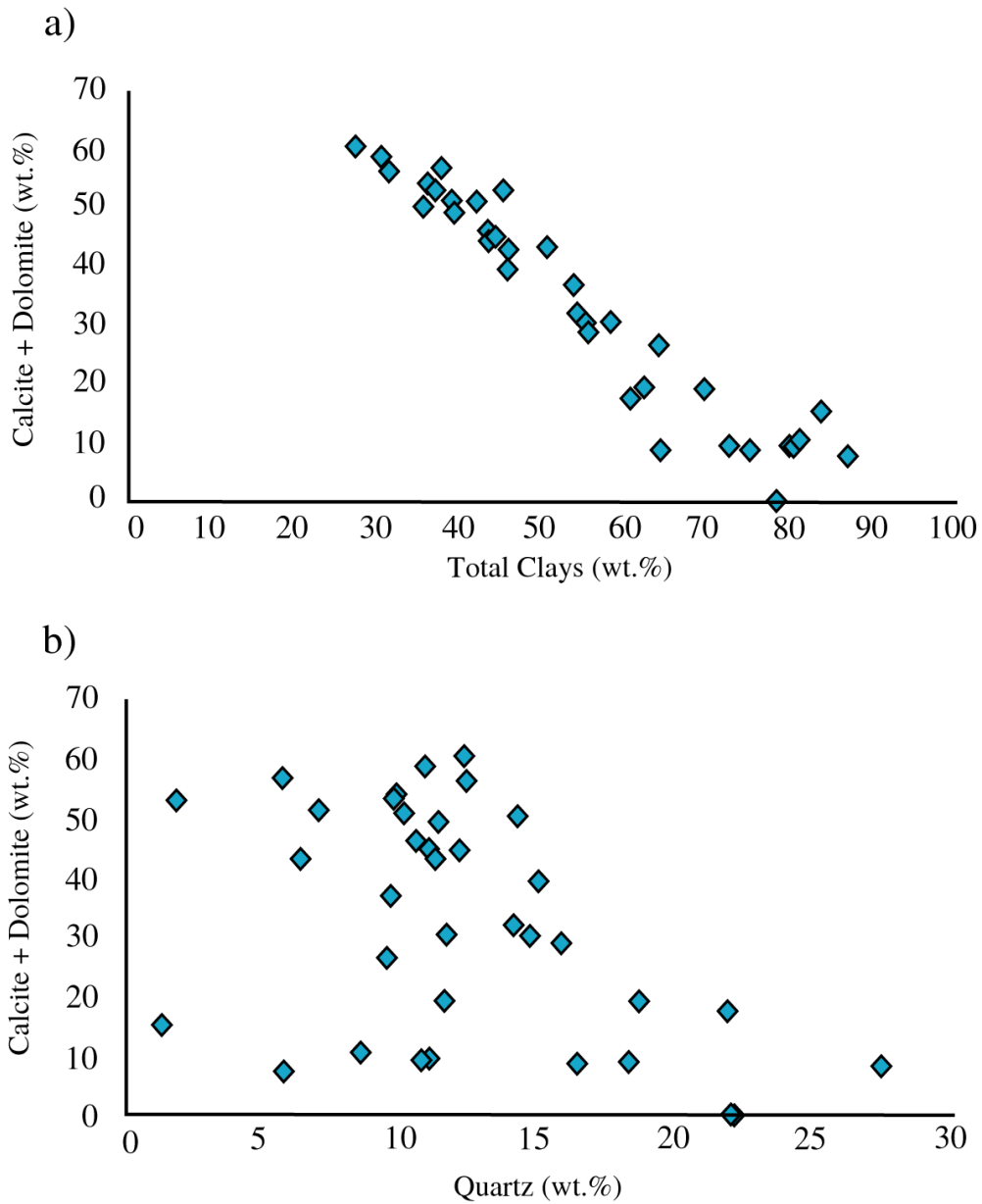


Figure 3.5 Cross-plots showing a) the inverse relationship between carbonates and clay minerals in the $<2\ \mu\text{m}</math> size fraction, and b) The relationship between quartz and carbonate abundances in the $<2\ \mu\text{m}</math> size fraction.$$

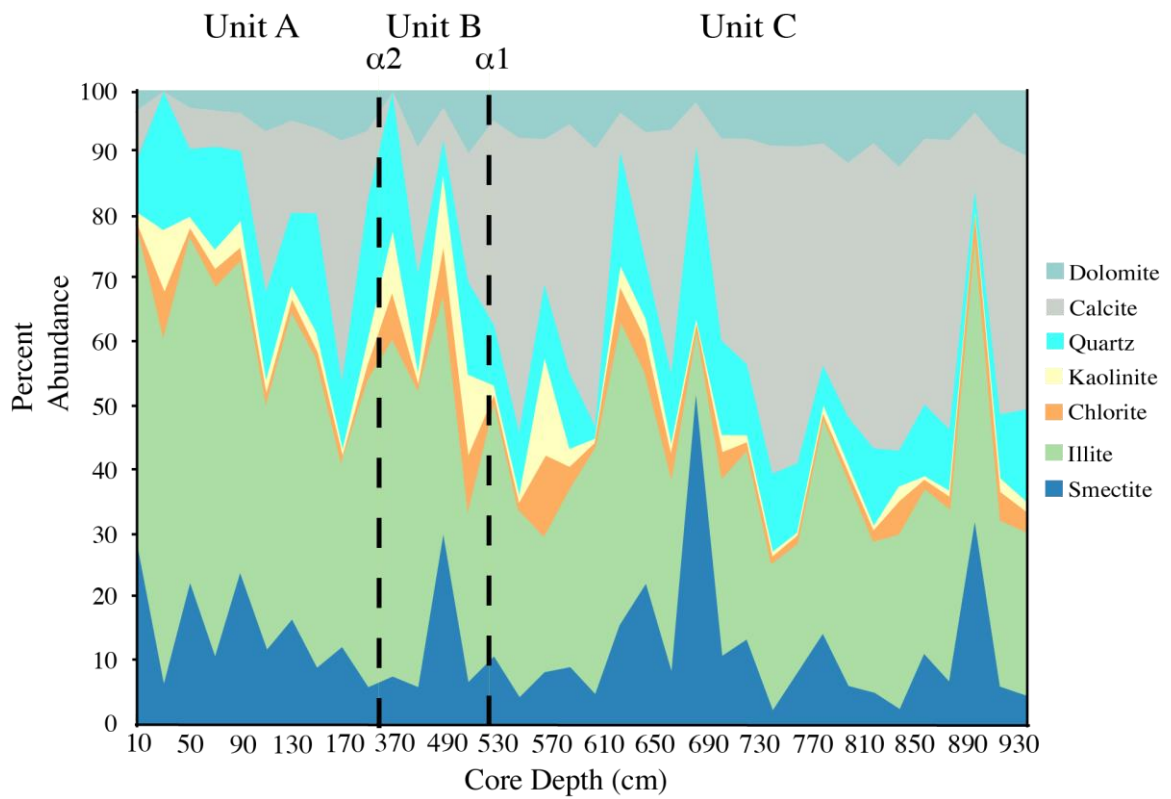


Figure 3.6 Wt.% abundance of minerals found in the <2 μm fraction of core MAR02-45 after scaling using procedures in §2.4.3. Unit B has a lower resolution due to a lack of sufficient clay-sized material at some sample depths.

Smectite abundance in Unit C is 12.2 wt.%, declining to 10.4 wt.% in Unit B; Unit A reverses this trend with an increase to 16.1 wt.%. Illite is the second most abundant < 2 μm mineral in Unit C (29.0 wt.%) and illite abundance increases through Unit B (39.1 wt.%) and into Unit A (50.5 wt.%) making it the most abundant < 2 μm mineral in the latter two units. Chlorite and kaolinite abundances both increase from Unit C (3.2 wt.%, 2.3 wt.%) into Unit B (3.9 wt.%, 5.2 wt.%) and decrease in Unit A (2.3 wt.%, 3.4 wt.%). The major differences in the behaviour of these minerals are that kaolinite abundance more than doubles from Unit C to Unit B, and in Unit A chlorite has a lower abundance than in Unit C, whereas kaolinite maintains a higher abundance. The interrelationship of the four phyllosilicates can be seen in Figure 3.7. Illite is the dominant phyllosilicate mineral with a core average of 67.1 ± 14.3 wt.%. Smectite is the second most abundant mineral (21.7 ± 13.7 wt.%) while chlorite and kaolinite account for 5.8 ± 4.7 wt.% and 5.4 ± 5.7 wt.% of the phyllosilicates, respectively. Readers should note that the within-unit variation in clay-mineral proportions is high, so although average values show particular trends, high standard deviations limit the potential to claim strong differences through the Holocene succession (Table 3.5).

Clay-sized mineral distribution in the detritus from potential source regions was also studied (Figure 3.8). The Danube delta-top is characterized by 25.0 wt.% smectite, 45.8 wt.% illite, 1.3 wt.% chlorite, 1.8 wt.% kaolinite, 13.8 wt.% quartz, 8.9 wt.% calcite and 3.4 wt.% dolomite. Clay fractions derived from the area around the Bosphorus Strait (MAR08–17) contain 43.0 wt.% smectite, 31.0 wt.% illite, 1.9 wt.% chlorite, 4.0 wt.% kaolinite, 19.2 wt.% quartz, 0.6 wt.% calcite and 0.34 wt.% dolomite.

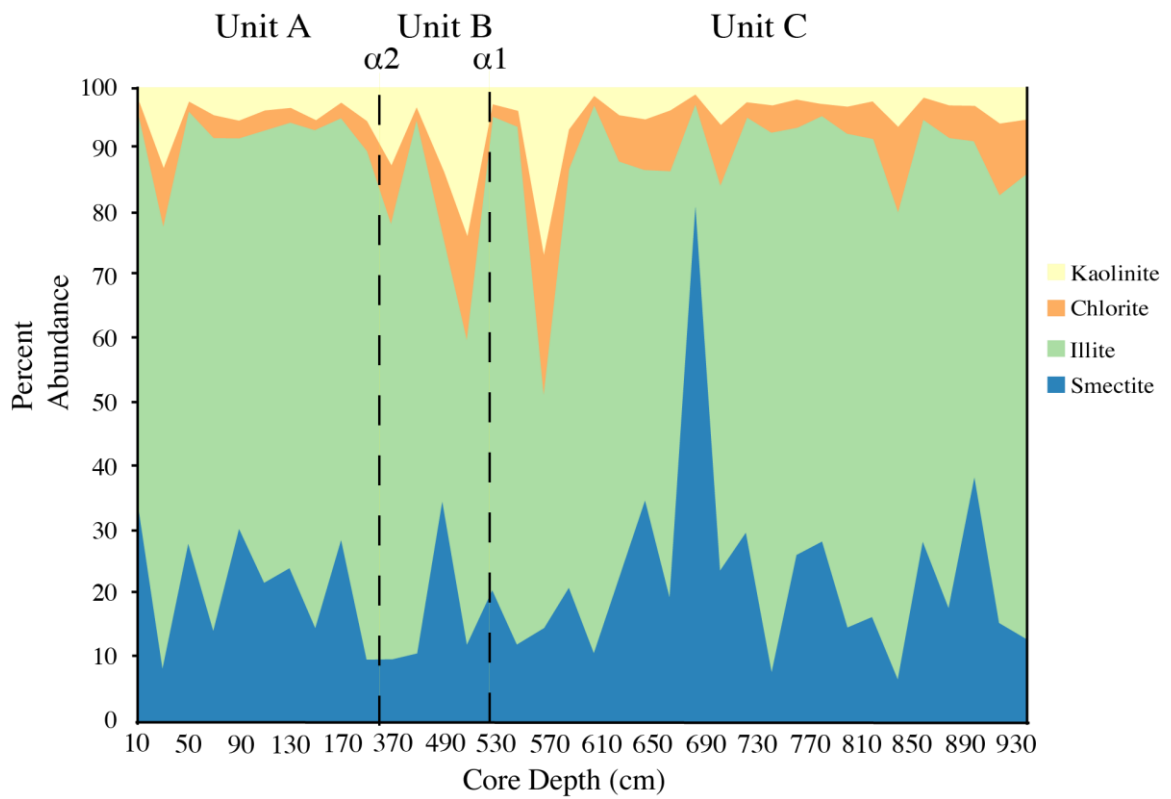


Figure 3.7 Recalculated abundances of the four major phyllosilicate minerals scaled using Biscaye (1965) methods and normalized to 100%.

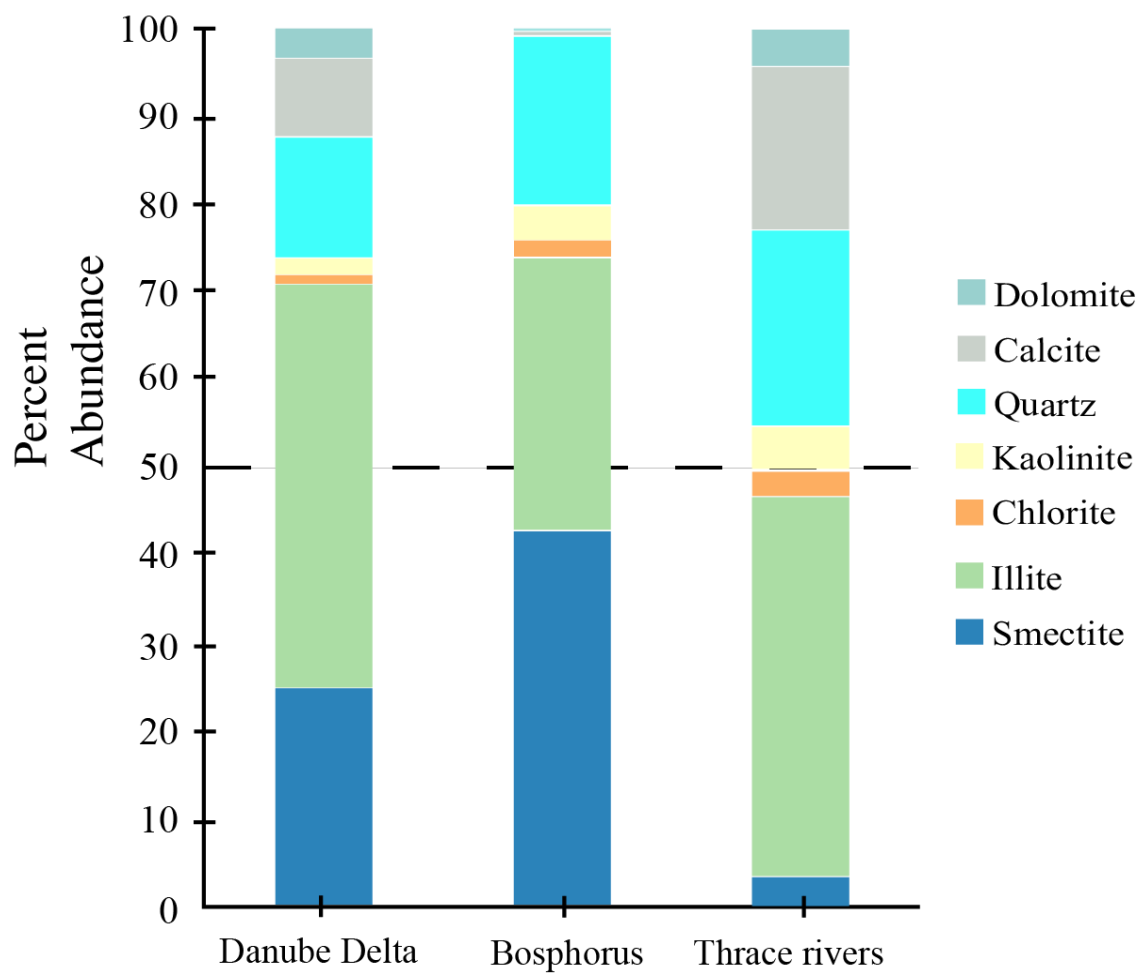


Figure 3.8 <math><2\ \mu\text{m}</math> mineral abundances of potential source areas.

These samples are believed to represent mixtures of detritus from diverse bedrock which underlies western Anatolia, having reached the Bosphorus Strait from many small drainage basins along its length. Of the Thracian river samples prepared at Memorial University of Newfoundland, only the Kuzan River sample contained enough clay to attempt an analysis. It was found to contain 3.6 wt.% smectite, 43.3 wt.% illite, 2.9 wt.% chlorite, 5.1 wt.% kaolinite, 22.3 wt.% quartz, 18.5 wt.% calcite and 4.4 wt.% dolomite.

3.5 Actlabs Geochemistry

3.5.1 Precision and Accuracy of Geochemical Analysis

Powdered samples from cores, MAR08-17, the Danube Delta and Thracian rivers were sent to Activation Laboratories (Ancaster, Ontario) for INAA and ICP-OES analysis. The package of 49 elements selected for the thesis was chosen to accommodate the small sample size (~3 g) of available material and to permit access to a wide spectrum of elements (see §2.2.1 for a detailed justification of analytical methods). The combined INAA and ICP-OES analysis generally used < 50% of the submitted powder, so that sufficient material remained for replication of a subset of the samples. The raw data (Appendix 3) show 14 elements with multiple samples below detection limits. These 14 elements (Au, Ag, Cd, Mo, Be, Bi, Br, Hg, Ir, Se, Ta, W, Sn and Tb) are eliminated from further consideration. During client runs in 2011, eight certified standards were analyzed to assess accuracy of the data (results in Appendix 4), and ICP-OES determinations were duplicated for six MAR02-45 samples to assess precision. These replicates used a fresh aliquot of powder and an independent second acid digestion. In January 2014, fresh aliquots of powder from the same six MAR02-45 sample vials were analyzed again, in

duplicate and with replication for samples with sufficient remaining power (hence $2 \times 2 = 4$ independent ICP-OES determinations and 2 independent INAA determinations for most samples in 2014). The aim was to thoroughly assess the precision of the INAA (Table 3.6) and ICP-OES (Table 3.7) analyses. When combined with the primary and replicate analyses from 2011, four of the six re-analyzed samples have six independent ICP-OES determinations and three independent INAA determinations. For elements with 5–6 repeat analyses, the ratio of the standard deviation to the mean is used to quantify precision (Table 3.7). For elements with 2–3 determinations (Table 3.6), it is not reasonable to calculate a standard deviation, so precision is estimated to be \pm half the range between the maximum and minimum results, divided by the average for that element.

Precision is best constrained for elements determined by ICP-OES because of more independent determinations. For these elements, precision is only considered acceptable if the sample standard deviation divided by the sample mean, averaged across the six samples, is $< 10\%$. For several elements this statistic is $< 5\%$ (Table 3.7). A less stringent requirement is placed on the consistency of the INAA replicates because of more limited data, and because small numerical values for some elements create higher percentage differences even when the offsets are small (e.g., 3 ppm and 2 ppm are very close results, but 50% different). For the INAA set of elements, reproducibility of results within 15% of the average is deemed acceptable; results within 20% are provisionally accepted for Hf, U and Yb because the numerical values are generally < 5 ppm.

Table 3.6 INAA results for six samples from MAR02–45 with sufficient material for duplicate or triplicate analysis. The overall precision of analyses is calculated as the average of half the sample ranges divided by corresponding sample averages – hence \pm a percentage of the amount present. **X** denotes cases for which precision could not be calculated because of one or more determination reported to be below the detection limit. U = Unit, R = Run. The last line of the table (next page) indicates whether precision is acceptable (Y) or unacceptable (N) according to criteria in footnote b.

Depth (cm)	U	R	As	Ba	Br	Co	Cr	Cs	Eu	Fe	Hf	Na	Rb	Sb	Sc	Ta	Th	U	La	Ce	Nd	Sm	Yb	Lu
			ppm	ppm	ppm	ppm	ppm	ppm	ppm	ppm	%	ppm	%	ppm	ppm	ppm	ppm	ppm	ppm	ppm	ppm	ppm	ppm	ppm
120	A	1	10.2	510	4.2	18	140	9	1.7	4.63	7	0.84	154	1.6	15.9	2.0	14.9	4.9	37.8	87	32	6.6	3.8	0.37
		2	10.5	450	<0.5	16	112	17	1.3	3.99	3	0.84	155	1.4	13.0	<0.5	14.4	4.2	31.5	77	41	5.3	2.7	0.14
		3	13.9	<50	<0.5	16	109	9	1.4	4.11	4	0.83	121	2.5	13.3	<0.5	16.0	3.1	30.4	72	59	5.2	2.5	0.15
		Avg	11.5			17	120	12	1.5	4.24	5	0.84	143	1.8	14.1		15.1	4.1	33.2	79	44	5.7	3.0	0.22
		0.5*range/ avg	12%	X	X	6%	13%	34%	14%	8%	43%	1%	12%	30%	10%	X	5%	22%	11%	10%	31%	12%	22%	52%
190	A	1	10.5	450	3.0	19	149	10	1.5	4.36	6	0.79	155	1.8	15.7	2.0	13.9	4.6	36.5	82	24	6.4	3.7	0.39
		2	9.9	610	<0.5	20	119	19	1.3	4.06	5	0.78	109	1.5	13.4	<0.5	15.9	3.8	31.0	65	43	5.3	2.3	0.17
		3	11.8	<50	<0.5	20	120	15	1.6	4.37	7	0.79	203	2.0	13.9	<0.5	15.5	4.1	31.2	77	47	5.4	2.9	0.16
		Avg	10.7			20	129	15	1.5	4.26	6	0.79	156	1.8	14.3		15.1	4.2	32.9	75	38	5.7	3.0	0.24
		0.5*range/ avg	5%	X	X	3%	12%	31%	10%	4%	17%	1%	30%	14%	8%	X	7%	10%	8%	11%	30%	10%	24%	48%
400	B	1	19.9	510	5.4	17	159	8	1.3	4.79	7	0.77	158	0.8	15.3	<0.5	13.2	2.0	37.8	90	30	5.5	3.1	0.51
		2	20.3	460	7.7	18	113	10	0.9	4.52	4	0.67	84	0.9	12.9	<0.5	14.9	3.5	30.5	63	60	5.4	2.9	0.18
		3	23.5	370	7.9	16	129	13	1.4	4.80	7	0.74	107	1.9	14.2	<0.5	17.3	3.1	32.5	100	23	5.7	2.2	0.20

Table 3.6 Continued

Depth (cm)	U	R	As	Ba	Br	Co	Cr	Cs	Eu	Fe	Hf	Na	Rb	Sb	Sc	Ta	Th	U	La	Ce	Nd	Sm	Yb	Lu
			ppm	%	ppm	%	ppm																	
400	B	Avg	21.2	447	7.0	17	134	10	1.2	4.70	6	0.73	116	1.2	14.1		15.1	2.9	33.6	84	38	5.5	2.7	0.30
		0.5*range/ avg	8%	16%	18%	6%	17%	24%	21%	3%	25%	7%	32%	46%	8%	X	14%	26%	11%	22%	49%	3%	16%	52%
540	C	1	6.2	350	1.8	13	108	4	1.7	3.18	10	0.91	102	0.7	13.0	3.6	9.2	3.5	37.8	74	32	6.2	3.6	0.32
		2	6.8	390	<0.5	13	88	5	1.2	2.89	9	0.85	125	0.9	9.8	<0.5	13.4	2.6	30.0	67	27	5.1	2.9	0.14
		Avg	6.5	370		13	98	5	1.5	3.04	10	0.88	114	0.8	11.4		11.3	3.1	33.9	71	30	5.7	3.3	0.23
		0.5*range/ avg	5%	5%	X	0%	10%	11%	17%	5%	5%	3%	10%	13%	14%	X	19%	15%	12%	5%	8%	10%	11%	39%
750	C	1	8.2	370	<0.5	16	153	7	1.3	3.72	4	0.66	72	0.9	13.9	1.9	10.3	2.6	34.6	70	24	5.6	2.6	0.44
		2	6.9	700	<0.5	14	87	7	1.0	3.05	5	0.60	113	1.1	10.3	<0.5	12.1	2.3	26.1	59	27	4.2	1.9	0.14
		Avg	7.6	535		15	120	7	1.2	3.4	5	0.6	93	1.0	12.1		11.2	2.5	30.4	65	26	4.9	2.3	0.3
		0.5*range/ avg	9%	31%	X	7%	28%	0%	13%	10%	11%	5%	22%	10%	15%	X	8%	6%	14%	9%	6%	14%	16%	52%
890	C	1	18.2	270	2.1	14	114	6	1.6	4.29	4	0.77	93	1.1	13.4	<0.5	9.2	2.7	34.2	70	37	5.3	2.9	0.39
		2	11.5	<50	<0.5	17	94	<1	0.9	3.91	3	0.73	211	1.3	10.4	<0.5	12.1	2.0	27.5	59	60	4.6	2.3	0.14
		3	16.7	<50	<0.5	14	108	9	1.7	3.78	4	0.78	107	1.0	10.7	<0.5	12.1	4.1	27.3	59	25	4.6	2.4	0.14
		Avg	15.5			15	105		1.4	3.99	4	0.76	137	1.1	11.5		11.1	2.9	29.7	63	41	4.8	2.5	0.22
		0.5*range/ avg	22%	X	X	10%	9%	X	29%	7%	14%	3%	43%	13%	13%	X	13%	36%	12%	9%	43%	7%	12%	56%
Overall precision ^a			10%	X	X	5%	15%	20%	17%	6%	19%	3%	25%	21%	11%	X	11%	19%	11%	11%	28%	9%	17%	50%
Considered acceptable (Y/N) ^b			Y	N	N	Y	Y	N	N	Y	Y	Y	N	N	Y	N	Y	Y	Y	Y	N	Y	Y	N

^a calculated as the average of half the sample ranges divided by corresponding sample averages – hence ± a percentage of the

amount present. ^b mostly < ±15% variation, but Hf, U, and Yb accepted at < ±20% because numerical values are so small only a

few ppm difference results in larger percentage variation.

Table 3.7 ICP-OES results for six samples from MAR02–45 with sufficient material for four to six independent analyses. The overall precision of analyses is calculated as the average of the sample standard deviations divided by corresponding sample averages – hence \pm a percentage of the amount present. For elements proposed to have acceptable precision (Y in last row of this table, 2 pages onward), there is $< \pm 10\%$ variation and mostly $< \pm 5\%$ variation. Ni and Zn were not replicated in runs 3 and 4.

Depth (cm)	Unit	Run	Cu	Pb	Ni ^a	Zn ^a	S	Al	Ca	K	Mg	Mn	P	Sr	Ti	V	Y
			ppm	ppm	ppm	ppm	%	%	%	%	%	%	ppm	%	ppm	%	ppm
120	A	1	44	23	65	90	0.05	5.05	5.27	2.20	1.80	533	0.253	181	0.44	112	17
"		2	45	27	64	89	0.03	5.23	5.14	2.12	1.74	518	0.169	172	0.25	89	17
"		3	47	26	61	100	0.07	7.60	4.92	1.88	1.79	550	0.228	185	0.38	103	18
"		4	49	25	62	113	0.07	7.75	4.95	2.28	1.80	555	0.245	189	0.41	107	18
"		5	44	24			0.07	7.30	4.84	1.76	1.74	558	0.239	181	0.39	103	18
"		6	48	27			0.07	7.76	4.97	2.30	1.81	564	0.255	188	0.43	106	18
"		Mean	46	25	63	98	0.06	6.78	5.02	2.09	1.78	546	0.232	183	0.38	103	18
"		SD/Mean	4.6%	6.4%	2.9%	11.4%	27.9%	18.9%	3.2%	10.6%	1.8%	3.2%	13.9%	3.4%	18.0%	7.5%	2.9%
190	A	1	42	37	71	100	0.03	5.21	4.94	2.22	1.79	518	0.163	164	0.21	109	17
"		2	43	36	72	100	0.03	5.24	4.86	2.15	1.80	527	0.166	162	0.24	110	17
"		3	47	42	73	112	0.07	8.04	4.80	2.22	1.88	574	0.253	182	0.32	108	19
"		4	46	39	70	112	0.07	8.03	4.69	2.25	1.87	551	0.226	178	0.35	109	19
"		5	44	38			0.07	7.78	4.58	1.84	1.81	552	0.231	173	0.36	107	18
"		6	46	41			0.08	8.17	4.69	2.38	1.87	565	0.262	181	0.41	112	19
"		Mean	45	39	72	106	0.06	7.08	4.76	2.18	1.84	548	0.217	173	0.32	109	18
"		SD/Mean	4.4%	6.0%	1.8%	6.5%	38.2%	20.4%	2.8%	8.3%	2.2%	3.9%	19.7%	5.0%	24.2%	1.6%	5.4%

Table 3.7 Continued.

			Cu	Pb	Ni ^a	Zn ^a	S	Al	Ca	K	Mg	Mn	P	Sr	Ti	V	Y
Depth (cm)	Unit	Run	ppm	ppm	ppm	ppm	%	%	%	%	%	ppm	%	ppm	%	ppm	ppm
400	B	Run 1	45	17	65	89	0.35	5.50	4.41	2.24	1.83	520	0.156	135	0.39	110	17
"		Run 2	44	18	65	90	0.37	5.59	4.51	2.27	1.86	531	0.158	136	0.39	111	18
"		3	43	22	67	100	0.38	7.64	4.22	2.39	1.84	551	0.152	140	0.37	105	18
"		4	44	19	62	100	0.37	7.85	4.23	1.96	1.86	560	0.145	142	0.35	104	18
"		5	44	19			0.33	7.74	4.20	2.26	1.82	556	0.131	141	0.31	105	18
"		6	44	19			0.39	7.70	4.21	2.18	1.83	533	0.156	141	0.38	103	18
"		Mean	44	19	65	95	0.37	7.00	4.30	2.22	1.84	542	0.150	139	0.37	106	18
"		SD/Mean	1.4%	8.8%	3.2%	6.4%	5.9%	16.2%	3.0%	6.5%	0.9%	3.0%	6.8%	2.1%	8.4%	3.1%	2.3%
540	C	1	28	14	46	66	0.13	4.43	5.75	1.99	1.59	508	0.214	176	0.41	88	18
"		2	28	14	45	66	0.08	4.63	5.61	1.97	1.57	505	0.146	173	0.26	82	18
"		3	28	13	43	69	0.14	6.43	5.22	2.05	1.54	515	0.192	179	0.38	80	19
"		4	29	14			0.13	6.43	5.28	1.97	1.54	515	0.180	180	0.36	79	19
"		Mean	28	14	45	67	0.12	5.48	5.47	2.00	1.56	511	0.183	177	0.35	82	19
"		SD/Mean	1.8%	3.6%	3.4%	2.6%	22.6%	20.1%	4.7%	1.9%	1.6%	1.0%	15.5%	1.8%	18.4%	4.9%	3.1%
750	C	1	39	14	52	67	0.03	4.15	10.70	1.77	1.75	676	0.175	251	0.28	88	16
"		2	39	14	53	68	0.02	4.27	10.90	1.84	1.80	684	0.156	255	0.25	88	16
"		3	41	16	51	76	0.08	6.35	10.70	1.92	1.81	707	0.210	269	0.33	86	17
"		4	49	15			0.09	6.36	10.80	1.92	1.83	717	0.211	271	0.34	87	17
"		Mean	42	15	52	70	0.06	5.28	10.78	1.86	1.80	696	0.188	262	0.30	87	17
"		SD/Mean	11.3%	6.5%	1.9%	7.0%	63.9%	23.5%	0.9%	3.9%	1.9%	2.8%	14.4%	3.8%	14.1%	1.1%	3.5%

Table 3.7 Continued.

Depth (cm)	Unit	Run	Cu ppm	Pb ppm	Ni ^a ppm	Zn ^a ppm	S %	Al %	Ca %	K %	Mg %	Mn ppm	P %	Sr ppm	Ti %	V ppm	Y ppm
890	C	1	31	14	50	64	0.07	4.09	9.90	1.79	1.79	687	0.256	225	0.32	89	16
"		2	32	13	51	64	0.08	4.10	9.98	1.81	1.81	706	0.273	225	0.34	91	16
"		3	35	10	53	72	0.12	6.28	9.50	1.92	1.81	732	0.269	235	0.32	85	17
"		4	32	13	46	71	0.12	7.75	9.05	1.75	1.66	729	0.268	224	0.34	82	13
"		5	48	14			0.11	6.35	9.63	1.86	1.83	733	0.254	236	0.29	85	17
"		6	35	16			0.10	6.17	9.43	1.73	1.78	738	0.224	231	0.25	83	17
"		Mean	36	13	50	68	0.10	5.79	9.58	1.81	1.78	721	0.257	229	0.31	86	16
"		SD/ Mean	17.9%	14.7%	5.9%	6.4%	21.0%	24.8%	3.5%	3.9%	3.4%	2.8%	7.0%	2.4%	11.2%	4.1%	9.7%
Overall precision ^a			6.9%	7.7%	3.2%	6.7%	29.9%	20.6%	3.0%	5.8%	2.0%	2.8%	12.9%	3.1%	15.7%	3.7%	4.5%
Considered acceptable (Y/N)			Y	Y	Y	Y	N	N	Y	Y	Y	Y	N	Y	N	Y	Y

^a calculated as the average of the sample standard deviations divided by corresponding sample averages

Because of an unacceptably low level of reproducibility, the results for 11 elements (S, Al, P, Ti, Cs, Eu, Ba, Rb, Sb, Nd, and Lu) are not discussed further in the thesis, and are not considered in making interpretations (Tables 3.6 and 3.7, columns with decision N rather than Y in the bottom row). The high standard deviations for S and Al (and therefore poor precision) may be due to systematic differences between the completeness of the 2011 acid digestions (Runs 1 & 2) relative to the 2014 digestions (Runs 3 and higher), because the data show clear clustering of results around two concentration levels. ActLabs warns in their brochures of potential incomplete liberation of these elements during the 4-acid digestion procedure.

To summarize, the following 24 elements (in order of increasing atomic number) are judged to have been analyzed with acceptable *precision* and will contribute to the discussion of sediment sources: Na, Mg, K, Ca, Sc, V, Cr, Mn, Fe, Co, Ni, Cu, Zn, As, Sr, Y, La, Ce, Sm, Yb, Hf, Pb, Th, U. Of course, the degree of stratigraphic variation shown by each element must be compared with the precision for that element (as \pm estimates of uncertainty) when deciding if downcore trends or differences are significant.

An assessment of the *accuracy* of the geochemical data depends on the degree to which the elemental abundances in certified standards were correctly determined by ActLabs during the 2011 and 2014 runs. Together with two batches of thesis samples from core MAR02–45, 9 certified standards were analyzed by ICP-OES, and 2 internal laboratory standards were analyzed by INAA (DMMAs-112 and DMMAs-116). The names, material types and collection sites of these standards are presented in Table 3.8. There are two requirements that must be met to support a claim that the results for a particular element are accurate in the thesis samples: (1) the measured concentrations in

certified standards should be close to the certified values, and (2) the certified standards should have concentrations (Table 3.9) and mineralogy similar to those in the unknown samples. Several of the ActLabs certified standards come from mining camps, contaminated sites or igneous rocks unlike the thesis materials (Table 3.10) so not surprisingly have concentrations for some elements that are outside the range of the thesis samples.

Table 3.8 Sample codes and descriptions of eleven certified and prepared laboratory standards used by ActLabs for quality control purposes.

Standard	Environment	Analysis Type
GXR-1	Jasperoid ‘reef’ in Cambrian limestone	ICP-OES
GXR-4	Unoxidized porphyry copper ore, primarily quartz and feldspar	ICP-OES
GXR-6	Collected in North Carolina near gold and base-metal deposits. A combination of sericitized mudstone and rhyolitic and andesitic basalt	ICP-OES
SDC-1	Upper Precambrian muscovite-quartz schist collected near Washington D.C.	ICP-OES
SCO-1	Cody Shale, a typical Upper Cretaceous silty marine shale	ICP-OES
DNC-1a	Triassic–Jurassic olivine-normative dolerite	ICP-OES
SAR-M	Anthropogenically contaminated Animas River sediment, blended from a variety of sites in the western United States	ICP-OES
OREAS 13b	Platinum group element-Cu-Ni reference material	ICP-OES
SBC-1	Brush Creek Shale. Marine shale collected in Pennsylvania	ICP-OES
DMMAAs 112/116	ActLabs internal standards made with tailings from the Giant Mascot Mine and the Parmour Porcupine Mine	INAA

Table 3.9 Certified values for eleven standards used by ActLabs. The table only includes the 24 elements having acceptable precision in MAR02–45 replicates. No values are shown if the element was not determined by ActLabs in quality control runs. Also shown for comparison is the average and standard deviation for the same elements in MAR02–45 samples.

	D. Lim.	GXR -1 Cert	GXR -4 Cert	GXR -6 Cert	SDC -1 Cert	SCO -1 Cert	DNC -1a Cert	OREAS 13b Cert	SBC -1 Cert	SAR -M Cert	DMMAs 112 Cert	DMMAs 116 Cert	MAR02 -45 Avg.	St Dev
Cu	1 ppm	1110	6520	66	30	29	100	2327	31	331			42	±12
Pb	3 ppm	730	52	101	25	31			35	982			19	±7
Ni	1 ppm	41	42	27	38	27	247	2247		42			57	±10
Zn	1 ppm	760	73	118	103	103	70	133	186	930			80	±17
As	0.5 ppm										1862	1560	10.7	±5.2
Ca	0.01 %	0.96	1.01	0.18	1.00	1.87				0.61			6.84	±2.42
Co	1 ppm										43	41	16	±3
Cr	2 ppm										80	77	135	±25
Fe	0.01 %										3.34	3.12	4.06	±0.76
K	0.01 %	0.05	4.01	1.87	2.72	2.30				2.94			2.04	±0.24
Mg	0.01%	0.22	1.66	0.61	1.02	1.64				0.50			1.80	±0.13
Mn	1 ppm	852	155	1010	883	410				5220			583	±84
Na	0.01 %										2.05	1.98	0.83	±0.09
Sc	0.1 ppm										7.17	6.30	14.6	±1.8
Sr	1 ppm	275	221	35	183	174	144		178	151			198	±78
V	2 ppm	80	87	186	102	131	148		220	67			97	±15
Y	1 ppm	32	14	14	40	26	18		37	28			17	±1
La	0.5 ppm										15.92	15.90	37	±2
Ce	3 ppm										26.56	30.00	81	±10
Sm	0.1 ppm										2.34	2.40	6.2	±0.6
Hf	1 ppm												7	±1
Th	0.2 ppm												12.1	±2.4
U	0.5 ppm										17.8	11.2	3.7	±1.2
Yb	0.2 ppm												3.4	±0.5

Table 3.10 Measured and certified (*italics*) values for six elements determined by INAA, and a comparison to the mean and standard deviation of MAR02–45 samples. The certified values come from standards DMMAs 112 and 116 (Table 3.9). Visual inspection demonstrates the level of accuracy. The limitation imposed by just two standards of very similar composition means that accuracy is not demonstrated across the range of values found in the MAR02–45 samples. Units are ppm unless otherwise noted.

	Co	Co	Cr	Cr	Fe%	Fe%	Na%	Na%	Sc	Sc	La	La
	meas	cert	meas	cert	meas	cert	meas	cert	meas	cert	meas	cert
DMMAs 112	46	<i>43</i>	90	<i>80</i>	3.54	<i>3.34</i>	2.12	<i>2.05</i>	7.30	<i>7.17</i>	18.30	<i>15.92</i>
DMMAs 112	45	<i>43</i>	86	<i>80</i>	3.45	<i>3.34</i>	2.04	<i>2.05</i>	7.00	<i>7.17</i>	18.20	<i>15.92</i>
DMMAs 116	44	<i>41</i>	80	<i>77</i>	3.28	<i>3.12</i>	2.04	<i>1.98</i>	5.90	<i>6.30</i>	15.50	<i>15.90</i>
MAR02–45												
Average		16		135		4.1		0.8		14.6		31.6
Std. Dev.		±3		±24		±0.8		±0.1		±1.8		±2.5

For elements determined by INAA (Table 3.10), the number of pairs of measured and certified values is small, so there is not a strong test available for the accuracy of determinations within the range of the MAR02–45 concentrations. La appears to have been determined with the lowest accuracy; for other elements in Table 3.10 the accuracy is consistent with the level of precision demonstrated in Table 3.6.

The approach used to assess accuracy for elements determined by ICP-OES is to cross-plot measured versus certified values within a range extending from 1/2 the minimum MAR02–45 value to 2× the maximum MAR02–45 value (Fig. 3.9). Outside this range, the reader is directed to Appendix 4 to see how well measured and certified values match. However, the closeness of matches well outside the MAR02–45 range (with potentially different mineralogy) might not be a reliable predictor of accuracy for the thesis samples.

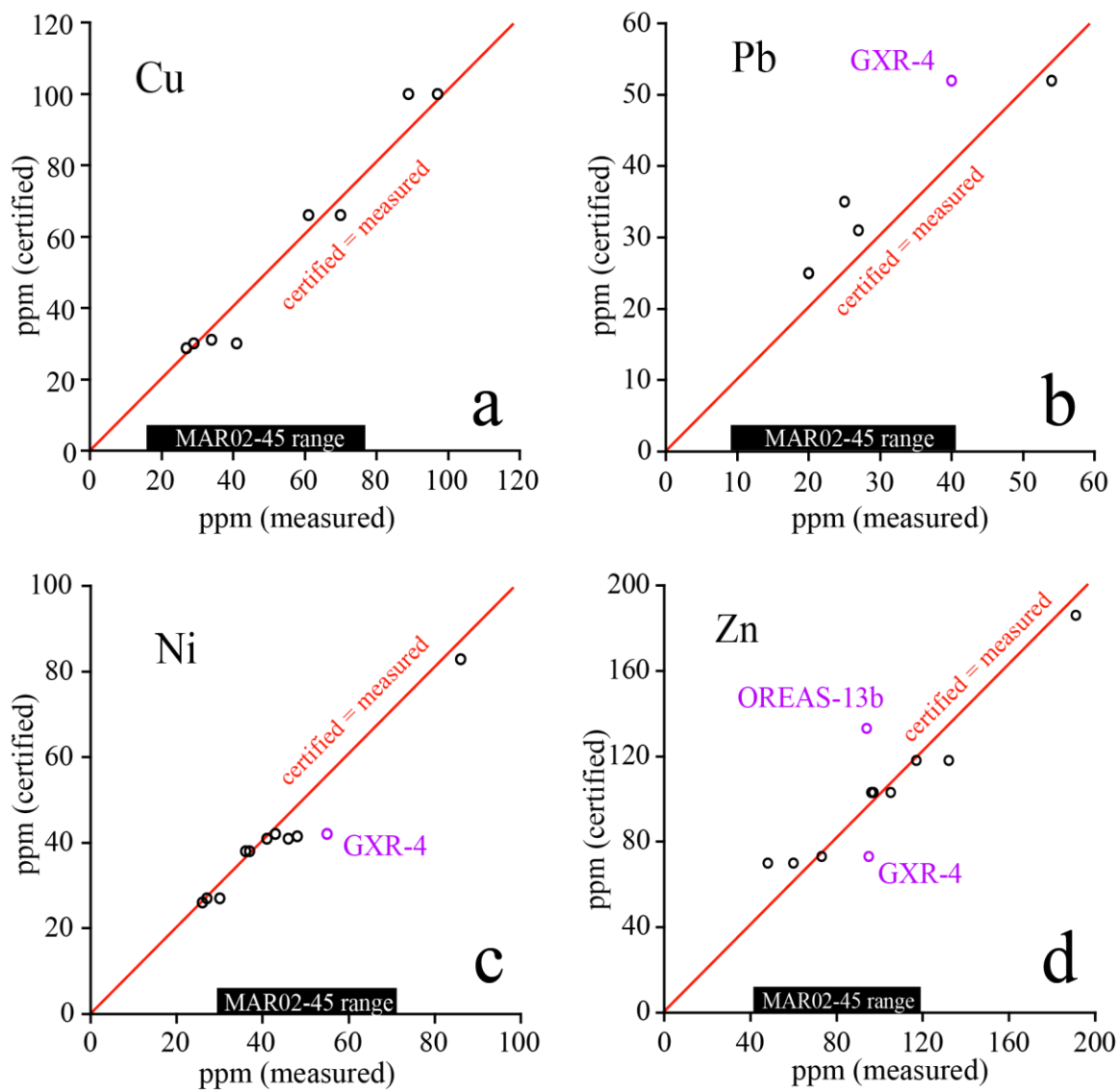


Figure 3.9 Plots of measured versus certified values for all 10 elements determined by ICP-OES using results for the standards GXR-1 (parts c, g, h, i, j), GXR-4 (parts b, c, d, e, f, h, i, j), GXR-6 (parts a, c, d, e, g, i, j), SDC-1 (all parts but d), SCO-1 (all parts), DNC-1a (parts d, h, i, j), SAR-M (parts c, e, h, i, j), SBC-1 (parts a, b, c, d, h, i, j) and OREAS-13b (part d). The standard responsible for each point can be determined from Table 3.4. Outliers distant from the measured=certified (red) line are coloured purple and are labelled with the code of the standard. The full range of MAR02–45 samples is indicated for each element.

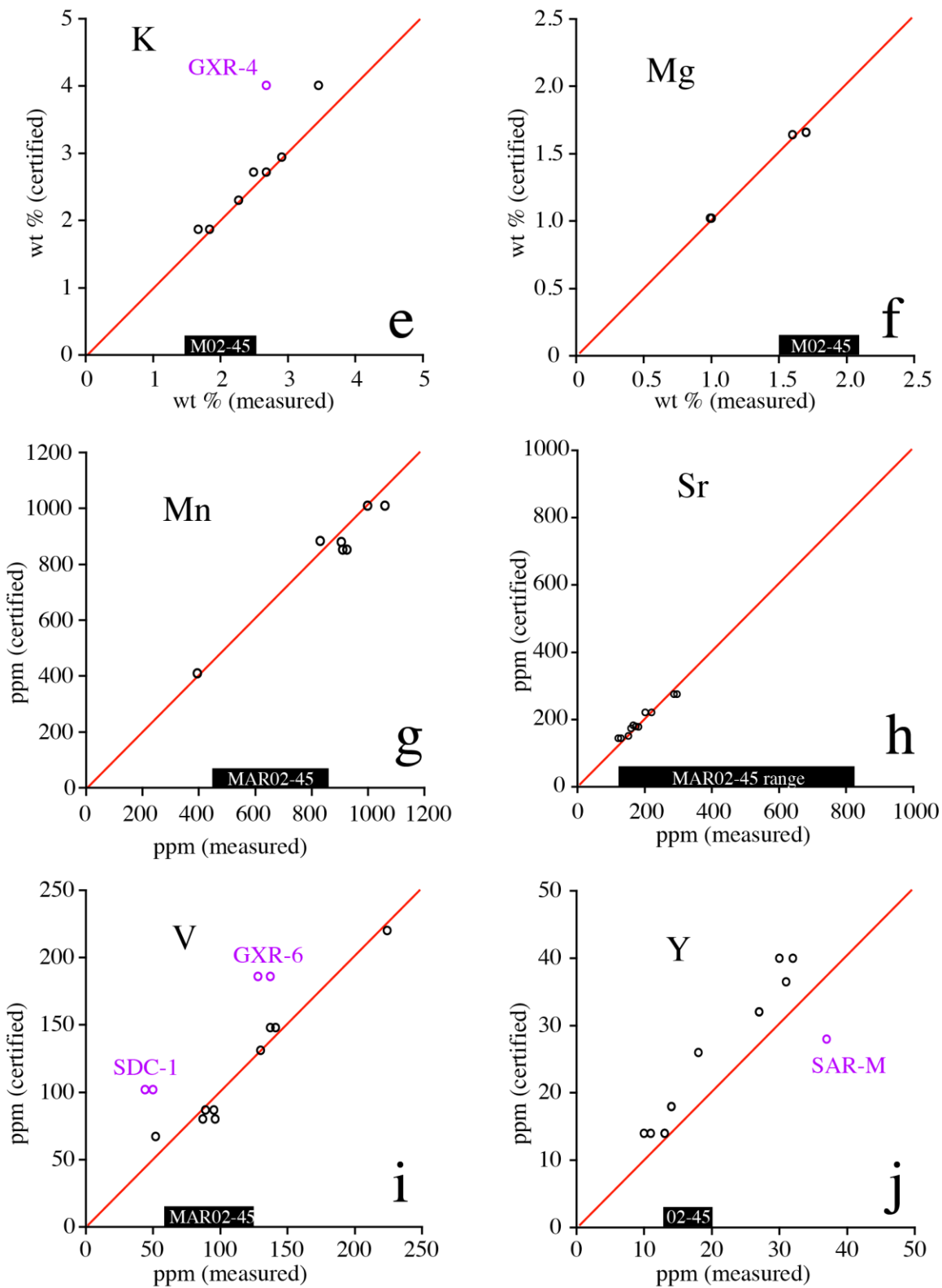


Figure 3.9 Continued

This thesis takes the conservative view that accuracy can only be evaluated with confidence if certified standards and MAR02–45 samples have similar concentrations. To begin, none of the certified standards analyzed by ActLabs match (within a factor of 0.5–2) the levels of As, Ca, Ce, Sm or U in the MAR02–45 samples. Hence, a definitive statement will not be made as to the accuracy of the determinations for these elements, although replicate analyses of the thesis samples show acceptable precision.

For all the standards with certified values near MAR02–45, ActLabs measured values for Cu, Mg, Mn and Sr fall very close (or essentially on) the measured=certified line (Fig. 3.9 a, f, g, h). For Pb, Ni and K (Fig. 3.9 b, c, e), ActLabs determinations for all of the standards fall along the 1:1 measured=certified line except for GXR-4. As GXR-4 was taken from a porphyry copper deposit dissimilar to the marine sediments of MAR02–45, its different mineralogy could explain mostly underestimation by ActLabs techniques (e.g., potential incomplete dissolution). Y and Pb are consistently underestimated (Fig. 3.9 b, j) except in the case of SAR-M on the Y plot. This underestimation might be due to difficulties during dissolution of the standard powders. Outliers in the cross-plots for Zn (OREAS 13-b, GXR-4) and V (SDC-1, GXR-6) come from non-sedimentary certified materials (Table 3.8).

For the elements having no good test of accuracy (As, Ca, Ce, Sm, U), acceptable precision (Table 3.6) provides reasonable comfort that relative downcore variations are reliable and meaningful. For Y and Pb, underestimation in the ActLabs certified materials might or might not suggest a similar level of underestimation in the MAR02–45 sedimentary samples. An examination of this issue is beyond the scope of this thesis, but

readers should be aware of possible underestimation if extracting quantitative elemental compositions from Appendix 4.

Overall, the ActLabs quality control data indicate an acceptable level of accuracy and precision for 24 of 35 elements present above detection limits throughout the MAR02–45 cored succession. Only these elements will be considered in subsequent sections and chapters. The exception will be a few elements with strong spikes in concentration at the two unconformities $\alpha 1$ and $\alpha 2$, which will receive comment only for those sample depths.

3.5.2 *Geochemical Data*

After removal from further consideration of imprecise elements and those mostly below detection limits, correlation coefficients were calculated for the remaining 24 elements (Tables 3.11–3.14). These matrices summarize the common behaviour and associations of elements. Elements with an R value ≥ 0.8 share strong relationships. The matrices of correlation coefficients are presented for each lithologic unit and for the entire MAR02–45 cored succession. However, data for samples adjacent to the $\alpha 1$ (correlative conformity) and $\alpha 2$ (unconformity) levels (470, 480 and 490; 250, 260, and 270 cm depths) were not used in calculating coefficients because of spikes in several elements that compromise otherwise good correlations above and below in Units A, B and C.

Table 3.11 Matrix of correlation coefficients for core MAR02–45. Elements with an R value ≥ 0.8 are considered to have a strong relationship and are indicated in **bold**.

	Cu	Pb	Ni	Zn	As	Ca	Co	Cr	Fe	Hf	K	Mg	Mn	Na	Sc	Sr	Th	U	V	Y	La	Ce	Sm	Yb	
Cu	1.00																								
Pb	0.70	1.00																							
Ni	0.82	0.81	1.00																						
Zn	0.86	0.86	0.93	1.00																					
As	0.42	0.19	0.44	0.46	1.00																				
Ca	-0.57	-0.67	-0.69	-0.77	-0.49	1.00																			
Co	0.73	0.53	0.78	0.76	0.69	-0.62	1.00																		
Cr	0.58	0.34	0.63	0.57	0.65	-0.47	0.78	1.00																	
Fe	0.73	0.49	0.79	0.77	0.79	-0.65	0.89	0.81	1.00																
Hf	-0.21	-0.12	-0.28	-0.17	-0.07	-0.28	-0.18	-0.14	-0.18	1.00															
K	0.77	0.72	0.90	0.89	0.39	-0.73	0.69	0.53	0.70	-0.15	1.00														
Mg	0.25	0.00	0.31	0.17	0.14	0.12	0.27	0.33	0.25	-0.24	0.30	1.00													
Mn	-0.17	-0.48	-0.22	-0.35	-0.08	0.59	-0.10	0.03	-0.02	-0.31	-0.26	0.47	1.00												
Na	-0.23	-0.03	-0.27	-0.15	-0.10	-0.25	-0.19	-0.21	-0.23	0.66	-0.21	-0.16	-0.36	1.00											
Sc	0.76	0.57	0.81	0.82	0.65	-0.66	0.89	0.77	0.93	-0.20	0.74	0.21	-0.09	-0.21	1.00										
Sr	-0.32	-0.34	-0.42	-0.44	-0.21	0.57	-0.42	-0.36	-0.41	-0.07	-0.41	-0.15	0.12	-0.16	-0.42	1.00									
Th	0.72	0.69	0.83	0.83	0.58	-0.80	0.85	0.72	0.87	0.05	0.75	0.20	-0.25	0.05	0.89	-0.49	1.00								
U	0.61	0.58	0.60	0.65	0.45	-0.64	0.65	0.52	0.63	0.16	0.52	-0.02	-0.33	0.13	0.67	-0.18	0.77	1.00							
V	0.82	0.74	0.96	0.93	0.45	-0.71	0.78	0.60	0.78	-0.23	0.95	0.34	-0.22	-0.22	0.82	-0.44	0.82	0.58	1.00						
Y	0.28	0.29	0.37	0.40	0.01	-0.43	0.20	0.07	0.19	0.13	0.61	0.18	-0.24	-0.06	0.29	-0.24	0.32	0.13	0.50	1.00					
La	0.32	0.14	0.27	0.36	0.51	-0.59	0.55	0.55	0.59	0.45	0.34	0.00	-0.12	0.25	0.63	-0.39	0.65	0.49	0.34	0.29	1.00				
Ce	0.65	0.54	0.72	0.74	0.64	-0.81	0.79	0.73	0.81	0.18	0.70	0.20	-0.26	0.10	0.80	-0.53	0.88	0.66	0.74	0.35	0.76	1.00			
Sm	0.42	0.44	0.44	0.50	0.41	-0.59	0.59	0.47	0.60	0.25	0.40	-0.02	-0.23	0.29	0.71	-0.35	0.78	0.66	0.47	0.23	0.72	0.62	1.00		
Yb	0.49	0.59	0.58	0.62	0.40	-0.73	0.63	0.51	0.62	0.33	0.54	0.04	-0.34	0.34	0.68	-0.49	0.85	0.73	0.59	0.32	0.67	0.74	0.87	1.00	

Table 3.12 Matrix of correlation coefficients for Unit A in core MAR02–45. Elements with an R value ≥ 0.8 are considered to have a strong relationship and are indicated in **bold**. Depths 250–270 cm were omitted due to geochemical spikes; see §3.7.

	Cu	Pb	Ni	Zn	As	Ca	Co	Cr	Fe	Hf	K	Mg	Mn	Na	Sc	Sr	Th	U	V	Y	La	Ce	Sm	Yb	
Cu	1.00																								
Pb	0.34	1.00																							
Ni	0.28	0.17	1.00																						
Zn	0.62	0.69	0.21	1.00																					
As	-0.25	0.19	0.04	-0.06	1.00																				
Ca	-0.31	-0.35	-0.01	-0.69	0.04	1.00																			
Co	0.28	0.12	0.56	0.43	0.18	-0.55	1.00																		
Cr	0.42	0.39	0.32	0.50	0.25	-0.51	0.67	1.00																	
Fe	0.40	0.08	0.46	0.39	0.22	-0.53	0.72	0.62	1.00																
Hf	-0.34	-0.44	-0.57	-0.33	-0.08	0.02	-0.31	-0.35	-0.33	1.00															
K	0.45	-0.03	0.41	0.33	-0.17	0.20	0.13	-0.03	0.18	-0.49	1.00														
Mg	-0.17	-0.42	0.07	-0.55	-0.14	0.91	-0.41	-0.53	-0.52	-0.08	0.41	1.00													
Mn	-0.30	-0.33	0.35	-0.54	0.22	0.76	-0.21	-0.27	-0.04	-0.06	0.29	0.65	1.00												
Na	-0.13	-0.09	-0.76	0.05	0.09	-0.14	-0.27	0.01	-0.26	0.48	-0.19	-0.14	-0.34	1.00											
Sc	0.53	0.29	0.30	0.71	0.12	-0.77	0.80	0.66	0.83	-0.24	0.17	-0.66	-0.42	-0.06	1.00										
Sr	0.07	-0.13	0.06	-0.15	0.02	0.73	-0.34	-0.35	-0.42	-0.20	0.62	0.81	0.46	0.01	-0.43	1.00									
Th	0.30	0.00	0.18	0.38	0.10	-0.56	0.56	0.56	0.69	-0.03	0.12	-0.49	-0.25	0.09	0.70	-0.34	1.00								
U	0.36	-0.02	-0.09	0.21	0.04	-0.20	0.11	0.30	0.15	0.34	-0.02	-0.26	-0.16	0.08	0.31	-0.07	0.31	1.00							
V	0.41	-0.27	0.54	0.23	-0.18	0.04	0.49	0.22	0.36	-0.20	0.73	0.29	0.29	-0.21	0.37	0.30	0.32	0.12	1.00						
Y	0.11	-0.28	0.02	0.00	-0.01	0.29	0.02	-0.29	-0.21	0.05	0.52	0.53	0.10	0.18	-0.05	0.62	0.02	-0.04	0.47	1.00					
La	0.29	0.22	-0.02	0.51	0.25	-0.65	0.49	0.47	0.64	0.24	-0.13	-0.66	-0.30	0.28	0.75	-0.54	0.66	0.26	0.17	-0.08	1.00				
Ce	0.35	0.10	-0.07	0.39	0.25	-0.37	0.37	0.40	0.52	0.09	-0.01	-0.42	-0.22	0.21	0.60	-0.20	0.32	0.27	0.21	-0.01	0.71	1.00			
Sm	0.19	0.18	-0.04	0.41	0.40	-0.48	0.44	0.36	0.58	0.23	-0.05	-0.51	-0.13	0.32	0.66	-0.34	0.62	0.25	0.17	0.06	0.93	0.72	1.00		
Yb	0.09	-0.05	-0.22	0.14	0.36	-0.26	0.18	0.13	0.23	0.55	-0.13	-0.32	-0.16	0.37	0.35	-0.10	0.45	0.55	0.04	0.28	0.57	0.32	0.62	1.00	

Table 3.13 Matrix of correlation coefficients for Unit B in core MAR02–45. Elements with an R value ≥ 0.8 are considered to have a strong relationship and are indicated in **bold**. Depths 470–490 cm were omitted due to geochemical spikes; see §3.7

	Cu	Pb	Ni	Zn	As	Ca	Co	Cr	Fe	Hf	K	Mg	Mn	Na	Sc	Sr	Th	U	V	Y	La	Ce	Sm	Yb	
Cu	1.00																								
Pb	0.67	1.00																							
Ni	0.66	0.48	1.00																						
Zn	0.88	0.71	0.85	1.00																					
As	-0.03	-0.20	-0.05	-0.04	1.00																				
Ca	0.04	0.26	-0.08	-0.03	-0.63	1.00																			
Co	0.38	0.25	0.38	0.33	0.37	0.05	1.00																		
Cr	0.24	0.19	0.41	0.32	0.24	0.05	0.78	1.00																	
Fe	0.36	0.15	0.37	0.33	0.60	-0.25	0.70	0.78	1.00																
Hf	0.12	0.08	0.11	0.09	0.00	0.19	0.29	0.47	0.29	1.00															
K	0.66	0.58	0.82	0.86	-0.09	0.11	0.19	0.19	0.10	0.01	1.00														
Mg	0.52	0.60	0.50	0.63	-0.24	0.43	0.45	0.36	-0.01	0.17	0.71	1.00													
Mn	0.37	0.38	0.44	0.42	-0.08	0.46	0.44	0.48	0.53	0.07	0.36	0.29	1.00												
Na	-0.23	-0.29	-0.34	-0.39	-0.06	0.00	0.21	0.16	-0.08	0.41	-0.41	0.01	-0.29	1.00											
Sc	0.38	0.33	0.40	0.38	0.27	-0.14	0.73	0.81	0.80	0.08	0.12	0.20	0.50	0.09	1.00										
Sr	0.11	0.17	-0.01	0.00	-0.51	0.85	0.03	0.11	-0.04	0.34	0.06	0.19	0.46	-0.08	-0.10	1.00									
Th	0.25	0.20	0.38	0.26	0.30	-0.05	0.80	0.93	0.85	0.39	0.08	0.20	0.50	0.23	0.90	0.01	1.00								
U	0.24	0.21	0.04	0.08	-0.12	0.35	0.46	0.54	0.53	0.47	-0.15	-0.01	0.55	0.27	0.57	0.51	0.66	1.00							
V	0.72	0.60	0.95	0.91	-0.07	-0.05	0.35	0.39	0.29	0.11	0.88	0.66	0.39	-0.26	0.39	-0.04	0.33	-0.01	1.00						
Y	0.19	0.39	0.52	0.48	-0.02	0.05	0.20	0.31	-0.05	0.00	0.70	0.71	0.04	-0.13	0.14	-0.12	0.11	-0.36	0.64	1.00					
La	0.15	0.19	0.31	0.22	0.20	-0.02	0.73	0.93	0.74	0.41	0.08	0.24	0.45	0.33	0.85	0.01	0.95	0.63	0.29	0.22	1.00				
Ce	0.13	0.27	0.48	0.35	0.07	-0.06	0.51	0.68	0.47	0.43	0.30	0.32	0.35	0.13	0.46	-0.09	0.64	0.24	0.47	0.41	0.73	1.00			
Sm	0.19	0.09	0.14	0.09	0.31	-0.12	0.68	0.76	0.74	0.16	-0.11	0.05	0.35	0.36	0.92	-0.07	0.88	0.63	0.13	-0.02	0.84	0.31	1.00		
Yb	0.15	0.17	0.23	0.13	0.30	0.02	0.77	0.88	0.76	0.38	0.02	0.21	0.46	0.37	0.85	0.06	0.95	0.67	0.22	0.15	0.95	0.57	0.90	1.00	

Table 3.14 Matrix of correlation coefficients for Unit C in core MAR02–45. Elements with an R value ≥ 0.8 are considered to have a strong relationship and are indicated in **bold**. Samples considered are from depths 500–940 cm, all below the upwardly adjusted position of the $\alpha 1$ level (see §5.1.1), as compared with the 525 cm depth assigned to $\alpha 1$ by Hiscott et al. (2007b).

	Cu	Pb	Ni	Zn	As	Ca	Co	Cr	Fe	Hf	K	Mg	Mn	Na	Sc	Sr	Th	U	V	Y	La	Ce	Sm	Yb	
Cu	1.00																								
Pb	0.59	1.00																							
Ni	0.76	0.65	1.00																						
Zn	0.72	0.70	0.76	1.00																					
As	0.23	0.14	0.20	0.29	1.00																				
Ca	0.33	-0.23	0.34	-0.07	0.18	1.00																			
Co	0.60	0.36	0.62	0.50	0.20	0.27	1.00																		
Cr	0.18	0.03	0.32	0.02	0.07	0.41	0.29	1.00																	
Fe	0.67	0.54	0.79	0.68	0.52	0.27	0.63	0.30	1.00																
Hf	-0.52	-0.29	-0.76	-0.47	-0.29	-0.60	-0.51	-0.35	-0.67	1.00															
K	0.47	0.79	0.72	0.78	0.01	-0.31	0.40	0.05	0.54	-0.29	1.00														
Mg	0.29	-0.25	0.34	0.04	0.10	0.77	0.18	0.25	0.23	-0.39	-0.09	1.00													
Mn	0.34	-0.12	0.42	0.05	0.16	0.80	0.26	0.20	0.36	-0.58	-0.12	0.73	1.00												
Na	-0.72	-0.60	-0.81	-0.60	-0.24	-0.49	-0.62	-0.43	-0.72	0.74	-0.45	-0.18	-0.41	1.00											
Sc	0.68	0.73	0.88	0.83	0.17	0.10	0.62	0.25	0.81	-0.59	0.79	0.10	0.18	-0.77	1.00										
Sr	0.40	-0.12	0.43	0.03	0.20	0.90	0.33	0.50	0.30	-0.58	-0.13	0.72	0.65	-0.51	0.19	1.00									
Th	0.12	0.41	0.11	0.26	-0.21	-0.32	0.21	0.01	0.14	0.16	0.39	-0.15	-0.14	-0.08	0.37	-0.28	1.00								
U	-0.01	0.10	-0.17	0.05	-0.06	-0.30	-0.02	-0.07	-0.27	0.28	-0.03	-0.28	-0.49	0.15	-0.12	-0.20	0.01	1.00							
V	0.67	0.70	0.91	0.85	0.21	0.07	0.58	0.16	0.75	-0.59	0.89	0.18	0.24	-0.67	0.89	0.21	0.27	-0.15	1.00						
Y	0.22	0.69	0.28	0.53	-0.12	-0.60	0.10	-0.19	0.14	0.18	0.79	-0.34	-0.43	-0.12	0.47	-0.40	0.58	0.21	0.56	1.00					
La	-0.28	0.08	-0.40	-0.08	-0.26	-0.63	-0.21	-0.20	-0.28	0.70	0.10	-0.37	-0.58	0.41	-0.06	-0.54	0.61	0.24	-0.17	0.55	1.00				
Ce	-0.11	0.17	-0.24	-0.04	-0.17	-0.49	-0.08	-0.14	-0.18	0.52	0.18	-0.27	-0.49	0.28	0.00	-0.33	0.55	0.26	-0.01	0.56	0.77	1.00			
Sm	-0.27	0.01	-0.42	-0.06	-0.22	-0.64	-0.23	-0.17	-0.29	0.69	0.11	-0.33	-0.56	0.44	-0.10	-0.52	0.58	0.18	-0.15	0.54	0.92	0.77	1.00		
Yb	-0.50	-0.14	-0.57	-0.32	-0.24	-0.62	-0.41	-0.21	-0.45	0.76	-0.09	-0.41	-0.63	0.55	-0.33	-0.57	0.28	0.21	-0.36	0.33	0.75	0.58	0.78	1.00	

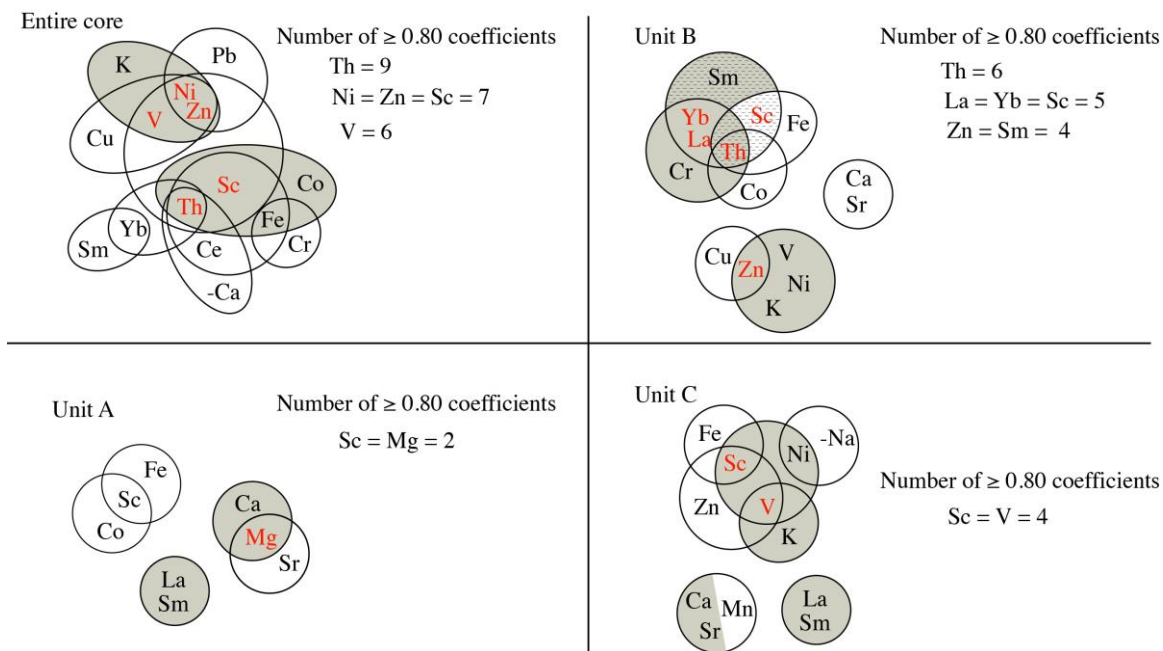


Figure 3.10 Venn-style diagrams expressing the relationships between elements from correlation coefficient tables. The diagrams represent relationships throughout MAR02–45 and in the individual lithologic units. All elements within each ring have correlations to one another with $R \geq 0.80$. Shaded areas show clusters of elements that share correlations with $R \geq \sim 0.90$ (some values of 0.89 are included). Within these shaded regions, the element(s) with the highest number of coefficients at the ≥ 0.80 level are in red text, and can be used as proxies for the behaviour of the other elements in the group. Hence, for the entire core, downcore plots of Ni, Zn, Th and Sc will give a good summary of the trends for a wider range of elements. Considering all units, Sc, La and perhaps Zn are useful guiding elements to understand cross-correlations. Ca variably correlates strongly with Mg, Sr and Mn, and tracks the abundance of calcite.

Elements with significant covariation ($R \geq 0.8$) are plotted on Venn-style diagrams to graphically express the relationships (Fig. 3.10). Negative correlations are indicated by an appropriate sign. The full core overview (Fig. 3.10) shows two main elemental associations with a high degree of cross-correlation at an $R \geq \sim 0.9$ level: (a) V, Ni, Zn, K; (b) Sc, Th, Fe, Co. Other elements correlate preferentially with some in these two groups; e.g., Cr with Fe, Yb and Sm with Th, Cu and Pb with Ni and Zn. In Unit A, Sm and La are strongly correlated, as are elements typically found in carbonates (i.e., Ca, Mg, Sr). Sc is correlated with Fe and Co at the $R \geq 0.8$ level. Compared with relationships for the entire core, the number of strongly correlated elements in Unit A is small. Relationships in Unit B are somewhat more complex. There are stand-alone elemental associations of (a) Ca with Sr, and (b) Zn with V, Ni, K and Cu. There is then a larger cluster of cross-correlating elements centred around Th, La, Yb and Sc, with correlation of Cr, Co, Fe and Sm to different subsets of Th, La, Yb and Sc. In Unit C, the carbonate-controlled elemental association involves Ca, Sr and Mn. La and Sm are highly correlated to one another but to no other elements. The main cluster of cross-correlated elements hinges on a strong correlation of Sc, V, Ni and K, with additional correlation pairs (and one triplet): Sc and V with Zn; Fe with Sc; Ni with -Na (i.e., a negative correlation).

Several elements have no noteworthy correlations with other elements at the $R \geq 0.8$ level or (in brackets below) only belong to a significant association in one stratigraphic unit: Pb, As, Hf, (Mn), (Na), U, Y, (Ce), (Yb). These elements will be de-emphasized in the subsequent interpretations and discussion unless they alone show strong and potentially meaningful stratigraphic trends.

3.5.3 *X-ray Fluorescence*

To assess the consistency of ActLabs data with other methods, four samples from core MAR02–45P were analyzed using X-ray fluorescence (XRF) at Memorial University. Operating conditions for the XRF can be found in ‘Analysis of Pressed Pellets of Geological Samples Using Wavelength-Dispersive X-Ray Fluorescence Spectrometry’ (Longerich, 1995). These samples were taken ~2 m apart in an effort to encapsulate the three lithologic units described by Hiscott et al. (2007b). As the ActLabs procedures and XRF target different suites of elements, results could only be compared for a subset of elements with abundances above detection limits for the different techniques (Appendix 5). ActLabs data were converted to oxide abundances, as needed, to allow comparison to conventional XRF laboratory reports. Table 3.15 shows the ratios of ActLabs determinations to Memorial University XRF results. Most of the geochemical species show similar concentrations although, relative to the XRF results, Cu and Zn are reported to be more abundant in the ActLabs data. Note that these samples are not certified standards, so it is not justified on the basis of these comparisons alone to claim that one laboratory or the other has the more accurate results. Determination of these four elements on international standards during the ActLabs runs show an underestimation of Zn, while ratios of measured to certified Cu values are nearly 1.0 (Fig. 3.9a,d).

Because of differences between the INAA and ICP–OES values and the XRF values, in spite of satisfactory levels of precisions in both laboratories, it is advised that inter-sample geochemical comparisons in this thesis be given much stronger weight than

comparisons to other data sets from the Black Sea area obtained using different analytical techniques. At a minimum, firm conclusions regarding differences in absolute concentrations (unless quite large) should only be based on those geochemical species (9 of 17) with inter-laboratory abundance ratios from 0.9–1.1 in Table 3.15.

3.5.4 Conversion to Calcite-free Abundances

In general, metal concentrations in shales and muds increase with the quantity of phyllosilicates, diagenetic sulphur (which scavenges metals) and organic matter (which promotes adsorption of metals onto particles (Loring, 1991).

Figure 3.11 plots ActLabs Ca against calcite abundances (from JADE output from silt-fraction XRD) after omitting three outliers. The regression equation based on all but the outliers can be used to estimate % calcite in each ActLabs sample, and hence the % non-calcite sediment (mainly silicate minerals). It was decided to examine the downcore geochemical trends on a non-calcite basis to compensate for dilution effects (because of a closed array) that would lead to reciprocal relationships between Ca abundance and the abundance of other elements (except, of course, elements like Sr, Mg and locally Mn that covary with Ca in parts of the succession). Such trends might mask variations in the abundances of elements residing in silicate minerals and the organic fraction. Figure 3.12 is a plot of downcore concentrations for a selection of elements, while Figure 3.13 shows recalculated (calcite-free) concentrations of the same elements. Below 600 cm depth, dilution by calcite seriously affects other geochemical trends. A full set of calcite-free downcore plots can be found in Appendix 6. Corresponding downcore variations in the raw data, without recalculation, can be extracted from the tables in Appendix 3.

Table 3.15 Ratios of (a) oxide and elemental abundances in four samples run using INAA and ICP–OES at Actlabs to (b) the abundances for the same samples analyzed using XRF at Memorial University. Ratios outside the range 0.9–1.1 are in *italics*. Only elements that passed quality control standards within INAA and ICP-OES results are compared to XRF data.

Element	Atomic Number	Ratio ActLabs/MUN				Average Ratio
		170 cm	480 cm	640 cm	840 cm	
Na ₂ O	11	<i>1.22</i>	<i>1.42</i>	<i>2.10</i>	<i>1.24</i>	<i>1.49</i>
MgO	12	<i>0.66</i>	<i>0.89</i>	<i>0.75</i>	<i>0.73</i>	<i>0.76</i>
K ₂ O	19	1.10	<i>1.29</i>	0.97	1.04	1.10
CaO	20	0.88	0.95	0.95	0.96	0.94
Sc	21	0.99	<i>1.21</i>	<i>0.75</i>	<i>0.76</i>	0.93
V	23	1.04	<i>1.40</i>	<i>0.87</i>	1.01	1.08
Cr	24	1.07	<i>1.46</i>	0.90	0.96	1.10
MnO	25	0.97	<i>1.38</i>	1.04	1.00	1.10
Fe ₂ O ₃ T	26	<i>1.15</i>	<i>1.29</i>	<i>0.88</i>	1.04	1.09
Ni	28	<i>1.33</i>	<i>1.60</i>	1.03	<i>1.20</i>	<i>1.29</i>
Cu	29	<i>1.91</i>	<i>2.30</i>	<i>1.20</i>	<i>1.56</i>	<i>1.74</i>
Zn	30	<i>2.35</i>	<i>2.82</i>	<i>1.98</i>	<i>2.34</i>	<i>2.37</i>
Sr	38	<i>0.88</i>	<i>0.58</i>	0.92	1.01	<i>0.85</i>
Y	39	<i>0.54</i>	<i>0.75</i>	<i>0.69</i>	<i>0.67</i>	<i>0.66</i>
Ce	58	<i>1.66</i>	<i>0.82</i>	<i>0.70</i>	<i>0.78</i>	0.99
Pb	82	<i>1.11</i>	<i>1.41</i>	<i>0.77</i>	<i>0.84</i>	1.03
Th	90	<i>1.18</i>	<i>1.22</i>	1.02	<i>1.16</i>	<i>1.15</i>

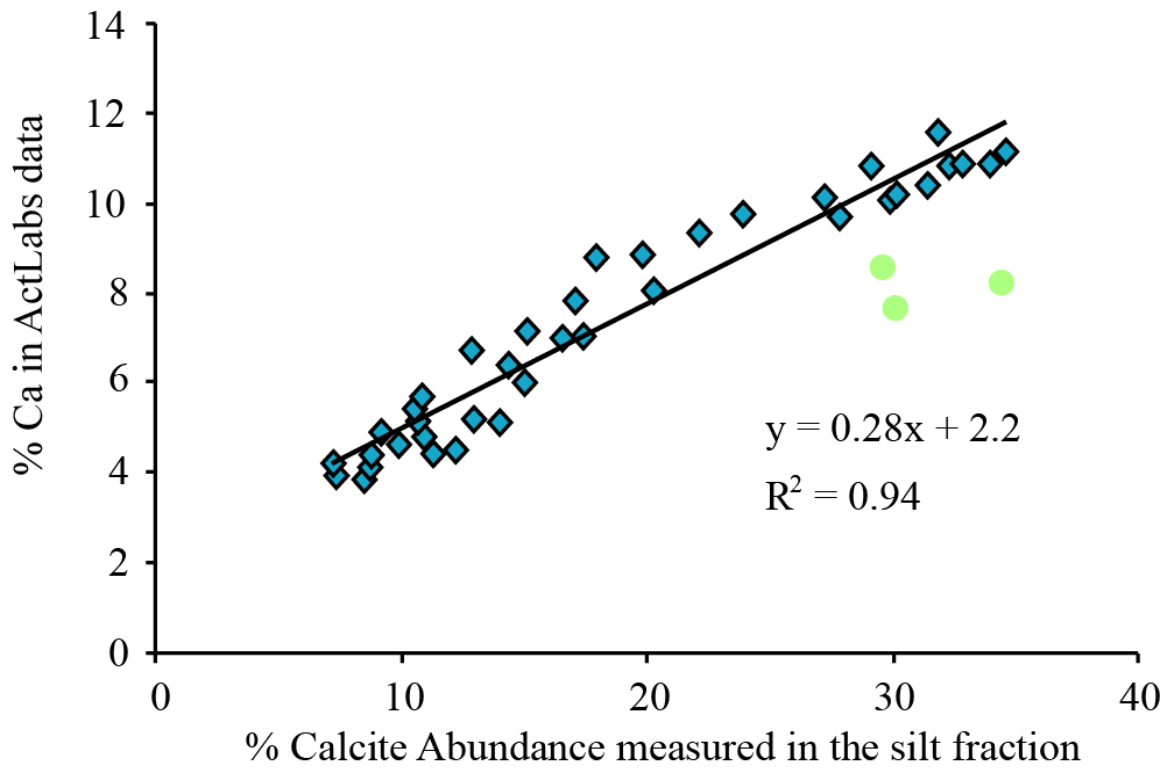


Figure 3.11 % Ca in ActLabs data vs % calcite abundance determined by XRD analysis of the silt fraction of MAR02–45. The three outliers that were excluded from the regression calculation are indicated by circles. The regression was used to calculate % calcite in each ActLabs sample.

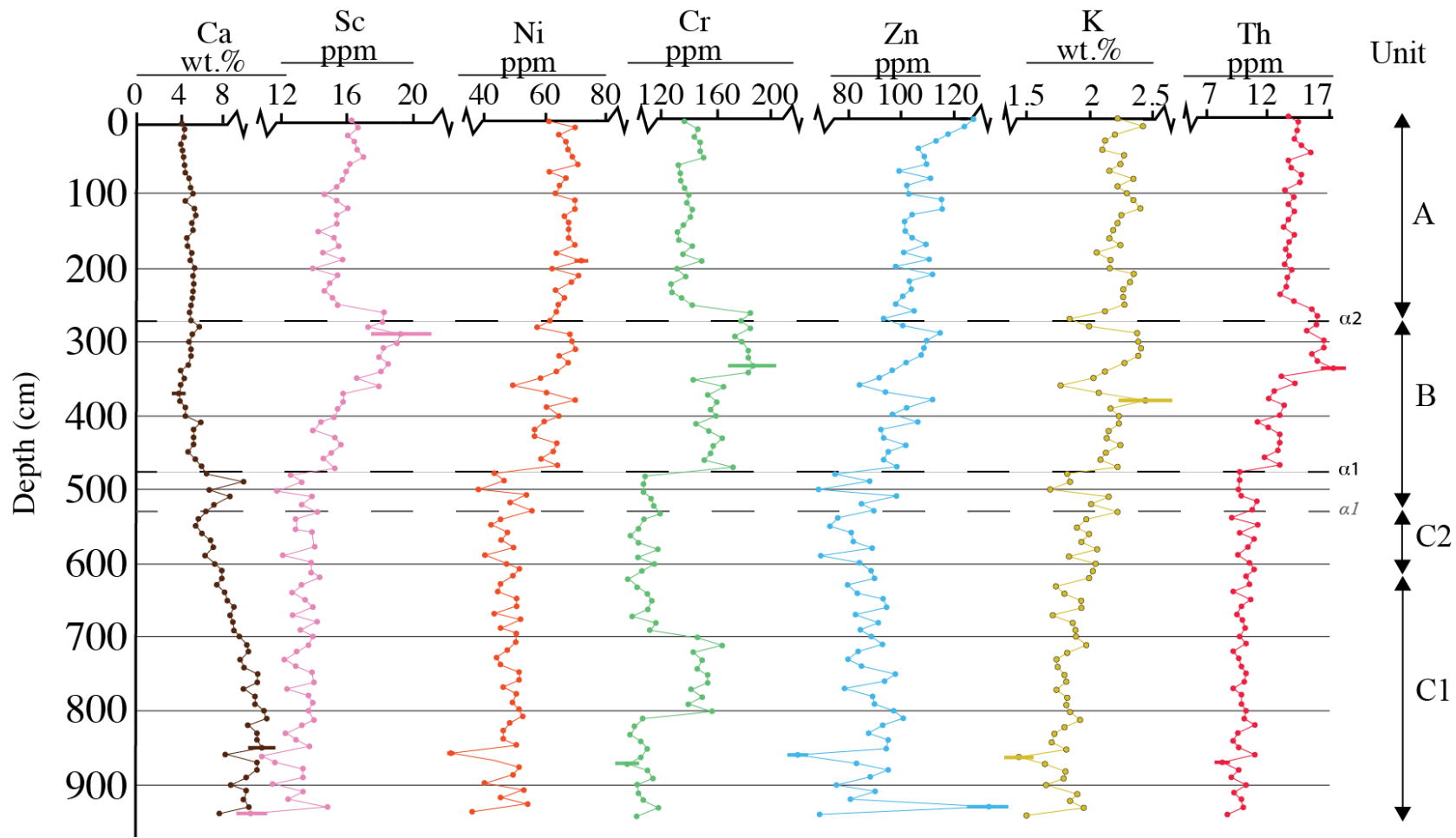


Figure 3.12 Caption can be found on the following page.

Figure 3.12 Caption. Downcore plots of selected elements in MAR02–45, it becomes clear below ~600 cm that dilution by calcite (tied to high Ca abundance) affects other downcore trends. These elements were selected to incorporate most of the elements having strong cross-correlations throughout the cored succession (Fig. 3.10). Cr is an exception; it is included because it shows large shifts in abundance in Unit C. Uncertainty in the minimum and maximum value in each plot is shown as an error bar that is \pm a percentage of the amount present, using the values for uncertainty obtained in the assessment of precision (Tables 3.6 and 3.7). For intermediate values, the uncertainty is between that shown for the minimum and maximum values.

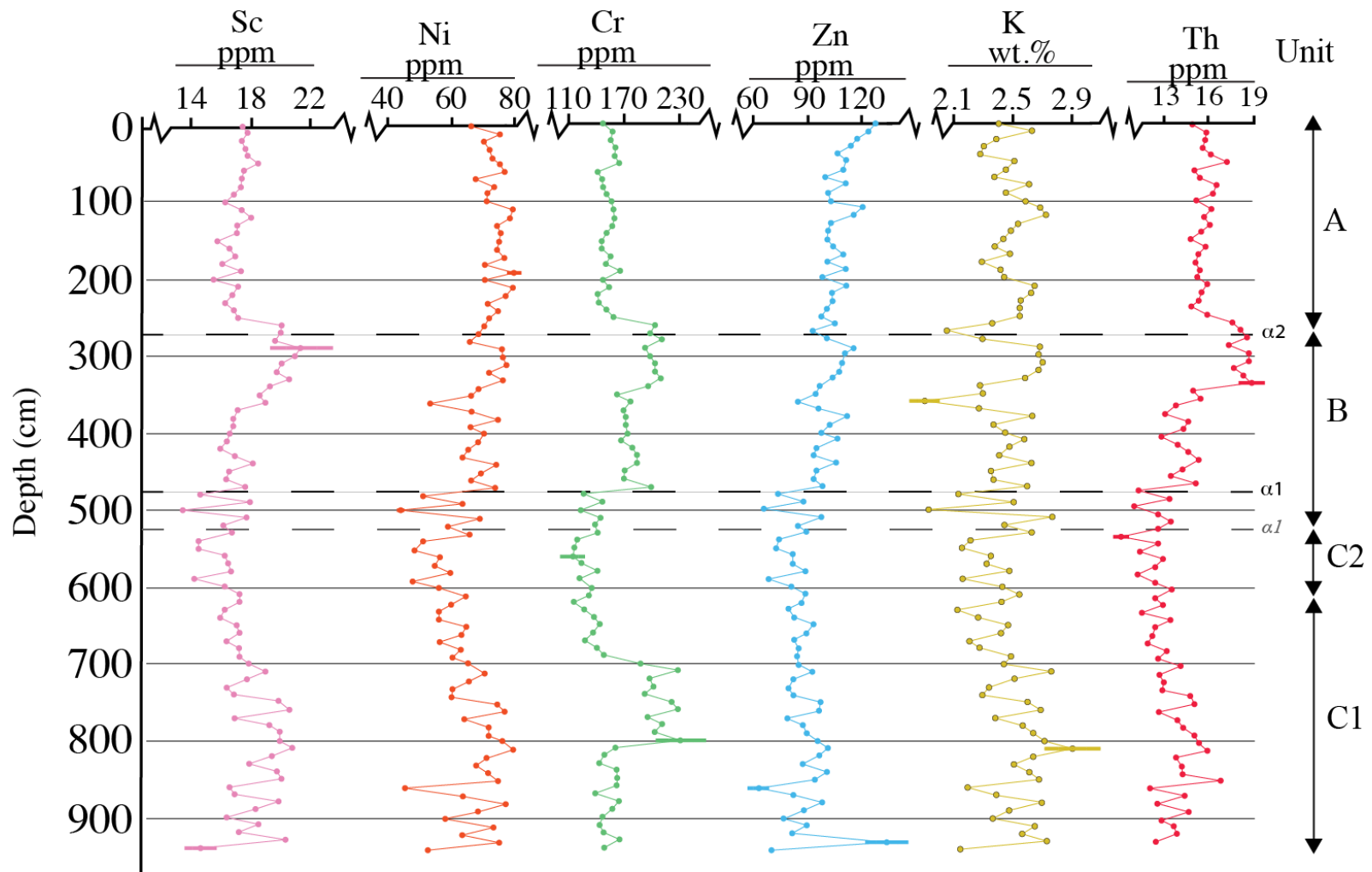


Figure 3.13 Caption can be found on the following page.

Figure 3.13 Caption. Downcore trends of recalculated calcite-free concentrations for the elements shown in Fig. 3.12, excluding Ca. It is believed that these plots better indicate stratigraphic trends in the silicate (+ organic) fraction. Uncertainty in the minimum and maximum value in each plot is shown as an error bar that is \pm a percentage of the amount present, using the values for uncertainty obtained in the assessment of precision (Tables 3.6 and 3.7). For intermediate values, the uncertainty is between that shown for the minimum and maximum values.

In Fig. 3.11 there is one minor issue that requires comment – a sample with 30% stoichiometric calcite should require a minimum of 12% Ca, whereas the XRD and ActLabs results predict 30% calcite in samples with only 11% Ca. This is not possible and provides no allowance for non-calcite Ca, so there must be a few percent error in the recalculated calcite abundances that will slightly affect the recalculation of other elemental abundances in calcite-rich samples. The second caveat is that only the XRD results from the silt fraction have been used to estimate bulk calcite abundance, not the entire < 62 µm sample that was powdered and submitted to ActLabs. However the < 2 µm clay percentage is so low (Fig 3.2) that calcite abundance in the silt fraction is considered to be a robust indicator of % calcite in the entire sample. The % error inherent in XRD measurements may also account for the discrepancy in non-calcite Ca.

Table 3.16 shows the average concentrations and associated standard deviations for Cu, Pb, Ni, Zn, As, Co, Cr, Fe, Hf, K, Mg, Mn, Na, Sc, Sr, Th, U, V, Y, La, Ce, Sm, and Yb in Units A, B, and C in core MAR02–45. Table 3.17 shows the geochemical composition of potential source areas from samples available to the author. Only Cr, Fe, and Mg are found in concentrations that are potentially unique indicators for each source area. However concentrations of Fe, and Mg show little variation throughout core MAR02–45.

Table 3.16 Average calcite-free concentration of Units A, B, and C of MAR02–45 in ppm unless otherwise noted. Elements in **bold** had, in a test involving four samples, concentrations within 0.90–1.10× the concentrations determined by XRF at Memorial University. These unit averages exclude samples which exhibit geochemical spikes near the α_1 and α_2 levels (470, 480 and 490; 250, 260, and 270 cm depths)

	Unit A		Unit B		Unit C	
	Average	St. Dev.	Average	St. Dev.	Average	St. Dev.
Cu	57	±11	55	±10	45	±10
Pb	32	±5	20	±2	18	±2
Ni	74	±4	70	±6	64	±9
Zn	109	±8	101	±8	87	±11
As	11.1	±1.7	19.5	±4.1	9.9	±4.0
Co	19	±1	21	±2	19	±3
Cr	153	±7	183	±15	158	±33
Fe (%)	4.81	±0.21	5.58	±0.64	4.61	±0.63
Hf	7	±1	8	±1	9	±2
K (%)	2.49	±0.12	2.46	±0.20	2.47	±0.19
Mg (%)	1.98	±0.16	2.09	±0.15	2.39	±0.34
Mn	568	±45	677	±114	837	±157
Na (%)	0.94	±0.06	0.91	±0.07	1.11	±0.17
Sc	17.2	±0.7	18.4	±1.8	13.3	1±.0
Sr	183	±14	165	±21	223	±27
Th	15.7	±0.6	15.8	±2.1	13.4	±1.3
U	5	±1	5	±1	3.6	±0.9
V	124	±7	119	±10	113	±13
Y	20	±2	19	±1	22	±1
La	41.0	±1.1	44.8	±2.4	48.4	±4.3
Ce	95	±4	104	±7	96	±8
Sm	6.5	±0.2	6.4	±1.0	5.8	±0.3
Yb	3.8	±0.2	3.6	±0.5	3.0	±0.3

Table 3.17 Average calcite-free concentration (ppm, unless otherwise noted) of potential source areas. Elements in **bold** had, in a test involving four samples, concentrations within 0.90–1.10× the concentrations determined by XRF at Memorial University.

	Thrace		Bosphorus		Danube	
	Average	St Dev	Average	St Dev	Average	St Dev
Cu	88	±30	67	±6	93	±27
Pb	19	±3	30	±2	46	±24
Ni	25	±1	92	±11	78	±17
Zn	88	±5	111	±9	152	±46
As	9.0	±2.8	13.2	±0.6	14.5	±4.2
Co	12	±1	19	±1	21	±3
Cr	76	±13	221	±9	157	±19
Fe (%)	3.22	±0.01	3.93	±0.05	4.87	±0.77
Hf	16	±8	7	±1	10	±9
K (%)	2.00	±0.38	1.93	±0.18	2.94	±1.02
Mg (%)	0.50	±0.23	1.11	±0.13	1.87	±0.24
Mn	555	±135	653	±50	981	±160
Na (%)	1.49	±0.67	0.95	±0.11	0.94	±0.33
Sc	12.3	±0.9	17.9	±1.7	17.8	±3.3
Sr	182	±159	145	±20	166	±15
Th	13.0	±1.6	13.6	±1.3	15.7	±3.2
U	5	±0.2	4	±0.2	4	±1.3
V	58	±15	103	±22	124	±33
Y	20	±4	22	±1	27	±7
La	47.0	±4.0	42.6	±0.9	51.3	±11.9
Ce	88	±4	76	±2	95	±24
Sm	6.5	±1.0	5.7	±0.2	7	±2
Yb	5.0	±1.0	3.6	±0.2	5	±1

3.6 Factor Analysis

Raw data was run through Q- and R-mode factor analysis, using varimax rotation. In addition to elemental abundances, several additional variables from earlier studies were added to the data matrix: total sulphur (TS), total organic carbon (TOC) and terrigenous TOC as reported by Hiscott et al. (2007b) and determined using a Carlo-Erba NA 1500 Elemental Analyzer. Normalization was achieved by first subtracting the minimum value recorded for a particular variable from all other determinations of that variable – this creates a value of 0 for the sample with the lowest abundance of that component. Then all thusly adjusted measurements of that variable were divided by the largest value seen in the set of data, creating a maximum value of 1. R-mode identifies sets of variables which consistently covary, so must have similar sources or chemical behaviour during transport or diagenesis. Q-mode quantifies the similarities between samples, with each Q-factor representing a distinct end-member composition (i.e., a virtual sample with a particular composition distinct from other sets of samples).

3.6.1 R-mode Factor Analysis

Results of the R-mode factor analysis can be seen in Figure 3.14. The Four R-factors account for 95.1% of the total variance in the samples. R-factor 1 accounts for 32.5% of the total variance, and has strong loadings on Pb, Ni, and Zn with minor contributions from Cu, Th, U, V, and (negative loading on) Ca. R-factor 2 accounts for 34.9% of the total variance with Mg, Mn, Ca, and terrigenous TOC as the largest

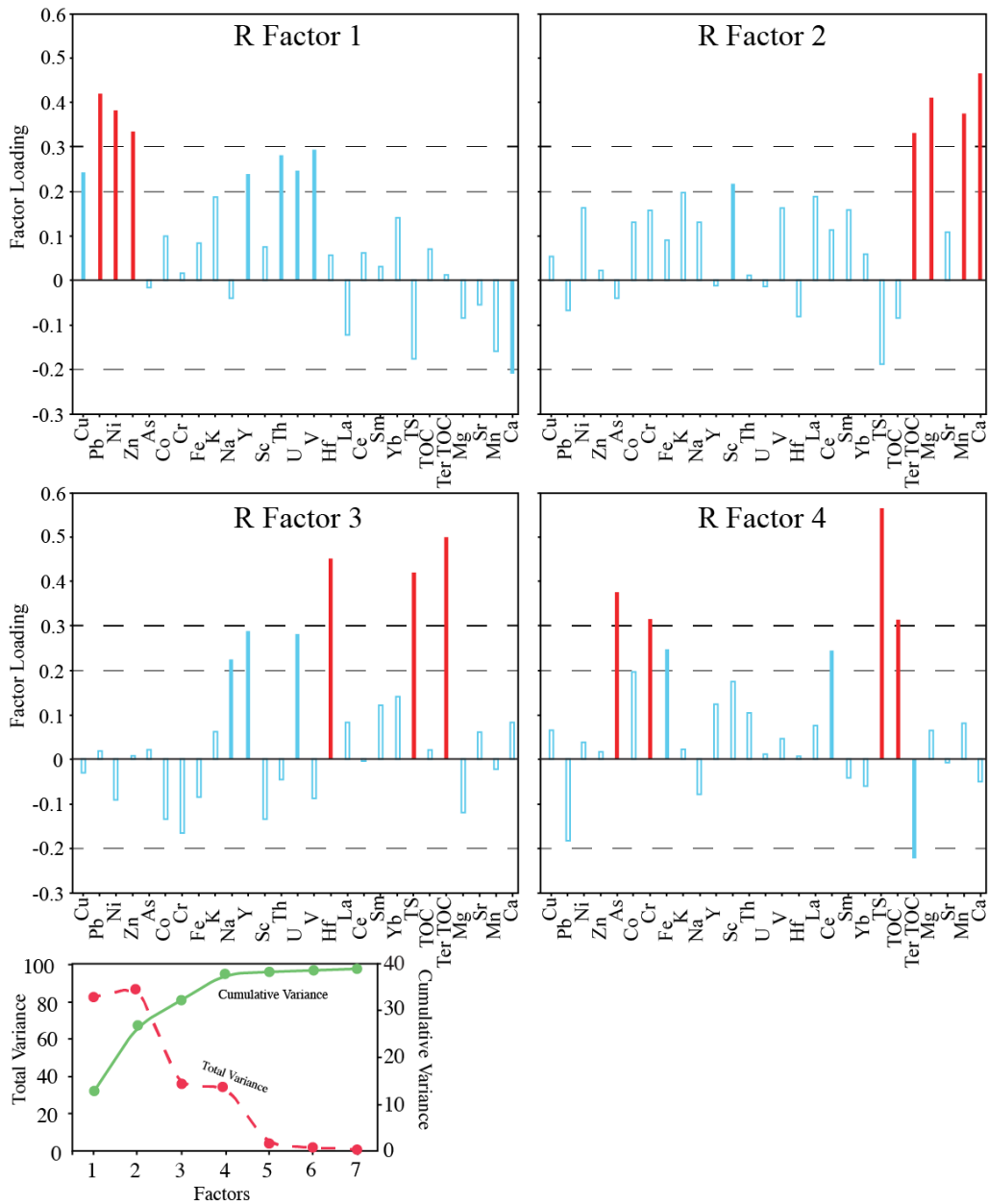


Figure 3.14 Plot of loadings of variables on R-factors 1–4. Loadings exceeding ± 0.3 (solid red) identify major controlling variables while loadings exceeding ± 0.2 (solid blue) are minor contributors to the factor. Blue outlines show the contributions of other variables. The final graph shows the variance accounted for by each factor (dashed, red line) and the cumulative variance of all the factors combined (solid, green line).

contributing variables, with smaller contributions from Sc, and K. R-factor 3 accounts for 13.4% of the total variance and its major component variables are terrigenous TOC, TS, and Hf. Minor contributions come from Na, Y, and U. R-factor 4 accounts for 14.3% of the total variance; major contributions to this factor are TS, As, Cr, and TOC. The minor contributing variables include terrigenous TOC (negative loading).

3.6.2 *Q-mode Factor Analysis*

The sample-by-sample values for the R-factors can be plotted against core depth, and where they define stratigraphic intervals with one dominant R-factor, a geochemically important Q-factor can be recognized. A Q-factor is dominant (Fig. 3.15) where stratigraphically contiguous samples show similar behaviour of their component variables (mostly elemental abundances). The end-member for each Q-factor can be thought of as a virtual sample having distinctive composition different to that shown by other Q-factors.

Q-factor 2 is dominant throughout Unit C1, from 940–610 cm depth, and identifies a region where the variables contributing to R-factor 2 (i.e., carbonate building blocks and terrigenous TOC) have their strongest convariation (Fig. 3.15). At 700 cm depth, Q-factor 2 begins a slow upward decline while Q-factors 1 and 3 increase. Q-factor 3 increases substantially at 590 cm and maintains its highest levels between 590–480 cm with a small decline from 530–510 cm that coincides with a small increase in Q-factor 2. Throughout Unit C, Q-factors 1 and 4 maintain relatively consistent values around 0.25 and 0.1, respectively. The upward decline of Q-factor 3 at 480 cm is consistent with the trends seen in the geochemistry and coincides with an upward increase of Q-factor 4.

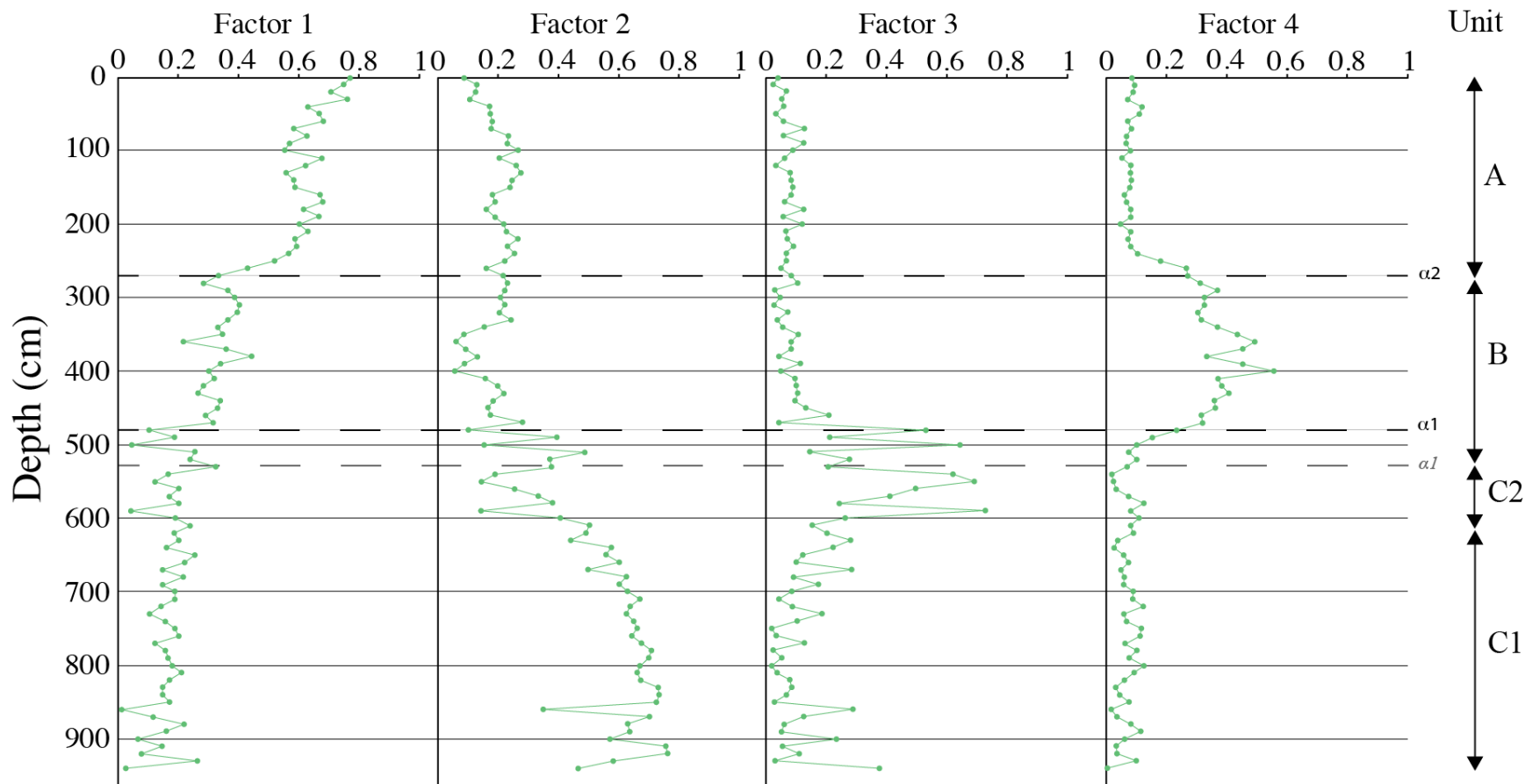


Figure 3.15 Q-factor plots (1–4) corresponding to R-factors (1–4) against depth. Note the new proposed location of the α_1 correlative conformity (at 480 cm), justified in §4.3.1

The lower portion of Unit B is dominated by Q-factor 4 which is controlled by TS, As, Cr, and TOC. Unit B acts as a transitional unit for Q-factors 1 and 2. An upward increase in Q-factor 4 becomes the dominant feature at 470 cm depth, and it reaches its peak at 400 cm, followed by a gradual decline to its Unit C levels by 240 cm (now into Unit A). However the dominance of Q-factor 4 is short-lived; by 340 cm Q-factor 1 has become the dominant factor (Fig. 3.15). Q-factor 2 has a sharp upward decline at the $\alpha 1$ correlative conformity (480 cm) and is no longer the dominant factor by 470 cm. By 400 cm it has become the third-most influential factor due to the rapid rise of Q-factor 4 and a gradual increase in the value of Q-factor 1.

Unit A is marked by an upward decline of Q-factor 4 at the $\alpha 2$ unconformity and the establishment of Q-factors 1 and 2 as the dominant factors. Q-factor 1 is the more dominant factor but shows a slight decline from 190–50 cm depth as Q-factor 2 increases. Q-factor 4 returns to its Unit C levels in Unit A, while the influence of Q-factor 3 is greatly reduced.

3.7 Geochemical Spikes at Unit Boundaries

Thus far, the results have focused on results from samples deemed typical of the three lithologic units, gauged by the fact that within each unit they have consistent relationships to other variables and generally do not vary strongly from one sample depth to the next. Spikes in elemental abundances at odds with this behaviour have been identified close to the levels of the $\alpha 1$ and $\alpha 2$ seismic markers, as correlated to core MAR02–45 by Hiscott et al. (2007b). Examples of the inconsistent behaviour of some elements at this level can be seen in cross-plots of strongly correlated elements in the

central parts of Units A (0–240 cm depths) and B (280–460 cm depths); the correlations would be more poor if results from sample depths of 250–270 cm and 470–490 cm were to be included. In many cases, samples from these restricted depths show dramatically different behaviour and plot well away from the regression line for other samples; i.e., they are outliers. The offending elements have prominent spikes in their abundance in these few samples.

Near the level of the α_2 unconformity, this anomalous behaviour was first seen in the downcore plots of Sc and Cr (Fig. 3.13). Figure 3.16 shows the calcite-free cross plots of some elements in Unit A which spike near the α_2 unconformity. Geochemical spikes in Cr and Sr slightly higher than the α_1 level were also noted in downcore plots (Fig. 3.13, Appendix 4). Figure 3.17 shows calcite-free cross plots of elements in Unit B that spike near the α_1 seismic marker. Because of these spikes, the analytical results from depths 250–270 cm and 470–490 cm were excluded from the correlation tables (Tables 3.12–3.14) to prevent correlations being skewed by a few inconsistent data points at sample depths found near unit boundaries. The occurrence of the geochemical spikes between 470–490 cm also prompted an upward adjustment of the correlation of the α_1 seismic marker from a depth of 525 cm in core MAR02–45 (Hiscott et al., 2007b) to a depth of 480 cm (see §4.3.1 for details).

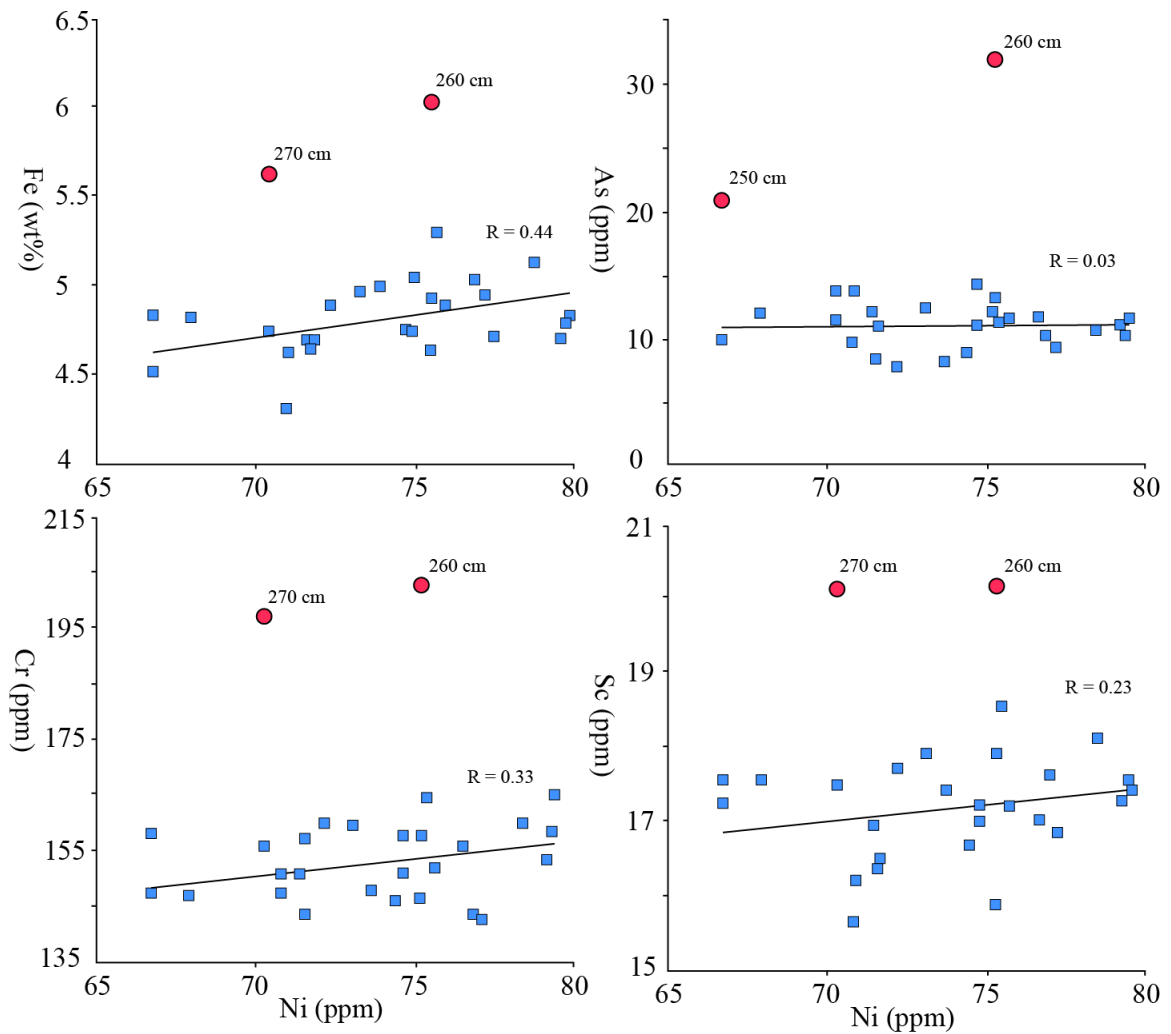


Figure 3.16 Calcite-free cross plots of some Unit A elements. Data for samples from depths of 0–240 cm are plotted as blue squares. Outliers (red circles), if they occur, are marked with their appropriate sample depth (250–270 cm). Data from this latter range of depths, if not anomalous, is plotted with blue squares like data from higher levels. Samples deeper than 240 cm behave differently than other samples higher in Unit A so have been excluded from the correlation table (Table 3.12) and the Venn-like diagrams (Figure 3.10) for Unit A.

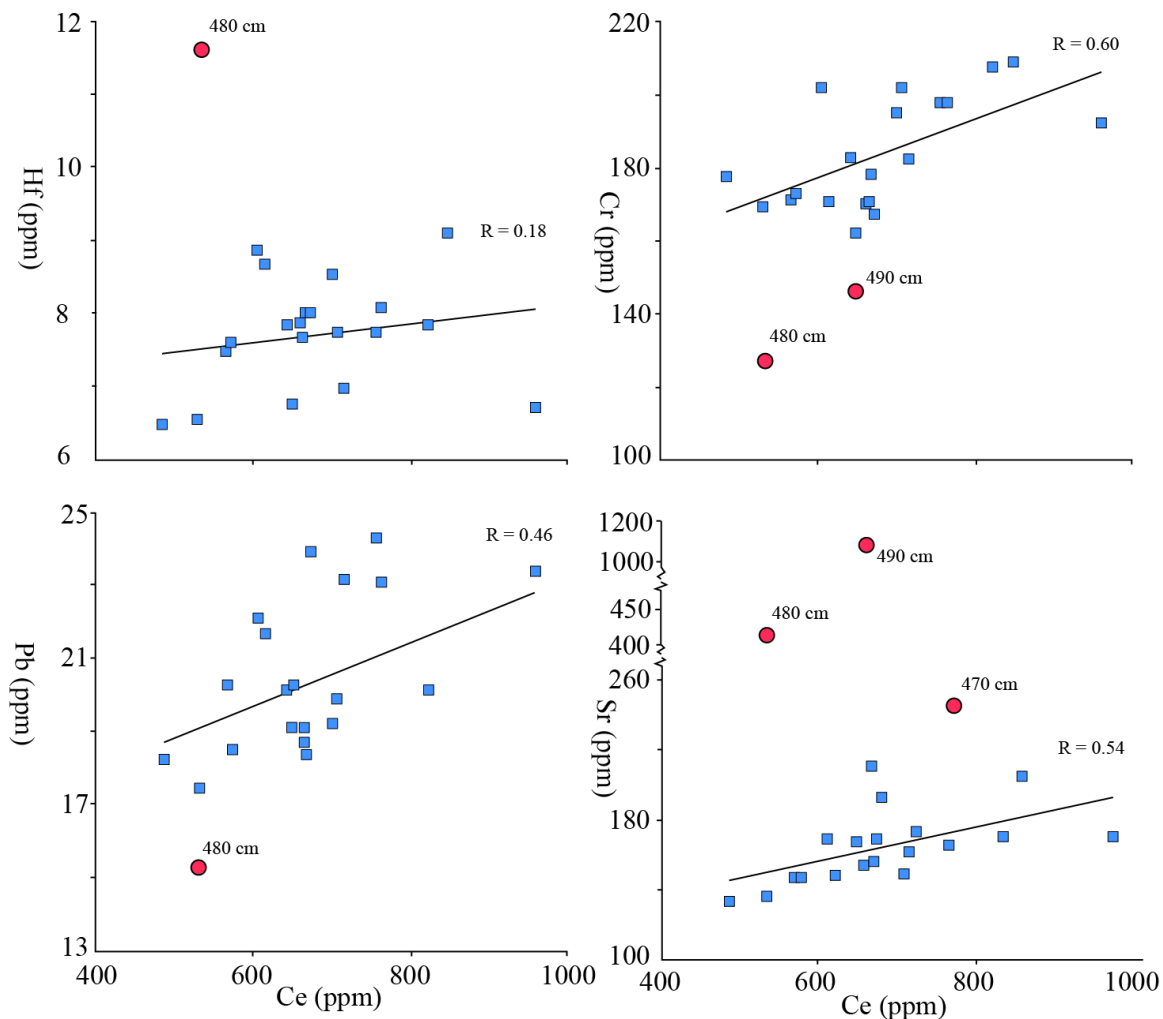


Figure 3.17 Calcite-free cross plots of some Unit B elements. Data for depths from 280–460 cm are plotted as blue squares. Outliers (red circles), if they occur, are marked with their appropriate sample depth (470–490 cm). Data from this latter range of depths, if not anomalous, is plotted with blue squares like data from higher levels. Samples deeper than 460 cm behave differently than other samples higher in Unit B, so are excluded from the correlation table (Table 3.13) and the Venn-like diagrams (Figure 3.10) for Unit B.

Chapter 4 Interpretation

4.1 Sediment Volume Estimate

There is a discrepancy between the amount of lower Holocene sediment (Unit C) located on the southwestern Black Sea shelf ($\sim 17 \text{ km}^3$) and the volume of sediment supplied by local sources as predicted by the BQART equation ($\sim 0.66 \text{ km}^3$, based on riverine supply for 5000 years). The volume of sand in the coastal beaches of Thrace does not contradict the low BQART prediction, as this sand need not have been derived mainly from Holocene river input; other reasonable sources for the sand include the erosion of coastal bluffs and the reworking and redeposition of shelf sediments during the Holocene transgression.

There are multiple ways to attempt to reconcile the discrepancy between the Unit C volume (seismic unit 1B) and local river supply. The simplest approach would be to increase the timespan for the input from local sources; however, with all BQART parameters fixed, it would take $\sim 250,000$ years for local sources to supply 17 km^3 of sediment. Obviously this scenario is unrealistic, as basin parameters would have changed over that time (e.g., glacial-interglacial cycles), promoting removal to deeper water areas of most of the sediment as a consequence of erosion during lowstands and transgressive phases.

A more plausible scenario involves contribution to Unit C from more distant sources. The Kamchiya River (Bulgaria) and the Danube River (Romania) are both significant sources of sediment that enter the Black Sea to the west and north of core site MAR02–45, in the upcurrent direction relative to the modern Black Sea circulation.

Distances from their deltas to the core site are ~130 and ~380 km, respectively. During the early Holocene, flooding of the shelf caused the Danube River to cease direct supply to its deep-sea fan (Lericolais et al., 2012), instead building delta lobes from which sediments could be transported along the shelf by currents like the modern Rim Current, contributing to accumulation on the southwestern Black Sea shelf. Sediment discharge rates for the Kamchiya River indicate a possible contribution to the shelf setting of ~7.1 km³ over a period of 5000 years, a portion of which might have moved farther southeastward along the shelf. There are other smaller rivers along the Bulgarian and Romanian coastline that might have added some of their sediment load to the counterclockwise-flowing Rim Current system leading to the SW shelf (e.g., drainage into the Varna and Veleka estuaries and their adjacent shelf areas). In the vicinity of Cape Emine just downdrift of the Kamchiya Delta, the Holocene shelf succession reaches thicknesses of ~50 m (Dimitrov et al., 1998, as reported in Filipova-Marinova et al., 2004). A significant contribution from river systems in general is supported by the considerable amount of coarse plant debris, pollen and fern spores in palynology samples from Unit C in core MAR02–45 (P. Mudie, pers. comm., 2012).

Along-shelf advection of sediment from major river deltas like the Danube is able to provide significant material over distances comparable to those noted above. For example, the Chenier plain of southwestern Louisiana is a ~5000 km² Holocene mud deposit, punctuated by sandy beach ridges, located up to 200 km west of the Mississippi Delta (McBride et al., 2007). This coastal succession receives the bulk of its sediment by westward advection in along-shelf currents from the mouth of the Mississippi River. Times of increased deposition on the Chenier plain occur when the Mississippi Delta has

undergone avulsion to the west (McBride et al., 2007). Liu et al. (2009) document even greater distances of along-shelf transport of significant quantities of mud from Asian deltas, up to 600–800 km from the river mouths. By similar processes, large amounts of Danube, and Kamchiya sediments might have been transported to the southwestern Black Sea shelf. The modern Rim Current facilitates the transport of sediments from more northern sources. If this current (or a similar earlier current) was established during the early Holocene it would provide a mechanism for transporting sediment from the Danube Delta to the southwestern Black Sea shelf.

A third possible source for some portion of the 17 km³ in Unit C is reworking of Pleistocene shelf deposits that were subaerially exposed on the coastal plain (now the modern shelf) during the early Holocene transgression. There are sparse, long spined (indicative of relatively high salinity) specimens of the dinoflagellate *Lingulodinium machaerophorum* toward the base of core MAR02–45 in Subunit C1 (P. Mudie, pers. comm. 2013). The last time the Black Sea had a salinity similar to today, in order to account for this long spine length, was in the period 126.5–121 cal ka BP (Shumilovskikh et al., 2013). There are also tentatively identified and rare specimens of the dinoflagellate genera *Multiplicisphaeridium* and *Romanodinium* in Subunit C1, the former being common in local Miocene successions, and the latter in Pliocene deposits of Romania (P. Mudie, pers. comm. 2013). These occurrences might indicate derivation of a small portion of the lowest Holocene succession by erosion of local unconsolidated or weakly consolidated deposits during the Holocene transgression, but P. Mudie (pers. comm. 2013) cautions that some of these cysts might instead have been introduced by meltwater

pulses from the Caspian Sea, where long-spined *L. machaerophorum* and other exotic genera are known from Pleistocene deposits.

Upper Pliocene – Quaternary strata below the Holocene transgressive unconformity, α , are restricted to the modern outermost shelf (Aksu et al., 2002). If there were more landward correlative deposits before the latest transgression, then they must have been stripped from the shelf by shoreface erosion (at a developing ravinement surface) to account for the apparent absence of deposits of this age beneath the middle and inner shelf. For such effective erosion to have occurred, the wave climate would need to have been energetic (like today), implying considerable fetch and therefore an open coastline rather than a restricted, enclosed embayment or isolated shelf lagoon (i.e., liman). With conditions similar to those in existence today, the finer size fractions eroded from the inner shelf in water depths (at that time) of only a few tens of metres likely would have been advected offshore, perhaps beyond the shelf edge.

To summarize, pre-Holocene dinoflagellate cysts are present in Subunit C1 but in very small numbers, suggesting some contribution from erosion of pre-existing shelf deposits during the early Holocene transgression. Holocene cysts are far more abundant and provide the basis for an internally consistent interpretation of paleo-salinity variations (Mertens et al., 2012). The interpretation favoured here is that the mud fractions present in seismic units 1B–1D (core units C–A) entered the Black Sea from terrestrial sources either during the time of the earliest Holocene transgression, or somewhat earlier following the Last Glacial Maximum. This influx could not have been supplied by local small rivers, so must have come from elsewhere along the Black Sea coast where large rivers enter the basin.

4.2 Texture and Mineralogy

The sediments deposited at MAR02–45 are fine grained (averaging more than 95% <63 μm particles in Units C and A). The dearth of sand might be explained by the relatively rapid transgression during the early Holocene, so that the MAR02–45 site has been in >50 m of water for almost all of the Holocene. Paradoxically, there is very little clay-sized material. This is consistent with the grain-size reported from core MAR05–50 which penetrated these same units 40 km to the east (Hiscott et al., 2007b). Full grain-size analysis of samples from core MAR02–45 was not undertaken for this thesis, so unpublished representative full analyses provided by R. Hiscott for core MAR05–50 (methods in Flood et al., 2009) are used to support this part of the interpretation (Fig. 4.1). The essential observation is that the <63 μm fraction of Unit C at site MAR05–50 is dominated by silt with mean size of $\sim 15 \mu\text{m}$. This is unlike typical marine muds which contain moderate amounts of clay (Weaver, 1990). The texture is similar, however, to that of loess deposits (e.g., Varga, 2011, Fig. 4.1), which are widespread in the Danube drainage basin (Fitzsimmons et al., 2012).

The sediments in core MAR05–50 are finer grained than the Hungarian loess. Below the $\alpha 1$ unconformity in core MAR05–50 (below 645 cm) there is a pronounced asymmetry of the particle size distribution indicating the presence of a secondary mode centred on $\sim 50 \mu\text{m}$, so $\sim 20 \mu\text{m}$ coarser than the mean particle size of the Hungarian loess. Loess deposits have a wide range of mean grain size (Fitzsimmons et al., 2012), but their essential characteristic is a predominance of silt that reflects an aeolian origin. The loess deposits in the Danube drainage basin can have thicknesses >5 m, and are deeply

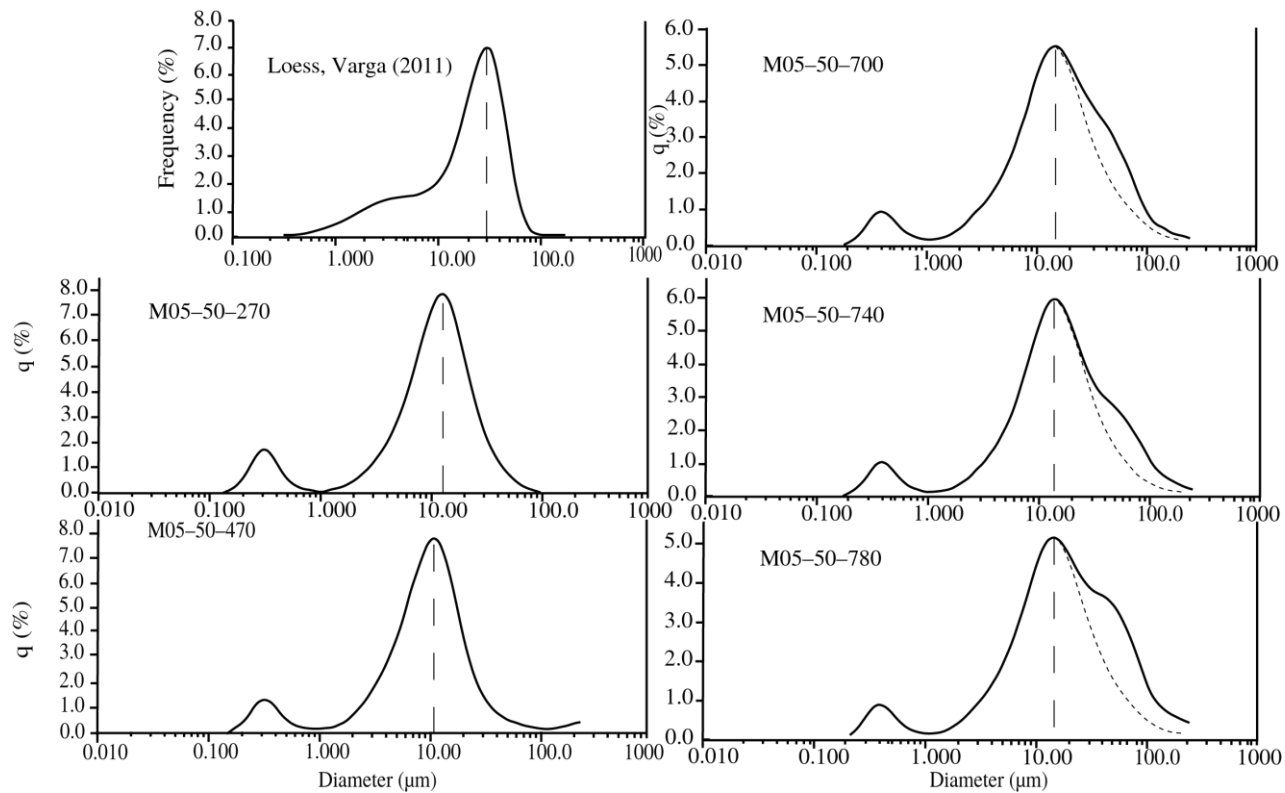


Figure 4.1 Comparison of grain size distribution of Hungarian loess (Varga, 2011) to particle size distribution found in Unit C correlative deposits of core MAR05-50, located to the southeast of MAR02-45. Dashed lines with short segments under curves represent log-normal components which overlap to form the final distributions. Vertical dashed lines indicate the mean particle size of the dominant sub-population.

dissected by tributaries to the Danube, and by northern tributaries to the Kamchiya River (Fitzsimmons et al., 2012). The loess has an age <1,000 ka with substantial loess accumulation occurring during the Last Glacial Maximum (LGM) and Younger Dryas (Fitzsimmons et al., 2012). Dissection has occurred since the LGM, feeding large quantities of sediment with the textural characteristics of loess into the Danube system, and onward to its delta on the Black Sea coast. The close textural similarity of the MAR05–50 muds to loess, the position of the MAR05–50 site downcurrent from the MAR02–45 site, and the presence of the same stratigraphic units at the two sites, are consistent with the hypothesis offered here that the primary source for significant amounts of the Unit C sediment might be reworked loess. The secondary mode found in MAR05–50 samples could be from coarser loess deposits, or from offshore transport by storm events, consistent with the origin proposed by Hiscott et al. (2007b) for the sand/silt beds of Unit C1 in core MAR02–45.

The streambed samples from local rivers in Thrace are considerably coarser than the offshore muds, so it is not possible to assess the potential for these rivers to have delivered a silt-dominant, clay-poor mud fraction. The presence of mollusk shells at site MAR02–45 (Hiscott et al., 2007b) and mollusks and ostracods in equivalent units at site MAR08–50 (Williams, 2012) proves that even the oldest muds recovered in core MAR02–45 (10.3 cal ka BP, Unit C) are marine to lacustrine in nature. Any loess-like material must, therefore, have experienced some transport by marine currents.

4.2.1 *Silt Mineralogy*

Silt (2–63 μm) is the dominant size fraction in core MAR02–45. XRD analysis shows a clear decrease in calcite through Unit C upward to Unit A (Figure 3.3). When mineral abundance is recalculated to exclude calcite (Figure 3.4), there is a clear upwards increase in K-mica coupled with a small increase in Na-plagioclase and a decrease in quartz beginning at the contact between Units A and B. Bayhan et al. (2005) interpreted that quartz and feldspar in their cores from the SW Black Sea shelf are primarily related to metamorphic sources and that 1-nm micas are magmatic in origin. If this is true then data from this thesis may suggest a shift in the source of detritus around the $\alpha 1$ correlative conformity (8.1 cal ka BP). The ~6% decrease in quartz and the increase in K-mica content (~5%) upwards through the core is a clear trend (Table 3.1). However the standard deviations for these components overlap throughout the cored succession, making a conclusive statement about changing provenance all but impossible using K-micas and quartz as indicators.

Comparison of the silt mineralogy of MAR02–45 to that of potential source areas is inconclusive. Thracian river samples were taken at sandy locations, downstream from dammed reservoirs, explaining the elevated quartz contents (64.7%) when compared to samples from core MAR02–45. The presence of dolomite differentiates the Danube Delta from northern Turkish sources (as recorded in detritus from the Bosphorus outflow; Table 3.2); however, the absence of detectable silt-sized dolomite in core MAR02–45 does not rule out the Danube River as a source because amounts <5% have peak

intensities too low for quantification. With all other major silt-sized minerals existing in relatively equal amounts from one potential source to the next, it is not possible to advocate that one source is more strongly represented than the others in the MAR02–45 samples.

4.2.2 *Clay Mineralogy*

The more clay-rich samples (>20% clay) in Units B and C (430, 620, 700, 770 and 890 cm depth) are coupled with a decrease in the abundance of non-clay minerals in the <2 μm size fractions. At 430 cm depth (Unit B) there is an upward increase in smectite, chlorite and kaolinite relative to its unit average and a decrease in quartz, calcite and dolomite abundance (Fig. 3.6). Of the two more clay-rich horizons analyzed from Unit C (770 and 890 cm depth) only the 890 cm sample shows significant variations in mineral abundances relative to the unit average. Smectite is 2.5x more abundant at 890 cm and this increase comes at the expense of the non-clay minerals (quartz, calcite and dolomite; Fig. 3.6). The increase in smectite and chlorite content implicates igneous and metamorphic sources for these muds; Thracian rivers have been identified by other workers as likely sources for smectite based on the composition of the bedrock (Major, 2002; Bayhan et al., 2005) so the more smectite-rich samples (430 and 890 cm depth) might indicate periods of increased contribution from the Thracian hinterland.

A pronounced trend in the clay-sized fraction is the increase in abundance of illite upwards through the core. Each unit shows an ~10% increase in illite abundance compared to the underlying unit (Table 3.5). As a caution, this pattern is not evident when clay minerals are recalculated to 100% using the Biscaye (1965) scaling factors.

The increase in illite abundance might indicate an increase in the importance of the Danube River as a sediment source throughout the Holocene (see below). As modern current pathways were established (e.g., the Rim Current), the Danube River would be expected to exert more influence on the mineralogy of clay-sized materials in the study area.

A comparison of potential source areas shows a dominance of smectite near the Bosphorus exit (Figure 3.8). This is expected, as outcrops near the northern mouth of the Bosphorus include mafic volcanics. Danube source material contains ~45% illite (~10% higher than the core average) and contains detrital calcite and dolomite. The Kuzan River sample (Thrace) was at first surprising due to its low smectite content and high carbonate content. However, this sample was taken in an area near Miocene sedimentary rocks, and might reflect their composition, as opposed to the Paleozoic igneous formations found along the Thracian coast (Fig. 1.5). The damming of the small rivers in this area makes it very difficult to obtain representative samples of fine-grained detritus, which now does not reach the coast.

Before undertaking the mineralogical studies, it was hypothesized that more extensive alpine glaciation in the headwaters of the Danube River might supply greater amounts of clay-sized quartz (as "rock flour") than sources that were not glaciated. The Danube samples indeed contain ~14% clay-sized quartz, but the single sample from the Kuzan River (Thrace) contains 22% clay-sized quartz. Without considerably more study of the clay fractions produced by weathering in northern Thrace, the significance of this quartz cannot be determined.

There are no clear distinguishing variations between the clay mineralogy of

material from potential source areas and samples from core MAR02–45. Even within the cored succession, the only case for which unit averages and their standard deviations do not overlap is the upcore increase in illite abundance previously discussed. Hay (1987) used illite/smectite ratios to distinguish sources areas. He noted a Danube ratio of ~5 and that Anatolian ratios are ~1 or less. Figure 3.8 shows an illite/smectite ratio of 0.73 for the Bosphorus samples. The illite/smectite ratio for Danube samples analyzed for this thesis is 1.83 and is 12.15 for the one Thracian sample. The average ratio for MAR02–45 is 2.85, and for Unit C is 2.46. These ratios are interpreted to rule out Anatolia as a source, however they cannot distinguish between Thrace and the Danube Delta. Although a single source cannot be identified with the data available, neither is there evidence for a change in provenance from ~10.3 cal ka BP to the present.

There is one caveat regarding all aspects of the clay mineral work. At site MAR05–50, Flood et al. (2009) found that a small, isolated mode forms the clay fraction (Fig. 4.1). They could not explain the absence of material in the range 0.9–2 μm , and speculated that the clay mode might actually be a bio-diagenetic product created by mineral transformations in the guts of burrowing organisms (cf., Needham et al., 2005). Without biological experiments in the thesis area or laboratory investigations using Black Sea sediment, it is not possible to comment further. However, it should be clear that an origin of the clay minerals by this type of biological activity would compromise all interpretations regarding source areas for what are considered to be primary detrital clay-sized components.

4.3 Geochemistry

Much of the geochemical interpretation of the Holocene succession is provisional because the effects of early diagenetic sulphate reduction/oxidation can not be systematically evaluated with available data. The mobility and fixation of metals can be influenced by these early diagenetic reactions, so that some of the assessments made in the thesis about primary compositional trends might require additional confirmation by pore-water studies to ensure that there is not a diagenetic overprint.

The matrix of correlation coefficients for the entire core (Table 3.11), and the associated Venn-style diagram showing relationships between variables (Fig. 3.10) portray a very complicated set of elemental associations. However, the relationships on a unit-by-unit basis (Fig. 3.10, Units A, B, C) are considerably simpler, and it is at this level that basic interpretations can be made. In reality, there are four distinct regions of the core with somewhat different associations between chemical elements: the central parts of Unit A (0-240 cm), Unit B (280-450 cm), Unit C (500-940 cm), and the cross-overs between the lithologic units just above the α_1 and α_2 levels where spikes occur in the abundances of several elements (460–490 cm and 250–270 cm, respectively, and highlighted in Appendix 3). Factor analysis has picked out the unit-by-unit variability as seen in the Q-mode downcore plot of factor scores (Fig. 3.15).

Elements which spike just above the α_2 level are K (a negative spike), As and Rb; the latter not considered except in this overview of elemental spikes because of a low level of overall precision (Table 3.6). Mn has higher than normal values just below the α_2 level (280 and 290 cm samples). Elements that display spikes above the α_1 level are

Br, Mn, Sr. These anomalous values are ascribed to enhanced absorption at the seafloor during a time of non-deposition (α_2 unconformity) and likely reduced accumulation (α_1 surface, here conformable but equivalent to the α_1 unconformity that is widespread on the shelf; Aksu et al., 2002). A key conclusion is that some fraction of these elements must have entered the sediment from the water column, or have been mobile during early diagenesis, rather than being entirely detrital in origin (i.e., bound in the lattices of detrital minerals). This might explain why Mn has no strong correlations with other elements above Unit 3.

Within each unit, strongly cross-correlated elements can serve as proxies for one another. There are two central issues to consider and explain when evaluating the unit-by-unit geochemistry: which elements are particularly abundant and why; how can the elemental associations inform us as to the detrital versus diagenetic origin of the observed trends in abundance? Sc and Fe are correlated at the $R \geq 0.80$ level in all units.

According to Das et al. (1971), Sc and Fe in fine grained sediments correlate with one another (and with Al) because they are present in clay minerals and other phyllosilicates. Co, Ce, La, Th and Y are generally found in detrital aluminosilicates (Dean and Arthur, 2011). In the MAR02–45 samples, Unit B in particular shows a strong association of four of these five elements with Sc and Fe (Fig. 3.10). R-factor 2 has a moderate loading on Sc and a strong loading on terrestrial TOC, all consistent with a detrital origin. R-factor 2 also carries the signature of carbonate minerals, and is particularly important in lithologic Unit C (Fig. 3.15). The following initial conclusions result:

1. Sc, Fe, Co, Ce, La, Th and Y are considered to have a detrital origin. Ce is included in this list because for the entire core it is closely correlated with Sc, Th and Fe. Sm is closely tied to La in Units A and C, so is believed to have a detrital origin.
2. Through a strong linkage to the terrestrial component of the TOC, carbonate minerals in Unit C also might have a predominantly detrital origin, leading to high scores for factor 2 in that unit. Caution is required, however, because it might be coincidence that carbonate abundance and a predominance of terrestrial TOC are characteristic of Unit C.

V, Ni, Zn and Cu tend to be concentrated in organic-rich Black Sea sediments, either because of biogenic fixation or adsorption under reducing conditions in the sediment (i.e., earliest diagenesis, Dean and Arthur, 2011). However, Dean and Arthur (2011) find that in some circumstances V and Ni can be tied to the detrital supply. Unit B in particular shows a strong cross-correlation of these elements, and K. In Unit C, V, Ni and Zn are correlated with one another, but also with Sc, Fe and K. R-factor 1 has strong to moderate loadings on Cu, Pb, Ni, Zn, Th, U, V. U is well known to accumulate under reducing conditions. The partial mingling of elements which are commonly found in detrital components (i.e., Sc, Fe, K, Th) with those known to accumulate from pore water and on organic components is interpreted to indicate adsorption onto fine-grained phyllosilicates during early diagenesis. Factor 1 (as Q-factor 1 in Fig. 3.10) is most important in Unit 1, presumably because sulphate reduction was particularly active during the deposition of that unit (Hiscott et al., 2007b), promoting the incorporation of several metals. Several of these elements (Cu, Pb, Ni, Zn, V) are in higher abundance in Unit 1 than at deeper stratigraphic levels (Fig. 3.13 and Appendix 6 plots). The most

important conclusion from this paragraph is that V, Ni, Zn, Cu and probably Pb cannot be used to track changes in the nature of detrital supply (i.e., provenance). Instead, they are viewed as elements incorporated from seawater and pore water during early diagenesis.

A prominent trend in subunit C1 is elevated Cr concentrations between 800 and 700 cm depth (~9.4 cal ka BP) that act independently of other elements. Cr has been previously attributed to the weathering of mafic or ultramafic source rocks (Kıratlı and Ergin, 1996). In the primary core descriptions of MAR02–45, these depths are associated with sandy horizons. The samples were taken to avoid the sandy layers, but it is possible that bioturbation has introduced Cr into the muds above and below sand horizons (Fig. 4.2). These sandy horizons have been previously interpreted as turbidites or tempestites sourced from Thracian rivers. Such event-beds may have a muddy top that was also emplaced by the energetic flow that carried the sand onto the shelf, although core descriptions did not identify two types of mud that might have different origins.

When comparing geochemical trends in MAR02–45 to potential source areas some major issues must be addressed. Samples from the Danube Delta and Thracian rivers are grab samples. This type of sample is prone to contamination from industrial pollution and agricultural runoff. Cu, Ni, Zn, and As values have been shown to be influenced by anthropogenic input (Dinescu and Duluiu, 2001; Oreščanin et al. 2005). Hence, only Fe, Co, Mg, Mn and Cr are considered to be reliable source indicators.

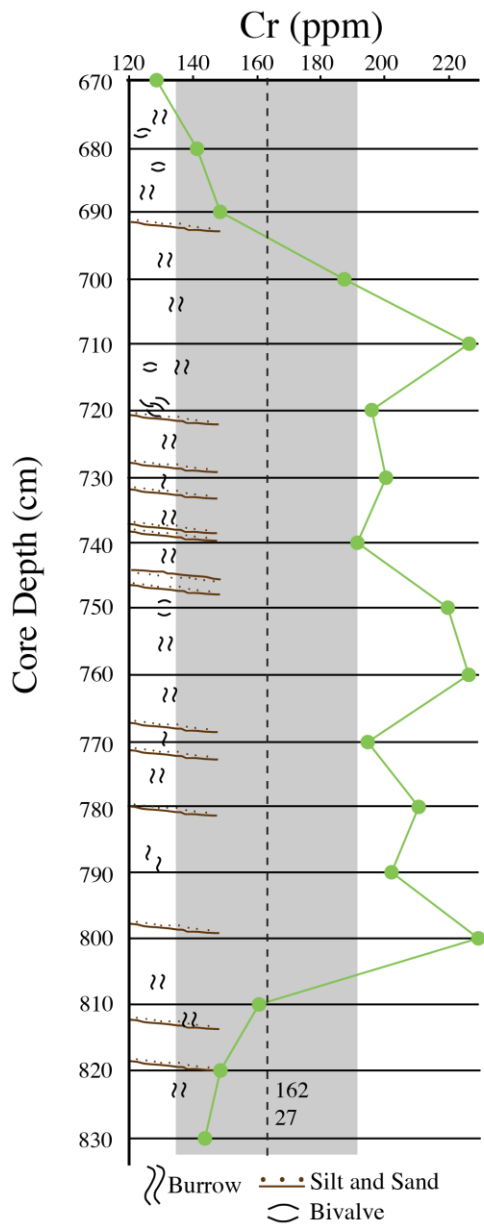


Figure 4.2 Elevated chromium values seen in geochemical data compared to lithologic description of MAR02–45 between 700 and 800 cm depth. 162 and 27 refer to the core average and standard deviation of Cr concentration in ppm. The shaded area represents \pm one standard deviation from the core average.

Even when comparing potential source areas (Table 3.17) to averages for each unit in core MAR02–45 (Table 3.16), finding diagnostic criteria for sediment provenance is a challenge. Cu, Pb, As, Hf, K, Na, Co, Mn, Sr, Th, U, Y, La, Ce, Sm, and Yb are found in similar concentrations in all potential source areas and overlap with unit averages in core MAR02–45. Fe concentrations in Unit B and C are similar to concentrations in the Bosphorus and Danube Delta samples. Mg and Cr values in Unit A and B are similar to those found in the Danube Delta samples.

The upwards increase in metal content through MAR02–45 could be related to pollutants for the uppermost tens of centimeters, and/or to an increasingly reducing environment. Based on these trends it would seem that both the Danube River and local Thracian rivers have been supplying detritus to the southwestern Black Sea shelf since the start of deposition of Unit C (~10.3 cal ka BP). However, due to the potential for contamination, and the lack of easily interpretable trends, this hypothesis is unconvincing. It does not seem possible, with the chemical data, to conclusively track the source of Fe, Co, Cu, Sr, Ni, Mg, and Pb. The exception is perhaps Cr, because of its expected derivation from mafic and ultramafic rocks. Samples characterizing northwestern Anatolia (taken at the northern exit of Bosphorus Strait) contain the highest levels of Ni and Cr, but the modern (and likely Holocene) shelf currents travel from west to east, so would not be able to move detritus westward toward the MAR02–45 site. Instead, the information from core MAR08–17 is helpful only as an indicator of the possible composition of detritus derived from similar mafic bedrock in Thrace.

A calcite-free comparison of elements analysed from Hungarian (Újvári et al., 2008), and Moravian (Czech Republic) loess (Adamova et al., 2002) to thesis results for

Unit C1 in core MAR02–45 is presented in Table 4.1. Of the 34 total elements compared (15 by Újvári et al., 2008; 19 by Adamova et al., 2002), only one (Y) has calcite-free concentrations that statistically overlap with that MAR02–45 concentrations, using a significance level (P-value) of 0.05, after student t-test analysis (95% confidence interval, 2-tailed test, assuming unequal variances). The sediments in MAR02–45 may share some textural characteristics with loess but there are distinct and statistically significant chemical differences with both the Hungarian and Czech loess. Of course loess in the Danube drainage basin is not expected to be homogeneous because it is derived from a wide range of source rocks and regions of northwestern Eurasia. Further study of those deposits would be required to rule out a compositional link between the shelf muds in the southwestern Black Sea and portions of the loess blanket of eastern Europe.

4.3.1 Refinement in the Placement of the $\alpha 1$ Correlative Conformity

Based on geochemical signatures, and Q-factor analysis presented in this thesis, the conformable surface equivalent to the $\alpha 1$ unconformity is likely ~45 cm higher in core MAR02–45 than proposed by Hiscott et al. (2007b). Q-factors 1, 2, and 3 exhibit erratic behaviour starting in subunit C2 (Fig. 3.15). This behaviour continues from ~600 cm depth upward until 480 cm. At this depth, Q-factor 4 becomes the factor with the highest scores (now into Unit B). Supporting the adjustment of the $\alpha 1$ position are the behaviour of Cr, Hf, Mn, and Sr (Fig 3.16, Appendix 4). These elements all have a spike in concentration between 480–500 cm depth. These geochemical anomalies likely developed during times of decreased deposition when sediment at the seabed would have

experienced an extended time of interaction with bottom waters. Although the α_1 level is conformable at the core site, elsewhere on the shelf a depositional hiatus is recorded.

Table 4.1 P-values for the student t-test (TTest function in Microsoft Excel) using calcite-free normalized data from Unit C1 of core MAR02–45, compared with calcite-free Hungarian loess chemistry from Újvári et al. (2008) and Moravian (Czech) loess chemistry from Adamova et al. (2002). The null hypothesis is that the means of randomly selected sets of samples from each population are equal, and when this is false the P-value will be less than a pre-determined significance level of, say, 0.05 (95% level) or 0.01 (99% level). P-values less than 0.01 indicate that the mean values are probably not from the same population; p-values >0.05 (**bold**) indicate that the concentrations are indistinguishable using a 95% confidence interval.

	P-Values	
	Hungarian	Czech
Fe	3.16 x10 ⁻²⁸	4.77 x10 ⁻¹⁹
Mn	6.54 x10 ⁻¹⁷	8.33 x10 ⁻¹¹
Mg	1.51 x10 ⁻³⁴	3.17 x10 ⁻³¹
Na	3.98 x10 ⁻⁹	1.13 x10 ⁻¹⁶
K	8.58 x10 ⁻¹⁴	6.79 x10 ⁻¹⁵
Pb	4.13 x10 ⁻¹⁵	2.43 x10 ⁻⁰⁷
La	1.78 x10 ⁻¹²	3.81 x10 ⁻¹¹
Ce	2.44 x10 ⁻¹³	2.46 x10 ⁻⁰⁹
Y	2.53 x10 ⁻⁵	0.10
V	1.06 x10 ⁻¹⁸	1.80 x10 ⁻¹⁶
Cr	1.10 x10 ⁻³²	3.85 x10 ⁻¹⁹
Ni	1.17 x10 ⁻²⁷	5.14 x10 ⁻²⁶
Cu	4.37 x10 ⁻³²	4.50 x10 ⁻¹⁹
Zn	4.49 x10 ⁻¹⁹	2.05 x10 ⁻¹³
Sr	5.47 x10 ⁻¹⁷	5.70 x10 ⁻¹⁸
Sm		1.26 x10 ⁻¹⁰
Yb		1.06 x10 ⁻⁰⁹
Y		3.74 x10 ⁻⁰⁴
Co		2.87 x10 ⁻¹³

The placement of the $\alpha 1$ unconformity in MAR02–45 by Hiscott et al. (2007b) was not based on an obvious facies break or discontinuity in radiocarbon dates, so has to be considered approximate and no more precise than the vertical resolution of the seismic profile over the site, which is ~30 cm (Huntec DTS technology). With a suspicion that the $\alpha 1$ level might be higher than reported by Hiscott et al. (2007b), the seismic profile was re-evaluated. The re-measured depths to the $\alpha 2$ unconformity and the $\alpha 1$ level are 270 cm and 490 cm, respectively. The latter measurement is consistent with figure 6 of Hiscott et al. (2007b). The position of the $\alpha 1$ unconformity in Hiscott et al. (2007b) was lowered ~45 cm by those authors based on changes in $\delta^{34}\text{S}$ and $\delta^{13}\text{C}$ trends.

Lithologic subunit C2 was defined by Hiscott et al. (2007b), so its upper limit is not moved in this thesis, but consideration should be given to moving the boundary between Unit C and Unit B upward to the new inferred $\alpha 1$ level. The closest ^{14}C dates to this level (~8.1 cal ka BP, 6.3 cal ka BP) are ~35 cm below and ~70 cm above the 480 cm depth in the composite core. Assuming a constant rate of sedimentation through this period, the upwardly adjusted correlative surface to the $\alpha 1$ unconformity has an age of ~7.5 cal ka BP.

Chapter 5 Discussion

The primary aim of this research is to assess whether the provenance of the fine fractions (silt and clay) of the Holocene sediments on the southwestern Black Sea shelf might have changed since the earliest Holocene. Hiscott et al. (2007b) have claimed that the middle part of the southwestern shelf was fully open and connected to the deep Black Sea basin, and hence regional sediment sources, since ~10.3 cal ka BP (calibration from Mertens et al., 2012), whereas Ryan et al. (2003) and Lericolais et al. (2007) maintain that the central Black Sea had a level below the modern shelf edge until ~9.15 cal ka BP (calibration from Mertens et al., 2012) so that Holocene mud deposits on the southwestern shelf older than ~9.15 cal ka BP would have had to accumulate in perched ponds or lagoons ('liman' in local terminology). In an isolated liman, sediment can only be derived from local sources, including rivers entering the liman and coastal erosion along its shores (although wave fetch and height would be small). If the lower Holocene sediment (seismic unit 1B, corresponding to lithologic subunit C1) at MAR02–45 was deposited in an isolated liman, do the geochemical, mineralogical, and sediment volume estimates support this hypothesis?

Geochemical analysis was performed on samples of sediment from core MAR02–45, and on samples from potential source areas. Published articles were examined to augment the data for potential source areas. If geochemical signatures of specific source areas could be distinguished in the MAR02–45 samples, it would be possible to establish changes in provenance. For example, if the geochemical signature and/or mineralogy of Thracian river deposits happened to be similar to that of Unit C, and if other potential

sources were not, this would support the Ryan et al. (2003) and Lericolais et al. (2007) argument that the lower Holocene succession penetrated by core MAR02–45 was deposited in an isolated liman. Also if the estimated volume of sediment in Unit C were to be similar to the calculated volume of sediment delivered by local rivers over a reasonable interval of time, this would be consistent with deposition in an isolated lagoon, or liman.

In subsequent sections, the evidence from sediment geochemistry, mineralogy and discharge estimates is used to evaluate the likelihood that lithologic Unit C was deposited in a perched, isolated liman, disconnected from the open Black Sea basin. Where possible, specific sources are proposed for particular sedimentary components.

5.1 Unit C (10.3–7.5 cal ka BP)

The geochemical data presented in Chapters 3 and 4 defines four distinct geochemical units within MAR02–45, consistent with the findings of Hiscott et al. (2007b). The four geochemical units are revealed by Q-mode factors 1–4. Excursions in the vertical trends of several metals (Br, Mn, Sr; Fig. 3.13, Appendix 4) have led to a refinement in the placement of the seismically-defined α_1 correlative conformity from 525 cm depth (Hiscott et al., 2007b) to 480 cm depth. This revised placement is not only a better fit to the geochemical trends, but conforms better to the seismic profile at the core site (Hiscott et al., 2007b, their figure 6).

Subunit C1 corresponds to the earliest recovered portion of Holocene shelf sediments. There is abundant calcite and evidence from sandy event beds and Cr content for some contribution from local sources. The calcite might be attributed to bio-

precipitation, as suggested by Bayhan et al. (2005), some amount might be authigenic (Major et al., 2002) or it could be detrital (consistent with the abundance of terrigenous TOC deep in the core). If the latter, then the fine particle size might indicate a pedogenic source in the soil profiles of river drainage basins. The very low salinity in the early Holocene Black Sea (Mertens et al., 2012) precludes derivation of the calcite from the accumulation of foraminifera or nannofossils, but ostracods are abundant in Unit C (Williams, 2012). It should also be noted that the latest Pleistocene to earliest Holocene climate around the Black Sea was cooler and drier than today, so physical weathering of carbonate rocks would have been enhanced, leading to a greater supply of calcitic detritus than under conditions favouring chemical weathering and carbonate dissolution. As a comparison, through much of the Neogene there has been significant karst and cave development in the Eocene carbonates of northern Thrace because of preferential chemical weathering of the bedrock in a warm, humid climate (Ekmekçi, 2005). Chromium spikes (Fig. 4.2) are attributed to detritus from mafic igneous rocks, which are known to occur in Thrace (Kıratlı and Ergin, 1996). There is a spatial correlation between high chromium levels and sandy, normally-graded beds found within subunit C1. These are either tempesites or distal prodelta turbidites (Hiscott et al., 2007b), so must have come from the coastal zone of Thrace or nearby southern Bulgaria. Factor analysis shows that most of the geochemical variation in subunit C1 is controlled by Q-factor 2 (Fig. 3.11), a factor related to R-factor 2, which has its highest loadings on terrigenous TOC, Mg, Ca, and Mn. The terrigenous TOC values are consistent with the presence of abundant fragments of vegetation in palynology residues (P.J. Mudie, pers. comm. 2013), and point to terrigenous input. Surprisingly, chromium is not a contributor

to R-factor 2 and Q-factor 2, apparently because variations in its abundance are poorly correlated with variations in terrigenous TOC, Mg and Mn. This suggests that the bulk of the subunit C1 sediment did not come directly from the nearby coastal zone during periods of river floods (as proposed for Cr), but instead was delivered by other processes that sampled a wider and more homogeneous source area.

The geochemical correlation of Sc, Fe, K (likely in mica and illite), Ni and V (Fig 3.10) also suggests a detrital component for the sediments in Unit C. Recall that Dean and Arthur (2011, p. 24) find correlation of Ni and V with detrital aluminosilicates in some cases. Geochemically, sediments on the southwestern Black Sea shelf are distinct from two loess profiles for which there are sufficient data for comparison (Újvári et al. 2008; Adamova et al. 2002); student t-tests show similar calcite-free abundances for only one of 33 elements (Table 4.1). In terms of their texture, however, the MAR02–45 silty muds and loess are quite similar, so perhaps the two available geochemical data sets do not encapsulate all types of loess in the drainage basin of the Danube and Kamchiya rivers.

Given the indicators for some local input to subunit C1, can a case be made that Unit C was deposited in an isolated liman? The most convincing answer to this question comes from a consideration of the sediment volume in seismic unit 1B (equivalent to Unit C1), and the expected input from local Thracian rivers that might have contributed to this observed volume. Based on sediment volume estimates, local Thracian rivers could have delivered a maximum of $\sim 0.66 \text{ km}^3$ of material to the southwestern shelf during the time of deposition of Unit C. Because Unit C has a total volume of $\sim 17.5 \text{ km}^3$, the disparity between river sediment yield and accumulated sediment demands a

contribution from distal sources and/or the reworking of sediment during the transgression. The presence of low numbers of long-spined *L. machaerophorum* in subunit C1 implies the reworking of some sediments deposited during periods of higher salinity (P. Mudie, pers. comm. to R Hiscott, 2013), but the extent of this reworking is believed to be minor.

Detailed textural analyses of nearby core MAR05–50 (Flood et al., 2009) shows a textural change between lithostratigraphic Units B and C (Fig. 4.1). All sediment in these two units has a major peak between 10 and 15 μm , but sediments sampled below the $\alpha 1$ unconformity show a second peak (shoulder) around 50 μm . This coarser grained component appears too coarse to be derived from reworking of loess (e.g., Varga, 2011) but this does not rule out a provenance from loess of coarser grain size. It is also possible that the coarser mode noted by Flood et al. (2009) is linked to more sandy/silty horizons in MAR05–50, horizons that are interpreted as tempestites, or turbidites sourced from local rivers as in core MAR02–45. A third possibility is that this shoulder represents a size fraction created *in situ* through either authigenic growth or bio-precipitation of calcite. Calcite is abundant at depth in core MAR02–45, in both the clay and silt size fractions of Unit C; it is possible the same is true for core MAR05–50, which has not been analyzed mineralogically.

Except for its carbonate components, lithologic Unit C has similar mineralogy to both Units B and A. If Unit C was deposited in an isolated liman, elevated smectite content might be expected from the weathering of volcanic rocks in the Thracian hinterland (Major, 2002; Bayhan et al., 2005). Thracian river samples in this thesis contained very little smectite (<5%, Fig. 3.8), although this discrepancy may be due to

these samples being taken from sandy channel banks (Table 3.2) which might not accurately represent the mineralogical signatures of the fine fraction of Thracian sediments. Elevated illite concentrations characterize the lower units off the Romanian shelf (Major, 2002). When compared to the Holocene sediments of the Romanian shelf, smectite abundance on the southwestern Black Sea shelf is ~5% higher than reported by Major (2002), and illite abundances are nearly the same at site MAR02–45 and on the Romanian shelf. The Romanian shelf has much higher chlorite and kaolinite abundances (~15% more chlorite, ~10% more kaolinite). Abundant illite characterizes Pleistocene terrigenous sediments at DSDP sites 380 and 381 (Stoffers and Müller, 1978), east of site MAR02–45 and well off the shelf. Although MAR02–45 has higher smectite concentrations than cores located to the north and east, it must be stressed that there is a weak upward increase of smectite into Units B and A (Table. 3.5; based on unit averages), so the somewhat higher smectite percentages presented in this thesis cannot be attributed to a stronger input from Thrace unless it is argued that Units B and A also have only a local provenance even though the Black Sea shelves were entirely flooded during their accumulation. An upwardly increasing trend in smectite content was also described in the upper Holocene sediments (Unit A) by Bayhan et al. (2005). Their cores 11 and 12 (closest cores to the MAR02–45 site) contained ~12% more smectite than seen in Unit A of core MAR02–45 although this may be due to different methods used to calculate mineral abundance; based on Biscaye (1965) scaling factors the difference is ~7%.

Hiscott et al. (2007b) differentiated subunit C2 from subunit C1 based on carbon and sulphur geochemistry. The chemistry of subunit C2 suggests a transitional environment, with its chemical variability tracking terrigenous TOC (as for subunit C1)

but also a new source or process delivering increased levels of sulphur to the sediment. This coincides with Q-factor 3 (Fig. 3.15), for which the corresponding R-factor is controlled primarily by TS and terrigenous TOC. Hiscott et al. (2007b) attribute the sulphur increase to a ‘first-pulse’ of sulphate-rich Mediterranean water entering the Black Sea, providing a larger sulphur resource for sulphate-reducing bacteria in the sediment, where the sulphur was fixed as sulphide minerals.

The disparity between the volume of seismic unit 1B (lithologic Unit C) and the calculated volume of solids that could have been delivered by local rivers implies that site MAR02–45 had an open connection to the Black Sea and regional sediment sources from the early Holocene onward (since 10.3 cal ka BP). Moderate smectite abundances (Fig. 3.7) suggest that terrigenous material was delivered to the southwestern shelf mostly from distal sources, with a minor contribution from Thracian rivers.

5.2 Unit B (7.5–5.4 cal ka BP)

Unit B is bounded by the α_1 unconformity (or the correlative conformity which can be traced into the α_1 unconformity; 480 cm depth, ~7.5 cal ka BP) and the α_2 unconformity (270 cm, ~5.4 cal ka BP just below the unconformity). Unit B exhibits very distinct geochemical correlations (Fig. 3.10); a Sc, Fe, Co, Cr, Sm, La, Th and Yb ‘detrital signature’ and a Cu, V, Ni and Zn, ‘organic signature’ (i.e., adsorbed on organic matter). TOC and the marine fraction of TOC are highest in Unit B (Hiscott et al., 2007b). Cu, Ni, and Zn are biogenous trace nutrients (Piper and Calvert, 2011). They are preferentially taken up by algae in the photic zone and settle to the sea floor as particulate detritus (Piper and Calvert, 2011). This ‘organic signature’ indicates a period of

increased organic accumulation and associated sediment dysoxia. The terrigenous signature that characterizes Unit C became overprinted with a new organic signature across the transition into Unit B.

High TOC indicates elevated organic accumulation at the sediment-seawater interface. By the middle of Unit B, TOC is ~50% marine (Hiscott et al., 2007b). Elevated levels of TS, (Fig 1.7) increasing towards the top of Unit B support the strong influence of sulphate-reducing bacteria in the sediment, creating hydrogen sulphide which then reacted with metals to produce sulphide minerals. Decaying organic matter consumed dissolved oxygen in the sediment, stabilizing sulphide minerals.

The dominance of Q-factor 4 (interpreted to indicate enhanced organic productivity) begins to wane at 370 cm depth (~5.9 cal ka BP), slowly being replaced by the reducing (dysoxic) environment represented by Q-factor 1 (Fig 3.15). This change in environmental conditions might have been synchronous with the expansion of euxinic conditions in the deep basin, with the chemocline rising to the edge of the shelf ~5.65 cal ka BP (~5.3 ^{14}C ka BP; Eckert et al., 2013).

Mineralogically, the sediments of Unit B are similar to those of Unit C. The only appreciable difference is an increase of K-mica at the expense of calcite (Fig 3.3). Calcite abundance is known to increase with depth (Bayhan et al., 2005), so the thesis data support earlier observations. The upwardly decreasing abundance of calcite is also seen in the clay-sized fraction, paralleled by increases in illite (Fig 3.6).

5.3 Unit A (2.1–0 cal ka BP)

The α_2 unconformity in core MAR02–45 represents ~3.3 ka of non-deposition at the site. Found directly atop this unconformity are sharp, geochemical spikes in K, As, and Rb. Mn levels just below α_2 are elevated. These anomalies (Fig 3.13, Appendix 4) may represent accumulation of elements at a surface of long-term exposure, perhaps by adsorption onto sedimentary particles. The adsorbed metals might have been drawn downward from overlying seawater, or upward by diffusion processes or compaction/expulsion in the sedimentary pore space. Elevated levels of elements such as Cu, Ni, Zn, Pb, U, and Th which load highly on Q-factor 1 and drive its ascendancy (Fig. 3.15) imply a reducing environment. Interestingly there are no strong cross-correlations of these elements within Unit A (Table 3.12). Q-factor 1 has the highest scores here only because the other three factors are even less important, and because when one element in the above list has a low concentration, another compensates to give a consistently high factor score.

The higher than average abundances of Cu, Ni, Zn, Pb, U, and Th is a possible indication that Unit A accumulated with reducing conditions just below the sediment-water interface (due to strong sulphate reduction) so metals were adsorbed onto mineral surfaces rather than being tied up in detrital phases. Piper and Calvert (2011) assert that these hydrogenous metals accumulate on the sea floor through adsorption/precipitation reactions under reducing conditions. Even though the metal concentrations are at the high end in this unit (Table 3.16), the uptake of metals likely varied according to changing pore-water chemistry and there would have been some element mobility in the

subsurface, so the distribution of each metal is believed to be patchy, resulting in low correlation coefficients (Table 3.12). Studies by Hiscott et al. (2007b) show reduced macrofaunal activity throughout Unit A and Linegar (2012) demonstrated the concurrent onset of dysoxic conditions at core site MAR05–50 ~40 km east of site MAR02–45 on the southwestern Black Sea shelf. During the deposition of Unit A, the terrigenous signature that defines Unit C1 (i.e., as represented by Q-factor 2, Fig 3.15) returns, albeit greatly reduced and now of secondary importance.

The mineralogy of Unit A shows an increase in illite in the clay fraction (Table 3.4) and a continuing decrease in calcite abundance (silt- and clay-sized fractions), possibly implicating the Danube River as a more significant contributor. The clay size-fraction of the Danube system is dominated by illite (52–64%, Haslinger et al., 2006). Danube Delta samples analysed for this thesis also show high illite content (~45%) and it has been speculated by Bayhan et al. (2005) and Hay (1987) that illite on the southwestern Black Sea shelf may have been delivered by the Danube River. Smectite values (possibly indicative of Thracian rivers) are also highest in Unit A, but differences are slight, so that statistical overlap with the older units makes definitive conclusions impossible.

5.4 Changing Provenance

In an effort to determine provenance, potential source area geochemistry and mineralogy were compared to the mineralogy and geochemistry of samples from core MAR02–45. The silt mineralogy of all the source areas is too similar to allow

differentiation. The one exception is the presence of detrital dolomite in samples from the Danube Delta, consistent with Haslinger et al. (2006).

The clay fractions of potential source areas show more mineralogical variation than the silt fractions. Samples characterizing northern Anatolia (core MAR08–17) contain the highest smectite values and Danube samples contain abundant illite. The clay mineralogy of MAR02–45 shows little downcore variation and no definitive relationship with any source area(s).

Geochemically, there is no consistent variation through core MAR02–45 in the abundances of elements believed to reside in detrital aluminosilicates. Furthermore, there is no compelling match to one source area over the others. As such, it is not possible to demonstrate changing provenance through the Holocene. Student t-tests performed on normalized geochemical data for two loess deposits show no marked relationship with the elemental abundances in Unit C1. To rule out central European loess as a potential source, more on-land studies would be required, because the wind-blown nature of loess supply makes it unlikely that the loess is itself geochemically homogeneous.

5.5 Evolution of sediment composition on the southwestern Black Sea shelf

The geochemical evolution of Holocene sediment on the southwestern Black Sea shelf has been characterized by the evaluation of samples from core MAR02–45. Results are consistent with the following time line (Fig 5.1). Starting ~10.3 cal ka BP, the Black Sea was ~40–50 m lower than today (Hiscott et al. 2007b).

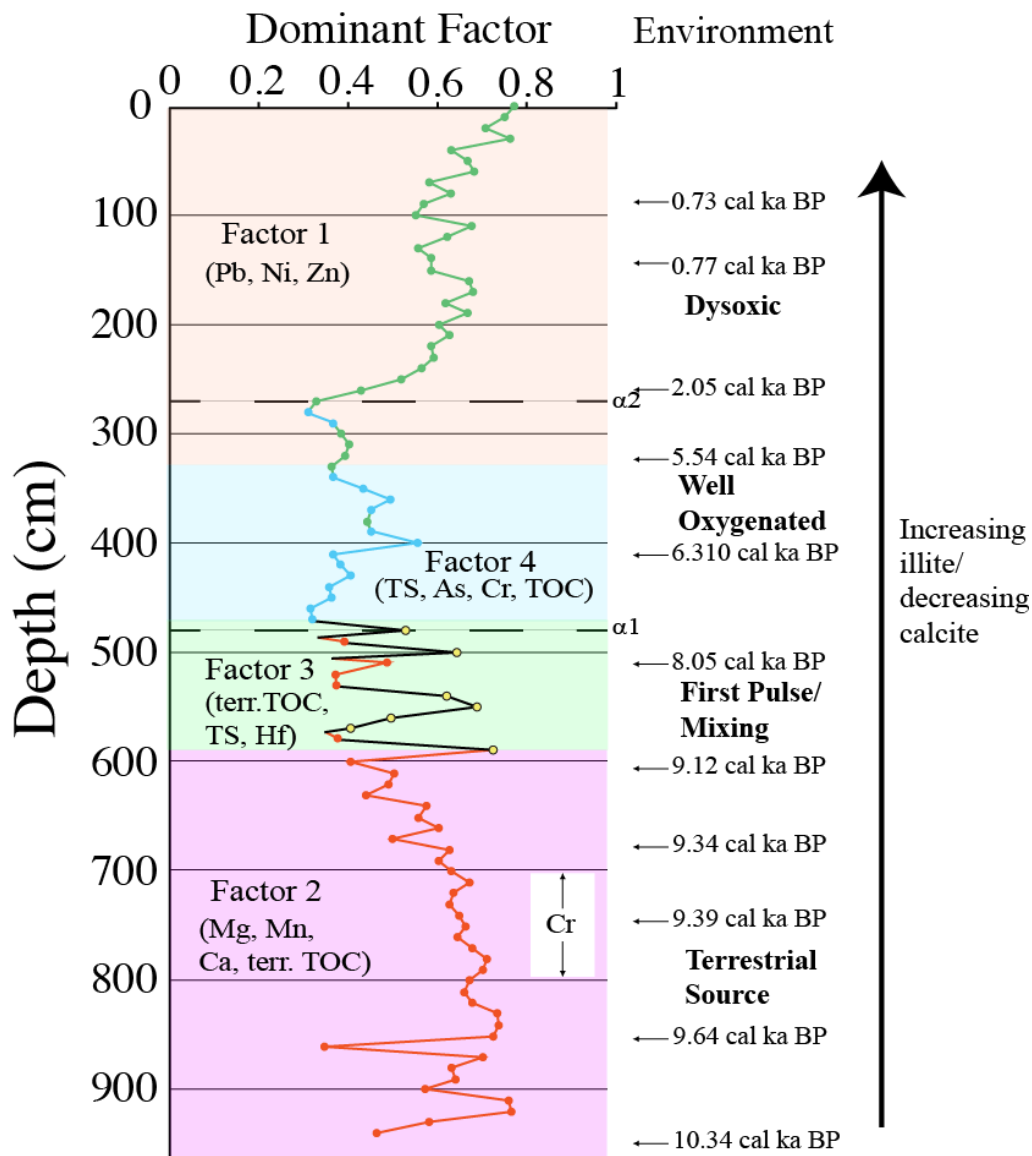


Figure 5.1 Dominant Q-factors and dominant elements through MAR02–45. The dominant factors from Fig 3.15 are combined into one Q-factor column with the dominant constituents of each Q-factor listed below. The section of MAR02–45 with elevated Cr values is indicated to show its independent behaviour from Q-factor 2. The environments that these factors and element concentrations imply are found in bold to the right. The far right of the figure expresses mineralogical trends seen through the core.

The MAR02–45 site was connected to the open Black Sea so received significant quantities of sediment from upcurrent sources that today are located to the west and northwest of the core site, where rivers larger than the local Thracian rivers enter the Black Sea. The currents that carried this sediment might have been geostrophically turned prodelta turbidity currents generated at the mouths of Bulgarian rivers (e.g., Kamchiya River), along-shelf wind-driven currents, or either of these assisted by wave stirring to keep sediment in suspension. The extent of reworking of older shelf deposits is believed to have been minor, based on scarce older dinocysts in the subunit C1 sediments. Pulses of increased local input created high Cr levels adjacent to sandy event-beds. Deposition under these conditions continued until ~9.2 cal ka BP.

The onset of accumulation of subunit C2 (~9.2 cal ka BP) coincides with the first pulse of Mediterranean water into the Black Sea; the newly arrived seawater sulphate was reduced and is recorded in the sediment profile as a peak in TS (Hiscott et al., 2007b). By 7.5 cal ka BP, a permanent two-way flow was established between the Black Sea and the Aegean Sea, leading to geochemical changes in the sediment that are mostly diagenetic (because of sulphate reduction in the sedimentary succession) or related to adsorption on organic matter.

Between 7.5–5.4 cal ka BP, sediments on the southwestern Black Sea shelf indicate a thriving, oxygenated, marine environment (Hiscott et al., 2007b; Major et al., 2002, 2006). Numerous shells have been found in life position and are interpreted as a biocoenose, or life assemblage (Hiscott et al., 2007b). Below the uppermost active layer, high TOC values and access to seawater sulphate promoted dysoxia in the pore waters. Elevated TS and As values imply reducing conditions in the sediments. Increased illite

abundance suggests a greater contribution from the Danube system (Haslinger et al. 2006), perhaps facilitated by strengthening of the Rim Current.

After a ~3.3 cal ka hiatus ($\alpha 2$ unconformity) Unit A records the establishment of stable dysoxic conditions across the southwestern shelf. Metals expected in sedimentary sulphides or adsorbed on organic fractions are higher than in older units (i.e., Cu, Ni, Zn, Pb, U). The dysoxic environment associated with Unit A continues to the modern day on the southwestern Black Sea shelf. Several CTD (conductivity, temperature, depth) profiles gathered by supervisors Hiscott and Aksu in 2011 indicate that oxygen levels in bottom waters are similar to those at the sea surface, so reducing conditions must be limited to pore waters.

While the geochemistry expresses a changing environment, the mineralogy shows little variation, implying no major changes in provenance. Slight increases in illite from the base of MAR02–45 to the top of the core might indicate a strengthening or shift in the track of the Rim Current; however, the changes in illite abundance are minor and cannot be shown to have statistical significance.

There are four strong arguments for an unimpeded connection of the southwestern shelf to the open Black Sea since ~10.3 cal ka BP, they are:

- 1) The discrepancy between the volume (or mass) of sediment available from local sources when compared to the actual amount of sediment deposited in seismic unit 1B (= lithologic Unit C). If the MAR02–45 site was located in an isolated liman, it would be all but impossible to explain the accumulation of so much sediment so quickly. Processes capable of reworking older strata to generate a new sedimentary succession *in situ* are

incompatible with the conditions in an isolated liman, because a restricted fetch would prevent the build up of large enough waves to significantly erode the seabed.

2) A lack of mineralogical variation from the early Holocene to the present day, which implies that multiple sources have been contributing material to the core site since the early Holocene.

3) The consistent behaviour of Sc, Fe, Co, Ce, La, Th and Y, interpreted to represent the contribution of aluminosilicates from a terrestrial source. One would expect some changes in the concentrations and ratios of these correlated elements between Units C and B if Unit C was solely supplied by Thracian rivers. The lack of variation throughout the entirety of the MAR02–45 succession suggests a wider, more homogenous source for these detrital elements.

4) The behaviour of Cr within Unit C suggests multiple sources contributing sediment at the same time. Most likely a large flux of mud was supplied to the shelf from local and distant sources, and carried trace and rare earth elements like Sc, Fe, Th, La, Yb, Sm and Cr. Superimposed upon this input was the episodic delivery of local sand and mud from coastal areas of Thrace during storms or river floods, bringing Cr-rich detritus with different mixtures of other elements, distinct from the regional supply so that correlations between other variables and Cr are not evident.

5.6 Future Work

Textural studies of MAR05–50 samples exposed a coarse grained shoulder in sediments correlated to Unit C. Similar textural work on samples from core MAR02–45 is predicted to expose a shoulder in lower Holocene sediments at that coresite as well. It

would be interesting to isolate the coarse mode through sieving, so that the minerals contributing to this mode can be determined, and perhaps ascribed to a particular source.

Detailed geochemical analysis of samples from core MAR05–50 and other cores located on the southwestern Black Sea shelf would allow the correlation and mapping of geochemical units across the entire shelf. If MAR05–50 contains enough material (>5 g per sample) XRF analysis or the 4B WRA-ICP analytical package offered by ActLabs, should be considered for analysis as they both offer superior precision for some major elements (i.e. Al, P). Mineralogical studies of other cores would also increase the understanding of the distribution of material across the shelf and might lead to a more successful provenance evaluation. Pore-water studies on nearby cores would help constrain the diagenetic processes of metal fixation but would require specialized and dedicated sampling.

Based on the limited number of samples and the type of material available to the author, it is recommended that potential source areas be resampled to provide mud samples with textural similarity to the shelf successions. Coring in the Danube and Kamchiya deltas might provide samples with more pristine geochemical signatures and would permit tracking of any mineralogical changes over time. It would also be interesting to analyze some samples from these deltas with an Horiba (or similar) size analyzer to see if they contain the shoulder recorded in samples from core MAR05–50. The sampling of Thracian river load would need to be improved for a proper comparison to the offshore muds. Samples made available to the author were taken in sandy deposits, masking the geochemical and mineralogical signatures which are better developed in muds. It is

recommended that more samples be taken across Thrace to better characterize the hinterland and possibly shed more light on the Thracian contribution to shelf sediments.

A more detailed geochemical comparison of loess deposits across Europe might expose unexpected relationships to guide future provenance studies. Of special importance to the determination of the provenance of Black Sea Holocene muds would be the documentation of geochemically distinct loess occurrences, to seek matches with the composition of the offshore muds.

Chapter 6 Conclusions

The primary objectives of this thesis are to determine the geochemistry of Holocene muds and to assess whether the provenance of the fine fractions of the Holocene sediments on the southwestern Black Sea shelf might have changed since the earliest Holocene. It was anticipated that the assembled data could be used to determine whether coresite MAR02–45 was in an isolated lagoon, often locally referred to as a “liman”. This is of importance because Hiscott et al. (2007b) have argued that deposition occurred at MAR02–45 with an open connection to the Black Sea and represents accumulation on a submerged shelf since 10.3 cal ka BP. If this were true, then the shelf would not have been subaerially exposed at the time of the catastrophic flood proposed by Ryan et al. (2003) at 9.15 cal ka BP. In some respects, the results of this thesis are negative, in that no significant evidence for changes in provenance have been demonstrated. This result could not be predicted without the range of analytical results presented in the thesis. The following major conclusions are derived from this thesis:

- 1) Over the course of the Holocene, there were only minor changes in mineralogical composition of sediments deposited on the southwestern Black Sea shelf. Quartz and calcite dominate the composition of silt-sized material from 10.3–7.5 cal ka BP; after 7.5 cal ka BP calcite abundance begins to decrease and is replaced by K-micas. The clay-sized fraction of sediments is predominantly illite, with smectite and some minor chlorite and kaolinite. Non-clay minerals in the clay fraction include quartz, calcite and dolomite, with calcite abundances increasing lower in the core.

- 2) The Holocene succession on the southwestern Black Sea shelf is silt dominated. MAR05–50 (~40 km east of MAR02–45) has a mean grain size of ~15 μm . Below the $\alpha 1$ unconformity a second peak (shoulder at ~50 μm) is seen in the sediments. Loess deposits have a wide range of mean grain size (Fitzsimmons et al., 2012) but are primarily silt dominated. Although the grain size of Hungarian loess (Varga, 2011) differs from the grain size of sediments measured at MAR05–50 the close textural similarity of the sediments at MAR05–50, to loess deposits means that they are a viable source for the shelf sediment.
- 3) Geochemical analysis of sediments from MAR02–45 shows four distinct geochemical units. This is in agreement with the four lithologic units proposed by Hiscott et al. (2007b). This thesis has proposed a refinement in the placement of the $\alpha 1$ correlative conformity based on geochemical trends. The position of the correlative conformity to the $\alpha 1$ unconformity has been raised by 45 cm, from 525 cm to 480 cm depth. This is consistent with the seismic interpretations of profiles recorded near the coresite by Hiscott et al. (2007b). As Huntect DTS profiles have an ~30 cm vertical resolution, Hiscott et al. (2007b) chose the location of the $\alpha 1$ correlative conformity in the core MAR02–45 based on trends seen in $\delta^{34}\text{S}$ and $\delta^{13}\text{C}$. Based on the expanded geochemical analysis in this thesis, it seems prudent to shift the core depth of $\alpha 1$ upwards, towards its seismically measured depth.
- 4) Correlation tables expose four groups of similarly behaving elements that govern the geochemical trends throughout MAR02–45. A carbonate group is composed of Ca, Mg, and Sr, and corresponds to elements found in calcite. Sc, Fe, Co, Ce, La, Th and Y are considered to have mainly a detrital origin. As, Rb, Br, Mn and Sr entered the sediment

from the water column, or were mobile during early diagenesis and Cu, Pb, Ni, Zn, Th, U and V are interpreted to indicate adsorption onto fine-grained phyllosilicates and/or organic matter during early diagenesis.

5) High levels of chromium are associated with sandy horizons in Unit C of core MAR02–45. Although samples were taken to avoid these sandy layers, it is possible that bioturbation has moved chromium-bearing detritus into the surrounding muds. These sandy horizons were interpreted by Hiscott et al. (2007b) to be either tempestites or turbidites (sourced from local rivers). As Cr is an expected tracer for Thracian source rocks, the elevated Cr levels may imply an episodic increased sediment contribution from the local hinterland.

6) Comparison of geochemical and mineralogical data to potential source areas is inconclusive. Potential source areas possess distinct markers (e.g., dolomite in Danube Delta silts, high smectite content near the mouth of the Bosphorus Strait) but these markers are not present or are too weak to guide interpretation in samples from core MAR02–45. Methods used to collect samples from potential source areas could be improved. Specifically, grab samples are prone to collecting contaminated surficial sediments, whereas coring deeply into fluvial or near-shore successions adjacent to potential sources would yield more pristine samples. A resampling of detritus contributed by Thracian rivers is also required as the samples for this thesis were particularly sandy, obscuring any geochemical trends that might be present in the silt-sized fraction.

7) Student t-tests to look for geochemical differences between the MAR02–45 samples of Unit C and the loess deposits in Hungary and Czech Republic showed similar calcite-

free abundances for only one element (Y, 1 of 33 total elements). Although there appears to be no significant geochemical relationship between these loess deposits (in the Danube drainage basin) and samples from core MAR02–45, there surely must have been a large volume of aeolian material eroded in the Danube drainage basin, and delivered to the Black Sea by the Danube River. It is entirely possible that other loess deposits in central and eastern Europe possess geochemical signatures more comparable to the sediments found on the southwestern Black Sea shelf. This is retained as a viable option to explain the loess-like texture (bimodal; little clay) of the Holocene muds on the SW Black Sea shelf.

8) Early Holocene sediment delivery by local rivers, $\sim 0.66 \text{ km}^3$ (using the BQART equation and a duration of 5000 years), was inadequate to supply the total volume material deposited on the shelf (based on sediment volume estimates from isopach thicknesses, $\sim 17 \text{ km}^3$). The most likely explanation for this serious mismatch is to invoke the contribution from a combination of sources. The presence of sparse, long-spined dinoflagellates suggests some minor reworking of sediment along the shelf (P. Mudie pers. comm. 2013). It is also probable that sediments were delivered from both the Danube and Kamchiya rivers, based on a comparison with the long distance along-shelf transportation of fine sediments from the Mississippi Delta and a number of Asian deltas.

9) Based on the consistent mineralogy over the course of the Holocene and the inadequacy of Thracian rivers to deliver large volumes of sediment to the shelf, it is concluded that the MAR02–45 core site was connected to the open Black Sea since at least 10.3 cal ka BP, in a way that allowed sediment delivery to the site by major marine wind-driven currents. For this to be true would mean that the southwestern Black Sea

shelf had been inundated by 10.3 cal ka BP, supporting the conclusions of Hiscott et al. (2007b), and contradicting the claims of Ryan et al. (2003) and Lericolais et al. (2007) that the southwestern Black Sea shelf was subaerially exposed until 9.15 cal ka BP.

10) Future studies that would assist a more thorough analysis of the thesis data include (a) a full textural analysis of sediments at the MAR02–45 site, (b) geochemical analysis and mineralogical studies of other long piston cores from the SW Black Sea shelf using larger samples compatible with XRF and similar methods, (c) collection and analysis of a broader range of representative mud samples from a number of potential source areas, avoiding anthropogenic contamination, (d) a more complete characterization of the chemistry of loess in the major drainage basins surrounding the western Black Sea, (e) a targeted study to determine the origin of the silt- and clay-sized carbonate component of the Holocene succession, and (f) pore-water and diagenesis studies to clarify which trace and rare-earth elements are adsorbed from the bottom waters and pore waters, to distinguish these from elements carried by detrital aluminosilicate minerals.

References

- Adamova, M., Havlicek, P., and Sibrava, V. 2002. Mineralogy and Geochemistry of Loesses in Southern Moravia. *Bulletin of Geosciences* 77: 29–41.
- Aksu, A.E., Hiscott, R.N., and Yaşar, D., 1999. Oscillating Quaternary water levels of the Marmara Sea and vigorous out-flow into the Aegean Sea from the Marmara Sea-Black Sea drainage corridor. *Mar. Geol.* 153: 275–302.
- Aksu, A. E., Hiscott, R. N., Yaşar, D., İşler, F.I., and Marsh, S. 2002. Seismic stratigraphy of Late Quaternary deposits from the Southwestern Black Sea Shelf: evidence for non-catastrophic variations in sea-level during the Last ~10,000 Yr." *International Journal of Marine Geology, Geochemistry and Geophysics* 190: 61-94.
- Bayhan, E., Ergin, M., Temel, A., and Keskin, S. 2005. Mineralogy of Holocene sediments from the Southwestern Black Sea Shelf (Turkey) in relation to provenance, sea-level and current regimes. *Journal of the Geological Society of China* 79.4: 552-63.
- Bedi, Y., Vasilev, E., Dabovski, C., Ergen, A., Okuyucu, C., Doğan, A., Tekin, K., Ivanova, D., Boncheva, I., Lakova, I., Sachanski, V., Kuşcu, I., Tuncay, E., Gülnur Demiray, D., Soycan, H., and Göncüoğlu, M. 2013. New age data from tectonostratigraphic units of the Istranca “Massif” in NW Turkey: a correlation with SE Bulgaria. *Geologica Carpathia* 64.4: 255–277.
- Biscaye, P. E. 1964. Distinction between Kaolinite and Chlorite in Recent Sediments. *American Mineralogist* 49: 1282–1289.
- Biscaye, P. E. 1965. Mineralogy and Sedimentation of Recent Deep-Sea Clay in the Atlantic Ocean and Adjacent Seas and Oceans." *Geological Society of America Bulletin* 76.7: 803–832.
- Bortolotti, V., Marroni, M., Nicolae, I., Pandolfi, L., Principi, G., and Saccani, E. 2002. Geodynamic implications of Jurassic ophiolites associated with island-arc volcanics, south Apuseni Mountains, western Romania. *International Geology Review*, 44.10: 938–955
- Bradley, L.R., Marret, F., Mudie, P.J., Aksu, A.E., and Hiscott, R.N. 2012. Assessing Holocene fossil dinoflagellate cyst records from the south-western shelf of the Black Sea. *Journal of Quaternary Science* 27: 835–843.

- Burchfiel, B. C., Nakov, R., and Tzankov, T. 2003. Evidence from the Mesta half-graben, SW Bulgaria for the Late Eocene beginning of Aegean extension in the Central Balkan Peninsula: *Tectonophysics* 375: 61–76.
- Channell, J. E.T, Brandner, R., Spieler, A., and Smathers, N.P. 1990. Mesozoic paleogeography of the Northern Calcareous Alps-evidence from paleomagnetism and facies analysis. *Geology* 18: 828–831.
- Crant, R. 2010. Lateral accretion deposits in a sinuous density underflow channel: a study of the channel evolution and rate of sediment accumulation [Honours dissertation]. St. John's: Memorial University.
- Das, H.A., Zonderhuis, J., and van der Marel, H.W. 1971. Scandium in rocks, minerals and sediments and its relation to iron and aluminum. *Contributions to Mineralogy and Petrology*. 32: 213–244.
- Davis, J. C. 1973. *Statistics and Data Analysis in Geology*. 1st ed. New York. J. Wiley.
- Dean, W.E., and Arthur, M.A. (2011). Geochemical characteristics of Holocene laminated sapropel (Unit II) and underlying lacustrine Unit III in the Black Sea. U.S. Geological Survey Open-File Report 2010-1323: 1–29.
- Demir, D., Bilim, F., Aydemir, A., and Ates, A. 2012. Modelling of Thrace Basin, NW Turkey using gravity and magnetic anomalies with control and seismic and borehole data. *Journal of Petroleum Science and Engineering*. 86-87: 44–53.
- Dimitrov, P., Michova, E. and Peytchev, V. 1998. Palaeoecological reconstructions of western part of the Black Sea during the Quaternary. *Proceedings of the Institute of Oceanology* 2: 127–139 (in Bulgarian with English summary).
- Dinescu, L. C., and Dului, O. G. 2001. Heavy metal pollution of some Danube Delta sediments studied by neutron activation analysis. *Applied Radiation and Isotopes* 54: 853–859.
- Doglionni, C., Busatta, C., Bolis, G., Marianini, L., and Zanella, M. 1995. Structural evolution of the eastern Balkans (Bulgaria). *Marine and Petroleum Geology* 13: 225–251.
- Eckert, S., Brumsack, H., Severmann, S., Schnetger, B., März, C., and Frollje, H. 2013. Establishment of Euxinic Conditions in the Holocene Black Sea. *Geology* 41: 523-24.
- Ekinci, Y., Demirci, A., Ekinci, R., and Erginal, A. Geophysical characterization of Late Pleistocene coquina and eolianite on western Black Sea coast of Turkey by using

- electrical resistivity tomography survey. 2013. *Geophysical Research Abstracts* 15.
- Ekmekçi, M. 2005. Karst in Turkish Thrace: Compatibility between geological history and karst type. *Turkish Journal of Earth Science*. 14: 73–90.
- Erginal, A., Ekinçi, Y.L., Demirci, A., Elmas, K., and Kaya, H. 2012. First not on Holocene coquinite on Thrace (Black Sea) coast of Turkey. *Sedimentary Geology* 267–268: 55–62.
- Eriş, K.K., Ryan, W.B.F., Çağatay, M.N., Sancar, U., Lericolais, G., Ménot, G., and Bard, E. 2007. The timing and evolution of the post-glacial transgression across the Sea of Marmara shelf south of Istanbul. *Marine Geology* 243: 57–76.
- Filipova-Marinova, M., Christova, R. and Bozilova, E. 2004. Palaeoecological conditions in the Bulgarian Black Sea area during the Quaternary. *Environmental Micropaleontology, Microbiology and Meiobenthology* 1: 136–154.
- Fitzsimmons, K. E., Marković, S. B., and Hambach, U. 2012. Pleistocene environmental dynamics recorded in the loess of the middle and lower Danube basin. *Quaternary Science Reviews* 41: 104–118.
- Flood, R. D., Hiscott, R. N., and Aksu, A. E. 2009. Morphology and evolution of an anastomosed channel network where saline underflow enters the Black Sea. *Sedimentology* 56: 807–839.
- Gealey, W.K. 1988. Plate tectonic evolution of the Mediterranean–Middle East region. *Tectonophysics* 155: 285–306.
- Gibbs, R. J. 1965. Error Due to Segregation in Quantitative Clay Mineral X-ray Diffraction Mounting Techniques. *American Mineralogist* 50: 741–751.
- Giosan, L., Filip, F., and Constaționescu, S. 2009. Was the Black Sea catastrophically flooded in the Early Holocene? *Quaternary Science Reviews* 28: 1–6.
- Görür, N. Çağatay, N., Emre, Ö., Alpar, B., Sakıncı, M., İslamoğlu, Y., Algan, O., Erkal, T., Keçer, M., Akkök, R., and Karlık, G., 2001. Is the abrupt drowning of the Black Sea at 7150 yr BP a myth? *Marine Geology*, 176: 65–73
- Gündoğdu, M.N., 1982. Geological, Mineralogical and Geochemical investigations of Neogene Bigadif Sedimentary Basin. Ph.D. Thesis, Hacettepe University, Beytepe, Ankara, 386 (in Turkish).

- Gürbüz A., and Leroy S.A.G., 2010. Science versus myth: Was there a connection between the Marmara Sea and Lake Sapanca? *Journal of Quaternary Science*, 25. 2: 103–114
- Gromet, L., L. Haskin, R. Korotev, and Dymek, R. 1984. The North American Shale Composite: Its Compilation, Major and Trace Element Characteristics. *Geochimica Et Cosmochimica Acta* 48.12: 2469–2482.
- Haase, D., Fink, J., Haase, G., Ruske, R., Pécsi, M., Richter, H., Altermann, M., and Jäger, K-D., 2007. Loess in Europe – its spatial distribution based on a European Loess Map, scale 1:2,500,000. *Quaternary Science Reviews*, 26: 1301–1312.
- Hanchar, J. M., Nagy, K. L. Fenter, P., Finch, R. J., Beno, D. J., and Sturchio. N.C., 2000. Quantifications of Minor Phases in Growth Kinetics Experiments with Powder X-ray Diffraction. *American Mineralogist* 85.9: 1217–1222.
- Hay, B. J. 1987. Particle flux in the western Black Sea in the present and over the last 5,000 years: temporal variability, sources, transport mechanisms. [PhD Thesis] Ithaca: Cornell University.
- Haslinger, E., Ottner, F., Lair, G.J., and Gerzabek, M.H., 2006. Bulk and clay mineralogy of stream sediments of the rivers Danube, Ebro and Elbe. In Stanjek, H. (ed), Contributions of the annual meeting, Deutschen Ton- und Tonmineralgruppe (DTTG), v. 12, Valkenburg, Netherlands
- Hirst D. M. 1974 Geochemistry of sediments from eleven Black Sea cores, in *The Black Sea-Geology, Chemistry, and Biology* (eds. Degens, E. T. and Ross, D. A.), American Association of Petroleum Geology Mem. 20: 430–455
- Hiscott, R.N., and Aksu, A.E., 2002. Late Quaternary history of the Marmara Sea and Black Sea from high-resolution seismic and gravity-core studies. *Mar. Geol.* 190.
- Hiscott, R.N., Aksu, A.E. Yaşar, D., Kaminski, M.A., Mudie, P.J., Kostylev, V., MacDonald, J., İşler, F.I., Lord, A.R., 2002. Deltas south of the Bosphorus Strait record persistent Black Sea outflow to the Marmara Sea since V10 ka. *Mar. Geol.* 190.1–2. 261–282.
- Hiscott, R.N., Aksu, A.E., Mudie, P.J., Kaminski, M.A., Abrajano, T., Yaşar, D., Rochon, A., 2007a. The Marmara Sea Gateway since ~16 ka: non-catastrophic causes of paleoceanographic events in the Black Sea at 8.4 and 7.15 ka. In: Yanko-Hombach, V., Gilbert, A.S., Panin, N., Dolukhanov, P.M. (Eds.), *The Black Sea Flood Question: Changes in Coastlines, Climate and Human Settlement*. Springer, Dordrecht: 89–117.

- Hiscott, R.N., Aksu A. E., Mudie P. J., Marret F., Abrajano T., Kaminski M., Evans J., Çakiroğlu A., and Yaşar, D. 2007b. A gradual drowning of the Southwestern Black Sea shelf: evidence for a progressive rather than abrupt Holocene reconnection with the Eastern Mediterranean Sea through the Marmara Sea Gateway. *Quaternary International* 167-168: 19-34.
- Hiscott, R.N., Aksu, A.E., and Mudie, P.J., 2008. Comment on “The timing and evolution of the post-glacial transgression across the Sea of Marmara shelf south of İstanbul” by Eriş et al., *Mar. Geol.* 243, 57–76. *Marine Geology* 248: 228–236.
- Jaoshvili, S. 2002. Rivers of the Black Sea. European Environment Agency Technical Report 71.
- Kıratlı, N., and Ergin, M. 1996. Partitioning of heavy metals in the surface Black Sea sediments. *Applied Geochemistry* 11: 775–788.
- Klovan, J. E. 1971. QR-mode Factor Analysis Program. University of Calgary. Revised in 1985 by Imbrie, J., and Kipp, N. G.
- Kozhoukharov, D., and Konzalova, M. 1990. First Findings of Microphytofossils in the Marbles of the Dobrostan Formation in the Northern and Southern Pirin Mts." *Geologica Balcanica* 20: 47-52. (in Russian, with English abstract)
- Linegar, A. E. 2012. Palaeo-environmental history of the southwestern Black Sea during the Late Holocene: an elemental and stable isotopic study. [Master’s Thesis] St. John’s: Memorial University.
- Lericolais, G., Popescu, I., Guichard, F., Popescu, S.M. 2007. A Black Sea lowstand at 8500 yr B.P. indicated by a relict coastal dune system at a depth of 90 m below sea level *Coastline Changes: Interrelation of Climate and Geological Processes*. GSA Books; Allen Press Inc., Special Paper V. 426: 171-188.
- Lericolais, G., Bourget, J., Popescu, I., Jermannaud, P., Mulder, T., Jorry, S., and Panin, N. 2012. Late Quaternary Deep-sea Sedimentation in the Western Black Sea: New Insights from Recent Coring and Seismic Data in the Deep Basin." *Global and Planetary Change* 103: 232-47.
- J.P. Liu, Xue Z., Ross K., Wang H.J., Yang Z.S., Li A.C., Gao S. 2009. Fate of sediments delivered to the sea by Asian large rivers: Long-distance transport and formation of remote alongshore clinothems. *SEPM-The Sedimentary Record* .7.4: 4-9
- Longerich, H. 1995. Analysis of pressed pellets of geological samples using wavelength-dispersive X-ray fluorescence spectrometry. *X-Ray Spectrometry* 24: 123–136.

- Loring, D. H. 1991. Normalization of Heavy-metal Data from Estuarine and Coastal Sediments. *ICES Journal of Marine Science* 48.1: 101-15.
- Major, C. O. 2002. Non-eustatic Controls on Sea-level Change in Semi-enclosed Basins. Ph.D. Thesis, Columbia University
- Major, C.O., Goldstein, S.L., Ryan, W.B.F., Lericolais, G., Piotrowski, A.M., and Hajdas, I. 2006. The co-evolution of Black Sea level and composition through the last deglaciation and its paleoclimatic significance. *Quaternary Science Reviews* 25: 2031–2047.
- Mann, U. and Müller, G. 1980. X-ray mineralogy of deep-sea drilling project. Legs 51 through 53, western north Atlantic. In: Donnelly, T., Francheteau, J., Brayn, W., Robinson, P., Flower, M., and Salisbury, M. (eds.), *init. Repts. DSDP, 51, 52, 53, (Pt.2)*. Washington: U.S. Govt. Printing Office: 721-729.
- Marret, F., Mudie, P., Aksu, A. E., and Hiscott, R. N. 2009. A Holocene Dinocyst Record of a Two-step Transformation of the Neoeuxinian Brackish Water Lake into the Black Sea." *Quaternary International* 193: 72-86.
- McBride, R. A., Taylor, M. J., and Byrnes, M. R. 2007. A geomorphic process-response model for Chenier-plain evolution in southwestern Louisiana, USA. *Coastal Sediments '07*: 1–14.
- Mertens, K.N., Bradley, L.R., Takano, Y., Mudie, P.J., Marret, F., Aksu, A.E., Hiscott, R.N., Verleye, T.J., Mousing, E.A., Smyrnova, L.L., Bagheri, S., Mansor, M., Pospelova, V. and Matsuoka, K. 2012. Quantitative estimation of Holocene surface salinity variation in the Black Sea using dinoflagellate cyst process length. *Quaternary Science Reviews* 39: 45–59.
- Muratov, V., Neprochnov, Y.P, Ross, D. A., and Trimonis, E. S. 1978. Basic features of the Black Sea late Cenozoic history based on the results of deep-sea drilling, leg 42B Deep Sea Drilling Project Reports and Publications XLII: 1141–1148.
- Natal'in, B., Sunal, G., Satir, M., and Toraman, E. 2012. Tectonics of the Strandja Massif, NW Turkey: history of a long-lived arc at the northern margin of Paleotethys. *Turkish Journal of Earth Sciences*. 21: 755–798.
- Needham, S. J., Worden, R. and McIlroy, D. 2005. Experimental production of clay rims by macrobiotic sediment ingestion and excretion processes. *Journal of Sedimentary Research*. 75: 1028–1037.
- Oğuz, T., Latun, V.S., Latif, M.A., Vladimirov, V.V., Sur, H.I., Markov, A.A., Özsoy, E., Kotovshchikov, B.B., Eremeev, V.V., and Ünlüata, U. 1993. Circulation in the surface and intermediate layers of the Black Sea. *Deep-Sea Res* 40: 1597-1612.

- Okay, A. 2008. Geology of Turkey: a synopsis. *Anschnitt* 21: 19–42.
- Okay, N. and Okay, A. 2002. Tectonically induced Quaternary drainage diversion in the northeastern Aegean. *Journal of the Geological Society, London*. 159: 393–399.
- Oreščanin, V., Lulic, S., Medunic, G., and Mikelic, L. 2005. Granulometric and chemical composition of the Danube River sediments, Batina Village, Croatia. *Geologica Croatica* 58: 185-94.
- Panin, N., and Jipa, D. 2002. Danube River sediment input and its interaction with the North-western Black Sea. *Estuarine, Coastal and Shelf Science* 54: 551-62.
- Pérez-Arrieta, L., and Tabares-Muñoz, C. 2002. Considerations about the variability of the Bragg's law fulfillment. *Revista Mexicana de Física* 50.2: 96–98.
- Petschick, R. 2000. MacDiff 4.2.2 freeware and manual, <http://www.geol-pal.unifrankfurt.de/Staff/Homepages/Petschick/classicsoftware.html>, last accessed 19/08/2014
- Piper, D.Z., and Calvert, S.E. 2011. Holocene and late glacial palaeoceanography and palaeolimnology of the Black Sea: changing sediment provenance and basin hydrography over the past 20,000 years. *Geochimica et Cosmochimica* 75. 5597–5624.
- Quakernaat, Joost. 1970. Direct Diffractometric Quantitative Analysis of Synthetic Clay Mineral Mixtures with Molybdenite as Orientation-indicator. *Journal of Sedimentary Research* 40. 506-13.
- Reynolds, R.R. 2012. Correlation of two sediment cores recovered from the SW Black Sea shelf using carbon and sulfur elemental and isotopic geochemistry: implications for paleoceanographic communication between the Black Sea and eastern Mediterranean Sea during the last 12,000 years. [Honours dissertation]. St. John's: Memorial University.
- Royse, C. F. J.R., Wadell, J. S., and Petersen, L. E. 1971. X-ray determination of calcite-dolomite: an evaluation. *Journal of Sedimentary Petrology* 41: 483–488.
- Ryan, W.B.F., Pitman III, W.C., Major, C.O., Shimkus, K., Maskalenko, V., Jones, G.A., Dimitrov, P., Gorür, N., Sakiñç, M., Yüce Seyir, H., 1997. An abrupt drowning of the Black Sea shelf. *Mar. Geol.* 138: 119–126.
- Ryan, William W.B.F, C. O. Major, G. Lericolais, and S. Goldstein. 2003: Catastrophic flooding of the Black Sea. *Annual Review Earth Planet Science* 31 525-54.

- Ryan, W.B.F., 2007. Status of the Black sea flood hypothesis, in: Yanko-Hombach, V., Gilbert, A.S., Panin, N. (Eds.), *The Black Sea Flood Question: Changes in Coastline, Climate and Human Settlement*. Springer, New York, pp. 63-88.
- Savov, I., Ryan, J., Haydoutov, I., and Schijf, J. 2001. Late Precambrian Balkan-Carpathian Ophiolite—a Slice of the Pan-African Ocean Crust? Geochemical and Tectonic Insights from the Tcherni Vrah and Deli Jovan Massifs, Bulgaria and Serbia." *Journal of Volcanology and Geothermal Research* 110: 299-318.
- Shumilovskikh, L.S., Marret, F., Fleitmann, D., Arz, H.W., Nowaczyk, N. and Behling, H. 2013. Eemian and Holocene sea-surface conditions in the southern Black Sea: organic-walled dinoflagellate cyst record from core 22-GC3. *Marine Micropaleontology*.
- Smalley, I. J., and Leach, J. A. 1978. The Origin and Distribution of the Loess in the Danube Basin and Associated Regions of East-Central Europe: a Review. *Sedimentary Geology* 21: 1-26.
- Stefanescu, M., Dicea, O., Butac, A., and Ciulavu, D. 2006. Hydrocarbon geology of the Romanian Carpathians, their foreland, and the Transylvanian basin, in Golonka, J., and Picha, F. J., eds., *The Carpathians and their foreland: Geology and hydrocarbon resources: AAPG Memoir 84: 521–567*.
- Stoffers, P., and Müller, G. 1978 Mineralogy and lithofacies of Black Sea sediments leg42B deep sea drilling project. *Deep Sea Drilling Project Reports and Publications XLII: 373-411*.
- Syvitski, J. P. M., and Milliman, J. D. 2007. Geology, geography and humans battle for dominance over the delivery of fluvial sediment to the coastal ocean. *Journal of Geology: 1–19*
- Trimonis, E. S., and Ross, D. A. 1978. Mineral composition of coarse-silt fraction of the Black Sea Late Cenozoic sediments. *Deep Sea Drilling Project Reports and Publications XLII: 413-26*.
- Trubelja, F., Burgath, K., and Marchig, V. 2004. Triassic Magmatism in the area of the central Dinarides (Bosnia and Herzegovina): geochemical resolving of tectonic setting. *Geologia Croatica* 57: 159–170.
- Turgut, S., and Eseller, G. 2000. Sequence stratigraphy, tectonics and depositional history in eastern Thrace Basin, NW Turkey. *Marine and Petroleum Geology*. 17: 61–100.

- Újvári, G., Varga, A., and Zsuzsanna, B. 2008. Origin, weathering, and geochemical composition of loess in southwestern Hungary. *Quaternary Research*: 421–437.
- Underwood, M.B., Basu, N., Steurer, J., and Udas, S., 2003. Data report: Normalization factors for semiquantitative X-ray diffraction analysis, with application to DSDP Site 297, Shikoku Basin. In Mikada, H., Moore, G.F., Taira, A., Becker, K., Moore, J.C., and Klaus, A. (Eds.), *Proc. ODP, Sci. Results*, 190/196: 1–28.
- Varga, G., 2011. Similarities among the Plio–Pleistocene terrestrial aeolian dust deposits in the World and in Hungary. *Quaternary International* 234: 98–108.
- Varol, B., Baykal, M., and Ayyildiz, T. 2009. Sedimentological-stratigraphical evaluation of tertiary carbonates (Soğucak Formation) of Thrace Basin (Bozcaada – Kiyiköy). *Mineral Resource Exploration Bulletin*. 139: 1–15.
- Vlahović, I., Tišljarić, J., Velić, I., and Matičec, D. 2005. Evolution of the Adriatic Carbonate Platform: Paleogeography, Main Events and Depositional Dynamics. *Palaeo* 222: 333-60.
- Walker R.G, and Plint, A. G. 1992. Wave- and Storm-dominated Shallow Marine Systems. In: Walker, R. G., and James, N.P.. *Facies Models: Response to Sea Level Change*. 2nd ed. St. John's, Nfld.: Geological Association of Canada 1992: 219-38
- Weaver, C. E. 1989. *Clays, Muds, and Shales*. Amsterdam: Elsevier. pp. 7–10
- Williams, L. 2012. Holocene ostracod paleoecology of the southwestern Black Sea shelf. [Master's Thesis] St. John's: Memorial University.
- Yanko-Hombach, V., Meriç, E., Avşar, N., Kerey, E., Görmuş, M. 2004. Micropaleontological evidence of the Black Sea-Marmara Sea connection for the last 800 ka BP. In: 4th EMMM 2004, Program and Extended Abstracts of the Fourth International Congress on Environmental Micropalaeontology, Microbiology and Meiobenthology (13-18 September 2004, Isparta, Turkey), Yanko-Hombach, V., Grömüş, M., Ertunç, A., McGann, M., Martin, R., Jacob, J., Ishman, S. (Eds): 228–230.
- Yanko-Hombach, V., 2007. Controversy over Noah's Flood in the Black Sea: geological and foraminiferal evidence from the shelf. In: Yanko-Hombach, V., Gilbert, A.S., Panin, N., Dolukhanov, P.M. (Eds.), *The Black Sea Flood Question*. Springer, Dordrecht: 149–204
- Yaltrak, C., Ülgen, U.B., Zabcı, C., Franz, S.O., Ön, S.A., Sakınç, M., Namık, Ç., Alpar, B., Öztürk, K., Tunoğlu, C., and Ünlü, S. 2012. Discussion: a critique of possible

waterways between the Marmara Sea and the Black Sea in the Late Quaternary: evidence from ostracod and foraminifer assemblages in lakes Iznik and Sapanca, Turkey. *Geo-Marine Letters* 32.3: 267–274.

Yılmaz, Y., Tüysüz, O., Yiğitbaş, E., Can Genç, S., and A. M.C Şengör. 1997. Geology and tectonic evolution of the Pontides. *AAPG Memoir: Regional and Petroleum Geology of the Black Sea and Surrounding Region* 68: 184-226.

Yaltrak, C., Ülgen, U.B., Zabcı, C., Franz, S.O., Ön, S.A., Sakınç, M., Namık, Ç., Alpar, B., Öztürk, K., Tunoğlu, C., and Ünlü, S. 2012. Discussion: a critique of possible waterways between the Marmara Sea and the Black Sea in the Late Quaternary: evidence from ostracod and foraminifer assemblages in lakes Iznik and Sapanca, Turkey. *Geo-Marine Letters* 32.3: 267–274.

Appendix 1 XRD Sample Preparation

Samples were prepared for XRD using the following 13-step method:

1. Start with 5–10 g dry sediment, or 10–15 g wet mud. For dry samples, weigh in a tared vessel then enter in the laboratory log book and assign a lab number. For wet muds, simply enter in the log book and assign a lab number.
2. In a labeled plastic beaker, mix each sample with ~ 100 ml of 5% hydrogen peroxide. After adding the peroxide, subject the sample to ultrasonic treatment for ~ 2 minutes or until full disaggregation is evident. React each sample for 24 hours on a shaker at low speed. Renew peroxide if necessary to ensure complete reaction by adding 10 ml of 30% hydrogen peroxide from a graduated cylinder in the fume hood, followed by additional agitation as required. This treatment should remove organic matter and oxidize/solubilize microcrystalline to amorphous FeS.
3. Wet sieve at 63 μm using a large sieve, porcelain bowl and normal tap water. Keep all washings and transfer these to a labeled brown plastic container. Wash the sand fraction into a small labeled aluminum dish, then decant off water and dry in a warm oven (or air dry if space allows). Weigh the sand on a piece of glossy or wax paper, then store the sand in a labeled vial with the original sample number. A paint brush will assist transfer of the sand from the aluminum dish.
4. Allow the washings to settle until water is clear [if settling does not occur overnight, then add ~10 ml of saturated (~6 M; 0.56 g/l) MgCl_2 to flocculate the clays]. Suck off the "clear" water (might have Fe stain) using an aspirator attachment to a water faucet and transfer the sediment, with a minimum of water, to a labeled small heat-resistant beaker to dry. Place in an oven at 60°C for ~24 hours or more if required to achieve dryness. Carefully remove the dried cake and residue on the side of the beaker, weigh and store in a suitable labeled plastic vial.
5. Transfer the dried mud from step 4 to a labeled small beaker, add 40 ml 0.05% Na-hexametaphosphate (50 mg powder per 100 ml distilled water), then use the ultrasonic probe to disaggregate (2 minutes might be sufficient -- trial and error).
6. After disaggregation, transfer the suspension to a 400 ml labeled beaker, washing it in with 0.05% Na-hexametaphosphate. This beaker should have a mark 2 cm from the bottom and a second mark 5 cm higher, on the side of the beaker. Fill to the upper mark with 0.05% Na-hexametaphosphate.
7. Stand the beaker on the divider between lab benches, stir vigorously, then allow settling to proceed under still conditions for 3 hours & 50 minutes \pm 5 minutes (if you

miss the schedule, then start again after shaking the contents). Then siphon off the suspension between the two marks (~200 ml) using a thin-diameter piece of tubing, first filled with distilled water by lowering it into a tall graduated cylinder, blocking the end of the tubing with a finger tip in order to retain the water in the tube so that it is able to activate the siphon action. A 90 degree bend at the lower end of the tubing will prevent suction of sediment from below the lower mark. The suspension between the two marks should be siphoned into a 600 ml labeled beaker. Set this aside. Then add fresh 0.05% Na-hexametaphosphate to the upper mark of the 400 ml beaker, stir vigorously, then repeat the separation procedure (i.e., 3 hours & 50 minutes ...) once more. As before, siphon the upper suspension into the same 600 ml beaker. This is a mostly <2 μm separate that needs a bit more cleaning (see step 9 -- experience with one sample showed that this step 7 separate still contains ~20% >2 μm silt, measured with the Horiba size analyzer). Retrieve, dry, weigh and store the 2–63 μm fraction that remains in the bottom of the 400 ml beaker (experience with one sample showed that this separate is free of <2 μm clay). Use a glass vial labeled with the original sample number and "2–63 μm ". NOTE: This might be the largest volume separate of the entire procedure, and larger vials might be needed to hold the full amount. This is the final 2–63 μm separate.

8. Allow the 400 ml of suspension in the 600 ml beaker to settle overnight (otherwise centrifuge), then aspirate the clear fluid down the drain.

9. Using a minimum of 0.05% Na-hexametaphosphate, transfer the <2 μm fraction from step 8 to a labeled bulb-bottomed glass tube (Fig. 2.1) and fill to 5 cm above the neck with more 0.05% Na-hexametaphosphate. NOTE: make sure the sample suspension itself does not exceed the 5 cm mark on the tube. Stand the tube in a rack and allow settling to proceed under still conditions for 3 hours & 50 minutes \pm 5 minutes (if you miss the schedule, then start again after shaking the contents). Then block the neck of each tube with a special-purpose plastic rod and pour off the upper suspension into a labeled plastic beaker. This is the final <2 μm separate. Discard the small amount of silt below the neck of the tube, as it is contaminated by a little <2 μm material.

10. Wash the <2 μm separate into a standard labeled centrifuge tube with distilled water. Centrifuge once, pour off water, then resuspend in fresh distilled water and centrifuge again. Do this a third time then save the mud by transferring to a labeled aluminum dish for air drying. Weigh, then transfer the dried material to a labeled and sealed vial (including the words "<2 μm ") until XRD mounts are made. The weight needs to be multiplied by a factor of 1.5 to account for the <2 μm material that was discarded from the lower bulb of the test tube.

11. Grind an appropriate (~1.5 g), weighed amount of the 2-63 μm fraction in an agate mortar, along with MoS₂ powder that is ~5% of the sample weight used (~.08 g). The powder that results can then be used to make one XRD mount (silt mineralogy). Prepare this random mount using the side-packing procedure of John Hanchar. Special holders are available in the XRD lab and require ~1 cm³ of packed material. As much as

possible, the same mass of powder and the same packing density should be maintained for each mount.

12. Using 40 mg of the $< 2 \mu\text{m}$ fraction from step 10 mix with 2 mg of MoS_2 and apply sparse amounts ($\sim 2 \text{ ml}$) of 0.2 M MgCl_2 in a small beaker. Create a 'paste' and apply to a small piece of film. With gentle pressure smear across a marked acrylic disk. Once this is complete place the slide in the oven for ~ 5 minutes at $\sim 50^\circ\text{C}$ to dry. After 5 minutes remove from the oven, this is the final smear slide.

13. To prepare the $< 2 \mu\text{m}$ smear slides for glycolation fill a poreclain bowl with ethylene glycol and place in it the bottom of a desiccator. Place a number of smear slides on the elevated platform in the desiccator and put the apparatus into the oven at $\sim 60^\circ\text{C}$. Leave the slides in the oven for at least 8 hours to ensure saturation.

Appendix 2 Underwood et al. (2003) Clay Proportions

Table A2.1 Clay proportions calculated using the methods of Underwood et al. (2003), after applying the kaolinite/chlorite split. Values in **bold** are negative abundances that prompted a decision to use Biscaye (1965) methods with only the quartz proportions retained from Underwood et al. (2003) calculations.

Depth (cm)	Smectite	Illite	Chlorite	Kaolinite	Quartz	Total
10	52	43	-2	-3	9	100
30	24	37	7	10	22	100
50	44	46	-1	-1	12	100
70	30	46	3	3	18	100
90	45	41	1	2	12	100
110	35	39	3	3	21	100
150	39	45	1	1	14	100
170	30	40	2	5	23	100
260	40	37	2	2	20	100
330	27	36	5	6	26	100
370	25	37	7	9	22	100
410	28	44	2	3	22	100
430	47	32	6	9	6	100
470	23	28	11	16	21	100
490	36	47	1	1	15	100
510	28	44	3	4	21	100
530	23	25	16	19	17	100
570	33	35	5	5	22	100
590	28	74	-3	-3	4	100
600	34	37	6	3	20	100
610	46	34	5	3	13	100
630	32	38	8	3	20	100
650	52	12	4	3	30	100
670	33	30	8	5	25	100
690	41	36	2	2	20	100
720	27	32	6	4	31	100
730	35	31	5	2	26	100
750	44	46	0	-1	11	100
770	31	51	2	2	14	100
810	30	32	7	3	28	100
830	21	50	11	5	13	100
850	38	34	3	2	22	100
870	32	40	4	2	21	100
890	59	41	-1	-1	1	100
910	29	37	9	4	21	100
930	28	31	8	5	29	100

Appendix 3 Raw Geochemical Data

Raw geochemical data for MAR02–45, MAR08–17G, Danube Delta samples, and Thracian river samples. The headings for each column are explained as follows:

Lab #: the number given to each sample analysed in the laboratory at Memorial University. These samples were used for mineralogical analysis.

MAR02–45: The true depth of each sample, as indicated by TWC (trigger weight core) or P (piston core).

Act #: The number given to samples sent to ActLabs for geochemical analysis. These samples were stored separately from the Lab # samples under distilled water, and on average contained < 5 g of material per sample depth.

CC (cm): This column is the adjusted depth used for downcore plots and comparisons. The cross over between the trigger weight core and piston core is described in Hiscott et al. (2007).

Elements analysed and their detection limits (ppb, ppm, %) and their methods of analysis compose the next group of columns. IN–INAA analysis, M–Multiple methods (both INAA and ICP), IC–ICP-OES analysis, CE–Carlo-Erba analysis from Hiscott et al. (2007b).

The Silicate Total column was used to calculate calcite-free abundances as described in Chapter 3.

Table A3.1 Raw geochemical data for Au, Ag, Cu, Cd, Mo, Pb, and Ni.

Lab#	MAR 02-45	Act#	CC (cm)	Au	Ag	Cu	Cd	Mo	Pb	Ni
				ppb 2	ppm 0.3	ppm 1	ppm 0.3	ppm 1	ppm 3	ppm 1
				IN	M	ICP	ICP	ICP	ICP	M
	TWC-00	A1	0	7	< 0.3	58	0.4	5	41	62
450	TWC-10	A2	10	< 2	< 0.3	72	0.6	< 1	37	70
451	TWC-20	A3	20	< 2	< 0.3	53	0.4	< 1	32	65
452	TWC-30	A4	30	3	< 0.3	73	< 0.3	< 1	31	67
453	TWC-40	A5	40	< 2	< 0.3	45	0.4	< 1	26	68
454	TWC-50	A6	50	< 2	< 0.3	56	< 0.3	< 1	27	69
455	TWC-60	A7	60	7	< 0.3	51	0.3	< 1	27	71
456	TWC-70	A8	70	5	< 0.3	45	0.4	1	23	62
457	TWC-80	A9	80	8	< 0.3	53	0.5	< 1	25	67
458	TWC-90	A10	90	< 2	0.3	42	< 0.3	< 1	24	65
546	TWC-100	A11	100	< 2	< 0.3	50	< 0.3	< 1	21	64
547	TWC-110	A12		< 2	< 0.3	49	0.4	< 1	24	65
548	TWC-120	A13		< 2	< 0.3	44	< 0.3	< 1	25	65
549	TWC-130	A14		< 2	< 0.3	42	0.4	< 1	22	60
550	TWC-140	A15		< 2	< 0.3	41	0.3	< 1	25	60
551	TWC-150	A16		8	< 0.3	52	< 0.3	< 1	31	71
552	TWC-160	A17		9	< 0.3	50	< 0.3	< 1	32	69
553	TWC-170	A18		< 2	< 0.3	44	< 0.3	< 1	30	64
	P-0	B1	110	< 2	< 0.3	50	0.3	< 1	30	70
	P-10	B2	120	< 2	< 0.3	77	0.4	< 1	30	70
	P-20	B3	130	< 2	0.3	48	0.3	< 1	29	67
	P-30	B4	140	< 2	< 0.3	55	0.3	< 1	26	68
	P-40	B5	150	< 2	< 0.3	44	0.3	< 1	26	68
	P-50	B6	160	< 2	< 0.3	54	0.3	< 1	30	68
	P-60	B7	170	7	< 0.3	48	< 0.3	< 1	35	70
	P-70	B8	180	< 2	< 0.3	37	< 0.3	< 1	32	64
	P-80	B9	190	< 2	< 0.3	43	< 0.3	< 1	37	72
	P-90	B10	200	< 2	< 0.3	49	0.4	< 1	30	63
	P-100	B11	210	< 2	< 0.3	61	0.3	< 1	29	71
	P-110	B12	220	< 2	< 0.3	42	< 0.3	< 1	25	69
	P-120	B13	230	< 2	< 0.3	42	< 0.3	< 1	25	64
	P-130	B14	240	7	< 0.3	42	< 0.3	< 1	26	67
	P-140	B15	250	< 2	< 0.3	40	0.4	< 1	22	65
665	P-150	B16	260	< 2	< 0.3	63	< 0.3	< 1	23	64
	P-160	B17	270	< 2	< 0.3	45	< 0.3	< 1	18	62
	P-170	B18	280	< 2	< 0.3	49	0.5	2	17	58
	P-180	B19	290	7	< 0.3	64	< 0.3	< 1	21	68
	P-190	B20	300	< 2	< 0.3	55	< 0.3	< 1	22	69

Table A3.1 Continued.

Lab#	MAR 02-45	Act#	CC (cm)	Au	Ag	Cu	Cd	Mo	Pb	Ni
				ppb 2	ppm 0.3	ppm 1	ppm 0.3	ppm 1	ppm 3	ppm 1
				IN	M	ICP	ICP	ICP	ICP	M
	P-200	B21	310	< 2	< 0.3	59	0.4	< 1	18	70
	P-210	B22	320	< 2	< 0.3	57	< 0.3	< 1	20	65
391	P-220	B23	330	5	< 0.3	45	0.4	< 1	18	68
	P-230	B24	340	< 2	< 0.3	53	< 0.3	< 1	18	64
53	P-240	B25	350	< 2	< 0.3	48	< 0.3	< 1	17	59
	P-250	B26	360	< 2	< 0.3	37	0.4	< 1	17	50
390	P-260	B27	370	< 2	< 0.3	46	< 0.3	< 1	16	61
	P-270	B28	380	< 2	< 0.3	63	0.4	< 1	19	70
	P-280	B29	390	< 2	< 0.3	50	< 0.3	< 1	20	61
	P-290	B30	400	< 2	< 0.3	45	< 0.3	< 1	17	65
392	P-300	B31	410	< 2	< 0.3	63	< 0.3	< 1	21	60
	P-310	B32	420	< 2	< 0.3	36	0.3	< 1	16	57
60	P-320	B33	430	< 2	< 0.3	37	0.4	< 1	18	57
	P-330	B34	440	< 2	< 0.3	44	0.4	< 1	20	64
	P-340	B35	450	< 2	< 0.3	41	< 0.3	< 1	17	63
	P-350	B36	460	< 2	< 0.3	41	0.4	< 1	17	59
393	P-360	B37	470	4	< 0.3	59	< 0.3	< 1	20	64
	P-370	B38	480	< 2	< 0.3	30	0.4	< 1	13	44
394	P-380	B39	490	< 2	< 0.3	35	< 0.3	< 1	15	47
52	P-390	B40	500	< 2	< 0.3	30	0.4	< 1	12	39
395	P-400	B41	510	< 2	< 0.3	37	0.4	< 1	16	54
396	P-410	B42	520	6	< 0.3	36	< 0.3	< 1	17	49
397	P-420	B43	530	< 2	< 0.3	43	< 0.3	< 1	17	56
398	P-430	B44	540	6	< 0.3	28	< 0.3	< 1	14	46
51	P-440	B45	550	< 2	< 0.3	27	0.4	< 1	14	43
399	P-450	B46	560	7	< 0.3	29	< 0.3	< 1	16	48
400	P-460	B47	570	< 2	< 0.3	26	< 0.3	< 1	16	46
55	P-470	B48	580	< 2	< 0.3	38	0.4	< 1	16	50
589	P-480	B49	590	< 2	< 0.3	26	0.4	< 1	14	41
590	P-490	B50	600	< 2	< 0.3	35	0.3	< 1	15	48
591	P-500	B51	610	< 2	< 0.3	38	0.4	< 1	16	52
57	P-510	B52	620	< 2	< 0.3	30	0.3	< 1	14	50
592	P-520	B53	630	< 2	< 0.3	32	0.3	< 1	12	46
593	P-530	B54	640	< 2	< 0.3	33	< 0.3	< 1	13	45
594	P-540	B55	650	< 2	< 0.3	37	0.5	< 1	14	51
595	P-550	B56	660	6	< 0.3	35	< 0.3	< 1	15	51
596	P-560	B57	670	< 2	< 0.3	41	0.4	< 1	14	44
597	P-570	B58	680	< 2	< 0.3	41	< 0.3	< 1	14	52

Table A3.1 Continued.

Lab#	MAR 02–45	Act#	CC (cm)	Au	Ag	Cu	Cd	Mo	Pb	Ni
				ppb 2	ppm 0.3	ppm 1	ppm 0.3	ppm 1	ppm 3	ppm 1
				IN	M	ICP	ICP	ICP	ICP	M
598	P-580	B59	690	< 2	< 0.3	29	< 0.3	< 1	12	46
54	P-590	B60	700	< 2	< 0.3	35	< 0.3	< 1	13	51
599	P-600	B61	710	< 2	< 0.3	36	0.4	< 1	14	51
600	P-610	B62	720	< 2	< 0.3	33	0.5	< 1	12	48
601	P-620	B63	730	< 2	< 0.3	31	0.4	< 1	13	45
602	P-630	B64	740	< 2	< 0.3	31	< 0.3	< 1	12	46
603	P-640	B65	750	< 2	< 0.3	39	0.4	< 1	14	52
604	P-650	B66	760	< 2	< 0.3	40	0.4	< 1	15	52
50	P-660	B67	770	< 2	< 0.3	26	< 0.3	< 1	12	47
604	P-670	B68	780	4	< 0.3	32	0.4	< 1	14	51
606	P-680	B69	790	< 2	< 0.3	32	0.4	< 1	13	50
607	P-690	B70	800	< 2	< 0.3	36	0.3	< 1	14	52
608	P-700	B71	810	< 2	< 0.3	38	0.5	< 1	13	53
655	P-710	B72	820	< 2	< 0.3	40	< 0.3	< 1	15	49
58	P-720	B73	830	< 2	< 0.3	33	0.4	< 1	13	47
656	P-730	B74	840	3	< 0.3	43	0.3	< 1	13	47
657	P-740	B75	850	< 2	< 0.3	33	0.4	< 1	13	51
658	P-750	B76	860	< 2	< 0.3	16	< 0.3	< 1	9	30
659	P-760	B77	870	< 2	< 0.3	32	< 0.3	< 1	12	44
660	P-770	B78	880	6	< 0.3	40	< 0.3	< 1	16	52
59	P-780	B79	890	< 2	< 0.3	31	< 0.3	< 1	14	50
661	P-790	B80	900	< 2	< 0.3	29	< 0.3	< 1	11	41
662	P-800	B81	910	< 2	< 0.3	33	< 0.3	< 1	12	53
663	P-810	B82	920	< 2	< 0.3	28	0.4	< 1	11	46
664	P-820	B83	930	< 2	< 0.3	45	0.4	< 1	14	54
56	P-830	B84	940	< 2	< 0.3	19	< 0.3	< 1	9	37
MAR08–17G (cm)										
589B	34–36	C1		< 2	< 0.3	70	0.5	2	32	101
590B	64–66	C2		< 2	< 0.3	64	0.4	2	28	86
591B	94–96	C3		136	0.4	58	< 0.3	< 1	28	78
Danube Delta										
St.										
61	Georges 1	D1		< 2	0.4	81	0.8	< 1	63	91
St.										
63	Georges 2	D2		< 2	< 0.3	59	0.4	< 1	27	58
64	Sulina	D3		< 2	< 0.3	85	0.7	< 1	27	48
65	Chilia 1	D4		< 2	< 0.3	113	0.8	< 1	64	70
62	Chilia 2	D5		< 2	< 0.3	65	0.5	< 1	22	74

Table A3.1 Continued

			Au	Ag	Cu	Cd	Mo	Pb	Ni
			ppb	ppm	ppm	ppm	ppm	ppm	ppm
			2	0.3	1	0.3	1	3	1
			CC						
Thracian rivers	Act#	(cm)	IN	M	ICP	ICP	ICP	ICP	M
1	Kiyikoy	E1	< 2	< 0.3	58	< 0.3	< 1	15	22
3	Cilingoz	E2	14	< 0.3	110	< 0.3	3	21	24

Table A3.2 Raw data for Zn, S, Al, As, Ba, Be, Bi, Br, Ca, and Co.

		Zn	S	Al	As	Ba	Be	Bi	Br	Ca	Co
		ppm	%	%	ppm	ppm	ppm	ppm	ppm	%	ppm
		1	0.01	0.01	0.5	50	1	2	0.5	0.01	1
		CC									
Act#	(cm)	M	ICP	ICP	IN	IN	ICP	ICP	IN	ICP	IN
A1	0	119	0.02	5.08	9.3	490	2	< 2	5.7	4.13	17
A2	10	115	0.02	5.66	12.3	440	2	< 2	< 0.5	4.26	18
A3	20	109	0.01	5.13	10.7	510	2	< 2	2.8	4.29	18
A4	30	106	0.01	4.38	7.3	430	2	< 2	< 0.5	3.97	18
A5	40	99	0.02	4.89	11.6	550	2	< 2	3.1	4.15	19
A6	50	101	0.01	5.60	10.4	500	2	< 2	3.0	4.14	20
A7	60	101	0.01	5.46	9.4	440	2	< 2	< 0.5	4.38	18
A8	70	91	0.02	5.25	11.0	430	2	< 2	3.1	4.43	18
A9	80	101	0.02	5.45	7.6	400	2	< 2	< 0.5	4.76	17
A10	90	92	0.03	4.99	11.1	430	2	< 2	3.4	4.93	17
A11	100	92	0.03	5.10	7.6	470	2	< 2	3.2	5.17	16
A12		91	0.03	5.39	10.6	420	2	< 2	3.3	5.12	17
A13		90	0.04	5.14	10.2	510	2	< 2	4.2	5.21	18
A14		85	0.02	4.69	9.6	400	2	< 2	2.8	5.00	16
A15		84	0.04	4.98	11.0	300	2	< 2	2.9	4.91	17
A16		96	0.01	5.42	9.4	460	2	< 2	2.2	4.90	19
A17		96	0.02	5.33	11.0	400	2	< 2	3.4	5.13	18
A18		90	0.05	5.39	9.5	430	2	< 2	3.3	5.06	17
B1	110	106	0.02	5.57	9.0	490	2	< 2	2.2	4.51	18
B2	120	103	0.03	5.60	9.6	560	2	< 2	3.3	5.27	18
B3	130	92	0.06	5.24	12.9	460	2	< 2	3.5	5.42	17
B4	140	91	0.03	5.11	10.5	460	2	< 2	3.5	5.08	17
B5	150	91	0.05	5.17	11.0	400	2	< 2	3.2	5.17	17
B6	160	95	0.03	5.29	8.2	420	2	< 2	2.7	4.64	17
B7	170	100	0.02	4.02	10.7	480	2	< 2	3.8	4.65	17
B8	180	91	0.03	4.89	12.5	490	2	< 2	3.3	4.92	16
B9	190	100	0.03	5.23	10.5	450	2	< 2	3.0	4.90	19

Table A3.2 Continued.

		Zn ppm 1	S % 0.01	Al % 0.01	As ppm 0.5	Ba ppm 50	Be ppm 1	Bi ppm 2	Br ppm 0.5	Ca % 0.01	Co ppm 1
	CC										
Act#	(cm)	M	ICP	ICP	IN	IN	ICP	ICP	IN	ICP	IN
B10	200	87	0.07	5.36	8.7	410	2	< 2	3.9	5.30	15
B11	210	100	0.05	5.53	10.0	500	2	< 2	3.2	5.17	18
B12	220	92	0.09	5.50	8.5	410	2	< 2	3.9	5.22	17
B13	230	93	0.05	5.34	9.9	430	2	< 2	2.9	5.19	16
B14	240	90	0.08	5.19	9.9	550	2	< 2	2.6	5.12	18
B15	250	88	0.12	5.27	18.8	450	2	< 2	5.1	5.00	19
B16	260	95	0.11	4.06	28.9	510	2	< 2	6.4	4.85	24
B17	270	84	0.19	5.02	12.4	630	2	< 2	4.2	4.98	21
B18	280	88	0.39	4.99	15.1	400	2	< 2	10.6	5.67	19
B19	290	103	0.17	5.88	17.7	540	2	< 2	6.3	5.12	21
B20	300	99	0.14	5.77	13.5	550	2	< 2	9.0	4.94	20
B21	310	98	0.20	5.68	19.2	580	2	< 2	6.4	4.95	24
B22	320	97	0.15	5.61	15.2	590	2	< 2	6.5	4.95	19
B23	330	92	0.26	5.43	19.2	630	2	< 2	6.5	4.76	20
B24	340	90	0.29	5.42	28.8	510	2	< 2	9.4	4.03	22
B25	350	84	0.20	4.42	18.1	410	2	< 2	5.2	4.41	17
B26	360	78	0.16	4.45	23.8	300	2	< 2	6.8	4.06	19
B27	370	88	0.15	5.00	16.3	420	2	< 2	5.9	3.91	17
B28	380	105	0.15	5.70	19.1	520	3	< 2	7.0	3.99	18
B29	390	94	0.20	5.06	18.8	570	2	< 2	5.9	4.42	18
B30	400	89	0.36	5.54	19.9	510	2	< 2	5.4	4.46	17
B31	410	93	0.13	5.54	12.4	420	2	< 2	< 0.5	5.74	18
B32	420	82	0.17	4.98	14.3	420	2	< 2	4.0	5.23	17
B33	430	83	0.16	5.20	20.3	480	2	< 2	5.1	5.21	20
B34	440	91	0.21	5.57	14.5	680	2	< 2	5.1	5.11	17
B35	450	86	0.17	4.92	14.2	450	2	< 2	7.6	4.73	17
B36	460	83	0.22	4.80	14.3	590	2	< 2	9.0	5.34	17
B37	470	85	0.36	4.98	12.6	550	2	< 2	11.4	6.01	18
B38	480	63	0.12	4.24	13.3	< 50	2	< 2	2.7	6.39	14
B39	490	65	0.19	4.22	14.4	410	2	< 2	< 0.5	9.61	13
B40	500	57	0.15	4.08	12.6	270	2	< 2	2.7	6.73	13
B41	510	76	0.18	4.81	6.0	340	2	< 2	3.1	8.40	13
B42	520	70	0.10	4.78	8.5	280	2	< 2	2.7	7.05	14
B43	530	76	0.08	5.15	5.9	350	2	< 2	2.0	6.44	15
B44	540	66	0.10	4.53	6.2	350	2	< 2	1.8	5.68	13
B45	550	64	0.06	4.19	5.9	350	2	< 2	< 0.5	5.46	13
B46	560	70	0.09	4.40	6.0	380	2	< 2	2.5	6.01	13

Table A3.2 Continued.

		Zn ppm 1	S % 0.01	Al % 0.01	As ppm 0.5	Ba ppm 50	Be ppm 1	Bi ppm 2	Br ppm 0.5	Ca % 0.01	Co ppm 1
	CC										
Act#	(cm)	M	ICP	ICP	IN	IN	ICP	ICP	IN	ICP	IN
B47	570	68	0.12	4.29	7.4	420	2	< 2	2.2	6.75	13
B48	580	74	0.20	4.54	7.4	280	2	< 2	< 0.5	6.99	14
B49	590	59	0.25	4.08	9.1	360	2	< 2	2.2	6.28	13
B50	600	69	0.16	4.50	6.2	360	2	< 2	2.3	7.17	16
B51	610	71	0.22	4.55	5.5	320	2	< 2	5.5	7.78	16
B52	620	72	0.03	4.36	4.6	450	2	< 2	2.8	7.84	15
B53	630	65	0.03	3.95	5.5	450	2	< 2	< 0.5	7.36	15
B54	640	66	0.03	4.24	5.2	280	2	< 2	< 0.5	8.02	15
B55	650	73	0.02	4.50	6.1	410	2	< 2	< 0.5	8.24	15
B56	660	72	0.03	4.57	10.0	450	2	< 2	< 0.5	8.89	13
B57	670	64	0.02	3.90	7.7	< 50	2	< 2	< 0.5	8.48	15
B58	680	70	0.04	4.58	8.7	350	2	< 2	2.3	8.77	15
B59	690	64	0.03	4.39	5.9	390	2	< 2	2.3	8.98	15
B60	700	66	0.03	4.34	6.6	< 50	2	< 2	2.0	9.38	14
B61	710	67	0.04	4.45	6.0	430	2	< 2	< 0.5	10.10	14
B62	720	60	0.05	4.23	10.6	490	2	< 2	2.1	10.10	16
B63	730	59	0.03	3.89	6.0	290	2	< 2	1.1	9.47	11
B64	740	62	0.03	4.06	5.0	360	2	< 2	1.9	9.78	13
B65	750	68	0.02	4.21	8.2	370	2	< 2	< 0.5	10.80	16
B66	760	65	0.02	4.06	6.3	370	2	< 2	2.4	10.80	16
B67	770	57	0.03	3.88	6.4	370	2	< 2	1.9	9.84	14
B68	780	62	0.04	4.16	8.7	290	2	< 2	< 0.5	10.80	16
B69	790	62	0.04	4.26	6.3	340	2	< 2	2.1	10.90	14
B70	800	65	0.04	4.20	10.0	390	2	< 2	< 0.5	11.60	17
B71	810	67	0.03	4.35	7.4	500	2	< 2	2.6	11.70	17
B72	820	66	0.02	4.08	6.0	270	2	< 2	< 0.5	10.40	14
B73	830	60	0.03	3.89	4.9	270	2	< 2	2.1	11.00	14
B74	840	66	0.02	3.80	5.9	360	2	< 2	< 0.5	10.90	13
B75	850	64	0.03	4.07	8.0	340	2	< 2	3.3	11.30	14
B76	860	41	< 0.01	3.41	4.4	290	1	< 2	1.9	8.28	10
B77	870	57	0.01	3.78	7.6	460	2	< 2	< 0.5	11.00	13
B78	880	66	0.02	4.12	10.7	290	2	< 2	< 0.5	10.90	13
B79	890	64	0.07	4.10	18.2	270	2	< 2	2.1	9.94	14
B80	900	54	0.02	3.84	6.3	370	2	< 2	< 0.5	8.64	14
B81	910	65	0.02	4.35	5.7	430	2	< 2	2.4	10.10	13
B82	920	59	0.03	4.23	7.0	190	2	< 2	< 0.5	9.71	12
B83	930	96	0.10	4.64	16.7	440	2	< 2	1.8	10.20	16
B84	940	49	0.01	3.75	5.8	360	2	< 2	< 0.5	7.67	11

Table A3.2 Continued.

	Zn	S	Al	As	Ba	Be	Bi	Br	Ca	Co	
	ppm	%	%	ppm	ppm	ppm	ppm	ppm	%	ppm	
	1	0.01	0.01	0.5	50	1	2	0.5	0.01	1	
	CC										
Act#	(cm)	M	ICP	ICP	IN	IN	ICP	ICP	IN	ICP	IN
C1		117	0.13	6.59	12.7	400	2	< 2	11.3	1.82	18
C2		101	0.14	5.53	13.4	410	2	< 2	12.9	2.01	19
C3		101	0.11	4.86	12.1	460	2	< 2	16.2	2.81	17
D1		181	0.08	9.17	19.8	570	3	< 2	3.2	3.33	21
D2		93	0.04	4.4	12.2	340	2	< 2	2.3	4.03	17
D3		100	0.04	3.84	9.1	340	2	< 2	3.8	4.91	15
D4		170	0.04	5.21	10.7	530	2	< 2	6.4	4.21	19
D5		120	0.05	5.86	12	380	3	< 2	1	2.81	20
E1		73	0.02	4.16	6.1	550	2	< 2	4.6	5.04	10
E2		92	< 0.01	4.24	11	470	3	< 2	1.9	0.23	13

Table A3.3 Raw data for Cr, Cs, Eu, Fe, Hf, Hg, Ir, K., Mg, and Mn.

	Cr	Cs	Eu	Fe	Hf	Hg	Ir	K	Mg	Mn	
	ppm	ppm	ppm	%	ppm	ppm	ppb	%	%	ppm	
	2	1	0.2	0.01	1	1	5	0.01	0.01	1	
	CC										
Act#	(cm)	IN	IN	IN	IN	IN	IN	IN	ICP	ICP	ICP
A1	0	137	9	1.5	4.20	7	< 1	< 5	2.24	1.66	444
A2	10	146	10	1.6	4.57	5	< 1	< 5	2.44	1.72	484
A3	20	144	9	1.6	4.38	7	< 1	< 5	2.21	1.62	454
A4	30	148	10	1.5	4.53	7	< 1	< 5	2.14	1.57	450
A5	40	148	10	1.8	4.61	7	< 1	< 5	2.12	1.66	506
A6	50	150	10	1.8	4.83	6	< 1	< 5	2.29	1.68	474
A7	60	132	10	1.4	4.55	7	< 1	< 5	2.26	1.69	518
A8	70	134	9	1.7	4.40	8	< 1	< 5	2.17	1.68	478
A9	80	134	9	1.7	4.53	7	< 1	< 5	2.37	1.81	528
A10	90	137	8	1.6	4.26	8	< 1	< 5	2.23	1.81	539
A11	100	140	9	1.4	4.14	7	< 1	< 5	2.31	1.92	517
A12		131	9	1.6	4.19	7	< 1	< 5	2.22	1.84	526
A13		140	9	1.7	4.63	7	< 1	< 5	2.16	1.77	526
A14		135	8	1.5	4.09	7	< 1	< 5	2.01	1.68	496
A15		134	8	1.5	4.02	7	< 1	< 5	2.02	1.71	512
A16		136	10	1.6	4.50	7	< 1	< 5	2.25	1.83	502
A17		137	10	1.6	4.54	7	< 1	< 5	2.20	1.85	516
A18		133	9	1.6	4.02	7	< 1	< 5	2.18	1.87	518
B1	110	139	9	1.5	4.21	7	< 1	< 5	2.36	1.79	516

Table A3.3 Continued.

Act#	CC (cm)	Cr	Cs	Eu	Fe	Hf	Hg	Ir	K	Mg	Mn
		ppm 2	ppm 1	ppm 0.2	% 0.01	ppm 1	ppm 1	ppb 5	% 0.01	% 0.01	ppm 1
		IN	IN	IN	IN	IN	IN	IN	ICP	ICP	ICP
B2	120	142	10	1.6	4.56	6	< 1	< 5	2.42	1.94	543
B3	130	141	8	1.7	4.51	7	< 1	< 5	2.27	1.87	602
B4	140	136	9	1.7	4.38	7	< 1	< 5	2.23	1.88	532
B5	150	132	9	1.5	4.18	7	< 1	< 5	2.20	1.90	536
B6	160	133	9	1.6	4.33	7	< 1	< 5	2.17	1.77	507
B7	170	142	9	1.5	4.58	6	< 1	< 5	2.26	1.65	551
B8	180	136	9	1.7	4.17	7	< 1	< 5	2.07	1.71	495
B9	190	149	10	1.5	4.36	6	< 1	< 5	2.18	1.80	523
B10	200	131	8	1.5	3.83	7	< 1	< 5	2.17	1.92	501
B11	210	137	9	1.6	4.20	7	< 1	< 5	2.36	1.94	530
B12	220	127	9	1.5	4.20	6	< 1	< 5	2.34	1.96	530
B13	230	128	10	1.5	4.18	7	< 1	< 5	2.28	1.94	530
B14	240	135	9	1.5	4.24	6	< 1	< 5	2.28	1.93	541
B15	250	142	9	1.6	4.34	6	< 1	< 5	2.29	1.86	488
B16	260	183	11	2.0	5.44	6	< 1	< 5	2.14	1.64	477
B17	270	177	9	1.8	5.06	8	< 1	< 5	1.85	1.86	577
B18	280	183	11	1.8	5.75	8	< 1	< 5	2.01	1.83	743
B19	290	172	12	1.8	5.66	6	< 1	< 5	2.40	1.98	861
B20	300	178	11	1.8	5.36	7	< 1	< 5	2.41	2.01	682
B21	310	182	11	1.8	5.40	7	< 1	< 5	2.43	2.09	637
B22	320	182	11	1.9	5.07	8	< 1	< 5	2.41	2.01	545
B23	330	185	12	1.9	5.58	7	< 1	< 5	2.30	1.89	734
B24	340	182	11	1.9	6.66	8	< 1	< 5	2.13	1.74	654
B25	350	144	9	1.5	4.87	6	< 1	< 5	2.04	1.69	577
B26	360	165	9	1.5	5.09	6	< 1	< 5	1.78	1.74	451
B27	370	155	8	1.5	4.64	6	< 1	< 5	2.08	1.74	485
B28	380	160	9	1.8	5.10	7	< 1	< 5	2.46	1.95	529
B29	390	157	7	1.8	4.76	8	< 1	< 5	2.18	1.87	565
B30	400	159	8	1.3	4.79	7	< 1	< 5	2.25	1.85	526
B31	410	146	8	1.7	4.22	7	< 1	< 5	2.25	1.99	588
B32	420	155	7	1.4	4.05	7	< 1	< 5	2.16	1.95	581
B33	430	163	9	1.8	4.72	7	< 1	< 5	2.15	1.96	573
B34	440	157	9	1.5	4.64	6	< 1	< 5	2.26	1.88	617
B35	450	155	8	1.7	4.58	7	< 1	< 5	2.14	1.72	603
B36	460	151	8	1.8	4.50	7	< 1	< 5	2.10	1.74	587
B37	470	171	9	1.9	4.47	7	< 1	< 5	2.24	1.85	659

Table A3.3 Continued.

Act#	CC (cm)	Cr	Cs	Eu	Fe	Hf	Hg	Ir	K	Mg	Mn
		ppm 2	ppm 1	ppm 0.2	% 0.01	ppm 1	ppm 1	ppb 5	% 0.01	% 0.01	ppm 1
		IN	IN	IN	IN	IN	IN	IN	ICP	ICP	ICP
B38	480	109	6	1.4	3.26	10	< 1	< 5	1.83	1.57	458
B39	490	108	7	1.3	3.63	7	< 1	< 5	1.85	1.57	480
B40	500	108	6	1.5	3.08	10	< 1	< 5	1.69	1.53	502
B41	510	113	6	1.3	3.28	6	< 1	< 5	2.16	1.81	600
B42	520	115	7	1.7	3.25	8	< 1	< 5	2.02	1.67	559
B43	530	120	6	1.7	3.57	7	< 1	< 5	2.23	1.76	523
B44	540	108	4	1.7	3.18	10	< 1	< 5	1.98	1.58	506
B45	550	104	7	1.5	3.15	8	< 1	< 5	1.91	1.52	527
B46	560	99	7	1.5	3.35	8	< 1	< 5	2.00	1.57	550
B47	570	104	7	1.7	3.46	7	< 1	< 5	1.95	1.57	570
B48	580	118	7	1.5	3.85	7	< 1	< 5	2.07	1.67	618
B49	590	104	6	1.5	3.29	9	< 1	< 5	1.85	1.54	490
B50	600	115	7	1.5	3.70	7	< 1	< 5	2.06	1.71	570
B51	610	107	7	1.7	3.64	6	< 1	< 5	2.04	1.74	608
B52	620	97	9	1.6	3.39	6	< 1	< 5	2.01	1.73	589
B53	630	104	7	1.6	3.48	7	< 1	< 5	1.74	1.57	568
B54	640	110	6	1.5	3.32	7	< 1	< 5	1.81	1.67	559
B55	650	113	7	1.6	3.71	6	< 1	< 5	1.94	1.76	616
B56	660	110	7	1.5	3.70	6	< 1	< 5	1.94	1.81	582
B57	670	100	6	1.5	3.34	9	< 1	< 5	1.72	1.78	559
B58	680	116	7	1.5	3.77	6	< 1	< 5	1.87	1.82	610
B59	690	113	6	1.6	3.28	7	< 1	< 5	1.89	1.92	569
B60	700	146	9	1.4	3.72	7	< 1	< 5	1.90	1.83	602
B61	710	163	7	1.1	3.52	6	< 1	< 5	1.99	1.89	619
B62	720	143	7	1.4	3.79	6	< 1	< 5	1.83	1.87	603
B63	730	149	6	1.6	3.17	7	< 1	< 5	1.74	1.81	615
B64	740	146	7	1.4	3.37	6	< 1	< 5	1.75	1.75	594
B65	750	153	7	1.3	3.72	4	< 1	< 5	1.81	1.77	680
B66	760	153	7	1.1	3.75	6	< 1	< 5	1.82	1.78	678
B67	770	142	6	1.4	2.97	7	< 1	< 5	1.74	1.77	589
B68	780	149	7	1.4	3.60	4	< 1	< 5	1.82	1.85	711
B69	790	140	7	1.6	3.68	6	< 1	< 5	1.83	1.80	632
B70	800	156	7	1.4	3.68	6	< 1	< 5	1.85	1.88	761
B71	810	107	7	1.6	3.68	6	< 1	< 5	1.93	1.94	720
B72	820	102	7	1.6	3.60	7	< 1	< 5	1.81	1.90	713
B73	830	99	7	1.4	3.09	6	< 1	< 5	1.73	1.86	654
B74	840	106	7	1.6	3.27	6	< 1	< 5	1.71	1.78	719

Table A3.3 Continued.

		Cr	Cs	Eu	Fe	Hf	Hg	Ir	K	Mg	Mn
		ppm	ppm	ppm	%	ppm	ppm	ppb	%	%	ppm
		2	1	0.2	0.01	1	1	5	0.01	0.01	1
	CC										
	(cm)	IN	IN	IN	IN	IN	IN	IN	ICP	ICP	ICP
B75	850	110	7	1.3	3.52	4	< 1	< 5	1.82	1.81	679
B76	860	106	3	1.9	2.36	13	< 1	< 5	1.44	1.83	542
B77	870	96	6	1.4	2.95	6	< 1	< 5	1.65	1.79	642
B78	880	110	6	1.3	3.70	6	< 1	< 5	1.81	1.84	655
B79	890	114	6	1.6	4.29	4	< 1	< 5	1.80	1.80	696
B80	900	103	4	1.6	3.02	9	< 1	< 5	1.66	1.88	708
B81	910	104	7	1.4	3.46	6	< 1	< 5	1.91	1.97	788
B82	920	107	7	1.2	3.51	7	< 1	< 5	1.85	1.99	730
B83	930	118	8	1.5	4.08	5	< 1	< 5	1.96	1.95	665
B84	940	104	4	1.2	2.47	8	< 1	< 5	1.50	1.73	577
C1		209	7	1.6	3.87	6	< 1	< 5	2.06	1.22	578
C2		209	6	1.6	3.76	7	< 1	< 5	1.8	1.02	648
C3		220	6	1.4	3.7	7	< 1	< 5	1.7	0.96	656
D1		149	9	1.4	5.14	4	< 1	< 5	2.64	2	1110
D2		115	6	1.2	3.62	6	< 1	< 5	2.03	1.41	744
D3		150	4	1.9	3.6	21	< 1	< 5	1.57	1.52	734
D4		131	7	1.5	4.08	9	< 1	< 5	2.74	1.6	874
D5		143	10	1.3	4.92	4	< 1	< 5	3.92	1.67	839
E1		58	4	1.5	2.79	19	< 1	< 5	1.96	0.58	564
E2		85	5	1.4	3.23	11	< 1	< 5	1.73	0.34	460

Table A3.4 Raw data for Na, P, Rb, Sb, Sc, Se, Sr, Ta, Ti, and Th.

		Na	P	Rb	Sb	Sc	Se	Sr	Ta	Ti	Th
		%	%	ppm	ppm	ppm	ppm	ppm	ppm	%	ppm
		0.01	0.001	15	0.1	0.1	3	1	0.5	0.01	0.2
	CC										
Act#	(cm)	IN	ICP	IN	IN	IN	IN	ICP	IN	ICP	IN
A1	0	0.96	0.252	144	1.9	16.3	< 3	163	< 0.5	0.39	13.9
A2	10	0.85	0.238	170	2.0	16.6	< 3	173	1.9	0.40	14.7
A3	20	0.90	0.205	154	1.6	16.1	< 3	168	2.1	0.30	14.6
A4	30	0.81	0.169	127	1.7	16.4	< 3	147	< 0.5	0.39	14.5
A5	40	0.86	0.213	151	1.5	16.6	< 3	143	3.2	0.39	15.0
A6	50	0.87	0.193	153	1.9	16.9	< 3	157	2.0	0.29	15.7
A7	60	0.78	0.165	137	1.5	16.2	< 3	157	2.7	0.26	13.9
A8	70	0.92	0.190	142	1.5	16.0	< 3	152	< 0.5	0.40	14.1
A9	80	0.82	0.236	112	1.5	15.8	< 3	165	1.9	0.42	15.0

Table A3.4 Continued.

		Na	P	Rb	Sb	Sc	Se	Sr	Ta	Ti	Th
		%	%	ppm	ppm	ppm	ppm	ppm	ppm	%	ppm
		0.01	0.001	15	0.1	0.1	3	1	0.5	0.01	0.2
	CC										
Act#	(cm)	IN	ICP	IN	IN	IN	IN	ICP	IN	ICP	IN
A10	90	0.93	0.212	162	1.5	15.4	< 3	169	2.0	0.44	14.8
A11	100	0.95	0.238	142	1.5	14.6	< 3	175	3.4	0.47	13.6
A12		0.90	0.264	154	1.5	15.0	< 3	170	2.8	0.44	14.0
A13		0.84	0.211	154	1.6	15.9	< 3	177	2.0	0.34	14.9
A14		0.91	0.193	164	1.4	14.6	< 3	163	1.9	0.32	13.9
A15		0.90	0.153	142	1.6	14.6	< 3	158	1.3	0.33	13.9
A16		0.84	0.164	124	1.5	15.7	< 3	160	3.6	0.25	14.3
A17		0.86	0.192	171	1.6	15.7	< 3	167	< 0.5	0.32	14.2
A18		0.88	0.195	129	1.5	14.5	< 3	165	2.4	0.43	13.8
B1	110	0.86	0.224	127	1.4	15.4	< 3	170	1.7	0.47	14.2
B2	120	0.81	0.253	135	1.5	16.1	< 3	181	3.2	0.47	14.0
B3	130	0.87	0.285	139	1.7	15.4	< 3	178	< 0.5	0.39	14.4
B4	140	0.84	0.280	161	1.9	15.4	< 3	172	2.1	0.44	13.9
B5	150	0.87	0.223	175	1.5	14.3	< 3	170	2.0	0.45	13.4
B6	160	0.83	0.219	122	1.6	15.2	< 3	156	< 0.5	0.36	14.4
B7	170	0.79	0.179	136	1.6	15.5	< 3	151	2.8	0.26	14.0
B8	180	0.84	0.158	139	1.8	14.6	< 3	162	1.7	0.28	13.7
B9	190	0.79	0.164	155	1.8	15.7	< 3	163	2.0	0.22	13.9
B10	200	0.89	0.183	139	1.5	13.9	< 3	169	1.8	0.40	13.6
B11	210	0.77	0.228	169	1.9	15.4	< 3	178	2.9	0.42	14.2
B12	220	0.79	0.201	136	1.4	15.0	< 3	180	1.6	0.41	13.9
B13	230	0.86	0.207	139	1.4	14.7	< 3	174	2.9	0.35	13.7
B14	240	0.79	0.187	169	1.4	15.2	< 3	170	1.9	0.37	13.3
B15	250	0.78	0.185	140	1.6	15.5	< 3	160	2.8	0.30	14.3
B16	260	0.90	0.161	209	1.8	18.2	< 3	157	2.5	0.23	15.9
B17	270	0.96	0.135	151	1.4	18.1	< 3	154	1.4	0.32	16.3
B18	280	0.81	0.230	166	1.4	17.3	< 3	179	2.6	0.26	16.2
B19	290	0.74	0.226	191	1.7	19.2	< 3	152	1.7	0.29	15.5
B20	300	0.79	0.200	173	1.5	19.0	< 3	149	3.5	0.33	16.8
B21	310	0.86	0.207	192	1.3	18.2	< 3	146	1.5	0.34	16.8
B22	320	0.91	0.173	164	1.3	17.9	< 3	152	3.8	0.35	15.9
B23	330	0.80	0.232	183	1.7	18.4	< 3	152	1.8	0.28	16.3
B24	340	0.83	0.231	157	1.3	18.1	< 3	139	3.3	0.24	17.6
B25	350	0.88	0.170	160	0.7	16.6	< 3	136	< 0.5	0.22	13.3
B26	360	0.83	0.129	163	1.2	17.8	< 3	124	< 0.5	0.25	14.4
B27	370	0.85	0.165	181	0.9	15.8	< 3	125	< 0.5	0.22	12.7
B28	380	0.72	0.243	164	1.1	15.8	< 3	137	< 0.5	0.17	12.3
B29	390	0.87	0.220	135	0.9	15.5	< 3	137	< 0.5	0.21	13.5

Table A3.4 Continued.

		Na	P	Rb	Sb	Sc	Se	Sr	Ta	Ti	Th
		%	%	ppm	ppm	ppm	ppm	ppm	ppm	%	ppm
		0.01	0.001	15	0.1	0.1	3	1	0.5	0.01	0.2
	CC										
Act#	(cm)	IN	ICP	IN	IN	IN	IN	ICP	IN	ICP	IN
B30	400	0.77	0.157	158	0.8	15.3	< 3	135	< 0.5	0.39	13.2
B31	410	0.80	0.288	132	0.7	14.4	< 3	169	1.9	0.29	11.3
B32	420	0.91	0.229	119	1.1	14.0	< 3	147	< 0.5	0.34	12.2
B33	430	0.84	0.218	152	1.2	15.2	< 3	149	< 0.5	0.32	13.1
B34	440	0.71	0.198	162	0.8	15.7	< 3	149	2.6	0.31	13.2
B35	450	0.76	0.160	114	1.1	15.1	< 3	142	< 0.5	0.24	13.0
B36	460	0.79	0.212	151	0.7	14.6	< 3	187	< 0.5	0.24	12.0
B37	470	0.72	0.164	< 15	0.8	15.3	< 3	211	< 0.5	0.29	13.1
B38	480	0.94	0.140	97	0.8	12.6	< 3	347	3.1	0.26	9.8
B39	490	0.76	0.244	98	1.0	13.3	< 3	828	< 0.5	0.21	9.9
B40	500	0.97	0.209	99	0.8	11.8	< 3	231	3.5	0.28	9.7
B41	510	0.77	0.213	81	1.0	13.9	< 3	254	< 0.5	0.39	9.9
B42	520	0.84	0.207	78	1.1	13.4	< 3	210	2.9	0.32	11.2
B43	530	0.81	0.256	101	0.8	14.3	< 3	192	2.1	0.40	10.8
B44	540	0.91	0.180	102	0.7	13.0	< 3	175	3.6	0.33	9.2
B45	550	0.90	0.167	102	0.6	12.9	< 3	158	3.1	0.26	11.2
B46	560	0.84	0.127	109	0.8	13.9	< 3	173	2.4	0.24	9.8
B47	570	0.83	0.135	99	1.0	13.9	< 3	186	2.2	0.23	10.9
B48	580	0.76	0.154	105	1.1	14.0	< 3	188	< 0.5	0.23	10.5
B49	590	0.93	0.194	93	0.7	12.2	< 3	179	3.6	0.27	9.7
B50	600	0.83	0.214	91	0.9	13.9	< 3	194	2.5	0.36	10.6
B51	610	0.80	0.230	102	1.0	13.9	< 3	210	2.8	0.34	10.9
B52	620	0.83	0.140	112	0.7	14.4	< 3	213	2.9	0.38	10.4
B53	630	0.86	0.199	135	1.0	13.3	< 3	194	< 0.5	0.35	10.6
B54	640	0.84	0.164	65	0.9	12.8	< 3	210	< 0.5	0.31	9.3
B55	650	0.80	0.159	77	1.0	13.5	< 3	224	2.9	0.31	10.6
B56	660	0.78	0.202	64	1.0	13.9	< 3	229	3.3	0.37	10.0
B57	670	0.93	0.181	74	0.7	12.8	< 3	217	< 0.5	0.32	9.6
B58	680	0.83	0.207	73	0.9	14.2	< 3	226	2.8	0.35	9.9
B59	690	0.88	0.165	102	0.7	13.2	< 3	231	2.9	0.40	10.1
B60	700	0.80	0.160	94	0.6	14.0	< 3	237	4.4	0.36	9.9
B61	710	0.80	0.179	74	0.7	13.7	< 3	256	2.4	0.39	10.2
B62	720	0.84	0.176	104	0.9	13.0	< 3	253	3.0	0.37	9.3
B63	730	0.89	0.186	83	0.7	12.3	< 3	234	< 0.5	0.33	9.7
B64	740	0.82	0.179	99	1.1	12.9	< 3	228	3.0	0.32	9.9
B65	750	0.66	0.165	72	0.9	13.9	< 3	253	1.9	0.27	10.3
B66	760	0.66	0.116	97	1.0	14.0	< 3	250	4.4	0.21	10.2

Table A3.4 Continued.

		Na	P	Rb	Sb	Sc	Se	Sr	Ta	Ti	Th
		%	%	ppm	ppm	ppm	ppm	ppm	ppm	%	ppm
		0.01	0.001	15	0.1	0.1	3	1	0.5	0.01	0.2
	CC										
Act#	(cm)	IN	ICP	IN	IN	IN	IN	ICP	IN	ICP	IN
B67	770	0.80	0.126	79	1.0	12.4	< 3	232	2.4	0.35	9.3
B68	780	0.74	0.200	90	0.9	13.7	< 3	252	2.0	0.33	9.9
B69	790	0.73	0.204	89	0.9	13.9	< 3	252	3.4	0.33	9.9
B70	800	0.67	0.255	96	1.0	13.7	< 3	263	3.3	0.32	10.3
B71	810	0.74	0.230	114	1.0	13.9	< 3	268	3.1	0.34	10.2
B72	820	0.79	0.267	86	0.6	13.4	< 3	238	4.1	0.30	10.9
B73	830	0.82	0.204	59	0.6	12.4	< 3	243	2.3	0.33	9.6
B74	840	0.70	0.200	56	0.9	13.0	< 3	242	3.3	0.32	9.3
B75	850	0.76	0.169	73	0.9	13.7	< 3	248	2.6	0.23	9.7
B76	860	1.13	0.067	47	0.7	10.9	< 3	198	3.4	0.34	11.0
B77	870	0.82	0.105	102	0.7	11.7	< 3	240	3.9	0.22	8.4
B78	880	0.70	0.175	124	0.9	13.4	< 3	241	4.3	0.26	9.7
B79	890	0.77	0.264	93	1.1	13.4	< 3	225	< 0.5	0.33	9.2
B80	900	1.00	0.124	63	0.9	11.6	< 3	202	3.0	0.38	10.3
B81	910	0.90	0.217	82	0.7	13.4	< 3	231	2.6	0.38	9.3
B82	920	0.99	0.176	77	0.8	12.5	< 3	235	4.1	0.39	9.9
B83	930	0.73	0.163	111	1.0	14.7	< 3	233	4.5	0.37	10.0
B84	940	1.18	0.103	67	0.7	10.3	< 3	198	< 0.5	0.32	8.8
C1		0.8	0.114	95	1.2	19	< 3	132	0.8	0.41	14.5
C2		0.98	0.116	86	1.2	17.3	< 3	126	0.8	0.38	13
C3		0.97	0.101	75	1.1	15.3	< 3	160	< 0.5	0.29	11.8
D1		0.63	0.423	133	3.8	18.7	< 3	154	1.4	0.61	13.3
D2		0.99	0.116	107	1.4	13.2	< 3	146	1.5	0.35	11.3
D3		1.16	0.095	55	1.1	12.1	< 3	155	0.7	0.34	17.5
D4		0.86	0.241	99	1.4	15.1	< 3	146	1.7	0.24	13.8
D5		0.47	0.221	142	1.4	18.8	< 3	127	1.5	0.41	12.6
E1		1.7	0.127	129	0.7	11.2	< 3	255	2	0.4	10.3
E2		1.01	0.104	107	1.3	11.7	< 3	69	3.1	0.19	14.1

Table A3.5 Raw data for U, V, W, Y, La, Ce, Nd, Sm, Sn, and Tb.

Act#	CC (cm)	U	V	W	Y	La	Ce	Nd	Sm	Sn	Tb
		ppm 0.5	ppm 2	ppm 1	ppm 1	ppm 0.5	ppm 3	ppm 5	ppm 0.1	% 0.01	ppm 0.5
		IN	ICP	IN	ICP	IN	IN	IN	IN	IN	IN
A1	0	4.3	108	< 1	18	39.4	93	33	7.0	< 0.01	< 0.5
A2	10	5.1	114	< 1	19	37.2	86	31	6.6	< 0.01	< 0.5
A3	20	5.0	106	< 1	17	37.6	90	25	6.6	< 0.01	0.8
A4	30	6.2	110	7	15	37.5	87	31	6.4	< 0.01	0.7
A5	40	4.7	117	< 1	17	39.8	91	37	6.9	< 0.01	< 0.5
A6	50	3.8	117	< 1	18	38.5	88	30	6.8	< 0.01	< 0.5
A7	60	4.4	113	< 1	18	37.5	87	26	6.6	< 0.01	< 0.5
A8	70	5.4	109	6	18	38.5	90	23	6.8	< 0.01	1.2
A9	80	4.7	117	8	19	38.2	88	36	6.7	< 0.01	0.8
A10	90	5.6	113	< 1	18	37.9	85	28	6.8	< 0.01	< 0.5
A11	100	4.8	115	< 1	18	35.4	87	29	6.2	< 0.01	< 0.5
A12		4.3	113	< 1	18	37.2	85	35	6.4	< 0.01	0.9
A13		4.9	101	5	17	37.8	87	32	6.6	< 0.01	1.2
A14		4.4	101	< 1	17	36.3	86	32	6.4	< 0.01	< 0.5
A15		3.8	99	< 1	17	36.9	87	33	6.5	< 0.01	< 0.5
A16		4.7	109	< 1	17	37.7	86	32	6.6	< 0.01	0.9
A17		4.2	107	7	17	38.1	88	31	6.7	< 0.01	1
A18		4.4	109	< 1	18	36.2	87	32	6.4	< 0.01	< 0.5
B1	110	4.4	123	< 1	19	36.9	81	30	6.4	< 0.01	0.8
B2	120	4.7	124	< 1	19	37.7	91	35	6.6	0.05	0.9
B3	130	5.2	113	< 1	18	37.8	89	34	6.9	< 0.01	0.8
B4	140	4.2	112	< 1	18	37.1	89	28	6.5	< 0.01	0.9
B5	150	3.8	110	< 1	18	36.7	86	29	6.5	< 0.01	< 0.5
B6	160	4.3	106	< 1	17	37.2	82	29	6.6	< 0.01	0.9
B7	170	4.1	108	< 1	13	37.4	86	30	6.5	< 0.01	< 0.5
B8	180	4.6	98	< 1	17	36.3	87	32	6.4	< 0.01	< 0.5
B9	190	4.6	109	5	17	36.5	82	24	6.4	< 0.01	1
B10	200	4.0	103	< 1	18	35.2	78	27	6.1	< 0.01	0.9
B11	210	5.6	121	< 1	19	36.6	87	27	6.5	< 0.01	< 0.5
B12	220	4.3	115	< 1	18	34.8	83	29	6.2	< 0.01	1
B13	230	4.4	108	< 1	18	35.5	77	30	6.2	< 0.01	< 0.5
B14	240	3.8	113	< 1	18	34.9	84	28	6.2	< 0.01	< 0.5
B15	250	5.1	113	< 1	18	36.8	89	28	6.6	< 0.01	1
B16	260	7.1	110	< 1	14	42.2	98	30	7.6	< 0.01	0.8
B17	270	5.9	105	7	17	42.4	98	33	7.6	< 0.01	0.8
B18	280	7.1	98	< 1	16	42.2	93	30	7.2	< 0.01	0.8
B19	290	5.2	118	< 1	18	41.4	96	39	7.2	< 0.01	0.8

Table A3.5 Continued.

		U	V	W	Y	La	Ce	Nd	Sm	Sn	Tb
		ppm	ppm	ppm	ppm	ppm	ppm	ppm	ppm	%	ppm
		0.5	2	1	1	0.5	3	5	0.1	0.01	0.5
	CC										
Act#	(cm)	IN	ICP	IN	ICP	IN	IN	IN	IN	IN	IN
B20	300	5.5	119	< 1	18	43.4	103	35	7.4	< 0.01	< 0.5
B21	310	5.0	118	< 1	18	42.4	96	35	7.4	< 0.01	< 0.5
B22	320	5.0	116	< 1	19	43.3	98	37	7.6	< 0.01	0.8
B23	330	4.4	116	< 1	18	42.7	97	34	7.6	< 0.01	< 0.5
B24	340	5.4	107	7	17	43.2	103	39	7.7	< 0.01	< 0.5
B25	350	4.8	100	< 1	16	38.6	79	27	7.3	< 0.01	< 0.5
B26	360	4.0	87	< 1	17	40.5	85	35	7.6	< 0.01	0.9
B27	370	2.6	105	< 1	17	39.5	98	34	5.8	< 0.01	< 0.5
B28	380	2.8	121	< 1	18	38.1	89	27	5.5	< 0.01	< 0.5
B29	390	5.0	108	< 1	17	39.8	96	27	5.5	< 0.01	< 0.5
B30	400	2.0	111	< 1	18	37.8	90	30	5.5	< 0.01	< 0.5
B31	410	3.8	106	< 1	17	36.5	85	28	5.2	< 0.01	1.2
B32	420	3.4	101	< 1	18	39.3	94	24	5.5	< 0.01	1.4
B33	430	2.7	99	< 1	18	39.8	94	26	5.7	< 0.01	< 0.5
B34	440	3.5	110	< 1	18	39.1	94	32	5.5	< 0.01	1.3
B35	450	4.0	100	< 1	17	39.1	94	30	5.5	< 0.01	0.9
B36	460	5.2	98	< 1	17	38.1	86	31	5.4	< 0.01	< 0.5
B37	470	3.8	102	< 1	18	39.3	93	27	5.5	< 0.01	< 0.5
B38	480	3.5	78	< 1	17	37.7	78	24	6.0	< 0.01	< 0.5
B39	490	5.3	81	< 1	16	35.1	66	31	5.7	< 0.01	< 0.5
B40	500	2.9	75	< 1	17	38.6	77	28	6.3	< 0.01	< 0.5
B41	510	3.9	100	< 1	20	36.7	74	27	5.9	< 0.01	< 0.5
B42	520	3.4	91	< 1	19	38.4	83	28	6.2	< 0.01	< 0.5
B43	530	3.2	101	< 1	20	38.2	78	28	6.2	< 0.01	< 0.5
B44	540	3.5	85	< 1	18	37.8	74	32	6.2	< 0.01	< 0.5
B45	550	3.2	81	< 1	18	37.7	69	28	6.2	< 0.01	< 0.5
B46	560	3.4	86	< 1	18	38.1	73	36	5.9	< 0.01	1.4
B47	570	3.1	85	< 1	18	38.1	76	36	6.0	< 0.01	< 0.5
B48	580	1.8	91	5	19	37.7	71	39	6.0	< 0.01	1.3
B49	590	2.0	77	< 1	17	36.8	73	23	5.9	< 0.01	< 0.5
B50	600	3.0	91	< 1	18	37.1	74	26	6.1	< 0.01	< 0.5
B51	610	2.3	93	< 1	18	38.0	73	32	5.8	< 0.01	< 0.5
B52	620	2.2	92	< 1	18	38.6	75	33	6.1	< 0.01	1.2
B53	630	2.5	82	< 1	16	37.3	77	36	6.1	< 0.01	< 0.5
B54	640	3.0	82	< 1	17	37.7	73	29	6.1	< 0.01	0.9
B55	650	3.5	90	< 1	17	36.0	71	33	5.8	< 0.01	< 0.5
B56	660	2.3	89	< 1	17	36.3	70	36	5.8	< 0.01	< 0.5
B57	670	3.9	76	< 1	16	37.0	74	30	5.7	< 0.01	< 0.5

Table A3.5 Continued.

		U	V	W	Y	La	Ce	Nd	Sm	Sn	Tb
		ppm	ppm	ppm	ppm	ppm	ppm	ppm	ppm	%	ppm
		0.5	2	1	1	0.5	3	5	0.1	0.01	0.5
	CC										
Act#	(cm)	IN	ICP	IN	ICP	IN	IN	IN	IN	IN	IN
B58	680	3.2	88	< 1	17	36.0	73	22	5.8	< 0.01	< 0.5
B59	690	3.0	82	4	17	37.6	75	22	6.2	< 0.01	< 0.5
B60	700	3.1	88	< 1	16	37.2	72	24	5.9	< 0.01	< 0.5
B61	710	2.1	91	< 1	17	35.6	76	34	5.9	< 0.01	< 0.5
B62	720	3.1	84	< 1	16	36.2	73	27	5.9	< 0.01	< 0.5
B63	730	3.3	76	< 1	16	36.5	72	36	5.9	< 0.01	< 0.5
B64	740	3.3	79	< 1	16	35.2	74	33	5.6	< 0.01	1.3
B65	750	2.6	88	< 1	16	34.6	70	24	5.6	< 0.01	< 0.5
B66	760	2.7	83	< 1	16	35.5	66	37	5.4	< 0.01	< 0.5
B67	770	2.6	79	< 1	16	35.0	70	26	5.4	< 0.01	1.1
B68	780	2.3	86	< 1	16	34.3	70	30	5.7	< 0.01	< 0.5
B69	790	2.0	87	< 1	16	35.9	67	26	5.7	< 0.01	< 0.5
B70	800	2.4	90	< 1	16	34.7	67	26	5.6	< 0.01	< 0.5
B71	810	3.0	94	< 1	17	34.0	73	29	5.4	< 0.01	< 0.5
B72	820	2.4	84	< 1	17	38.8	76	27	6.1	< 0.01	1.4
B73	830	3.3	81	< 1	16	33.7	66	26	5.3	< 0.01	< 0.5
B74	840	2.3	82	< 1	16	34.3	69	27	5.7	< 0.01	< 0.5
B75	850	2.1	87	< 1	16	34.6	69	26	5.4	< 0.01	< 0.5
B76	860	3.3	58	< 1	17	44.3	82	36	7.0	< 0.01	< 0.5
B77	870	2.9	74	5	15	31.6	66	23	5.1	< 0.01	0.9
B78	880	2.4	83	< 1	16	34.0	70	21	5.6	< 0.01	< 0.5
B79	890	2.7	90	< 1	16	34.2	70	37	5.3	< 0.01	< 0.5
B80	900	2.6	75	< 1	16	37.6	76	34	6.1	< 0.01	< 0.5
B81	910	1.6	92	< 1	16	34.0	66	31	5.4	< 0.01	< 0.5
B82	920	< 0.5	85	< 1	16	34.7	70	26	5.8	< 0.01	1.2
B83	930	3.0	98	< 1	17	35.3	67	33	5.8	< 0.01	< 0.5
B84	940	3.4	62	< 1	14	34.0	64	25	5.5	< 0.01	1.2
C1		4	117	146	< 1	22	28	41.8	73	28	5.7
C2		4.4	107	134	2	21	26	41.7	75	34	5.6
C3		4	75	94	< 1	20	25	39.5	70	26	5.2
D1		3.6	129	161	< 1	35	44	42.8	80	31	5.9
D2		2.8	84	105	2	18	23	37.5	70	23	5.4
D3		5	73	91	4	23	29	59.6	114	40	8.3
D4		3	112	140	< 1	22	28	45.2	84	33	6.5
D5		2.1	144	180	< 1	19	24	38.5	68	24	5.4
E1		4.3	59	74	< 1	20	25	43.2	79	28	6.2
E2		5.2	47	59	3	17	21	44.2	85	30	5.8

Table A3.6 Raw data for Yb, Lu, sample mass, TS, TOC, Terr. Toc, and silicate total

Act#	CC (cm)	Yb	Lu	Mass	TS	TOC	Terrigenous	Silicate
		ppm 0.2	ppm 0.05	g	%	%	fraction of TOC (x/1)	Tot.
		IN	IN	IN	CE		Method in Hiscott et al. (2007b)	
A1	0	3.8	0.43	1.31	0.14	1.43	0.48	92.9
A2	10	3.8	0.42	1.22	0.16	1.25	0.59	92.7
A3	20	3.9	0.44	1.27	0.19	1.05	0.63	92.3
A4	30	3.8	0.37	1.34	0.15	0.90	0.63	92.6
A5	40	3.8	0.40	1.23	0.21	0.99	0.70	92.8
A6	50	3.8	0.44	1.15	0.18	0.95	0.69	91.2
A7	60	3.8	0.41	1.33	0.14	0.82	0.71	92.0
A8	70	4.2	0.43	1.16	0.18	0.90	0.74	91.2
A9	80	3.8	0.48	1.27	0.17	0.85	0.74	90.7
A10	90	4.0	0.44	1.14	0.12	0.91	0.81	90.8
A11	100	3.5	0.40	1.25	0.24	1.02	0.74	89.2
A12		3.5	0.40	1.35				89.4
A13		3.8	0.37	1.13				89.1
A14		3.7	0.38	1.34				89.8
A15		4.1	0.45	1.23				90.2
A16		3.7	0.37	1.27				90.2
A17		4.0	0.56	1.18				89.4
A18		3.7	0.37	1.25				89.6
B1	110	3.9	0.40	1.27	0.22	0.90	0.77	87.8
B2	120	3.7	0.35	1.20	0.13	1.10	0.76	88.9
B3	130	4.1	0.41	1.26	0.21	0.86	0.79	89.4
B4	140	3.9	0.39	1.18	0.28	0.84	0.79	89.6
B5	150	3.6	0.36	1.20	0.22	0.82	0.72	90.1
B6	160	3.7	0.34	1.26	0.29	1.00	0.75	91.1
B7	170	3.4	0.42	1.14	0.20	0.97	0.78	91.1
B8	180	3.8	0.36	1.15	0.34	1.07	0.76	90.1
B9	190	3.7	0.39	1.22	0.35	1.15	0.77	90.2
B10	200	3.6	0.39	1.35	0.35	0.98	0.76	88.8
B11	210	3.8	0.39	1.15	0.32	1.05	0.76	89.2
B12	220	3.5	0.41	1.33	0.32	1.10	0.80	89.1
B13	230	3.8	0.33	1.37	0.42	0.92	0.66	89.2
B14	240	3.3	0.34	1.22	0.41	1.07	0.77	89.4
B15	250	3.7	0.40	1.21	0.51	1.07	0.73	89.8
B16	260	4.2	0.46	1.13	0.73	0.91	0.72	90.4
B17	270	4.1	0.45	1.26	1.22	1.09	0.69	89.9
B18	280	3.9	0.40	1.14	1.69	0.85	0.74	87.5
B19	290	3.9	0.38	1.20	1.80	1.62	0.55	89.4

Table A3.6

Act#	CC (cm)	Yb	Lu	Mass	TS	TOC	Terrigenous	Silicate Tot.
		ppm 0.2	ppm 0.05	g	%	%	fraction of TOC (x/1)	
		IN	IN	IN	CE	CE	Method in Hiscott et al. (2007b)	
B20	300	4.2	0.40	1.29	1.85	1.41	0.59	90.0
B21	310	4.2	0.38	1.20	1.18	1.54	0.55	90.0
B22	320	4.2	0.45	1.21	1.40	1.97	0.68	90.0
B23	330	4.2	0.41	1.31	1.05	1.23	0.63	89.0
B24	340	4.5	0.48	1.06	1.17	1.16	0.67	93.2
B25	350	3.4	0.54	1.19	1.62	1.63	0.48	88.7
B26	360	3.8	0.42	1.39	1.54	1.29	0.50	93.1
B27	370	3.0	0.55	1.31	1.34	1.52	0.59	91.5
B28	380	2.8	0.55	1.30	1.37	1.18	0.60	93.4
B29	390	3.4	0.59	1.18	2.13	1.30	0.54	91.9
B30	400	3.1	0.51	1.14	2.05	2.43	0.43	91.7
B31	410	2.8	0.54	1.42	2.27	1.52	0.60	87.3
B32	420	3.4	0.63	1.35	1.33	1.39	0.57	87.0
B33	430	3.3	0.52	1.23	1.46	1.40	0.78	89.1
B34	440	3.2	0.52	1.30	1.95	1.22	0.73	86.0
B35	450	3.0	0.48	1.45	1.55	1.32	0.75	90.8
B36	460	3.2	0.52	1.43	1.71	1.63	0.86	88.7
B37	470	3.3	0.59	1.25	1.55	1.35	0.73	86.3
B38	480	3.2	0.34	1.56	1.44	1.28	0.65	85.6
B39	490	2.5	0.22	1.38	1.21	0.54	0.75	73.7
B40	500	3.4	0.35	1.60	1.13	0.97	0.82	87.1
B41	510	3.1	0.50	1.44	1.09	0.53	0.85	78.0
B42	520	2.9	0.32	1.38	0.91	0.78	0.85	82.6
B43	530	3.4	0.50	1.60	0.93	0.60	0.88	84.8
B44	540	3.6	0.32	1.44	0.76	0.48	0.79	89.2
B45	550	3.2	0.29	1.45	1.05	0.54	0.86	88.2
B46	560	3.2	0.31	1.40	0.88	0.58	0.86	85.0
B47	570	3.2	0.31	1.37	1.07	0.76	0.92	83.7
B48	580	2.8	0.28	1.52	1.34	0.61	0.88	83.5
B49	590	3.3	0.35	1.61	1.67	0.61	0.91	85.4
B50	600	3.2	0.36	1.44	1.31	0.53	0.90	84.8
B51	610	3.0	0.46	1.49	0.91	0.51	0.88	80.1
B52	620	2.9	0.29	1.29	1.17	0.49	0.87	82.9
B53	630	3.3	0.25	1.32	0.14	0.75	0.87	81.6
B54	640	3.2	0.51	1.53	0.19	0.60	0.87	79.7
B55	650	2.9	0.25	1.29	0.34	0.70	0.88	78.5
B56	660	3.3	0.29	1.23	0.41	0.79	0.87	80.1

Table A3.6 Continued.

Act#	CC (cm)	Yb	Lu	Mass	TS	TOC	Terrigenous	Silicate
		ppm 0.2	ppm 0.05	g	%	%	fraction of TOC (x/1)	Tot.
		IN	IN	IN	CE	CE	Method in Hiscott et al. (2007b)	
B57	670	2.9	0.23	1.40	0.38	0.81	0.92	77.7
B58	680	3.0	0.42	1.25	0.21	0.50	0.92	82.0
B59	690	3.2	0.23	1.23	0.32	0.95	0.93	75.9
B60	700	2.9	0.44	1.20	0.19	0.91	0.92	77.8
B61	710	3.1	0.20	1.17	0.17	0.70	0.93	72.0
B62	720	2.9	0.14	1.12	0.33	0.92	0.96	72.8
B63	730	2.9	0.17	1.26	0.37	0.72	0.95	74.2
B64	740	3.1	0.19	1.25	0.12	0.65	0.90	76.1
B65	750	2.6	0.44	1.27	0.24	0.85	0.99	69.6
B66	760	2.9	0.41	1.18	0.27	0.84	0.93	67.6
B67	770	2.9	0.17	1.25	0.17	0.75	0.94	72.9
B68	780	2.9	0.14	1.20	0.13	0.76	0.95	70.8
B69	790	3.0	0.19	1.35	0.14	0.71	0.97	69.2
B70	800	2.9	0.09	1.15	0.16	0.82	0.93	68.1
B71	810	2.6	0.13	1.36	0.12	0.97	0.96	66.5
B72	820	3.0	0.47	1.20	0.16	0.72	0.93	68.5
B73	830	2.9	0.17	1.40	0.12	0.53	0.92	68.9
B74	840	2.9	0.16	1.29	0.12	0.65	0.96	65.4
B75	850	2.7	0.41	1.23	0.08	0.84	0.93	67.8
B76	860	4.0	0.33	1.33	0.28	0.83	0.93	65.4
B77	870	2.6	0.16	1.30	0.06	0.65	0.90	68.9
B78	880	2.9	0.44	1.15	0.12	0.78	0.90	67.1
B79	890	2.9	0.39	1.26	0.16	0.62	0.93	72.6
B80	900	3.3	0.47	1.38	0.71	0.83	0.95	70.1
B81	910	2.7	0.17	1.14	0.04	0.51	0.90	72.0
B82	920	3.0	0.18	1.22	0.10	0.79	0.97	72.1
B83	930	2.7	0.08	1.28	0.04	0.57	0.94	71.7
B84	940	3.0	0.29	1.40	0.10	1.00	0.99	69.8
C1		< 0.01	< 0.5	3.3				86.7
C2		< 0.01	0.5	3.6				100.0
C3		< 0.01	0.7	3.4				97.0

Table A3.6 Continued.

Act#	CC (cm)	Yb	Lu	Mass	TS	TOC	Terrigenous	Silicate
		ppm 0.2	ppm 0.05	g	%	%	fraction of TOC (x/1)	Tot.
		IN	IN	IN	CE	CE	Method in Hiscott et al. (2007b)	
D1		< 0.01	1.1	3.7				96.5
D2		< 0.01	0.7	3.5				95.1
D3		< 0.01	1.1	5.7				90.8
D4		< 0.01	0.7	3.8				91.5
D5		< 0.01	0.9	3.1				84.2
E1		< 0.01	0.7	5				84.0
E2		< 0.01	< 0.5	4.3				87.7

Appendix 4 XRD Standards Analysis

Measured and certified values for elements analyzed during 2011 and 2014 for this thesis. ^a represents standards run during 2011, ^b represents standards run during 2014.

Table A4.1 Measured and certified values for elements analyzed using INAA. Only elements analyzed during both (2011 and 2014) runs are included.

	Detection Limit		Method	DMMA _s 112 ^a		DMMA _s 112 ^a		DMMA _s 116 ^b	
				Meas	Cert	Meas	Cert	Meas	Cert
Au	2	ppb	INAA	1830	1721	1810	1721	1830	1610
As	0.5	ppm	INAA	1790	1862	1770	1862	1460	1560
Ba	50	ppm	INAA	1400	1288	1290	1288	1240	1190
Co	1	ppm	INAA	46	43	45	43	44	41
Cr	2	ppm	INAA	90	80	86	80	80	77
Fe	0.01	%	INAA	3.54	3.34	3.45	3.34	3.28	3.12
Na	0.01	%	INAA	2.12	2.05	2.04	2.05	2.04	1.98
Sc	0.1	ppm	INAA	7.30	7.17	7.00	7.17	5.90	6.30
U	0.5	ppm	INAA	17.80	17.84	17.90	17.84	10.40	11.20
La	0.5	ppm	INAA	18.3	15.92	18.2	15.92	15.5	15.9
Ce	3	ppm	INAA	30.00	26.56	28.00	26.56	30.00	30.00
Sm	0.1	ppm	INAA	2.70	2.34	2.50	2.34	2.30	2.40

Table A4.2 Measured and certified values for elements run using ICP analysis for the GXR-1, GXR-4, SDC-1, and OREAS 13b standards. Only elements analyzed during both (2011 and 2014) runs are included.

	Detection Limit			GXR-1 ^a		GXR-1 ^b		GXR-4 ^a		GXR-4 ^b		SDC-1 ^a		SDC-1 ^b		OREAS 13b ^a	
				Meas	Cert	Meas	Cert	Meas	Cert	Meas	Cert	Meas	Cert	Meas	Cert	Meas	Cert
Ag	0.3	ppm	ICP	28.3	31.0	31.2	31.0	2.9	4.0	3.7	4.0	< 0.3	0.041	< 0.3	0.041	0.70	0.86
Cu	1	ppm	ICP	1230	1110	1110	1110	6410	6520	6420	6520	29	30	41	30		
Cd	0.3	ppm	ICP	3.3	3.3	2.7	3.3	0.50	0.86	0.40	0.86	< 0.3	0.08	< 0.3	0.08	2210	2327
Mo	1	ppm	ICP	15	18	17	18	313	310	308	310	< 1	0.25	< 1	0.25	9	9
Pb	3	ppm	ICP	691	730	737	730	40	52	54	52	20	25	20	25		
Ni	1	ppm	ICP	46	41	41	41	43	42	55	42	37	38	36	38	2010	2247
Zn	1	ppm	ICP	722	760	799	760	73	73	95	73	96	103	105	103	94	133
S	0.01	%	ICP	0.230	0.257	0.240	0.257	1.80	1.77	1.78	1.77	0.060	0.065	0.070	0.065	1.05	1.20
Al	0.01	%	ICP	1.68	3.52	2.71	3.52	4.87	7.20	7.04	7.20	5.93	8.34	8.32	8.34		
Be	1	ppm	ICP	1.00	1.22	1.00	1.22	2.0	1.9	2.0	1.9	3	3	3	3		
Bi	2	ppm	ICP	1390	1380	1370	1380	12	19	10	19	< 2	2.6	< 2	2.6		
Ca	0.01	%	ICP	0.96	0.96	0.88	0.96	1.17	1.01	1.08	1.01	1.16	1.00	1.10	1.00		
K	0.01	%	ICP	0.05	0.05	0.05	0.05	3.45	4.01	2.68	4.01	2.68	2.72	2.49	2.72		
Mg	0.01	%	ICP	0.220	0.217	0.230	0.217	1.70	1.66	1.70	1.66	0.99	1.02	1.00	1.02		
Mn	1	ppm	ICP	926	852	910	852	151	155	161	155	830	883	905	880		
P	0.001	%	ICP	0.060	0.065	0.058	0.065	0.134	0.120	0.131	0.120	0.053	0.069	0.055	0.069		
Sr	1	ppm	ICP	296	275	287	275	202	221	220	221	166	183	174	180		
Ti	0.01	%	ICP			0.03	0.036			0.29	0.29	0.130	0.606	0.210	0.606		
V	2	ppm	ICP	96	80	87	80	95	87	89	87	44	102	50	102		
Y	1	ppm	ICP	27	32	27	32	13	14	13	14	30	40	32	40		

Table A4.3 Measured and certified values for elements run using ICP analysis for the SCO-1, GXR-6, DNC-1a, SAR-M, and SBC-1 standards. Only elements analyzed during both (2011 and 2014) runs are included.

	Detection Limit			SCO-1 ^a		GXR-6 ^a		GXR-6 ^b		DNC-1a ^a		DNC-1a ^b		SAR-M ^b		SNC-1 ^b	
				Meas	Cert	Meas	Cert	Meas	Cert	Meas	Cert	Meas	Cert	Meas	Cert	Meas	Cert
Ag	0.3	ppm	ICP	< 0.3	0.134	0.5	1.3	0.4	1.3					3.30	3.64		
Cu	1	ppm	ICP	27.0	28.7	61	66	70	66	89	100	97	100	307	331	34	31
Cd	0.3	ppm	ICP	0.40	0.14	0.40	0.10	< 0.3	1					4.90	5.27	0.3	0.4
Mo	1	ppm	ICP	< 1	1.37	< 1	2.4	3	2.4					8.0	13.1	4.0	2.4
Pb	3	ppm	ICP	27	31	81	101	91	101					983	982	25	35
Ni	1	ppm	ICP	30	27	26	27	27	27	241	247	238	247	48	41.5	86.0	82.8
Zn	1	ppm	ICP	97	103	117	118	132	118	48	70	60	70	911	930	191	186
S	0.01	%	ICP			0.010	0.016	0.020	0.016					6.29	6.30		
Al	0.01	%	ICP	5.01	7.24	10.6	17.7	14.5	17.7								
Be	1	ppm	ICP	2.00	1.84	1.0	1.4	1.0	1.4					3.0	2.2	3.0	3.2
Bi	2	ppm	ICP	< 2	0.37	< 2	0.29	< 2	0.29					< 2	1.084	< 2	0.7
Ca	0.01	%	ICP	2.13	1.87	0.27	0.18	0.21	0.18					0.67	0.61		
K	0.01	%	ICP	2.27	2.3	1.67	1.87	1.84	1.87					2.91	2.94		
Mg	0.01	%	ICP	1.60	1.64	0.680	0.609	0.640	0.609					0.5	0.5		
Mn	1	ppm	ICP	394	410	999	1010	1060	1010					4800	5220		
P	0.001	%	ICP	0.082	0.090	0.032	0.035	0.034	0.035					0.061	0.070		
Sr	1	ppm	ICP	159	174	48	35	45	35	121	144	129	144	152	151	182	178
Ti	0.01	%	ICP	0.31	0.38							0.27	0.29	0.30	0.38	0.52	0.51
V	2	ppm	ICP	130	131	137	186	128	186	141	148	137	148	52.0	67.2	224	220
Y	1	ppm	ICP	18	26	10	14	11	14	14	18	14	18	37	28	30.0	36.5

Appendix 5 XRF Data for Elements Analysed by XRF and ActLabs

Table A5.1 Raw data for elements analysed using the XRF at Memorial University.

Only elements which were analysed by both ActLabs and Memorial are presented in the table. Table 3.15 shows the ratios of the results for the two analytical techniques.

		Lab #			
		M36670D	M36671W	M36672Q	M36673K
		M02-45p 60	M02-45p 370	M02-45p 530	M02-45p 730
Na ₂ O	%	0.87	0.68	0.54	0.76
MgO	%	4.14	3.44	3.71	4.03
K ₂ O	%	2.47	2.10	2.25	1.98
CaO	%	7.42	8.86	11.87	15.84
Sc	ppm	16	13	17	17
V	ppm	104	73	95	81
Cr	ppm	133	117	122	111
MnO	%	0.07	0.07	0.09	0.10
Fe ₂ O ₃ T	%	5.68	4.96	5.38	4.50
Ni	ppm	53	40	44	39
Cu	ppm	31	26	28	28
Zn	ppm	42	30	33	28
Sr	ppm	171.0	366.8	229.3	240.5
Y	ppm	24.3	24.0	24.5	24.0
Ce	ppm	52	113	104	89
Pb	ppm	32	14	17	16
Th	ppm	12	11	9	8

Appendix 6 Calcite-free Downcore Plots

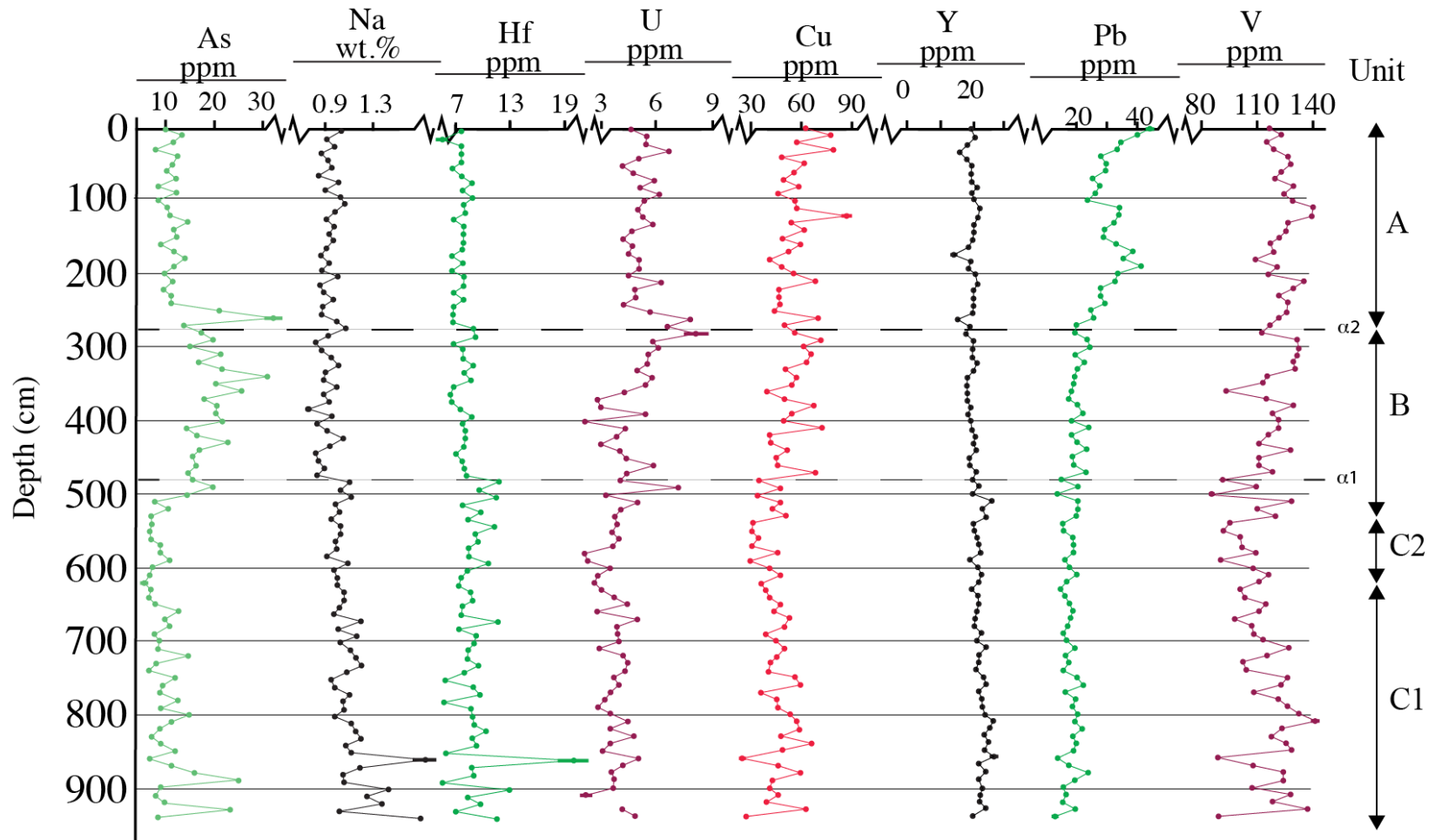


Figure A6.1 Caption can be found on the following page.

Figure A6.1 Caption. Downcore plots of calcite-free abundances for elements not presented in Fig. 3.13 and Fig. 4.2. These plots are considered to be the best estimate of actual trends in elemental composition in the silicate and organic fractions. Calcite-free abundances are determined as set out in §3.5.4. Mg, Mn and Sr are not included because they have moderate to strong cross-correlations with Ca and are therefore interpreted to occur mainly in detrital and biogenic calcite; presenting these elements on a calcite-free basis would only exaggerate the abundances in calcite-rich samples because of an invalid assumption that the elements are in the silicate and organic fractions. Fig. 3.13 presents equivalent plots for Sc, Ni, Cr, Zn and K; Fig. 4.2 for Co, Ce, Sc, La, Sm, Th, Fe and Y.